Analysis of Scattered Protons in Deuteron Electrodisintegration with a Polarized Electron Beam and an Internal Polarized Target

by

Aaron J. Maschinot

Submitted to the Department of Physics
in partial fulfillment of the requirements for the degree of

Doctor of Philosophy

at the

MASSACHUSETTS INSTITUTE OF TECHNOLOGY

September 2005

Author . . . .
Department of Physics
September 2, 2005

Certified by . . . .
Robert P. Redwine
Professor, Dean for Undergraduate Education
Thesis Supervisor

Accepted by . . . .
Thomas J. Greytak
Chairman, Department Committee on Graduate Students

Analysis of Scattered Protons in Deuteron Electrodisintegration with a Polarized Electron Beam and an Internal Polarized Target

by

Aaron J. Maschinot

Submitted to the Department of Physics
on September 2, 2005, in partial fulfillment of the
requirements for the degree of
Doctor of Philosophy

Abstract

Nuclear structure and the underlying internucleon (NN) interaction are central to the understanding of how nucleons interact. However, despite decades of research, Quantum Chromodynamics, which governs the interactions of quarks making up nucleons, continues to evade a fully tractable solution. As a result, understanding of the nucleon and how it interacts with other nucleons is not complete.

Due to its simple composition, the deuteron has long been important in understanding the structure of the NN potential. In particular, the tensor asymmetry, A_d^T, and beam-vector asymmetry, A_{ed}^V, from deuteron electrodisintegration, ${}^2\vec{H}(\vec{e}, e'N)N'$, are sensitive to the existence of a tensor component in the NN interaction.

The Bates Large Acceptance Spectrometer Toroid (BLAST) provides a unique opportunity to measure deuteron electrodisintegration asymmetries at low momentum transfer. BLAST combines a high-duty polarized electron beam, an Atomic Beam Source (ABS) target of highly-polarized deuterium atoms, and a large-acceptance spectrometer detector. This work reports on measurements of A_d^T and A_{ed}^V for Q^2 ranges between 0.1 and 0.5 $(\mathrm{GeV/c})^2$. Comparisons with Monte Carlo simulations based on the current understanding of the deuteron are made, and conclusions are drawn.

Thesis Supervisor: Robert P. Redwine
Title: Professor, Dean for Undergraduate Education

Acknowledgments

I would like to express my deepest gratitude to my thesis advisor, Prof. Robert Redwine. Bob has always been a supportive mentor, providing me with guidance when needed but yet allowing me the independence required of a scientist. Bob has always been approachable and encouraging of ideas; he treats his students like physicists and respects and values their opinions. Bob's enthusiasm for physics is contagious, and he is a great scientist for junior physicists to aspire to be like.

I would like to thank Dr. Douglas Hasell for, more than anyone, teaching me how to be a scientist. Working with Doug was watching a master with his craft. His intuitive understanding of experimental science and techniques is something that I will always strive for. Doug never once turned me away from his door; on the contrary, he was always quick to offer suggestions and new ways to think about problems.

I would also like to thank Dr. Tancredi Botto and Dr. Michael Kohl for all of the help and advice they offered me during my time at Bates. Both of them possess a wealth of physics knowledge and intuition; their help made my work much easier. I also owe a great deal of thanks to Dr. Tong-Uk Lee who took me under his wing during my first few years at MIT. I would also like to thank the other members of my thesis committee, Dr. William Donnelly and Prof. William Bertozzi, for their comments and critiques of my thesis. I would also like to thank Prof. Kevin McIlhany for all of our talks and guiding advice.

My research would not have been possible if not for the hard work of the Bates scientists and staff. Dr. Wilbur Franklin and Dr. Taylan Akdogan were very successful in the smooth operation and incorporation of the Compton polarimeter. Dr. Evgeni Tsentalovich, Ernie Ihloff, and Dr. Hauke Kolster worked long and hard to produce a highly-polarized atomic beam source and target. Dr. Karen Dow spent many hours supplying answers to my magnetic field and data acquisition questions; additionally, I would like to thank her for the useful critiques she gave me on my thesis. Dr. Tim Smith laid out nearly all of the computer code for all aspects of the BLAST project, and Ernie Bisson had the daunting task of successfully keeping all of the Bates computers running. Dr. William Turchinetz served as the resident theoretician and all-around voice of experience on the project, and I always looked forward to talks with Dr. Townsend Zwart regarding his theories of the universe. The "glue" which kept the entire project running smoothly was the Bates leaders, Prof. Richard Milner, Dr. Chris Tschalaer, and Dr. Manouchehr Farkhondeh. I would also specifically like to thank the members of the Bates' mechanical engineering group. Jim Kelsey and Ernie Ihloff were great mentors and offered me lots of good advice. Peter Binns, Steve Ciacera, and Brian O'Rourke were great to work with and they always had a joke and smile ready to lighten the mood.

But the unsung heroes are the other BLAST graduate students. I am indebted to Adam DeGrush who, with his wit and sense of humor, made the long hours spent building the drift chambers go by much more quickly. I would also like thank Vitaliy Ziskin who was very helpful with my analysis and, all in all, was quite good at helping me keep things in perspective. Chi Zhang was amazingly tolerant of all of my tensor analysis questions, and Chris Crawford helped with any reconstruction problems that I ran into; it is difficult to overestimate how helpful these two guys really were. I would like to offer a special thank you to Nikolas Meitanis who, in addition to providing analytical help, was a kindred spirit that I could talk to when the road seemed long. Additionally, Jason Seely and Ben Clasie were great friends to have over the years, and I thank Yuan Xiao for his help over the years. I am also thankful to the UNH students, Adrian Sindile, Peter Karpius, and Octavian Filati, as well as to Eugene Geis for all of their help. Additionally, I would like to thank Sean Stave for his friendship over the years; lunches spent with Sean are some of my favorite memories at MIT.

The debt that I owe to my parents is simply not measurable. The support that they have given me over the years has meant all of the difference. Quite simply, none of this would have been possible without their support.

Last but certainly not least, I would like to thank my girlfriend, Jodi. Through good times and bad, she was always there for me, answering my problems with a hug and a smile.

Contents

List of Figures

List of Tables

Chapter 1

Theoretical Motivation

1.1 Introduction

Nuclear structure and the underlying internucleon (NN) interaction have always played a central role in nuclear physics. However, despite decades of research, calculations of the NN interaction based on Quantum Chromodynamics, which governs the interactions of quarks in nucleons, continue to evade solution. Since nucleons interact with each other via the strong force, which ultimately takes the form of quarks interacting via gluon exchange, understanding of the nucleon and how it interacts with other nucleons is not complete.

The tensor component of the NN interaction is one such area currently under study. The observation that certain nuclei exist in multiple orbital angular momentum admixture states with $\Delta L = 2$ provides evidence of the existence of a tensor component in the NN interaction. However, the relative strength and effective range of this component are still under debate.

The deuteron is in many ways the ideal nucleus for studying the NN interaction. Consisting of a single proton and neutron in an $I(J^P) = 0(1^+)$ state, it is the simplest nucleus. In particular, since the deuteron lies in an admixture of S- and D- wave states, it is an ideal candidate for obtaining information about the tensor component of the NN interaction.

In this chapter, motivation is given for using polarized electrodisintegration as a measure of tensor effects and deuteron structure in general. The non-relativistic deuteron wave function is examined in depth in both position and momentum space in order to gain an understanding of how the tensor component of the NN interaction manifests itself. Deuteron electrodisintegration using a polarized beam and target is then discussed, and observables emphasizing deuteron structure are examined. It is concluded that the electrodisintegration tensor asymmetry, A_d^T, and beam-vector asymmetry, A_{ed}^V, are both viable observables to examine in order to study tensor effects as well as reaction mechanism contributions from meson exchange currents and nucleon excitation.

1.2 Deuteron Wave Functions in Position-Space

The NN interaction conserves only total angular momentum; conservation of respective intrinsic and orbital angular momenta are guaranteed only to the extent of consistency with total angular momentum conservation. As such, the deuteron wave function, consisting of two spin-1/2 nucleons coupled in an overall $J = 1$ state, is an admixture of S- and D-state components. In position-space, the non-relativistic polarized deuteron wave function takes the following form [25]:

$$\Psi_d^{m_J}(\vec{r}) = R_0(r)\mathcal{Y}_{110}^{m_J}(\Omega_r) + R_2(r)\mathcal{Y}_{112}^{m_J}(\Omega_r) \tag{1.1}$$

Here, $R_0(r) \equiv u(r)/r$ and $R_2(r) \equiv w(r)/r$ are the respective S- and D-state radial wave functions[1], m_J denotes the projection of the deuteron's total spin vector onto

[1] In keeping with pre-existing notation conventions [25], physics quantities in this chapter will be expressed in terms of two position vectors. The first vector, the internucleon position vector, is defined as the difference between the deuteron's proton and neutron constituent position vectors:

$$\vec{r} \equiv (r, \Omega_r) \equiv (r, \theta_r, \phi_r) \equiv \vec{r}_p - \vec{r}_n$$

The second vector is defined as the difference between the proton position vector and that of the deuteron's center-of-mass:

$$\vec{r}\,' \equiv (r', \Omega_{r'}) \equiv (r', \theta_{r'}, \phi_{r'}) \equiv \vec{r}_p - \frac{1}{2}(\vec{r}_p + \vec{r}_n) = \frac{1}{2}(\vec{r}_p - \vec{r}_n) = \frac{1}{2}\vec{r}$$

The relations between these vectors are: $r = 2r'$ and $\Omega_r = \Omega_{r'}$. These variables will be used interchangeably throughout this chapter.

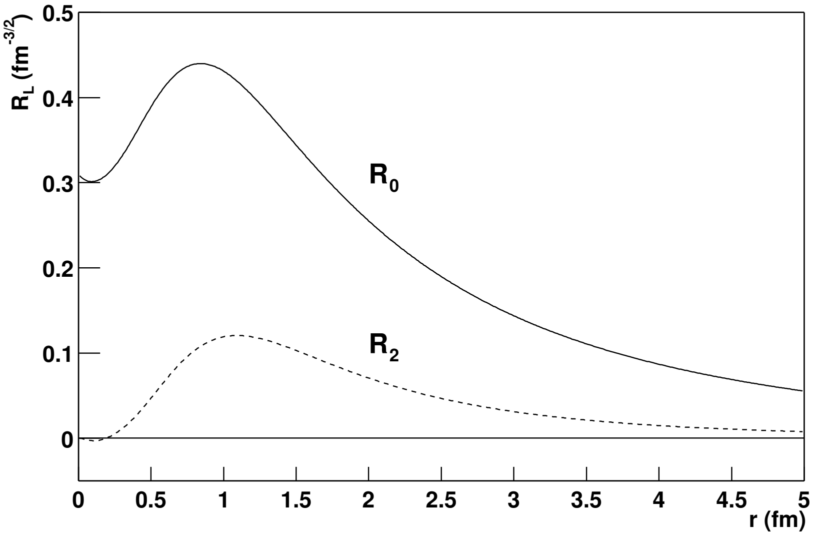

Figure 1-1: The S- and D-state radial wave functions, $R_0(r)$ and $R_2(r)$, for the Bonn potential [40].

its polarization axis (taken to be the $\hat{z}$ axis), and, for any m_J value, $\mathcal{Y}_{JSL}^{m_J}(\Omega_r)$ is the corresponding spin-angle function for a state with respective total, intrinsic, and orbital angular momenta J, S, and L.

Plots of the S- and D-state radial wave functions for a recent formulation of the Bonn potential [40] are shown in Fig. 1-1. From the plots, a drop in amplitude at small r originating from the presence of the nuclear core is readily apparent. Both radial wave functions reach a maximum around $r \sim 1$ fm and then fall off quickly with increasing r. The rapid fall-off is consistent with the fall-off at large r due to the one-boson exchange interpretation. It should be noted that the radial wave functions in these plots have been normalized so that:

$$\int_0^\infty r^2 \left[R_0(r)^2 + R_2(r)^2\right] dr = 1 \tag{1.2}$$

Using the Clebsch-Gordon formalism along with the fact that the deuteron is a spin-1 nucleus, the results in (1.1) can be used to write down an explicit form for the position-space polarized deuteron wave functions in each m_J substate:

$$\begin{aligned}
\Psi_d^0(\vec{r}) &= \sqrt{\frac{4}{\pi}}\left[R_0(r) - \sqrt{2}R_2(r)\left(\frac{3}{2}\cos^2\theta_r - \frac{1}{2}\right)\right]|1,0\rangle \\
&+\sqrt{\frac{9}{\pi}}R_2(r)\sin\theta_r\cos\theta_r\left[e^{-i\phi_r}|1,1\rangle - e^{i\phi_r}|1,-1\rangle\right] \qquad (1.3)\\
\Psi_d^{\pm1}(\vec{r}) &= \sqrt{\frac{4}{\pi}}\left[R_0(r) + \sqrt{\frac{1}{2}}R_2(r)\left(\frac{3}{2}\cos^2\theta_r - \frac{1}{2}\right)\right]|1,1\,(1,-1)\rangle \\
&\pm\sqrt{\frac{9}{\pi}}R_2(r)e^{\pm i\phi_r}\sin\theta_r\cos\theta_r\,|1,0\rangle \\
&+\sqrt{\frac{9}{2\pi}}R_2(r)e^{\pm 2i\phi_r}\sin^2\theta_r\,|1,-1\,(1,1)\rangle \qquad (1.4)
\end{aligned}$$

Equations for the corresponding probability densities, $\rho_d^{m_J}(\vec{r}\,') \equiv \Psi_d^{m_J *}(\vec{r})\Psi_d^{m_J}(\vec{r})$, follow directly:

$$\rho_d^0(\vec{r}\,') = \frac{4}{\pi}\left[C_0(r) - 2C_2(r)P_2(\cos\theta)\right] \qquad (1.5)$$

$$\rho_d^{\pm1}(\vec{r}\,') = \frac{4}{\pi}\left[C_0(r) + C_2(r)P_2(\cos\theta)\right] \qquad (1.6)$$

where:

$$C_0(r) \equiv R_0(r)^2 + R_2(r)^2 \qquad (1.7)$$

$$C_2(r) \equiv R_2(r)\left(\sqrt{2}R_0(r) - \frac{1}{2}R_2(r)\right) \qquad (1.8)$$

and where $P_2(\cos\theta) \equiv \frac{3}{2}\cos^2\theta - \frac{1}{2}$ is the Legendre polynomial of order 2. It should be noted that the wave functions and probability densities have been normalized in the standard manner [25] so that:

$$\int \vec{r}\,'\rho_d^{m_J}(\vec{r}\,')d^3\vec{r}\,' = 2 \qquad (1.9)$$

Symmetries of the deuteron densities can be seen from examining these equations. The $\phi_{r'}$ dependence in the wave functions disappears in the density calculations. The densities themselves are functions of only two of the spherical position variables,

$\rho_d^{m_J}(\vec{r}') = \rho_d^{m_J}(r', \theta_{r'})$, and thus possess azimuthal symmetry about the deuteron's polarization axis. Additionally, the densities are symmetric about a flip of the position vector according to $\vec{r}' \equiv (r', \theta_{r'}, \phi_{r'}) \rightarrow -\vec{r} \equiv (r', \pi - \theta_{r'}, \pi + \phi_{r'})$. This latter symmetry is enforced by the experimental observation that the deuteron exists in a positive parity state.

To help visualize the deuteron's densities, it is useful to change from spherical to cylindrical coordinates via $x' = r' \sin\theta_{r'}$ and $z' = r' \cos\theta_{r'}$. Plots of $\rho_d^{m_J}(x', z')$ are shown in Fig. 1-2. In the $m_J = 0$ state, there is high density near the x' axis but very low density along the z' axis (i.e., the polarization axis). Since the deuteron densities are azimuthally symmetric about the polarization axis, it follows that the $m_J = 0$ density distribution resembles a toroid (a "donut" shape) with most of its density lying in or near the $x' - y'$ plane and with very low density along the z' axis. On the other hand, the $m_J = \pm 1$ distributions have significant densities along the z' axis but less-dominant densities in the $x' - y'$ plane. It follows that the $m_J = \pm 1$ densities form two identical but nearly disjoined lobes (a "dumbbell" shape) centered on either end of the polarization axis.

Examining (1.5) - (1.8) shows that all of the polar angle dependence in $\rho_d^{m_J}(\vec{r}')$ disppears when $C_2(r) = 0$, or, equivalently, when $R_2(r) = 0$. Thus, in the limit of an $L = 0$ deuteron, the corresponding densities are radially symmetric and form degenerate spherical equidensity shells. The extent to which this degeneracy is broken and causes the deuteron densities to form respective donut and dumbbell shapes is thus a direct consequence of the deuteron possessing a nonzero D-state component. The existence of a nonzero D-state component implies the existence of a tensor component in the NN interaction, as such a component allows for $\Delta L = 2$ admixture[2].

[2] A straightforward mathematical argument showing how the simultaneous existence of both an S- and D-state implies the existence of a tensor operator in orbital angular momentum space can be found in Section 3-4 in Ref [57].

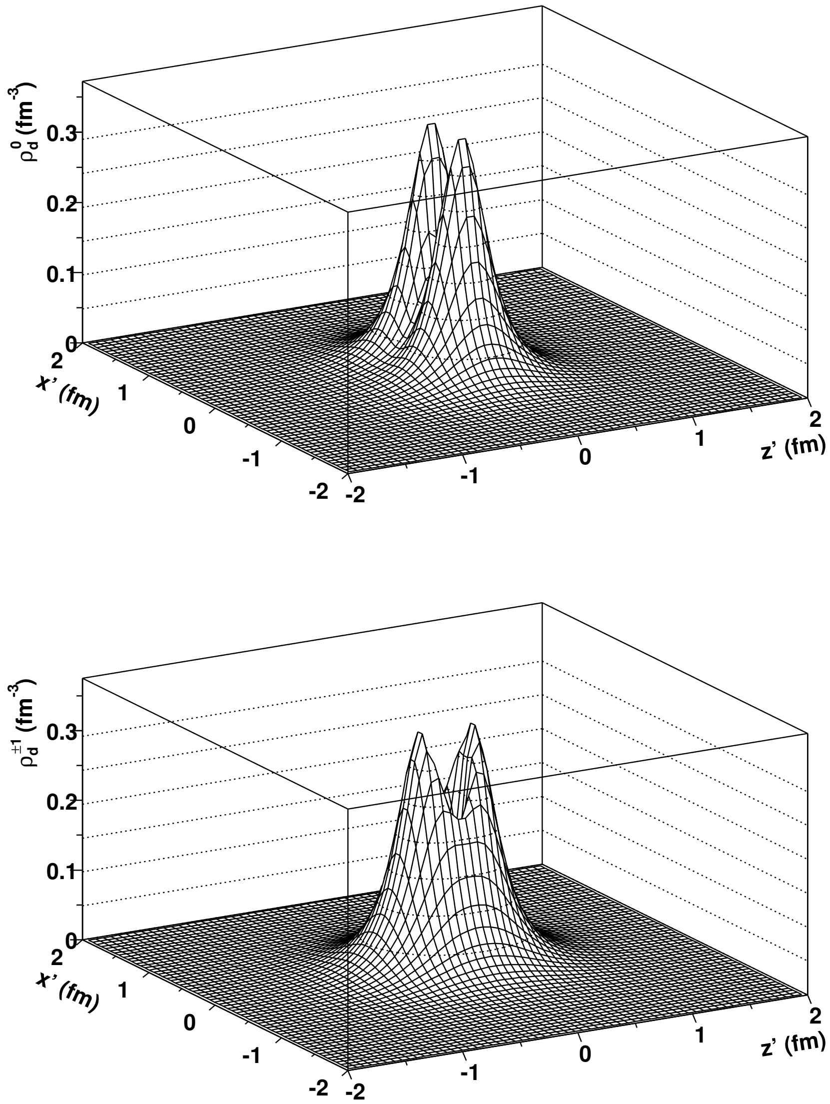

Figure 1-2: The $m_J = 0, \pm 1$ deuteron probability densities for the Bonn potential [40] as a function of $x' = r' \sin\theta_{r'}$ and $z' = r' \cos\theta_{r'}$.

Profiles of the densities in parallel ($\theta_{r'} = 0$) and perpendicular ($\theta_{r'} = \frac{\pi}{2}$) directions can be seen in Fig. 1-3. From examining the properties of deuteron wave functions, the $m_J = 0$ density as a function of r' is largest for $\theta_{r'} = \frac{\pi}{2}$ and smallest for $\theta_{r'} = 0$ while the $m_J = \pm 1$ densities' extrema are just the opposite. In particular, as concluded from (1.5) and (1.6), all three densities reach the same maxima as a function of r', though for different $\theta_{r'}$:

$$\rho_d^0 \left(r', \theta_{r'}\right)\Big|_{MAX} = \rho_d^0 \left(r', \theta_{r'} = \frac{\pi}{2}\right) = \rho_d^{\pm 1} \left(r', \theta_{r'}\right)\Big|_{MAX} = \rho_d^{\pm 1} \left(r', \theta_{r'} = 0\right) \quad (1.10)$$

These maximum-density functions reach an absolute maximum value of $\rho_d \sim 0.35$ fm^{-3} at $r \sim 0.5$ fm. The fact that this absolute maximum density is approximately twice that of normal nuclear matter (~ 0.16 fm^{-3}) is not completely understood.

The ratio $\rho_d^0 \left(r', \theta_{r'} = \frac{\pi}{2}\right) / \rho_d^0 \left(r', \theta_{r'} = 0\right)$ has a maximum of ~ 4.5 whereas the ratio $\rho_d^{\pm 1} \left(r', \theta_{r'} = 0\right) / \rho_d^{\pm 1} \left(r', \theta_{r'} = \frac{\pi}{2}\right)$ has a maximum of ~ 1.6, though less pronounced. Both ratios reach their respective maxima at $r' \sim 0.7$ fm ($r \sim 1.4$ fm).

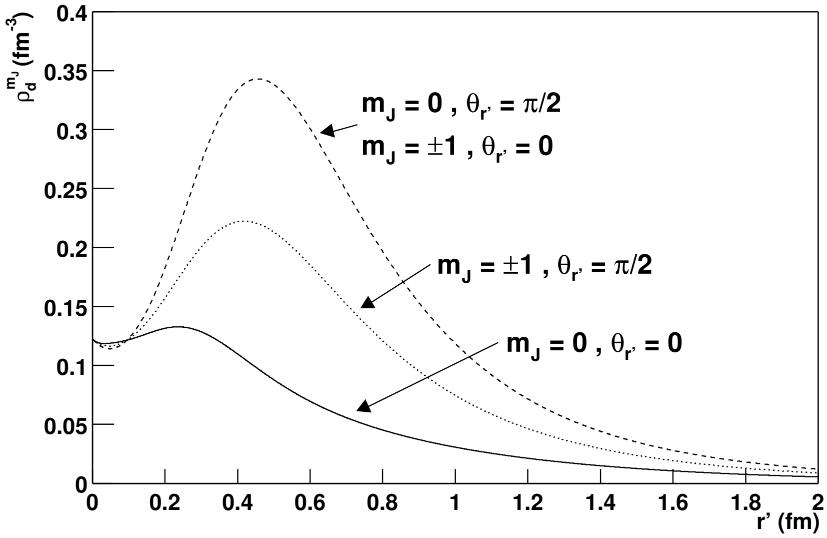

Figure 1-3: Plots of $\rho_d^{m_J} \left(r', \theta_{r'}\right)$ as a function of r' for $m_J = 0, \pm 1$ and $\theta_{r'} = 0, \frac{\pi}{2}$.

The conclusion that can be reached from these results is that measurements of the deuteron's spin-dependent densities carry information on the D-state component of its wave function, which implies the existence of and carries information regarding the tensor component of the NN interaction. This information is maximized by probing deuteron properties at small r' (~ 0.7 fm).

1.3 Static Property Measurements of the Deuteron

Attempts to probe nuclear properties typically fall into one of two categories: static property measurements and scattering measurements. Static property measurements return information in position-space. Scattering measurements, on the other hand, which involve utilizing high-momentum particles to probe nuclei, return information in momentum-space.

The root-mean-square radius, r'_d, gives a measure of the size of the charge distribution in the deuteron:

$$(r'_d)^2 = \frac{1}{4}\int_0^\infty \left[u(r)^2 + w(r)^2\right] r^2 dr \tag{1.11}$$

Measurements of this observable, though, are insensitive to D-state aspects of the deuteron, since the S-state component completely dominates the D-state one.

The electric quadrupole moment, Q_0, measures to lowest-order a nucleus's deviation from sphericity:

$$Q_0 \equiv \left\langle \Psi_d^{+1}(\vec{r}) \middle| \hat{Q}_0(\vec{r}) \middle| \Psi_d^{+1}(\vec{r}) \right\rangle \sim \int_0^\infty w(r)\left[\sqrt{8}u(r) - w(r)\right] r^2 dr \tag{1.12}$$

The quadrupole moment operator is a spherical tensor of rank 2. As such, any nucleus with total spin $J < 1$ must have zero quadrupole moment. However, the traditional non-relativistic quadrupole operator operates only in orbital spin space; in the usual non-relativistic picture of the NN system, one can thus further conclude that any nucleus with orbital angular momentum $L < 1$ also has a vanishing quadrupole moment. Thus, in the traditional non-relativistic picture, measurement of a nonzero quadrupole moment in the deuteron is direct evidence of a nonzero D-state component. This fact can also be seen by noting that the integrand in (1.12) vanishes if $w(r) \equiv 0$. Despite this fact, the electric quadrupole moment is not an optimal measure of the D-state contribution. The corresponding integrand is weighted by r^2 which thus tends to lend weight towards large r wave function contributions. Since one must probe low r in order to access D-state information, measurements of the electric quadrupole moment are limited in the amount of D-state information that they return.

Another important static observable is the magnetic moment of the deuteron. In the independent-particle model, the magnetic moment can be expressed as:

$$\mu_d = \mu_p + \mu_n - \frac{3}{2}\left(\mu_p + \mu_n - \frac{1}{2}\right) P_D \tag{1.13}$$

where $\mu_p = 2.79285\mu_N$ and $\mu_n = -1.91304\mu_N$ are the respective proton and neutron magnetic moments expressed in units of the nuclear magneton, μ_N, and $P_D \equiv \int w^2(r)dr$ is the D-state probability. From recent experiments [28], the deuteron magnetic moment is found to be $\mu_d = 0.85744\mu_N$. Substituting this value directly into (1.13) returns $P_D = 0.0393$, implying a D-state contribution of $\sim 4\%$. However, due to meson-exchange corrections, isobar configurations, and relativistic corrections, one cannot use (1.13) to obtain more than an estimate of the D-state contribution.

1.4 Deuteron Wave Functions in Momentum-Space

The canonical momentum partner to the relative position, $\vec{r} \equiv \vec{r}_p - \vec{r}_n$, is the relative momentum[3], $\vec{p} \equiv \frac{1}{2}(\vec{p}_p - \vec{p}_n)$. Starting with the position-space wave functions listed in (1.3) and (1.4), a standard application of a Fourier transform gives the corresponding

[3] The factor of 1/2 in the definition of the relative momentum is needed in order to satisfy the canonical commutation relations defining the pair:

$$[\vec{r},\vec{p}] = \left[\vec{r}_p - \vec{r}_n, \frac{1}{2}(\vec{p}_p - \vec{p}_n)\right] = \frac{1}{2}\left([\vec{r}_p,\vec{p}_p] + [\vec{r}_n,\vec{p}_n]\right) = \frac{1}{2}(i+i) = i \tag{1.14}$$

polarized deuteron wave functions, $\tilde{\Psi}_d^{m_J}(\vec{p})$, in momentum-space:

$$\tilde{\Psi}_d^{m_J}(\vec{p}) \equiv \frac{1}{(2\pi)^{3/2}} \int e^{-i\vec{p}\cdot\vec{r}} \Psi_d^{m_J}(\vec{r}) \tag{1.15}$$

The corresponding momentum-space density functions, $\tilde{\rho}_d^{m_J}(\vec{p}) \equiv \tilde{\Psi}_d^{m_J *}(\vec{p})\tilde{\Psi}_d^{m_J}(\vec{p})$, take on a form similar to that of the position-space densities, (1.5) and (1.6):

$$\tilde{\rho}_d^{0}(\vec{p}) = \frac{1}{4\pi}\left[\tilde{C}_0(p) - 2\tilde{C}_2(p)P_2(\cos\theta_p)\right] \tag{1.16}$$

$$\tilde{\rho}_d^{\pm 1}(\vec{p}) = \frac{1}{4\pi}\left[\tilde{C}_0(p) + \tilde{C}_2(p)P_2(\cos\theta_p)\right] \tag{1.17}$$

The $\tilde{C}_L(p)$ terms are defined in a similar manner as the $C_L(r)$ ones, (1.7) and (1.8):

$$\tilde{C}_0(p) \equiv \tilde{R}_0(p)^2 + \tilde{R}_2(p)^2 \tag{1.18}$$

$$\tilde{C}_2(p) \equiv \tilde{R}_2(p)\left(\sqrt{2}\tilde{R}_0(p) - \frac{1}{2}\tilde{R}_2(p)\right) \tag{1.19}$$

In these equations, $\tilde{R}_L(p)$ is the Fourier-transformed radial wave function:

$$\tilde{R}_L(p) \equiv i^L \sqrt{\frac{2}{\pi}} \int_0^\infty r^2 j_L(pr) R_L(r) \tag{1.20}$$

where $j_L(x)$ is the spherical Bessel function of order L. It should be noted that the following conventional normalization has been chosen here:

$$\int \tilde{\rho}_d^{m_J}(\vec{p}) d^3\vec{p} = 1 \tag{1.21}$$

Plots of the magnitudes of the Fourier-transformed radial wave functions, $\left|\tilde{R}_L(p)\right|$, are shown in Fig. 1-4. At low p, the S-state is completely dominant. However, the dominance decreases as p increases until $p \sim 0.3$ GeV, where both states have nearly equal magnitudes. Above $p \sim 0.3$ GeV, the D-state is dominant. High p must thus be probed in order to obtain D-state information. Probing the deuteron at high p is equivalent to probing the low r region.

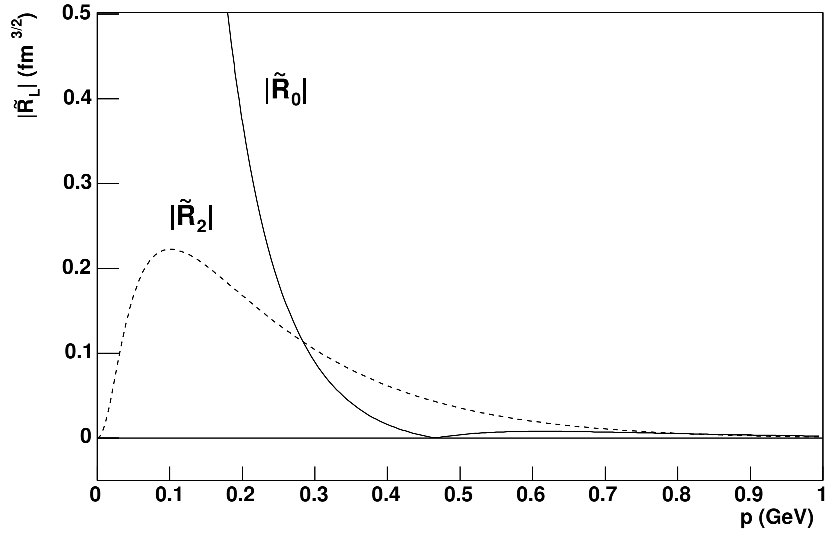

Figure 1-4: The magnitudes of the Fourier-transformed S- and D-state radial wave functions, $\left|\tilde{R}_0(p)\right|$ and $\left|\tilde{R}_2(p)\right|$, for the Bonn potential [40].

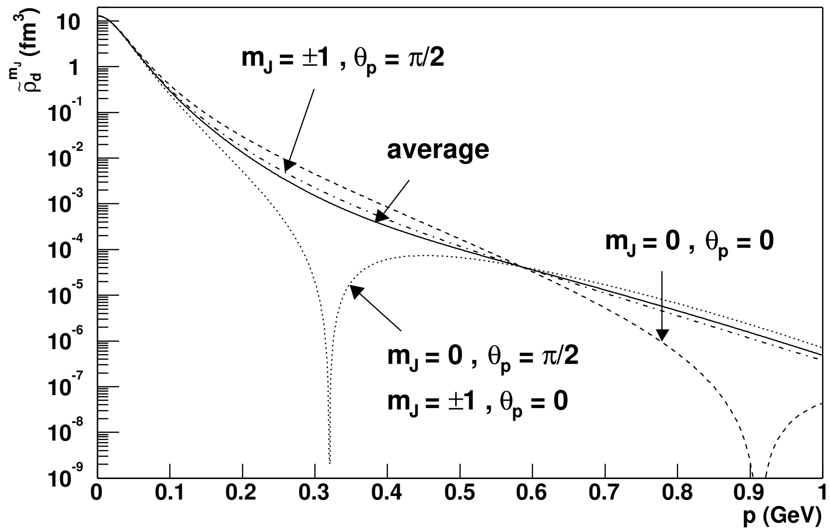

Figure 1-5: Plots of $\tilde{\rho}_d^{m_J}(p, \theta_p)$ for the Bonn potential [40] for $m_J = 0, \pm 1$ and $\theta_p = 0, \frac{\pi}{2}$.

Plots of $\tilde{\rho}_d^{m_J}(\vec{p})$ are shown in Fig. 1-5. Similar to the position-space densities, analysis of (1.16) and (1.17) shows that $\tilde{\rho}_d^0(p, \theta_p = \pi/2) = \tilde{\rho}_d^{\pm 1}(p, \theta_p = 0)$. For all three m_J states, there is a difference in densities for relative momenta parallel ($\theta_p = 0$) and perpendicular ($\theta_p = \frac{\pi}{2}$) to the polarization axis. This difference is most noticable for $p \sim 0.3$ GeV. Also shown in this graph is the average momentum-space density:

$$\tilde{\rho}_d^{avg}(\vec{p}) \equiv \frac{1}{3}\left(\tilde{\rho}_d^0(\vec{p}) + \tilde{\rho}_d^{+1}(\vec{p}) + \tilde{\rho}_d^{-1}(\vec{p})\right) \tag{1.22}$$

From (1.16) and (1.17), all polar angle dependence in the m_J substate densities cancels out in the average momentum-space density; thus, the average density is only a function of p. The average density defined above is also equal to the density that would exist in the limit of an $L = 0$ deuteron, as, in this case, $\tilde{R}_2(p) \equiv 0$. The existence of a D-state component in the deuteron is thus responsible for nonzero θ_p dependence in the $\tilde{\rho}_d^{m_J}(\vec{p})$, which in turn is responsible for differences in $\tilde{\rho}_d^0(\vec{p})$ and $\tilde{\rho}_d^{\pm 1}(\vec{p})$ for the same values of $\vec{p}$.

In order to measure D-state deuteron properties, quantities that provide sensitivity to the differences in the various momentum-state densities need to be analyzed. The tensor asymmetry, A_d^T, is one such measure:

$$\begin{aligned} A_d^T(p, \theta_p) &\equiv \frac{\frac{1}{2}\left[\tilde{\rho}_d^{+1}(p, \theta_p) + \tilde{\rho}_d^{-1}(p, \theta_p)\right] - \tilde{\rho}_d^0(p, \theta_p)}{\tilde{\rho}_d^{+1}(p, \theta_p) + \tilde{\rho}_d^{-1}(p, \theta_p) + \tilde{\rho}_d^0(p, \theta_p)} \\ &= \frac{\tilde{C}_2(p)}{\tilde{C}_0(p)} \cdot P_2(\cos\theta) \\ &= \frac{\sqrt{2}\tilde{R}_2(p)\left(\tilde{R}_0(p) - \sqrt{\frac{1}{2}}\tilde{R}_2(p)\right)}{\tilde{R}_0(p)^2 + \tilde{R}_2(p)^2} \cdot \left(\frac{3}{2}\cos^2\theta_p - \frac{1}{2}\right) \end{aligned} \tag{1.23}$$

A plot of A_d^T is shown in Fig. 1-6, and projections of A_d^T with respect to p and θ_p are shown in Fig. 1-7. From the functional form of A_d^T, the tensor asymmetry vanishes when $P_2(\cos\theta_p) = 0$, or, equivalently, when $\cos\theta_p = \pm\sqrt{\frac{1}{3}}$. With respect to p, the tensor asymmetry is extremized when $\tilde{R}_2(p) = \sqrt{2}\tilde{R}_0(p)$, which occurs at $p \sim 0.3$ GeV.

Due to the $\tilde{R}_2(p)$ factor in its numerator, the tensor asymmetry must vanish if

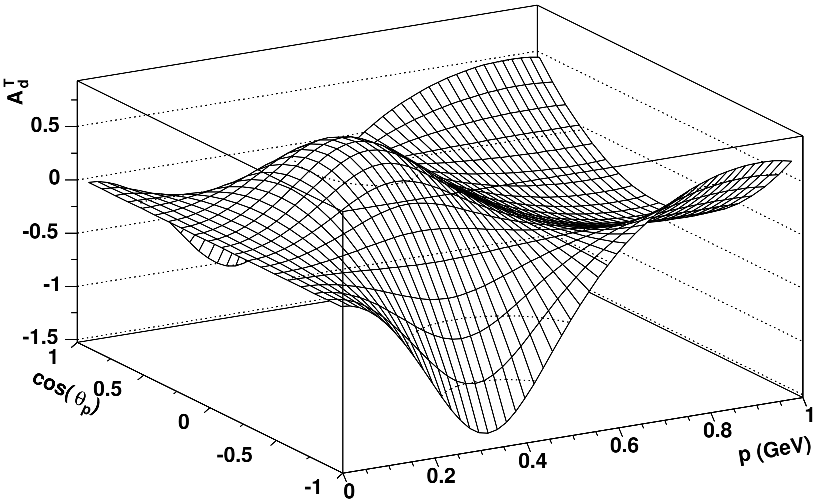

Figure 1-6: Plot of A_d^T for the Bonn potential [40] as a function of p and $\cos\theta_p$.

there is no D-state contribution (i.e., in the limiting case of an $L = 0$ deuteron, where $\tilde{R}_2(p) \equiv 0$). Furthermore, to the extent that $\tilde{R}_0(p) \gg \tilde{R}_2(p)$, the tensor asymmetry is directly proportional to the ratio $\tilde{R}_2(p)/\tilde{R}_0(p)$.

However, in order to reconstruct A_d^T experimentally as has been discussed here, one must be able to measure the internal momenta of the nucleons while still in the bound deuteron nucleus. Due to the fact that the nucleons in the deuteron are bound (albeit weakly), any attempt to measure the bound nucleons' momenta must involve the use of some other "probing" particle in order to break up the nucleus. Such a process inherently introduces contamination in the form of four-momenta, $Q \equiv (\omega, \vec{q})$, transferred from the probing particle to either of the nucleons.

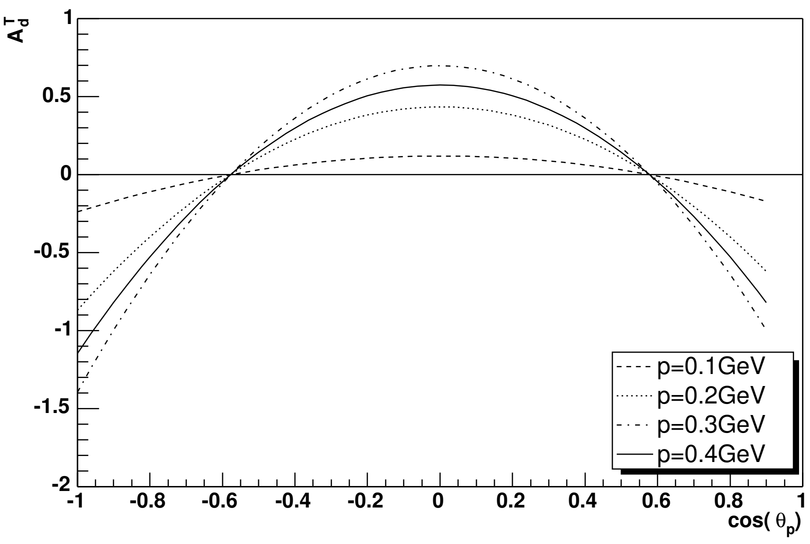

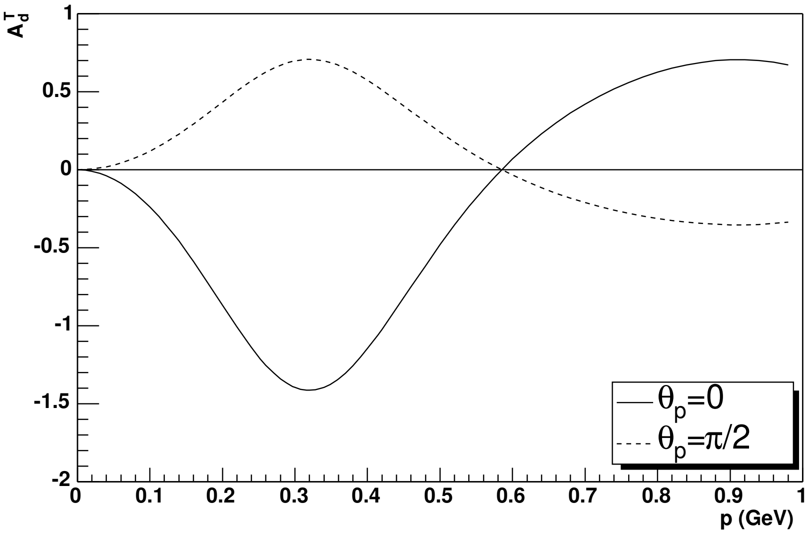

Figure 1-7: The top figure contains plots of A_d^T for the Bonn potential [40] as a function of θ_p for various p values. The bottom figure shows plots of A_d^T as a function of p for various θ_p values.

Furthermore, exchange processes also exist where the struck nucleon is not the one detected. Such processes occur because the nucleons in a nucleus are bound and thus possess nonzero internal momenta. In addition, reaction mechanism processes, such as meson-exchange currents (MEC) and isobar configurations (IC), can also introduce contamination into measurements. Finally, outgoing nucleons may themselves interact with each other via final state interactions (FSI). In practice, there exists no method of completely ruling out all such occurrances with complete certainty. As such, the "internal" nucleon momenta that are measured are only approximations to the internal momenta. To the extent that one can rule out the above-listed sources of contamination, one can directly compare the theoretical results derived here to experimental ones. The set of approximations necessary for such theoretical comparison is commonly referred to as the Plane Wave Impulse Approximation (PWIA) [45]. The question of how well the PWIA describes the total model is one that needs to be quantized. This will be discussed later on when "full" theoretical models are considered.

Because the internal nucleon momentum is not directly observable, a "missing momentum" vector, $\vec{p}_M$, is used to approximate it. It is defined as the difference of the measured proton momentum, $\vec{p}_{p,M}$, and the momentum transfer, $\vec{q}$:

$$\vec{p}_M \equiv \vec{p}_{p,M} - \vec{q} \tag{1.24}$$

To the extent that nucleons retain their individual identity within the deuteron, bound state effects of the deuteron cause the bound nucleons to possess a nonzero (Fermi) momentum inside the nucleus. Since the proton's final (measured) momentum is equal to the sum of its initial (bound) momentum, $\vec{p}_{p,I}$, and the momentum it receives from the virtual photon, $\vec{p}_{p,\gamma}$, and since the sum of the nucleons' momenta before interaction is zero (i.e., $\vec{p}_{p,I} + \vec{p}_{n,I} = 0$), it follows that:

$$
\begin{aligned}
\vec{p}_M &\equiv \vec{p}_{p,M} - \vec{q} \\
&= (\vec{p}_{p,I} + \vec{p}_{p,\gamma}) - \vec{q} \\
&= \frac{1}{2}(\vec{p}_{p,I} - \vec{p}_{n,I}) + \frac{1}{2}(\vec{p}_{p,I} + \vec{p}_{n,I}) + \vec{p}_{p,\gamma} - \vec{q} \\
&= \vec{p} + \vec{p}_{p,\gamma} - \vec{q}
\end{aligned}
$$

where the identification of $\vec{p} = \frac{1}{2}(\vec{p}_{p,I} - \vec{p}_{n,I})$ has been made. To the extent that all of the momentum transfer is transferred to the proton (and thus $\vec{p}_{p,\gamma} - \vec{q} = 0$), the missing momentum vector will equal the bound relative nucleon momentum. In such a situation, the deuteron target is effectively reduced to a proton target with a "spectator" neutron. Such scattering is referred to as quasi-elastic (QE) scattering from the proton. Kinematically, it occurs when $Q^2 = 2m_p\omega$, where m_p is the mass of the proton. By imposing QE kinematics constraints, the PWIA can be studied; relaxing the constraints allows non-PWIA effects to be measured, such as MEC, IC, and FSI. QE scattering becomes increasingly dominant as $p_M \rightarrow 0$.

1.5 Electron-Deuteron Scattering

Both elastic electron-deuteron (e-d) scattering as well as deuteron electrodisintegration scattering return D-state information. Due to the success of quantum electrodynamics, the electron contribution to these processes is well known. This allows for a cleaner, more direct comparison of theoretical and experimental deuterium analyses than more complex probing particles would provide.

Since the deuteron is a spin-1 nucleus, it can be polarized in two ways: vector and tensor [19, 47]. The vector polarization, $\tilde{P}_z$, is given by $\tilde{P}_z \equiv \sqrt{\frac{3}{2}}P_z = \sqrt{\frac{3}{2}}(n_+ - n_-)$, where $n_\pm$ is the relative population of deuterons in the $m_d = \pm 1$ state. Similarly, the tensor polarization, $\tilde{P}_{zz}$, is given by $\tilde{P}_{zz} \equiv \sqrt{\frac{1}{2}}P_z = \sqrt{\frac{1}{2}}(1 - 3n_0)$, where n_0 is the relative population of deuterons in the $m_d = 0$ state. All deuterons must exist in one of these three polarization states which thus leads to the constraint

$n_+ + n_- + n_0 = 1$. This constraint enforces relations between achievable simultaneous vector/tensor polarization states of the deuteron (see Fig. 1-8). In particular, a large positive tensor polarization can exist with a wide range of positive and negative vector polarizations, but maximum negative tensor polarization can exist only with zero vector polarization.

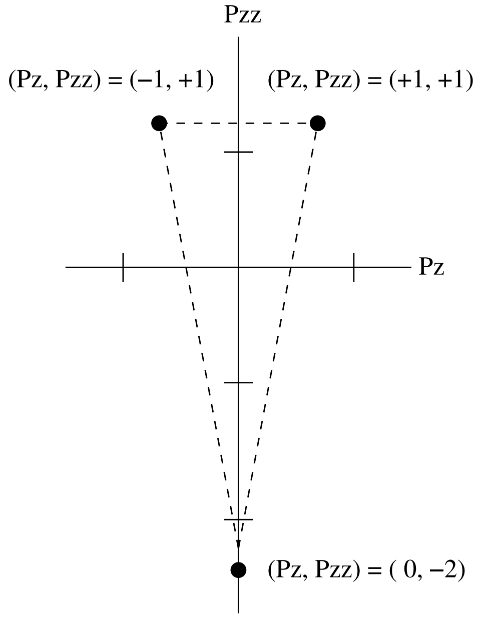

Figure 1-8: Accessible vector/tensor deuteron polarization region. The boundaries are shown as broken lines.

1.5.1 Elastic Electron-Deuteron Scattering

In the Born approximation, the cross section for elastic e-d scattering with a longitudinally polarized electron beam of helicity h and a deuterium target with respective vector and tensor polarizations, $\tilde{P}_z$ and $\tilde{P}_{zz}$, is given by [9, 43, 59]:

$$\frac{d\sigma}{d\Omega}\left(h, \tilde{P}_z, \tilde{P}_{zz}\right) = S_0\left(1 + \tilde{P}_{zz}\Gamma + h\tilde{P}_z\Delta\right) \tag{1.25}$$

Here, S_0 is the totally unpolarized cross section:

$$S_0 \equiv \frac{d\sigma}{d\Omega}(0,0,0) = \left(\frac{d\sigma}{d\Omega}\right)_M \cdot \frac{1}{f}\left[A(Q^2) + B(Q^2)\tan^2\frac{\theta_e}{2}\right] \tag{1.26}$$

where $\left(\frac{d\sigma}{d\Omega}\right)_M$ is the Mott cross section for scattering from a spin-0 point particle, and $f \equiv 1 + 2(E_e/m_d)\sin^2(\theta_e/2)$ is the recoil factor in terms of the electron's incident energy, E_e, and polar scattering angle, θ_e. The $A(Q^2)$ and $B(Q^2)$ structure functions are kinematically-weighted linear combinations of the squares of the deuteron's charge monopole ($G_C(Q^2)$), magnetic dipole ($G_M(Q^2)$), and charge quadrupole ($G_Q(Q^2)$) form factors:

$$A(Q^2) \equiv G_C^2(Q^2) + \tfrac{8}{9}\eta^2 G_Q^2(Q^2) + \tfrac{2}{3}\eta G_M^2(Q^2) \tag{1.27}$$

$$B(Q^2) \equiv \tfrac{4}{3}\eta(1+\eta)G_M^2(Q^2) \tag{1.28}$$

where $\eta \equiv \frac{Q^2}{4m_d^2}$. The Γ and Δ terms in (1.25) are given by:

$$\Gamma \equiv \tfrac{1}{\sqrt{2}}\left[\left(\tfrac{3}{2}\cos^2\theta_d - \tfrac{1}{2}\right)T_{20} - \sqrt{\tfrac{3}{2}}\sin 2\theta_d \cos\phi_d T_{21} + \sqrt{\tfrac{3}{2}}\sin^2\theta_d \cos 2\phi_d T_{22}\right] \tag{1.29}$$

$$\Delta \equiv \sqrt{3}\left[\tfrac{1}{\sqrt{2}}\cos\theta_d T_{10}^e - \sin\theta_d\cos\phi_d T_{11}^e\right] \tag{1.30}$$

where the deuteron is polarized in the direction $\Omega_d \equiv (\theta_d, \phi_d)$ with respect to the momentum transfer vector. The various $T_{ij}^{(e)}$ terms are kinematically-weighted combinations of the deuteron's three form factors:

$$T_{20} \equiv -\frac{\sqrt{2}\eta}{3\tilde{S}}\left[4G_C(Q^2)G_Q(Q^2) + \frac{4\eta}{3}G_Q(Q^2)^2 + \left(\frac{1}{2}+\epsilon\right)G_M(Q^2)^2\right] \tag{1.31}$$

$$T_{21} \equiv \frac{2}{\tilde{S}}\sqrt{\frac{\eta^3(1+\epsilon)}{3}}G_Q(Q^2)G_M(Q^2) \tag{1.32}$$

$$T_{22} \equiv \frac{\eta}{2\sqrt{3}\tilde{S}}G_M(Q^2)^2 \tag{1.33}$$

$$T_{10}^e \equiv \frac{\eta}{\tilde{S}}\sqrt{\frac{2}{3}(1+\eta)\left(1+\eta\sin^2\frac{\theta_e}{2}\right)}G_M(Q^2)^2\sec\frac{\theta_e}{2}\tan\frac{\theta_e}{2} \tag{1.34}$$

$$T_{11}^e \equiv \frac{2}{\sqrt{3}\tilde{S}}\sqrt{\eta(1+\eta)}G_M(Q^2)\left(G_C(Q^2) + \frac{1}{3}\eta G_Q(Q^2)\right)\tan\frac{\theta_e}{2} \tag{1.35}$$

where $\tilde{S} \equiv A(Q^2) + B(^2)\tan^2\frac{\theta_e}{2}$ and $\epsilon \equiv (1+\eta)\tan^2\frac{\theta_e}{2}$.

Comprehensive measurements of all three of the deuteron's form factors are required for detailed understanding of the deuteron. Using totally unpolarized e-d scattering and applying Rosenbluth techniques to the resulting cross section, (1.26) can be decomposed to provide information on $A(Q^2)$ and $B(Q^2)$. However, to separate all three form factors, it is necessary to include a measurement of one of the $T_{ij}^{(e)}$ observables by utilizing either a tensor polarized target or tensor polarization transfer or else beam polarization with a vector polarized target. Because of its relative size, T_{20} is often chosen for the third measurable.

In the non-relativistic impulse approximation, where the virtual photon is assumed to interact with only the individual nucleons in the deuteron, $G_Q(Q^2)$ vanishes in the limiting case of an $L = 0$ deuteron [59]. Thus, measurements of $G_Q(Q^2)$ can provide information of the deuteron D-state contribution. From (1.31), one sees that T_{20} contains a term that is linear in $G_Q(Q^2)$, thus making it more sensitive to D-state effects.

1.5.2 Deuteron Electrodisintegration

The tensor asymmetry in (1.23) is expressed as a function of variables requiring knowledge of the relative nucleon momenta in the deuteron: $p = \frac{1}{2}|\vec{p}_p - \vec{p}_n|$ and $\cos\theta_p = \hat{z} \cdot \frac{(\vec{p}_p - \vec{p}_n)}{|\vec{p}_p - \vec{p}_n|}$. To measure such quantities, the deuteron nucleus needs to be probed (i.e., broken up) on a nucleon level. This leads one to consider deuteron electrodisintegration.

Within the formalism of the one-photon exchange PWIA, the kinematics of the ${}^2\vec{H}(\vec{e}, e'p)n$ reaction in the rest frame of the deuteron are shown in Fig. 1-9. An electron of initial (four-) momentum $K = (\epsilon, \vec{k})$ and final momentum $K' = (\epsilon', \vec{k}')$ transfers a momentum $Q = (\omega, \vec{q}) = (\epsilon - \epsilon', \vec{k} - \vec{k}')$ to a deuteron nucleus of initial momentum $P_d = (m_d, 0)$. At relativistic electron energies, the magnitude of the momentum transfer can be expressed in terms of the incident and scattered electron energies and the angle, θ_e, into which the electron scatters with respect to the incident direction[4]:

$$Q^2 = 4\epsilon\epsilon' \sin^2 \frac{\theta_e}{2} \tag{1.36}$$

The momentum transfer breaks up the deuteron into its two nucleon constituents. The resulting proton and neutron scatter with respective momenta $P_p = (E_p, \vec{p}_p)$ and $P_n = (E_n, \vec{p}_n)$. To ease the theoretical calculations [55], observables relating to the two emerging nucleons are evaluated in the proton-neutron center of mass (CM) system moving with velocity $\vec{\beta} = \vec{q}/(\omega + m_d)$ with respect to the laboratory frame. In this CM frame, the relative proton-neutron momentum is denoted by[5] $P_{pn} = (E_{pn}^{CM}, \vec{p}_{pn}^{\,CM})$.

The incident and scattered electron (three-) momentum vectors, $\vec{k}$ and $\vec{k}'$, respectively, as well as the momentum transfer vector, $\vec{q}$, all lie in a plane referred to as the scattering plane. The following "q" coordinate system is defined using these vectors:

$$\begin{aligned}
\hat{z}_q &\equiv \frac{\vec{q}}{|\vec{q}|} \\
\hat{y}_q &\equiv \frac{\vec{k_e} \times \vec{k_{e'}}}{|\vec{k_e} \times \vec{k_{e'}}|} \\
\hat{x}_q &\equiv \hat{y}_q \times \hat{z}_q
\end{aligned}$$

With respect to the q coordinate system, the remaining planes are defined. The orientation plane is defined by $\hat{z}_q$ and the deuteron's polarization vector, $\hat{d} = (\theta_d, \phi_d)$. Here, θ_d and ϕ_d are the respective polar and azimuthal angles that the deuteron polarization vector makes with respect to the q coordinate system. The reaction plane is defined by $\hat{z}_q$ and the relative proton-neutron momentum vector, $\vec{p}_{pn}^{\,CM}$. This latter vector has respective polar and azimuthal angles of θ_{pn}^{CM} and ϕ_{pn} with respect to the q coordinate system[6]. In general, one does not expect ϕ_{pn} and ϕ_d to be equal. Their difference is defined as $\tilde{\phi} \equiv \phi_{pn} - \phi_d$.

[4]With a slight abuse of notation, Q^2 will be used to indicate the negative of the square of the momentum transfer, that is $Q^2 = q^2 - \omega^2$, not $Q^2 = \omega^2 - q^2$. Doing so guarantees that $Q^2 > 0$, which is the convention in nuclear physics.

[5]Throughout this section, observables evaluated in the proton-neutron CM frame will carry a "CM" superscript; variables without such a superscript are evaluated in the rest frame of the deuteron (i.e., the lab frame).

[6]Since the boost to the proton-neutron CM frame is entirely along the $\hat{z}_q$ axis, azimuthal angles defined in the q coordinate system are not altered by the Lorentz boost. As such, to simplify the notation, the "CM" superscript on relevant azimuthal angles will be dropped.

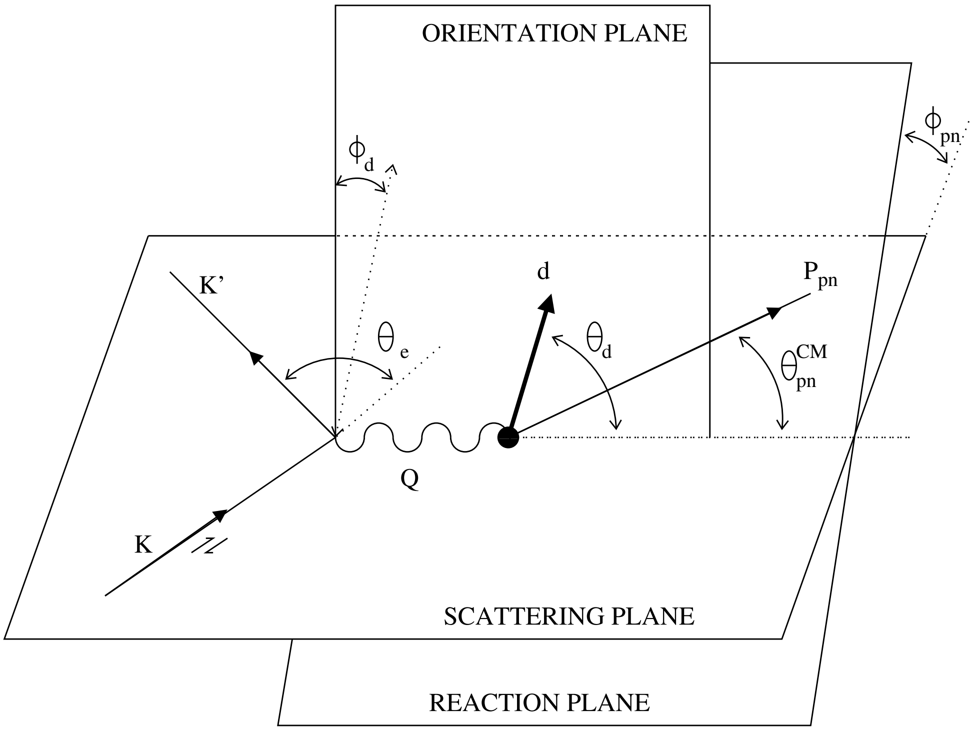

Figure 1-9: Geometry of exclusive deuteron electrodisintegration with longitudinally polarized electrons and oriented deuteron target. The respective incoming (outgoing) electron four-momenta are denoted by K (K'), the virtual photon four-momentum is denoted by Q, the relative proton-neutron momentum is denoted by P_{np}, and the deuteron's orientation axis vector is denoted by $\hat{d}$.

The differential cross section for deuteron electrodisintegration can be written as a sum of asymmetries weighted by different combinations of beam and target polarizations [6, 7]:

$$\begin{aligned} \frac{d\sigma}{d\omega d\Omega_e d\Omega_{pn}^{CM}} &\equiv S\left(h, \tilde{P}_z, \tilde{P}_{zz}\right) \\ &= S_0\left(1 + \tilde{P}_z A_d^V + \tilde{P}_{zz} A_d^T + h\left(A_e + \tilde{P}_z A_{ed}^V + \tilde{P}_{zz} A_{ed}^T\right)\right) \end{aligned} \quad (1.37)$$

Here, h is the helicity of the electron beam, and $\tilde{P}_z$ and $\tilde{P}_{zz}$ are the respective vector and tensor polarizations of the deuteron target as described above. Also, $\Omega_e \equiv (\theta_e \phi_e)$ and $\Omega_{pn}^{CM} \equiv (\theta_{pn}^{CM}, \phi_{pn})$ are the respective scattered electron and proton-neutron spherical angles. S_0 is the totally unpolarized cross section:

$$S_0 \equiv S\left(0, 0, 0\right) = c\left(\rho_L f_L + \rho_T f_T + \rho_{LT} f_{LT} \cos\phi_{pn} + \rho_{TT} f_{TT} \cos 2\phi_{pn}\right) \quad (1.38)$$

and A_d^V, A_d^T, A_e, A_{ed}^V, and A_{ed}^T are the respective vector, tensor, beam, beam-vector, and beam-tensor asymmetries:

$$\begin{aligned}
A_d^V &= \frac{c}{S_0}\sum_{M=0}^{1}\Big[\Big(\rho_L f_L^{1M} + \rho_T f_T^{1M} \\
&\quad + \rho_{LT} f_{LT}^{1M+}\cos\phi_{pn} + \rho_{TT} f_{TT}^{1M+}\cos 2\phi_{pn}\Big)\sin M\tilde{\phi} \\
&\quad + \Big(\rho_{LT} f_{LT}^{1M-}\sin\phi_{pn} + \rho_{TT} f_{TT}^{1M-}\sin 2\phi_{pn}\Big)\cos M\tilde{\phi}\Big]\, d_{M0}^{1}(\theta_d) && (1.39) \\
A_d^T &= \frac{c}{S_0}\sum_{M=0}^{2}\Big[\Big(\rho_L f_L^{2M} + \rho_T f_T^{2M} \\
&\quad + \rho_{LT} f_{LT}^{2M+}\cos\phi_{pn} + \rho_{TT} f_{TT}^{2M+}\cos 2\phi_{pn}\Big)\cos M\tilde{\phi} \\
&\quad - \Big(\rho_{LT} f_{LT}^{2M-}\sin\phi_{pn} + \rho_{TT} f_{TT}^{2M-}\sin 2\phi_{pn}\Big)\sin M\tilde{\phi}\Big]\, d_{M0}^{2}(\theta_d) && (1.40) \\
A_e &= \frac{c}{S_0}\rho'_{LT} f'_{LT}\sin\phi_{pn} && (1.41) \\
A_{ed}^V &= \frac{c}{S_0}\sum_{M=0}^{1}\Big[\Big(\rho'_T f_T^{'1M} + \rho'_{LT} f_{LT}^{'1M-}\cos\phi_{pn}\Big)\cos M\tilde{\phi} \\
&\quad - \rho'_{LT} f_{LT}^{'1M+}\sin\phi_{pn}\sin M\tilde{\phi}\Big]\, d_{M0}^{1}(\theta_d) && (1.42) \\
A_{ed}^T &= \frac{c}{S_0}\sum_{M=0}^{2}\Big[\Big(\rho'_T f_T^{'2M} + \rho'_{LT} f_{LT}^{'2M-}\cos\phi_{pn}\Big)\sin M\tilde{\phi} \\
&\quad + \rho'_{LT} f_{LT}^{'2M+}\sin\phi_{pn}\cos M\tilde{\phi}\Big]\, d_{M0}^{2}(\theta_d) && (1.43)
\end{aligned}$$

Here, the $d_{m'm}^{(j)}(\theta_d)$ are Wigner rotation matrices [50]:

$$d_{00}^{(1)}(\theta_d) \equiv \cos\theta_d \ , \ d_{10}^{(1)}(\theta_d) \equiv -\sqrt{\frac{1}{2}}\sin\theta_d \tag{1.44}$$

$$d_{00}^{(2)}(\theta_d) \equiv \frac{3}{2}\cos^2\theta_d - \frac{1}{2} \ , \ d_{10}^{(2)}(\theta_d) \equiv -\sqrt{\frac{3}{2}}\sin\theta_d\cos\theta_d \ , \ d_{20}^{(2)}(\theta_d) \equiv \sqrt{\frac{3}{8}}\sin^2\theta_d \tag{1.45}$$

and c is a kinematic variable:

$$c \equiv \frac{\alpha}{6\pi^2}\frac{\epsilon'}{\epsilon Q^4} \tag{1.46}$$

where α is the fine structure constant. The various $\rho^{(\prime)}_{(L)(T)}$ terms in (1.38) - (1.43) are the spherical components of the virtual photon density matrix. In the q coordinate system, they take the following forms:

$$\rho_L = \beta^2 Q^2 \frac{\xi^2}{2\eta} \quad , \qquad \rho_{LT} = \beta Q^2 \tfrac{\xi}{\eta}\sqrt{\tfrac{\xi+\eta}{8}} \quad , \qquad \rho_T = \frac{1}{2} Q^2 \left(1 + \frac{\xi}{2\eta}\right)$$
$$\rho_{TT} = -Q^2 \frac{\xi}{4\eta} \quad , \qquad \rho'_{LT} = \tfrac{1}{2}\beta Q^2 \tfrac{\xi}{\sqrt{2\eta}} \quad , \qquad \rho'_T = \frac{1}{2} Q^2 \sqrt{\frac{\xi+\eta}{\eta}}$$

where $\beta = |\vec{\beta}| = |\vec{q}|/(\omega + m_d)$ is the boost from the laboratory to the CM frame and $\xi \equiv Q^2/|\vec{q}|^2$ and $\eta \equiv \tan^2(\theta_e/2)$ are kinematic variables. The "L" and "T" refer to the respective longitudinal and transverse polarization states of the virtual photon.

The various $f^{(\prime)(IM)(\pm)}_{(L)(T)}$ are the nuclear structure functions. In general, a dynamical model is needed in order to calculate them. Such a dynamical model has been created by Arenhövel et al. [6, 7, 55]. In their model, the nucleons are considered to behave non-relativistically thus allowing for a non-relativistic expansion of the relativistic electromagnetic nucleon current in orders of (p_p/m_N), where m_N is the mass of the nucleon. A consistent non-relativistic calculation was made by solving the Schrödinger equation using a potential model for the NN interaction. Additionally, relativistic corrections (RC), final state interactions (FSI) between the outgoing nucleons, meson exchange currents (MEC) due to the exchange of π, ρ, or ω mesons, and nuclear isobar configurations (IC) such as $N\Delta(1232)$, $N\Delta(1470)$, and $\Delta\Delta$ were also accounted for. Exchange contributions, wherein the detected nucleon is not the one scattered from, were taken into account by appropriate symmetrization of the wave functions; the Plane Wave Born Approximation (PWBA) refers to the PWIA with nucleon exchange reactions accounted for. Examples of lowest-order Feynman diagrams for these various effects are shown in Fig. 1-10.

Sensitivity to the PWBA and to non-PWBA reaction mechanisms change depending on the kinematic region probed. Sensitive regions can be identified by examining a plot of the relative proton-neutron CM kinetic energy, T^{CM}_{pn}, versus the square of the CM three momentum transfer magnitude, $(q^{CM})^2$:

$$T^{CM}_{pn} = \sqrt{(\omega + m_d)^2 - q^2} - (m_p + m_n) \qquad (1.47)$$

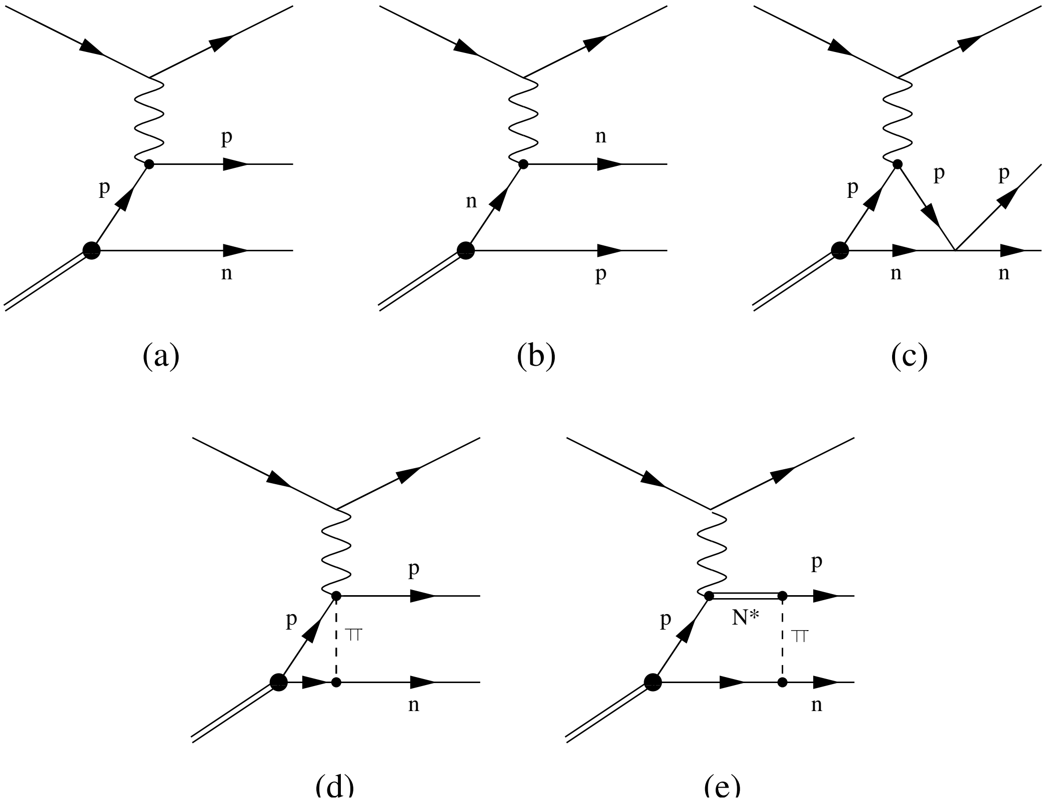

Figure 1-10: Lowest-order Feynman diagrams for $^2H(e,e'p)n$ scattering. (a) PWIA e-p scattering (b) PWIA e-n scattering (c) final state interaction between the exiting nucleons (d) a π exchange current, and (e) an N^* isobar excitation. Proper symmetrization of the wave function over diagrams (a) and (b) leads to the PWBA.

$$q^{CM} = \frac{m_d q}{\sqrt{(\omega + m_d)^2 - q^2}} \tag{1.48}$$

In these kinematics, for $T_{pn}^{CM} \ll 4m_N$ where $m_N \equiv (m_p + m_n)/2$, the QE ridge can be shown to approximately obey the following [55]:

$$T_{pn}^{CM} \approx \frac{m_N}{m_d^2}(q^{CM})^2 = 0.267(q^{CM})^2 \tag{1.49}$$

A plot of T_{pn}^{CM} versus $(q_{CM})^2$ is shown in Fig. 1-11. Four regions can be identified in which specific effects dominate [6]. In the neighborhood of the QE ridge, as defined by (1.49), MEC, IC, and FSI are all expected to be small due to the neutron being essentially removed from the scattering. In the disintegration threshold region, located at low T_{pn}^{CM}, MEC are dominant. In the intermediate region, between the disintegration threshold and QE regions, FSI are important while MEC and IC are sizable. Finally, as one proceeds to even higher T_{pn}^{CM}, IC, such as Δ-excitation, become increasingly dominant.

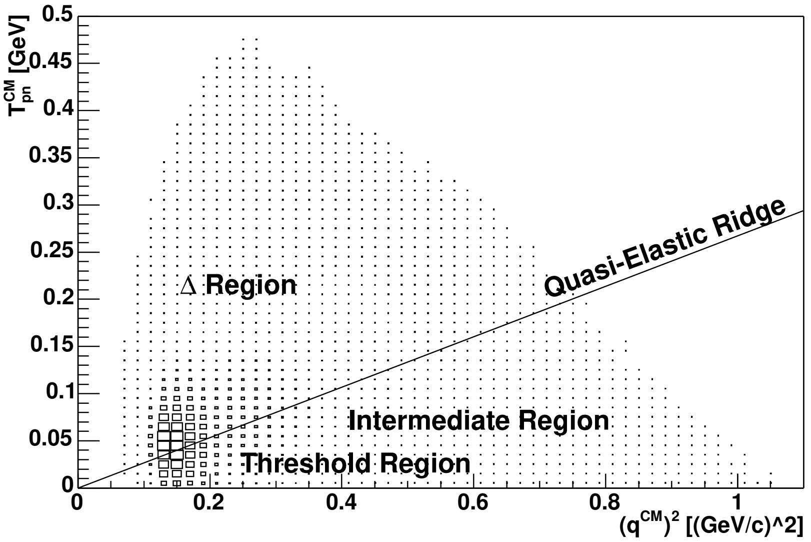

Figure 1-11: Kinematic plane showing T_{pn}^{CM} versus $\left(q^{CM}\right)^2$. The boxes represent data weighted by the kinematic acceptance of the BLAST detector. QE kinematics dominate the acceptance, but the acceptance of BLAST is such that data in all kinematic sectors is attainable.

By varying the beam and target polarizations, it is possible to separate each of the asymmetries in (1.38) - (1.43). In particular, six independent polarization states are sufficient to completely separate S_0 and the five asymmetries:

$$\begin{aligned} S_0 &= \frac{1}{6}\Big[S(h,\tilde{P}_z,\tilde{P}_{zz}) + S(-h,\tilde{P}_z,\tilde{P}_{zz}) + S(h,-\tilde{P}_z,\tilde{P}_{zz}) \\ &\quad + S(-h,-\tilde{P}_z,\tilde{P}_{zz}) + S(h,0,-2\tilde{P}_{zz}) + S(-h,0,-2\tilde{P}_{zz})\Big] \qquad (1.50) \\ A_e &= \frac{1}{6hS_0}\Big[S(h,\tilde{P}_z,\tilde{P}_{zz}) - S(-h,\tilde{P}_z,\tilde{P}_{zz}) + S(h,-\tilde{P}_z,\tilde{P}_{zz}) \\ &\quad - S(-h,-\tilde{P}_z,\tilde{P}_{zz}) + S(h,0,-2\tilde{P}_{zz}) - S(-h,0,-2\tilde{P}_{zz})\Big] \qquad (1.51) \\ A_d^V &= \frac{1}{4\tilde{P}_z S_0}\Big[S(h,\tilde{P}_z,\tilde{P}_{zz}) + S(-h,\tilde{P}_z,\tilde{P}_{zz}) \\ &\quad - S(h,-\tilde{P}_z,\tilde{P}_{zz}) - S(-h,-\tilde{P}_z,\tilde{P}_{zz})\Big] \qquad (1.52) \\ A_d^T &= \frac{1}{12\tilde{P}_{zz}S_0}\Big[S(h,\tilde{P}_z,\tilde{P}_{zz}) + S(-h,\tilde{P}_z,\tilde{P}_{zz}) + S(h,-\tilde{P}_z,\tilde{P}_{zz}) \end{aligned}$$

$$+S(-h,-\tilde{P}_z,\tilde{P}_{zz}) - 2[S(h,0,-2\tilde{P}_{zz}) + S(-h,0,-2\tilde{P}_{zz})]\Big] \quad (1.53)$$

$$A^V_{ed} = \frac{1}{4h\tilde{P}_z S_0}\Big[S(h,\tilde{P}_z,\tilde{P}_{zz}) - S(-h,\tilde{P}_z,\tilde{P}_{zz})$$
$$-S(h,-\tilde{P}_z,\tilde{P}_{zz}) + S(-h,-\tilde{P}_z,\tilde{P}_{zz})\Big] \quad (1.54)$$

$$A^T_{ed} = \frac{1}{12h\tilde{P}_{zz} S_0}\Big[S(h,\tilde{P}_z,\tilde{P}_{zz}) - S(-h,\tilde{P}_z,\tilde{P}_{zz}) + S(h,-\tilde{P}_z,\tilde{P}_{zz})$$
$$-S(-h,-\tilde{P}_z,\tilde{P}_{zz}) - 2[S(h,0,-2\tilde{P}_{zz}) - S(-h,0,-2\tilde{P}_{zz})]\Big] \quad (1.55)$$

Once an asymmetry has been separated, the various structure functions internal to it can be separated or emphasized by appropriate use of kinematics. For example, when the momentum transfer vector, $\vec{q}$, is aligned parallel to the deuteron polarization axis, $\hat{d}$, then $\theta_d = \phi_d = 0$ and thus $\sin\theta_d = 0$. Due to (1.44) - (1.45), asymmetries measured in this configuration will contain information regarding only those component structure functions weighted by $\cos\theta_d$. If the outgoing proton is further restricted to also lie along $\vec{q}$, then $\phi_{pn} = \tilde{\phi} = 0$. Eq. (1.40) and (1.42) then reduce to the following:

$$\left(A^T_d\right)_{\parallel} = \frac{c}{S_0}\left[\rho_L f^{20}_L + \rho_T f^{20}_T + \rho_{LT} f^{20+}_{LT} + \rho_{TT} f^{20+}_{TT}\right] \quad (1.56)$$

$$\left(A^V_{ed}\right)_{\parallel} = \frac{c}{S_0}\left[\rho'_T f'^{10}_T + \rho'_{LT} f'^{10-}_{LT}\right] \quad (1.57)$$

On the other hand, if the momentum transfer is restricted so that $\theta_d = \pi/2$ and $\phi_d = \pi$, then only those terms weighted by $\sin\theta_d$ will contribute. If the proton is further restricted to lie along $\vec{q}$, then $\phi_{pn} = 0$ and $\tilde{\phi} = 0 - \pi = -\pi$. Eq. (1.40) and (1.42) then reduce to the following:

$$\left(A^T_d\right)_{\perp} = \sqrt{\frac{3}{8}}\frac{c}{S_0}\left[\rho_L f^{22}_L + \rho_T f^{22}_T + \rho_{LT} f^{22+}_{LT} + \rho_{TT} f^{22+}_{TT}\right] \quad (1.58)$$

$$\left(A^V_{ed}\right)_{\perp} = \sqrt{\frac{1}{2}}\frac{c}{S_0}\left[\rho'_T f'^{11}_T + \rho'_{LT} f'^{11-}_{LT}\right] \quad (1.59)$$

As will be discussed in Section 2, the acceptance of the BLAST detector is such that detected electron-proton coincidences from ${}^2\vec{H}(\vec{e},e'p)n$ have the electron and proton in opposite detector sectors. As such, electron-proton coincidences with the electron in the left (right) sector will have corresponding momentum transfer vectors directed into the right (left) sector. With the deterium target polarized to point in-plane into the left sector, it then follows that, to first order, an electron-proton coincidence with the electron scattering into the left sector in BLAST will have respective tensor and beam-vector asymmetries dominated by (1.58) and (1.59). Similarly, an electron-proton coincidence with the electron scattering into the right sector in BLAST will have asymmetries dominated by (1.56) and (1.57). For this reason, asymmetries generated by an electron in the left (right) sector are referred to as perpendicular (parallel) asymmetries throughout this work.

The Tensor Asymmetry, $\mathbf{A_d^T}$

As discussed in Section 1.4, the ${}^2\vec{H}(\vec{e}, e'p)n$ electrodisintegration tensor asymmetry, A_d^T, as expressed in (1.40) vanishes in the limit of an $L = 0$ deuteron in the PWBA. The tensor asymmetry thus provides information on the D-state contribution to the deuteron, or, equivalently, on the tensor component of the NN interaction.

In addition to contributions from the D-state, A_d^T will in general also have contributions from the various non-PWBA reaction mechanisms (MEC, IC, and FSI). On the QE ridge, such mechanisms are expected to be small. However, as one progresses kinematically away from QE scattering, reaction mechanism effects play an ever increasing role. Plots of the tensor asymmetry, A_d^T, versus missing momentum magnitude, p_M, are shown in Fig. 1-12 for different Q^2 regions accessible in BLAST. The data for these plots were generated from the deuteron electrodisintegration model from Arenhövel et al. using the Bonn potential [6, 7]; the data have also been weighted for acceptance in the BLAST detector.

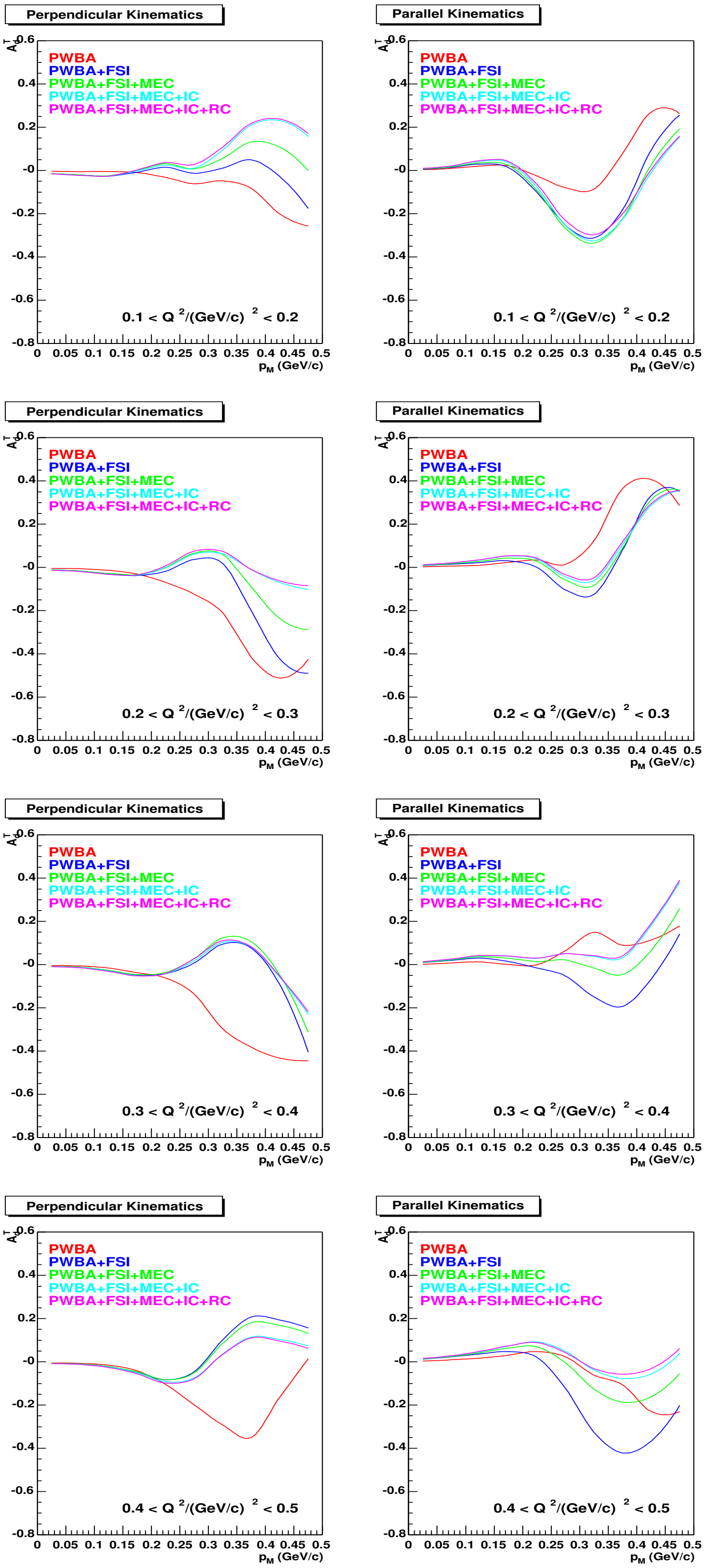

Figure 1-12: Plots of the tensor asymmetry, A_d^T, versus missing momentum, p_M, for perpendicular and parallel kinematics in BLAST. All plots were generated using the model in [7] with the Bonn potential.

Each plot in Fig. 1-12 shows a comparison of the relative reaction mechanism contributions to A_d^T. The contributions due to FSI, MEC, IC, and RC are progressively added onto the PWBA. The total model is equal to the model incorporating PWBA, FSI, MEC, IC, and RC contributions. From examining the plots, the following conclusions are apparent:

- At low p_M ($\lesssim 0.25$ GeV/c), A_d^T is consistent with zero in all kinematics.
- As p_M increases, nonzero structure begins to appear. On the whole, the asymmetries in all kinematics reach a maximum $|A_d^T|$ value around $p_M \sim 0.35$. The onset of this structure around p_M was predicted from D-state arguments in Section 1.4.
- In perpendicular kinematics, away from the QE ridge (i.e., $p_M > 0$), the contributions to A_d^T from non-PWBA reaction mechanisms are of the same magnitude as the PWBA ones. At low Q^2, the contributions from FSI, MEC, and IC are all of the same size. At high Q^2, FSI dominate.
- In parallel kinematics, away from the QE ridge, FSI contributions dominate the non-PWBA contributions at low Q^2. However, at high Q^2, the contributions between FSI, MEC, and IC once again become nearly equal.
- RC are negligible for all kinematics.

Plots of A_d^T versus $\cos\theta_M$, where θ_M is the angle between the deuteron polarization and missing momentum vectors, are shown in Fig. 1-13 for the same kinematics and setup as in Fig. 1-12. Since A_d^T vanishes in the limit of an $L = 0$ deuteron, the presence of the D-state causes deviation from zero. It should also be noted that, as seen in (1.16) and (1.17) as well as Fig. 1-7, A_d^T is a purely even function of θ_M in the PWIA. To the extent that A_d^T is dominated by the PWBA in the plots in Fig. 1-13, it then follows that any deviation from symmetry when $\theta_M \to -\theta_M$ is a result of proton-neutron exchange processes.

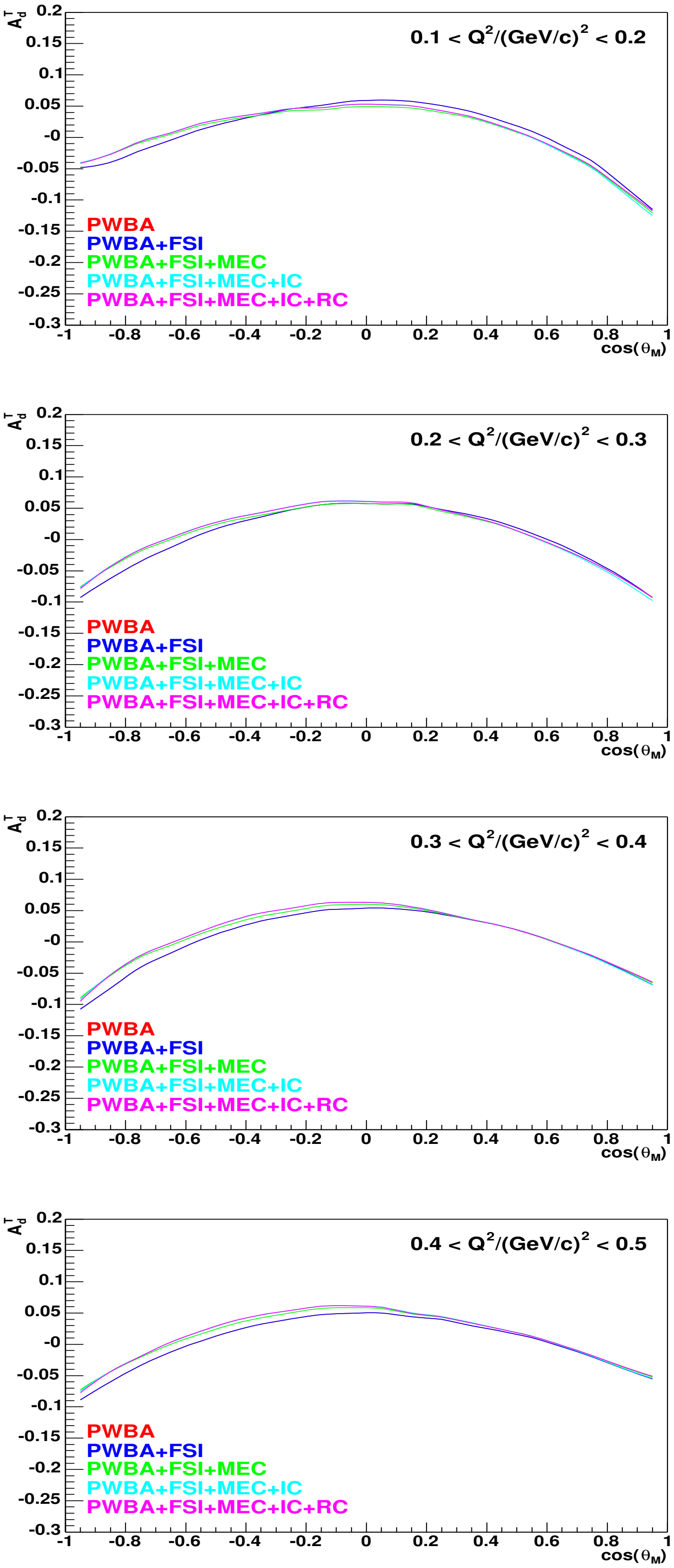

Figure 1-13: Plots of the tensor asymmetry, A_d^T, versus $\cos\theta_M$, where θ_M is the angle between the deuteron polarization and missing momentum vectors. All plots were generated using the model in [7] with the Bonn potential.

Finally, it should be noted that experimentally only the total tensor asymmetry is measurable and thus directly observable. As such, D-state effects are convoluted with those from non-PWBA reaction mechanisms. In general, this places constraints on how definitively information can be extracted on any one particular contribution to an asymmetry.

The Beam-Vector Asymmetry, $\mathbf{A_{ed}^{V}}$

Similar to the tensor asymmetry, the ${}^2\vec{H}(\vec{e}, e'p)n$ electrodisintegration beam-vector asymmetry, A_{ed}^{V}, as expressed in (1.42), has structure influenced by the D-state and the various reaction mechanism contributions. Fig. 1-14 compares A_{ed}^{V} versus p_M for various progressive models [44]. In the PWIA, in the limit on an $L = 0$ (i.e., S-state only) deuteron, A_{ed}^{V} is approximately constant and negative for all p_M. However, when a nonzero D-state component is added in, a large rise at high p_M appears. Smaller (but still significant) contributions from the various reaction mechanisms further increase the rise.

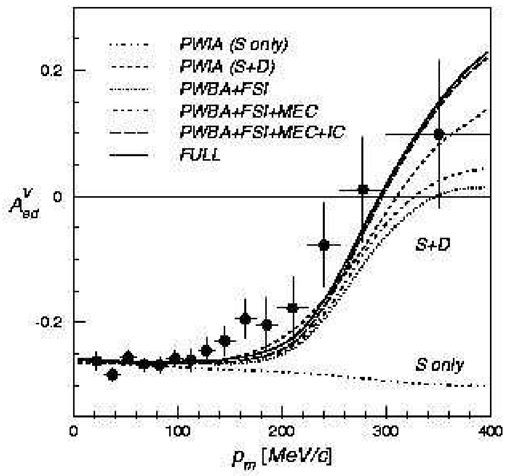

Figure 1-14: The ${}^2\vec{H}(\vec{e}, e'p)n$ electrodisintegration beam-vector asymmetry, A_{ed}^{V}, versus missing momentum, p_M, for subsequent models: PWIA with only an S-state; PWIA with S- and D-states; PWBA with FSI; PWBA with FSI and MEC; PWBA with FSI, MEC, and IC; and the full model (i.e., PWBA with FSI, MEC, IC, and RC). The experimental data were taken at NIKHEF with the BigBite spectrometer. This plot is reprinted from [44].

For BLAST kinematics, the ${}^2\vec{H}(\vec{e}, e'p)n$ beam-vector asymmetry, A^V_{ed}, versus the missing momentum, p_M, is plotted in Fig. 1-15 for the same kinematics and setup as in Fig. 1-12. The following conclusions are apparent:

- For all kinematics, in the QE limit ($p_M \to 0$), contributions from the various non-PWBA reaction mechanisms disappear, and the total model is consistent with the PWBA one.

- As p_M increases, A^V_{ed} starts to rise in general in all kinematics. This rise occurs around $p_M \sim 0.35$ GeV/c which is conistent with the onset of the D-state as discussed in Section 1.4.

- Unlike the tensor asymmetry results in Fig. 1-12, non-PWBA reaction mechanism contributions to A^V_{ed} at high p_M are smaller in magnitude than the general rise due to the existence of the D-state (i.e., the PWBA). For this asymmetry, the PWBA is to first order consistent with the total model; the various non-PWBA reaction mechanism contributions are more perturbative than radically structure-changing.

- RC are negligible for all kinematics.

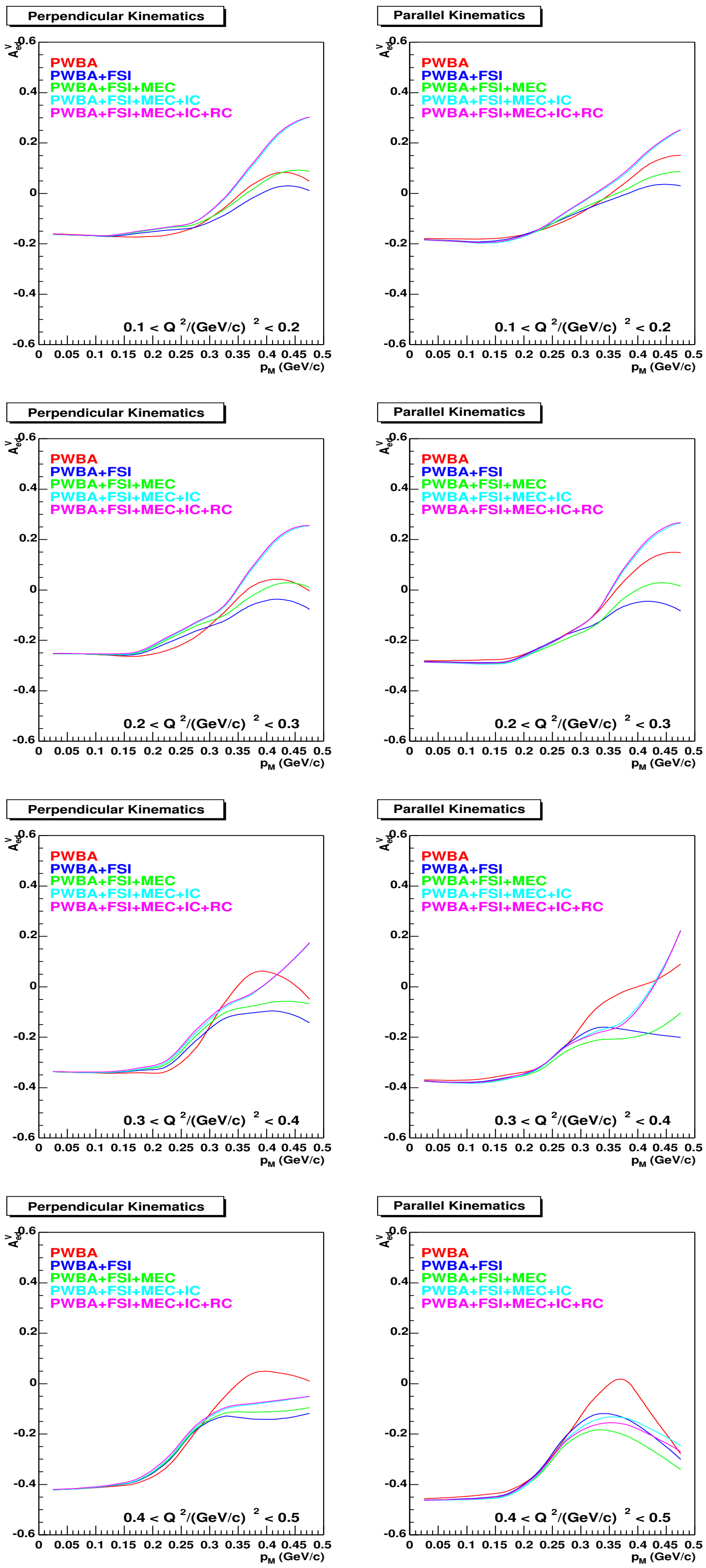

Figure 1-15: Plots of the beam-vector asymmetry, A^V_{ed}, versus missing momentum, p_M, for perpendicular and parallel kinematics in BLAST. All plots were generated using the model in [7] with the Bonn potential.

As seen from Fig. 1-15, in the QE limit (i.e., as $p_M \to 0$), non-PWBA contributions to A^V_{ed} become negligible. Additionally, as shown in Fig. 1-14, D-state effects also disappear in this limit. Thus, ${}^2\vec{H}(\vec{e}, e'N)N'$ in the QE limit effectively reduces to $\vec{N}(\vec{e}, e'N)$ with a spectator nucleon, N'. In this limit, the ${}^2\vec{H}(\vec{e}, e'N)N'$ beam-vector asymmetry takes the following form [6]:

$$A^V_{ed}\left(\theta_d, \phi_d\right)_{p/n} = -\sqrt{\frac{2}{3}}\frac{1}{\left(1 + \frac{\rho_L}{\rho_T}R^2_{p/n}\right)}\left[\frac{\rho'_T}{\rho_T}\cos\theta_d + 2\frac{\rho'_{LT}}{\rho_T}\sin\theta_d\cos\phi_d R_{p/n}\right] \tag{1.60}$$

where the "p/n" subscript refers to whether the proton/neutron is detected. Furthermore, $R_{p/n}$ is directly proportional to the ratio of the proton's/neutron's electric and magnetic form factors, $G^{p/n}_E/G^{p/n}_M$:

$$R_{p/n} \equiv \frac{\sqrt{2}m_{p/n}}{Q}\left(\frac{G^{p/n}_E}{G^{p/n}_M}\right) \tag{1.61}$$

If the kinematics are chosen so that $\theta_d = \pi/2$ and $\phi_d = 0$, then the ${}^2\vec{H}(\vec{e}, e'N)N'$ beam-vector asymmetry is directly proportional to the corresponding detected nucleon form factor ratio:

$$A^V_{ed}\left(\theta_d = \frac{\pi}{2}, \phi_d = 0\right)_{p/n} = -2\sqrt{\frac{2}{3}}\frac{\rho'_{LT}\rho_{p/n}}{\rho_T}R_{p/n} \tag{1.62}$$

Due to the absence of free-neutron targets, the above equation is frequently used to extract measurements of G^n_E via QE neutron scattering [61]. Such measurements require knowledge of the beam-vector polarization, $h\tilde{P}_z$, in order to extract G^n_E successfully. To reduce uncertainties, QE scattering from the proton can be used to extract a value for $h\tilde{P}_z$ via normalization of the measured beam-vector asymmetry to the theoretical one. This measurement extracts $h\tilde{P}_z$ with small model uncertainty, since D-state effects as well as reaction mechanism effects are negligible in the QE limit. Additionally, the relatively large value for QE proton scattering as well as the high detector efficiency for proton detection guarantee small statistical errors in the extraction.

Chapter 2

The BLAST Experiment

2.1 Introduction

The experiment discussed in this thesis was undertaken with the Bates Large Acceptance Spectrometer Toroid (BLAST) detector at the MIT-Bates Linear Accelerator Center in Middleton, MA. In this chapter, the BLAST experiment is described in detail.

2.2 Stored Polarized Electron Beam

Longitudinally polarized electrons are produced by photoemission using a $\lambda = 810$ nm circularly-polarized multimode fiber-coupled diode array laser system incident on a $GaAs_{0.95}P_{0.05}$ crystal. The polarization state of the beam is determined by a half-wave plate in the path of the laser source; the plate is moved in or out with each fill, thus resulting in alternating fills having opposite polarization.

After an initial 360 keV acceleration away from the crystal, the electrons enter into a linear accelerator consisting of 190 m of accelerating RF cavities. A recirculator transports the beam back to the beginning of the accelerator for a second pass through the RF cavities. The polarized beam leaves the linear accelerator at an energy of 0.850 GeV.

The electron beam is injected into the South Hall Ring (SHR) shown in Fig. 2-1.

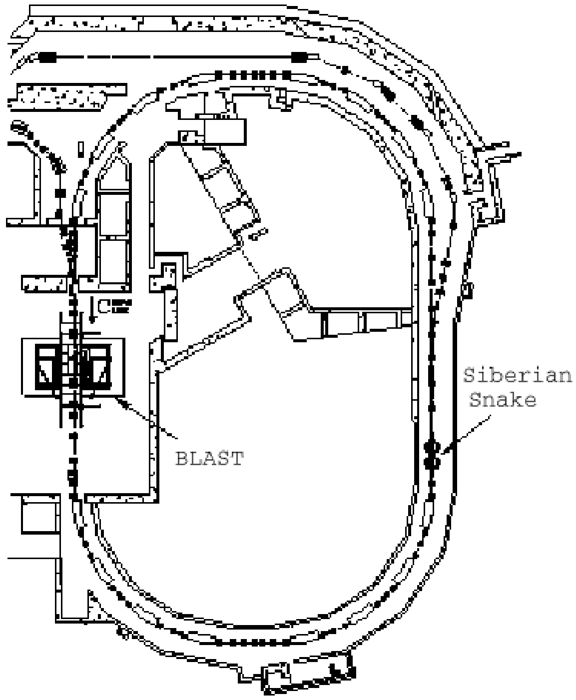

Figure 2-1: Overhead view of the MIT-Bates South Hall Ring.

The SHR operates as either a storage ring for internal target experiments (such as BLAST) or as a pulse stretcher ring to produce nearly continuous-wave beam for external target experiments [14]. In storage mode, currents in excess of 200 mA are achieved by stacking beam pulses of a few mA head-to-tail at an injection rate of $2-20$ Hz. This head-to-tail injection results in the storage ring having a duty factor of 99% [20].

The SHR has an oval, racetrack design with sixteen dipole magnets, each bending the beam by 22.5°. An RF cavity internal to the ring is used to stabilize the beam energy as well as to compensate for synchroton radiation loss. Near the interaction region, four beam-quality monitor scintillators are placed to assist in tuning the beam fills. A listing of the SHR parameters for the BLAST experiment is given in Tab. 2.1.

The beam tune must accomodate the storage cell in the center of the west straight section of the ring (the left side of Fig. 2-1). Due to the small radius of the storage

SHR Parameter	Value	Units
Energy Range	300 – 1000	MeV
Circumference	190.204	m
Revolution Frequency	1.576	MHz
Bend Radius	9.144	m
Stored Current	≥ 100	mA
Internal Duty Factor	99	%
Injection Frequency	1 – 1000	Hz
RF Frequency	2.856	GHz
Harmonic Number	1812	

Table 2.1: South Hall Ring Parameters.

cell, a low β-function of the beam is required within this region to minimize scattering from the cell walls. To decrease background scattering further, a tungsten collimator with a radius slightly smaller than that of the target cell was placed slightly upstream of it. The collimator also helps to protect the target cell's coating from damage caused by the electron beam and synchrotron radiation [61].

The current in the ring is measured non-destructively with a zero-flux DC current transformer (LDCCT) [54]. It has a frequency response from DC to 100 kHz and an absolute accuracy of 0.05%; the output voltage is proportional to the beam current and is routinely calibrated. The output voltage goes to a 16 bit ADC and broadcasts it to EPICS [18], the slow-control system utlized in the project. It then goes to a voltage-to-frequency converter which is then digitized in a scaler.

The longitudinal polarization of the electron beam in the storage ring is preserved by a Siberian snake [62] located on the opposite side of the ring from the target. The snake rotates the electron's spin vector to the opposite side of the momentum vector so that the $g-2$ precession in the north arc of the ring cancels that in the south arc.

A Compton polarimeter is used to monitor the beam polarization in a nondestructive manner [26]. The Compton polarimeter exploits the spin asymmetry of back-scattered polarized photons. Circularly polarized photons from a 5 W laser at 532 nm are incident on the stored electron beam in a section of the ring upstream of the target. Photons are scattered into a narrow cone centered around the incident photon path. By alternating the polarization of the incident photons via a Pockels cell [2],

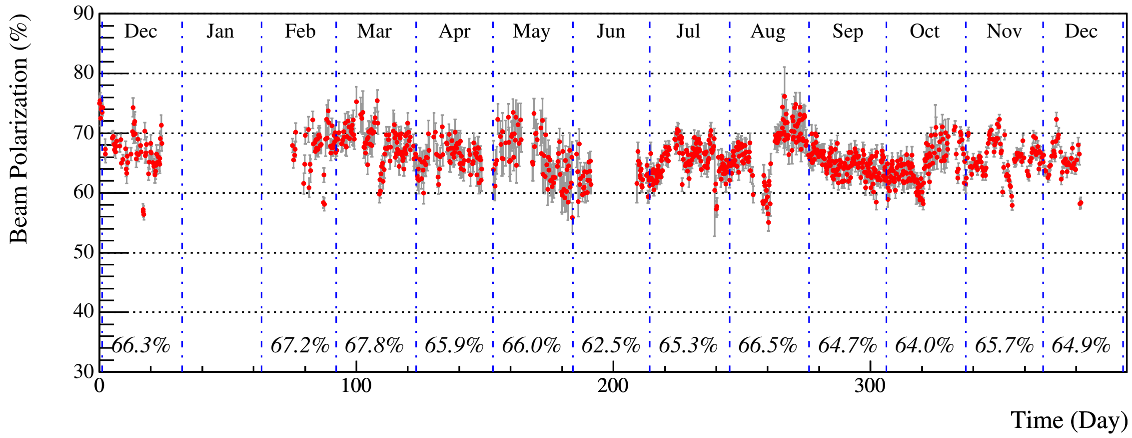

Figure 2-2: Daily measurement results of the polarization of the stored electron beam over the BLAST running period.

the spin-dependent asymmetry for this reaction can be measured. Normalization to the theoretical asymmetry gives the beam polarization. A set of absorbers, sweep magnets, and charged-particle veto counters reduce the charged particle and synchroton radiation backgrounds. The energy spectrum of the back-scattered photons is measured by a CsI calorimeter. The average polarization during the experiment as determined by the Compton polarimeter was $65 \pm 4\%$. The uncertainty in this measurement is dominated by the internal systematic uncertainties of the polarimeter.

2.3 The Polarized Deuterium Gas Target

BLAST utilizes an Atomic Beam Source (ABS) to inject polarized deuterium atoms into an internal storage cell [61]. The ABS was originally used in the AmPS Ring at the NIKHEF laboratory [24, 60] and modified to operate efficiently in the BLAST toroidal magnetic field [29].

The physical layout of the ABS is shown in Fig. 2-3. Molecular deuterium is pumped into a dissociator. An RF frequency of 27.12 MHz is applied, and the molecular gas dissociates into its atomic constituents. The atomic beam is then ejected from the nozzle; the nozzle is cooled to ~ 70 K to inhibit molecular recombination of the dissociated atoms as well as to reduce the individual atomic thermal velocities for more efficient focusing. The ejected beam is focused by the sextupole magnet system and passes into the ABS RF transition units.

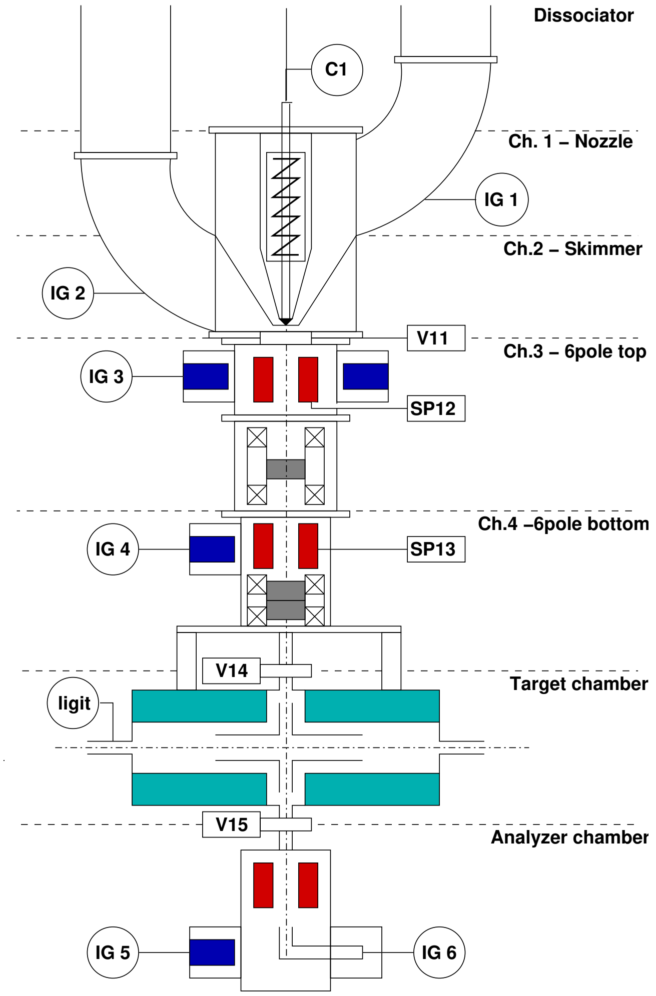

Figure 2-3: Schematic representation of the ABS and target storage cell.

Polarization of the atomic beam is achieved by exploiting the hyperfine degeneracy of deuteron spin states in the presence of a magnetic field (see Fig. 2-4). By applying a superposition of a time-varying and static magnetic field, transitions between the hyperfine states can be induced. Atoms populating undesired hyperfine states are defocused by a sextupole (6-pole) magnet and removed from the atomic beam using the Stern-Gerlach effect [11]. Depending on the desired polarization state, the atomic beam passes through three kinds of transitions: a strong field transition (SFT), a

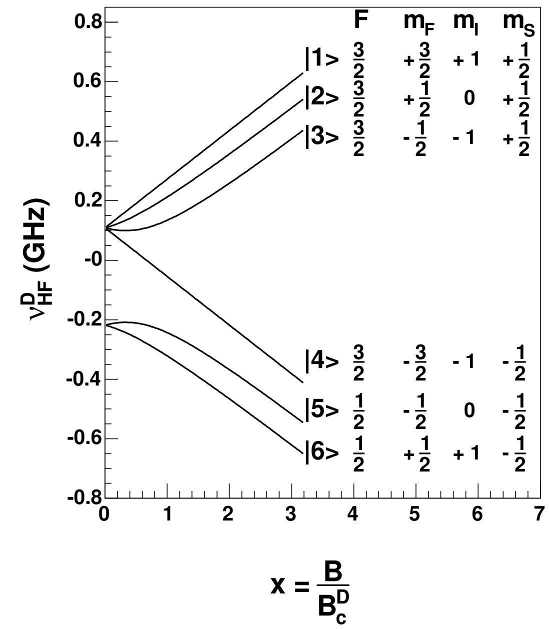

Figure 2-4: The hyperfine structure of deuterium. In the presence of an external magnetic field, B, the hyperfine energy levels, ν_{HF}^{D}, become nondegenerate. Here, I is the nuclear spin, S is the electron spin, and F is the total atomic spin. The various m_X $(X = I, S, F)$ are the corresponding azimuthal spin projections along the polarization axis. $B_C^D = 117$ G is the characteristic magnetic field for hyperfine interactions in deuterium.

weak field transition (WFT), and a medium field transition (MFT). The SFT uses a time-varying magnetic field directed perpendicular to a static one to cause atoms to switch populations between different hyperfine multiplets; the WFT and MFT use a time-varying magnetic field directed along the static one to cause population changes within a hyperfine multiplet. By applying the correct sequence of transitions, it is possible to produce positively and negatively vector/tensor (P_Z/P_{ZZ}) polarized deuterium beam. As an example, the series of transitions that result in deuterium having a $P_Z = P_{ZZ} = +1$ vector/tensor polarization is shown in Table 2.2.

Upon leaving the ABS chamber, the polarized atomic beam enters the target cell within the scattering chamber. The target cell is internal to the SHR and is cylindrical in shape. It has a diameter of 15 mm and runs 60 cm parallel to the beam-line. The target cell is used to maximize the luminosity of the polarized atomic beam while preserving the stored electron beam in the SHR. The atomic beam enters via the

$$\begin{pmatrix} n_1 \\ n_2 \\ n_3 \\ n_4 \\ n_5 \\ n_6 \end{pmatrix} \underset{\longrightarrow}{6 - pole} \begin{pmatrix} n_1 \\ n_2 \\ n_3 \\ 0 \\ 0 \\ 0 \end{pmatrix} \underset{\longrightarrow}{MFT} \begin{pmatrix} n_1 \\ n_2 \\ 0 \\ n_3 \\ 0 \\ 0 \end{pmatrix} \underset{\longrightarrow}{6 - pole} \begin{pmatrix} n_1 \\ n_2 \\ 0 \\ 0 \\ 0 \\ 0 \end{pmatrix} \underset{\longrightarrow}{SFT} \begin{pmatrix} n_1 \\ 0 \\ 0 \\ 0 \\ 0 \\ n_2 \end{pmatrix}$$

Table 2.2: The ABS transitions and sextupole magnet process for producing deuterium with positive vector and tensor polarization. The six n_i entries in the leftmost column correspond to the populations in the six hyperfine states in Fig. 2-4 as they enter the ABS transition region. As the atomic beam progresses through the ABS, various states are switched and/or removed.

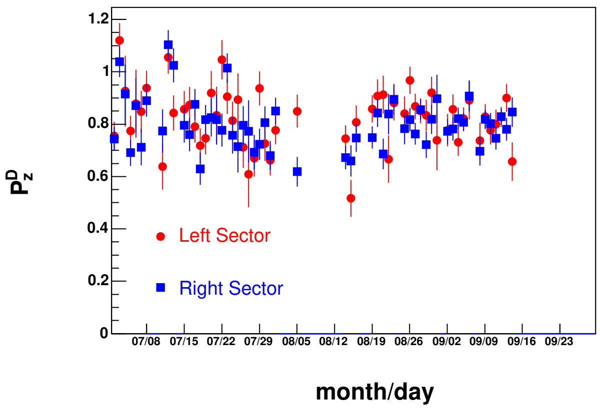

Figure 2-5: Plot of the target vector polarization, P_Z^D, over the course of the experiment.

inlet tube at the middle and disperses throughout the entire 60 cm length of the cell. The density profile along the cell is approximately triangular [48]. To decrease depolarization within the target cell, the inside of the cell is coated with Drifilm and kept at ~ 100 K. A holding field magnet is used to define the target polarization axis. It is capable of generating longitudinal and transverse magnetic fields. The holding magnet is limited in length, however, to 40 cm. As such, only the innermost 40 cm of the target cell contain reliably polarized atoms.

Over the course of the experiment, the ABS achieved an average intensity of 2.6×10^{16} atoms/sec corresponding to a target thickness of $\sim 4.5\times10^{13}$ atoms/cm^2 [61].

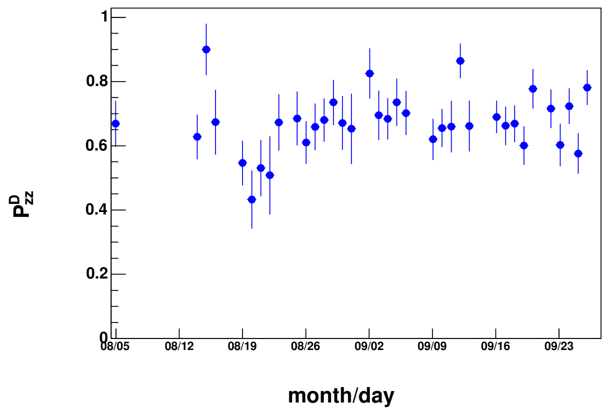

Figure 2-6: Plot of the target tensor polarization, P^D_{ZZ}, over the course of the experiment.

The respective vector and tensor polarization magnitudes, P_z and P_{zz}, were obtained through known electron scattering reactions. The vector polarization was determined from quasi-elastic $^2\vec{H}(\vec{e}, e'p)n$ scattering and will be discussed in detail in Chap. 4. The tensor polarization was determined from elastic $^2\vec{H}(\vec{e}, e'd)$ scattering [58]. Both polarizations were monitored daily during the experiment; weekly polarization results are shown in Figs. 2-5 and 2-6.

2.4 The Toroid Magnet

The magnetic field used in BLAST is generated by eight copper conductor coils arranged symmetrically around the beam line (see Fig. 2-7). The resulting magnetic field is toroidal about the beam line and serves to provide curvature to the trajectories of charged particles in the detector region. Such curvature is required to measure particles' momenta and charge sign. Each coil consists of two adjacent layers of thirteen windings of 1.5 x 1.5 in^2 hollow copper conductor. The operating current of a coil is 6731 A. The maximum field produced by the coils is $\sim$ 3800 G and occurs $\sim$ 1 m from the beam line in the vicinity of the drift chambers.

The magnetic field has been extensively mapped in the target and detector regions [20, 53]. The resulting map is used to reconstruct the trajectories of charged particles.

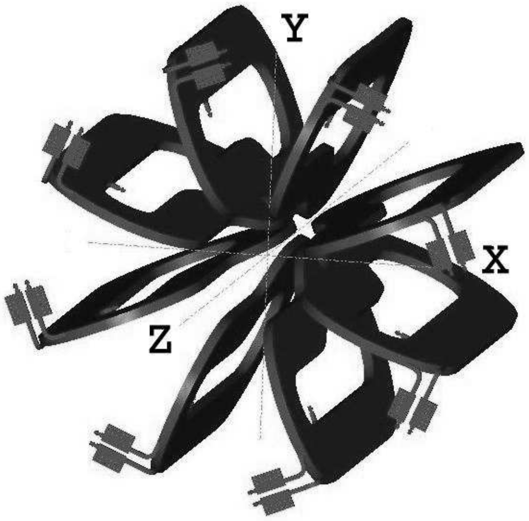

Figure 2-7: Magnetic coils in BLAST. Beam runs along the z-axis.

Fig. 2-8 is a plot comparing the vertical component of the magnetic field with that of a Biot-Savart calculation assuming the coils are in their ideal, designed positions. The plot shows measurements in-plane ($y = 0$) and is plotted versus increasing perpendicular distance from the center of the target ($z = 0$). Good agreement with the Biot-Savart calculation assuming ideal coil placement is seen. The major source of discrepancy is due to misalignment of the coils, which was not accounted for using the Biot-Savart calculation. In addition, some ferro-magnetic hardware has been added (e.g., iron shielding for the Cerenkov counters; see Sec. 2.5.1) since the mapping was performed; the presence of such material will also cause some deviation from the results in the plot. A re-mapping of the field in the presence of the ferro-magnetic hardware is scheduled in the near future.

2.5 The BLAST Detector

The BLAST detector is designed to accommodate the geometry of the toroidal magnetic coils (see Fig. 2-9). As discussed in Section 3.5, the drift chambers are designed to lie between the magnetic coils. To maximize acceptance, the chambers' entrance

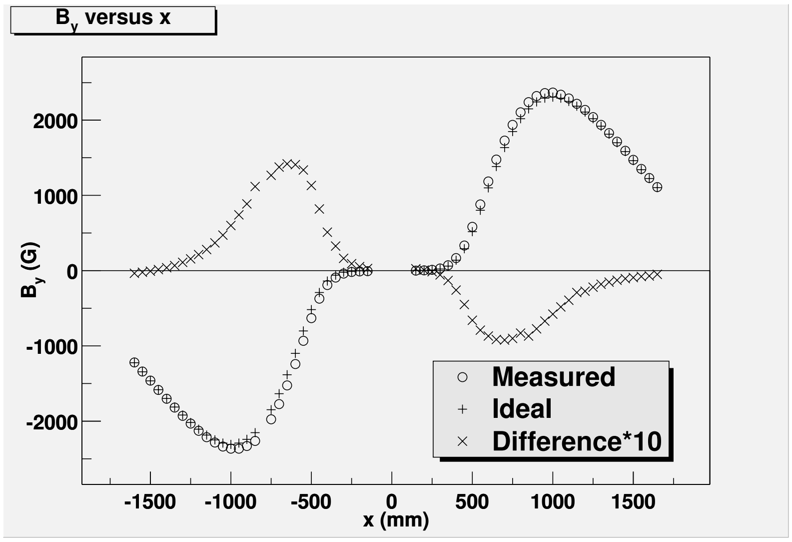

Figure 2-8: Vertical component of the magnetic field along the in-plane axis perpendicular to the beam axis at $y = 0$ and $z = 0$. Comparison is shown to the (ideal) Biot-Savart field calculation. The difference between the measured value and that of the corresponding Biot-Savart calculation, multipled by 10 (to aid in visualization), is also shown.

plane is adjacent to the exit windows of the target chamber. Directly behind the drift chambers is a layer of Cerenkov counter (CC) detectors followed by a layer of time-of-flight (TOF) scintillators. Neutron counters are behind the TOFs. The drift chambers, CC detectors, and TOFs in either sector are mounted onto a subframe. The subframe can be moved away from the magnetic coils to allow detector maintenance and access to the target chamber. The neutron counters have their own support frame[1].

High voltage is supplied to all of the detectors by remotely controlled HV modules (LeCroy 1458 HP [37]). The HV is controlled using the EPICS [18] slow-control system. Since this system also operates the South Hall Ring, integration of the two is straightforward. The integrated package is named Automatic Ring Fill (ARF) software. The ARF software allows for the safe, automatic injection of electron beam into the South Hall Ring [23]. The automated beam fill procedure starts by sending an electronic inhibit to stop data taking. The detector HV is next lowered to safe

[1]The neutron counters are installed for neutron-sensitive measurements such as that of the neutron electric form factor, G_E^n [61]. They are not relevant to the research done in this thesis, however, and will not be discussed here.

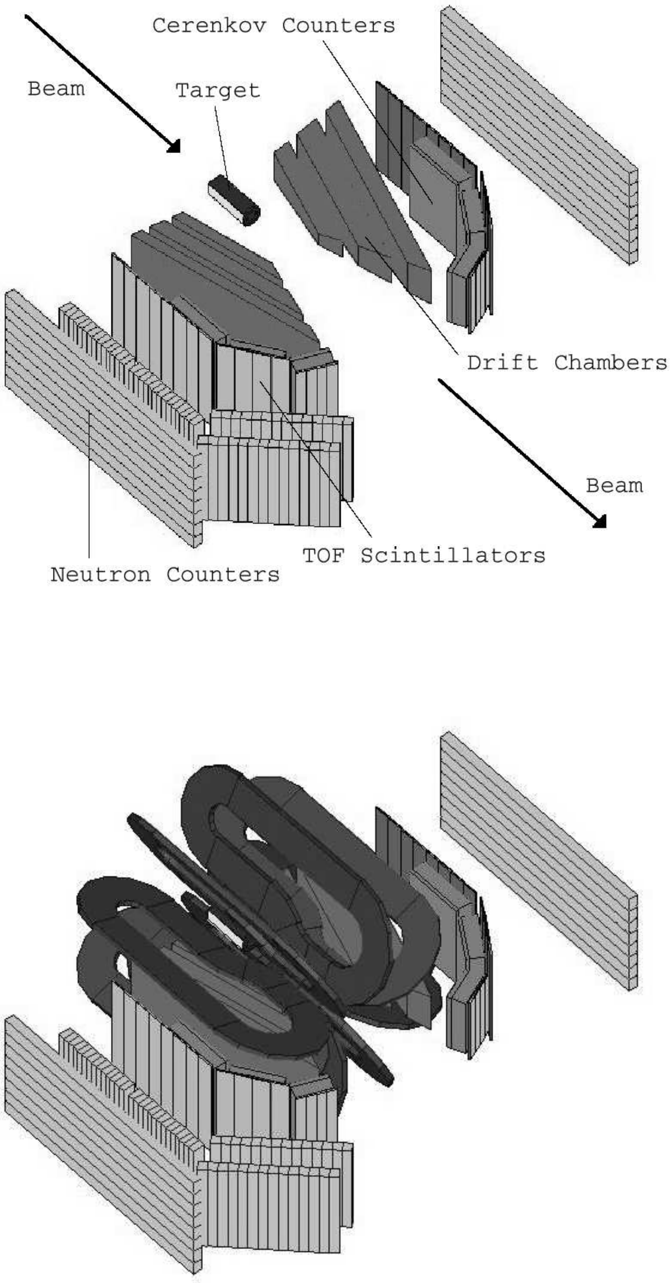

Figure 2-9: Views of the BLAST detectors. The top picture shows the various detectors with respect to the target in the absence of the magnetic coils. The bottom picture shows the same setup as it actually is seen in the presence of the magnetic coils.

standby values. Once in standby, a set of beam scraping slits is moved out of the path of the beam, and any remaining beam in the ring is dispersed by targets placed in its path. The polarized source is turned on, and the state of the half-wave plate is reversed from its previous state. The resulting polarized beam is then stacked in the South Hall Ring to $\sim$ 200 mA. Once fully stacked, the slits are moved back in to predetermined background-optimized positions, and the detector HV is ramped back up to operating values. Finally, the data inhibit is removed, and data taking commences once more. The entire ARF process is automated and takes $\sim$ 1.5 min; it starts when the beam current drops below a preset value determined to maximize luminosity. By automating the process, data-taking time is used efficiently, and data acquisition dead time is minimized.

2.5.1 Cerenkov Counter Detectors

The Cerenkov counter (CC) detectors in BLAST discriminate electrons from pions. At sufficiently high pion energies, the timing resolution of the TOFs is not sufficient to discern between electrons and pions. Furthermore, since both particles have the same charge and thus similar curvatures in the BLAST magnetic field, the drift chambers also cannot discriminate between them.

The CC detectors exploit the phenomenon of Cerenkov radiation [30]. A relativistic particle traveling at a velocity, β, will emit Cerenkov radiation in the form of light when it passes through a medium with a velocity greater than that of light in that medium. If n denotes the index of refraction of the medium, then it follows that Cerenkov radiation will be emitted by the traveling particle when:

$$\beta > \frac{1}{n}$$

or, equivalently, when:

$$E > \frac{mc^2}{\sqrt{1 - 1/n^2}}$$

where E and m are the respective energy and mass of the particle. By choosing a medium with an appropriate index of refraction, one can make it kinematically possible for only one type of particle (electrons, in the case of BLAST) to emit radiation.

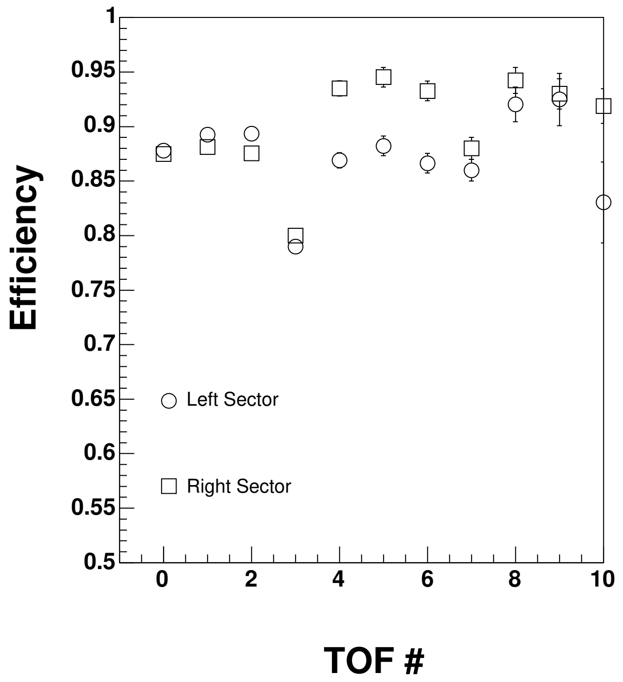

Figure 2-10: Plot of CC detector efficiency as a function of TOF number. The TOF number increases as one goes further upstream. The falloff in Cerenkov efficiency for TOFs #3, #7, and #10 is due to edge-effects.

There are four CC detectors used in each sector of BLAST[2]. The most downstream one in either sector contains 7 cm of radiator (silica aerogel) with an index of refraction of $n = 1.02$; the other ones all contain 5 cm of radiator with $n = 1.03$. The smallest, most-downstream counter has six photomultiplier tubes (PMTs) attached to it. The second counter has eight PMTs while the third has twelve. The size (width $\times$ height $\times$ depth) of the largest CC detector is $100 \times 150 \times 19$ cm^3. All of the CC detectors' PMTs were shielded with iron to avoid losing efficiency due to the BLAST magnetic

[2]The fourth CC detector is used in front of the back-angle scintillators (BATs; see Sect. 2.5.2) and is not considered in this work.

field.

The efficiencies of the CC detectors for electron detection are obtained from elastic electron scattering on hydrogen. Scattered electrons are identified by coincidences between drift chamber tracks (with appropriate elastic cuts) and scintillator hits in the TOFs behind the CC detectors. The resulting efficiencies are plotted in Fig. 2-10. On average, the CC detectors are $\sim 85\%$ efficient with a slight falloff in efficiency with increasing TOF number. The falloff in efficiency is due to the fact that the downstream-curved electrons hitting the most upstream TOFs miss the corresponding Cerenkov box.

2.5.2 Time-Of-Flight Scintillators

Timing for the trigger as well as particle identification is provided by the time-of-flight (TOF) scintillators. Sixteen TOFs are situated in both of the left and right sides of the detector[3] immediately behind the three forward-most Cerenkov counter detectors. The acceptance of the TOFs covers the entire acceptance of the drift chambers; particles passing through the drift chambers will thus also pass through the TOFs.

The TOFs all consist of 2.5 cm thick Bicron BC-408 scintillator [49]. The four most downstream TOFs are each 120 cm tall; the remaining twelve TOFs are each 180 cm tall. The variation in TOF height is due to the fact that the azimuthal acceptance of the drift chambers decreases with decreasing polar angle.

On either end of each TOF, a photomultiplier tube (PMT) is mounted. Assuming the velocity of light to be constant within a TOF, the hits in each TOF's two PMTs can be mean-timed together to return a time independent of position along the TOF. All thirty-two TOFs have their (delayed) mean-timed hits 'OR'ed together so that the earliest TOF hit provides the common stop by which to reference the drift chamber hits in the event.

The TOFs have an intrinsic timing resolution of ~ 350 ps [17]. At kinetic energies

[3] An additional four backward-angle TOF scintillators (BATs) are located at extreme backward angles to allow large Q^2 measurements. However, the BATs are not considered in this work.

of 0.400 GeV or lower, the time difference between a pion and a proton traveling from the target to a TOF is $\sim$ 7 ns. Thus, the TOFs can reliably be used for particle identification.

2.6 Trigger and Data Acquisition

The BLAST trigger is a programmable trigger capable of accepting the simultaneous physics channels arising in the large-acceptance BLAST spectrometer. A schematic of the trigger is shown in Fig. 2-11. Although originally developed in conjunction with JLab Hall A, the trigger software has been updated and overhauled for the BLAST project.

Raw signals from each detector are split into two signals. One signal is delayed and passed into a FASTBUS ADC module (LeCroy 1881 M [35]) for integrated charge measurement. The other (non-delayed) signal is sent to a detector-specific discriminator (a LeCroy 3412 Constant Fraction Discriminator [38] for the TOF scintillators and a LeCroy 3420 Leading Edge Discriminator [36] for the CC detectors). The output of the PMT at the top of each TOF is mean-timed with that of the PMT at the bottom of the TOF; the CC detectors' output for all CC detectors is 'OR'ed together before discrimination. The resulting signals for the detectors in a sector are then passed into LeCroy 2373 Memory Lookup Units (MLUs) [33]. The outputs of these two units are connected to a cross sector memory lookup unit (XMLU), which is programmed for various desired left/right sector detector combinations. The output of this unit is referred to as the first-level trigger.

After initial analysis of the data, it was discovered that the data for the majority of the first-level triggers did not reconstruct into drift chamber tracks. The source of the large number of such events is presumed to be upstream electron-positron showers from the collimator that scatter into the detectors. In order to reduce the number of these trackless events, a second-level trigger was instituted. The second-level trigger demands at least one hit in each of the three drift chambers in a sector. Usage of the second-level trigger lowered the data readout deadtime from $\sim$ 40%s to $\sim$ 15%s.

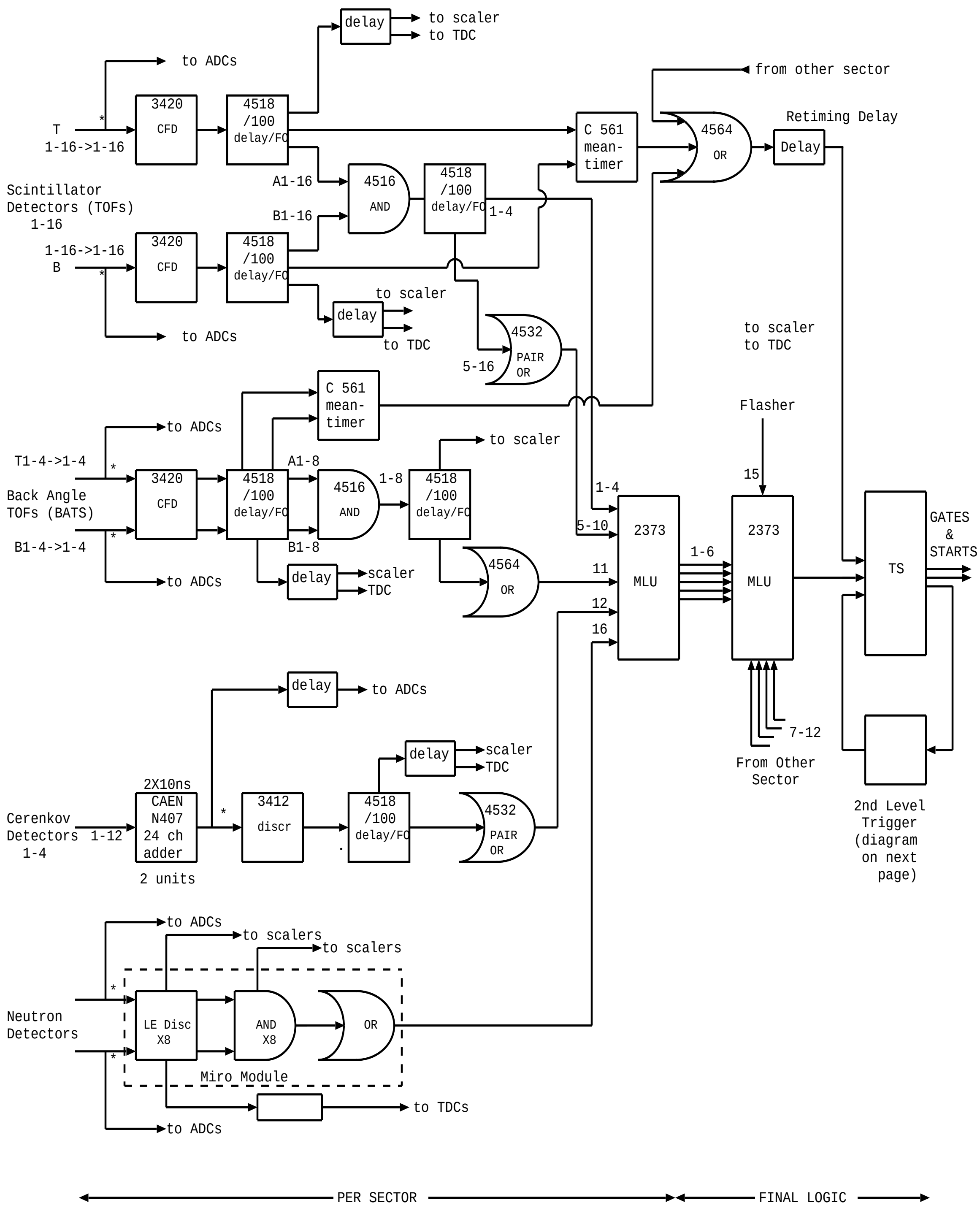

note: * all analog signal division in matched impedance passive splitters

Figure 2-11: A schematic of the BLAST trigger logic. Only one circuit is shown for each detector type, and only the left sector circuit is shown. The logic from the left sector (LMLU) and the right sector (RMLU) are combined into the cross MLU (XMLU) to form the total trigger.

Trigger	Description	Prescale Value
0	1+ TOF in each sector	1
1	1+ TOF in one sector, a NC in the other	1
2	2+ TOFs in the same sector with a CC	10
3	2+ TOFs in the same sector	100
4	1+ TOF in one sector, a BAT in the other	1
5	1+ of the four upstream TOFs in one sector	1000
6	1+ TOF in one sector with a CC	9
7	Flasher	1

Table 2.3: Listing of recorded XMLU physics triggers: TOF = time-of-flight scintillators, CC = Cerenkov counter, NC = neutron counter, BAT = back-angle-TOF scintillator.

A listing of the various classes of triggers recorded in BLAST is shown in Tab. 2.3. Some of the higher-rate triggers were prescaled in order to not lose lower-rate events due to deadtime.

2.7 The BLAST Monte Carlo

Simulation of the BLAST experiment is divided into two components: event generation and particle propagation. Event generation is handled by the DGen event generator, a C++ object-oriented library developed specifically for the BLAST project. Originally designed for elastic and quasi-elastic deuteron target event generation only (hence the name DGen), it has since grown to include hydrogen target event generation as well as more exotic deuteron reaction channels (e.g., Δ resonances and pion creation). Given a reaction type and target, DGen generates initial event kinematics for all particles in the reaction consistent with current theory (see below). Events can be distributed according to cross section or else in a flat "white" distribution.

Particle propagation is handled by a GEANT [16] Monte Carlo code simulating the beam, target, and detector hardware as well as physics processes occuring during propagation (e.g., energy loss, multiple scattering, hadronic interactions, etc.). Detectors are positioned within a master coordinate system referred to as the BLAST coordinate system with Cartesian axes defined as follows:

$\hat{z}_B$: points in the direction of electron beam flow (i.e., downstream)

$\hat{y}_B$: points towards the ceiling of the South Hall Ring

$\hat{x}_B$: points in the remaining direction so as to form a right-handed coordinate system with the $\hat{y}_B$ and $\hat{z}_B$ vectors (i.e., 90° left of the beam direction)

The center of the BLAST system is defined to coincide with the center of the target cell. Each detector also has its own detector-specific coordinate system and origin. The detector's origin is positioned within the BLAST coordinate system, and the detector's coordinate system is then oriented about that point. The detectors were surveyed to provide realistic position and orientation information.

Event generation for deuteron electrodisintegration is based on the formalism of Arenhövel et al. [6, 7]. Events are generated in a six-dimensional phase space[4]:

ϕ_e : azimuthal angle of the scattered electron

ϕ_{pn}^{CM} : azimuthal angle of the proton in the $p - n$ center-of-mass frame

θ_{pn}^{CM} : polar angle of the proton in the $p - n$ center-of-mass frame

ω : energy transfer

θ_e : polar angle of the scattered electron

z : event vertex position along the $\hat{z}_B$ axis

When using the "white" generator, for each event, a spin-dependent cross section is assigned as a weight (see (1.37)). The various deuteron electrodisintegration structure functions have dependence on θ_e, θ_{pn}^{CM}, and ω; the asymmetries, composed of kinematically-weighted linear combinations of the structure functions, have additional dependence on ϕ_{pn}^{CM} and, indirectly[5], on ϕ_e. The structure functions are calculated by Arenhövel and collaborators on a grid of θ_e, θ_{pn}^{CM}, and ω relevant to the BLAST acceptance. The sixth variable, z, is generated using a triangular distribution func-

[4]Additionally, the beam energy is taken to be a known constant of 0.850 GeV

[5]The asymmetries have direct dependence on θ_d, the polar angle of the deuteron's polarization vector with respect to the three-momentum transfer vector, $\vec{q}$. However, in order to specify $\vec{q}$ completely, the polar angle of the scattered electron, ϕ_e, must be known.

tion in accordance with the target density distribution. A map of the target holding field is used to calculate the target polarization angle along the $\hat{z}_B$ axis.

The particles in the events are then propagated outward through the BLAST detector. All physics interactions are allowed[6] including secondary particle generation. Hits in the detectors are tracked and recorded at the end of each event. Depending on the desired reaction ($^2\vec{H}(\vec{e}, e'p)n$ or $^2\vec{H}(\vec{e}, e'n)p$), various detector hit combinations are demanded; events passing those cuts are deemed "good" events. Detector kinematic resolutions are determined from real data and then convoluted into the Monte Carlo event list.

[6]One exception to this is radiative effects which are absent in GEANT.

Chapter 3

The BLAST Drift Chambers

3.1 Introduction

Drift chambers are designed to return position information on the trajectory of charged particles. Such position information can be used to extract information regarding the particle's momentum and charge and as well as information regarding the corresponding track's vertex position. When used in tandem with other detectors (e.g., time-of-flight detectors), drift chambers can be an effective particle identification mechanism.

In this chapter, the BLAST drift chambers are discussed in detail. A short summary of the physics behind drift chambers is first presented. Afterwards, an individual BLAST drift cell is described, followed by a general layout of the drift chambers and details of their construction. Finally, calibration, operation, and performance of the drift chambers are discussed.

3.2 Overview of Drift Chamber Theory

This section gives a short summary of the essential ideas and physics behind the principles of a drift chamber. Refs. [15] and [51] provide a more comprehensive description of their properties.

Charged particles traversing a gas leave a trail of stochastically-distributed free electrons. By applying an electric field, the electrons "drift" from their origination sites to designated readout wires in a series of repeated accelerations and decelerations. The electrons accelerate for an average distance given by the gas's mean free path ($\sim 1\,\mu$m) and decelerate by colliding with gas molecules. The net effect is a fairly constant, calculable drift velocity as a function of the applied field. Gas mixtures used in drift chambers have drift velocities on the order of $\sim$ 1 - 2 cm/μs. With drift distances of $\sim$ 3 - 4 cm, drift times around $\sim$ 2 - 4 μs are typical. By measuring the drift time, the position of the ionization can be determined. The limitation on drift distance is the diffusion of ionized electrons in the gas: longer drift distances have larger diffusion which worsens the resolution.

At low gas densities, the energy lost by the traversing particle is relatively very small ($\sim$ 1 keV/cm of gas), and the particle's momentum is not significantly perturbed. Such a quality is essential in a momentum-determining detector since any momentum change is inherently convoluted into the measurement.

To detect the electrons reaching the readout wires, a mechanism must exist for their amplification. Gain factors of $\sim 10^6$ are desirable. The electric field near the readout wires goes as $\sim 1/r$. Very close to the wires, the electric field is strong enough to accelerate the electrons enough to ionize the gas. This ionization produces another free electron, and the pattern repeats, evolving into an electron "avalanche". For typical drift chamber gas densities and corresponding mean free paths, the field starting the avalanche is of the order of $\sim$ 10 kV/cm. To achieve such high fields and allow for sufficient ionizations, the readout wires must be very thin ($\sim$ 10 - 30 μm). The region in which the avalanche occurs is small (within $\sim 75\,\mu$m of the readout wires), and it takes $\sim$ 1 ns to occur. Thus, the total time between ionization and charge collection on the wire is dominated by the drift time.

3.3 Drift Chamber Gas

The gas mixtures used in drift chambers typically consist of two gases: an ionization gas and a quenching gas. The ionization gas produces most of the ionization caused

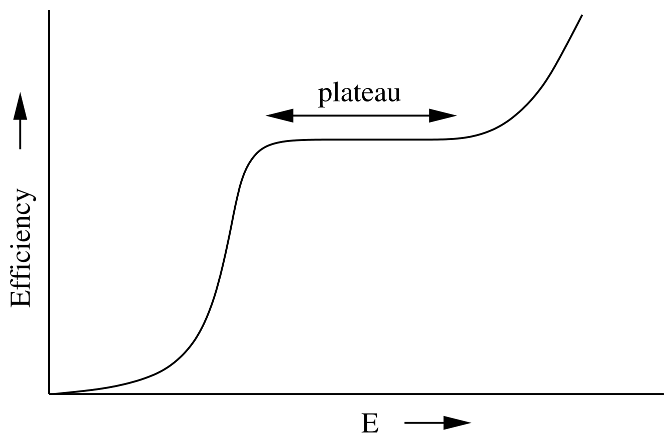

Figure 3-1: Plot of efficiency as a function of the electric field, E, at the surface of a readout wire.

by traversing charged particles. Typically, the ionization gas is a noble gas; helium, argon, and krypton are common. Because of their high excitation energies, noble gas molecules excited by a traversing charged particle can ionize quenching gas molecules, thus leading to further ionized electron production via secondary reactions.

Recombination effects in the avalanche region produce a large number of energetic photons. These photons, left unchecked, would cause more ionization, resulting in constant electric discharge and breakdown. To avoid this problem, a quenching gas is used to absorb the resulting photons. Quenching gases are typically large hydrocarbon molecules, such as methane, ethane, propane, and isobutane. Such large molecules have numerous rotational and vibrational excitation states which allow them to absorb many of the unwanted photons. However, the quenching gas also tends to absorb the (wanted) ionized electrons, becoming worse for longer drift distances. For this reason, a balance must be achieved to provide sufficient quenching but retention of efficiency throughout the drift region.

Due to small differences in the wires and their geometry, it is not possible to have all wires with exactly the same gain. It is therefore important to use a gas mixture with a plateau of voltages over which detection is efficient. A typical efficiency curve is shown in Fig. 3-1. At low electric fields, the gas gain is not large enough to

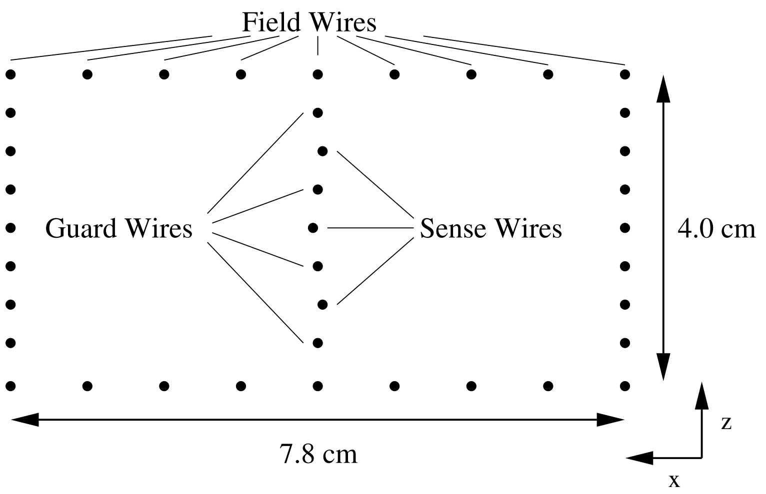

Figure 3-2: Overhead view of a drift cell in BLAST.

be detected, and the efficiency is thus low. At too high an electric field, the gas becomes ionized near the readout wires without an initial ionization electron, and the detector is "noisy". Between the limits, a plateau region exists along which the gains are sufficient for efficient detection. The wires' voltages are adjusted to lie on this plateau. For argon the plateau region is large ($\sim$ 500 V) while for helium it is only $\sim$ 100 - 200 V in width. Lighter gases, however, cause less multiple scattering of the traversing particles which improves the position resolution. There thus exists a tradeoff in plateau voltage range and position resolution.

3.4 Drift Cell Design

The drift chambers used in BLAST are made up of "drift cells." The drift chambers can be understood by studying an individual drift cell. In BLAST, a drift cell is a rectangular array of thirty-nine wires (see Fig. 3-2). A cell has transverse dimensions of 4.0 cm x 7.8 cm.

The wires in a cell fall into one of three functional categories: sense, field, and guard. Sense wires are the readout wires. The charge from ionization amplified by the gas gains acculumates on them and is read out via amplifier-discriminator

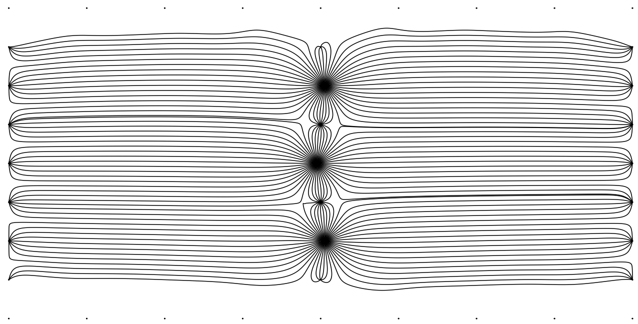

Figure 3-3: Drift lines in a drift cell in the absence of an external magnetic field.

cards. There are three sense wires in each cell. The sense wires consist of 25 μm-thick tungsten wire with 3% rhenium alloy; the wire was electrolytically cleaned to remove oils used in its manufacture. Neighboring the sense wires are guard wires. Adjusting the guard wire voltages allows the gains to be matched on all three sense wires and helps to contain the electric field. The guard wires consist of 100 μm-thick berilium copper alloy. The remaining wires are collectively referred to as field wires and are used to shape the electric field. The field wires are also 100 μm-thick berillium-copper.

The drift cell geometry and wire voltages must be optimized to achieve sufficient gas gain on the sense wires and to transport ionization electrons from all parts of the drift cell to the sense wires. In the absence of a magnetic field, the electric field for a drift cell is shown in Fig. 3-3. The electric field resembles two oppositely-directed "jets" for each sense wire. Ionized electrons produced within the cell drift along the electric field lines to one of the sense wires. Increasing guard wire voltages would make the jets narrower and simplify reconstruction but reduce the efficiency of the electron collection. In practice, a tradeoff must be reached.

In BLAST, the voltages on various cell wires are as indicated in Fig. 3-5. The voltage on the middle guard wires was chosen to make the gain on the central sense wire the same as the other two. The voltage drop between field wires was chosen to

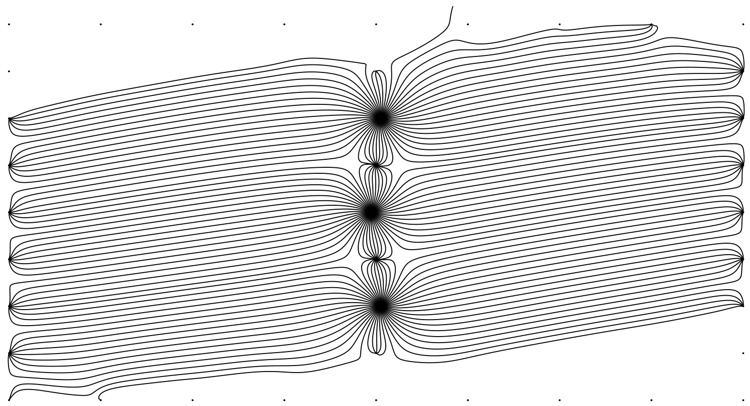

Figure 3-4: Drift lines in the presence of a 3800 G magnetic field.

make the drift region uniform.

In BLAST there is an external magnetic field. In general, in the presence of arbitrary electric and magnetic fields, $\vec{E}$ and $\vec{B}$, the resulting velocity, $\vec{v}$, that a particle of mass m and charge q achieves satisfies:

$$m\frac{d\vec{v}}{dt} = q\left(\vec{E} + \vec{v} \times \vec{B}\right) - K\vec{v} \tag{3.1}$$

Here, a frictional force proportional to $\vec{v}$ has been assumed. In the steady state, the general solution to this equation is given by:

$$\vec{v} = \frac{q\tau\left|\vec{E}\right|}{m\left(1+\omega^2\tau^2\right)}\left[\hat{E} + \omega\tau\left(\hat{E} \times \hat{B}\right) + \omega^2\tau^2\left(\hat{E} \cdot \hat{B}\right)\hat{B}\right] \tag{3.2}$$

where $\omega \equiv |q||B|/m$ is the electron's cyclotron frequency and $\tau \equiv m/K$ is the characteristic time of the system. In BLAST, the magnetic field is approximately perpendicular to the electric field (i.e., $\hat{E} \cdot \hat{B} = 0$). Taking this into account reduces (3.2) to:

$$\vec{v} = \frac{q\tau|\vec{E}|}{m\left(1+\omega^2\tau^2\right)}\left[\hat{E} + \omega\tau\left(\hat{E}\times\hat{B}\right)\right] \tag{3.3}$$

The presence of a nonzero magnetic field causes the ionized electrons to travel at an angle, ψ_L, with respect to the electric field. This angle is commonly referred to as the Lorentz angle:

$$\tan\psi_L \equiv -\omega\tau \tag{3.4}$$

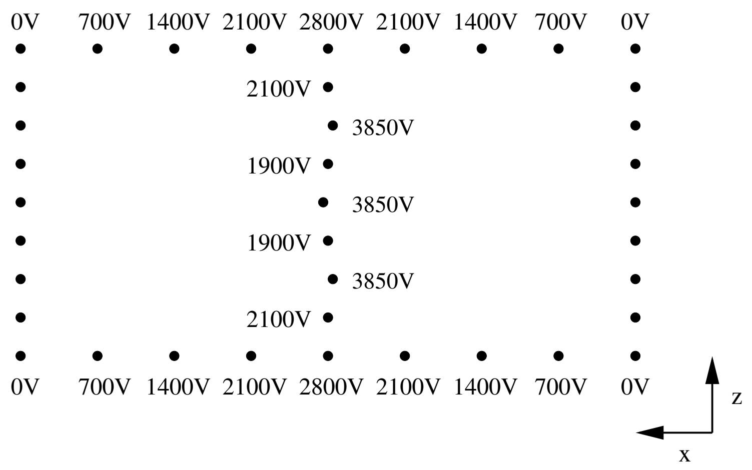

Figure 3-5: Wire voltage distribution within a cell.

In BLAST, the magnetic field varies over a range between $\sim 700 - 3800$ G. Thus, the Lorentz angles vary from cell to cell. Typical Lorentz angles in BLAST are $\sim 2 - 8°$. A plot of the drift lines with a 3800 G magnetic field (i.e., the maximum magnetic field in BLAST) is shown in Fig. 3-4.

Due to various reaction processes that occur during photon recombination, positively-ionized quenching gas molecules are produced after an ionization avalanche occurs. These ions drift to wires containing a net negative charge. If the electric field on the surface of these negatively-charged wires is too high, quenching gas ions can attach and develop "whiskers", i.e., chains of ionized quenching gas molecules. Over time, whiskers can grow long enough to cause breakdown with the sense wires and make a drift chamber inoperable. To prevent the growth of whiskers, the electric field on the surface of these wires should be as low as possible. This is accomplished by using large diameter wire to ensure that the surface field is small (< 30 kV/cm). Such low fields are sufficient to inhibit whisker growth.

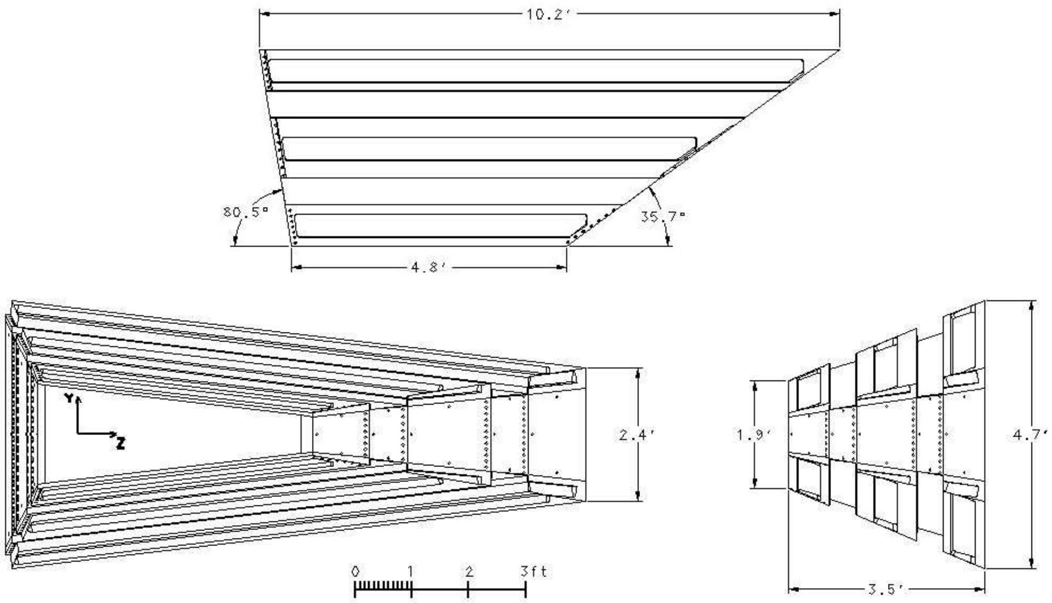

Figure 3-6: Different views of a drift chamber sector in BLAST. Starting from the top picture and going clockwise: 1) an overhead view, 2) a sideways view, and 3) a front view.

3.5 Drift Chamber Design

The six drift chambers in BLAST are arranged into two assemblies of three-chamber "sectors". The basic schematics of a sector are shown in Fig. 3-6.

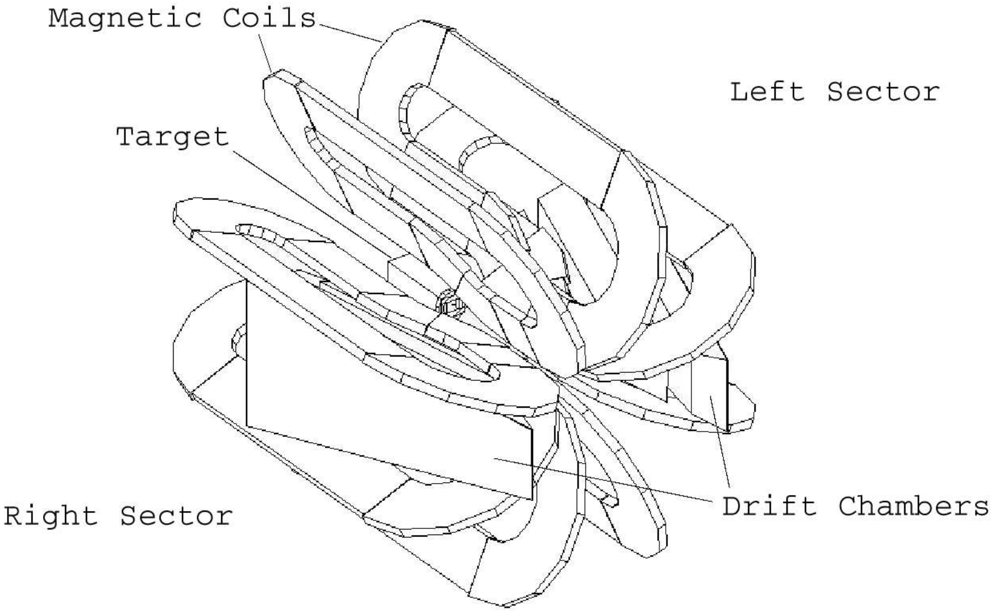

Figure 3-7: View of the two drift chamber sectors as positioned in BLAST between the magnetic coils.

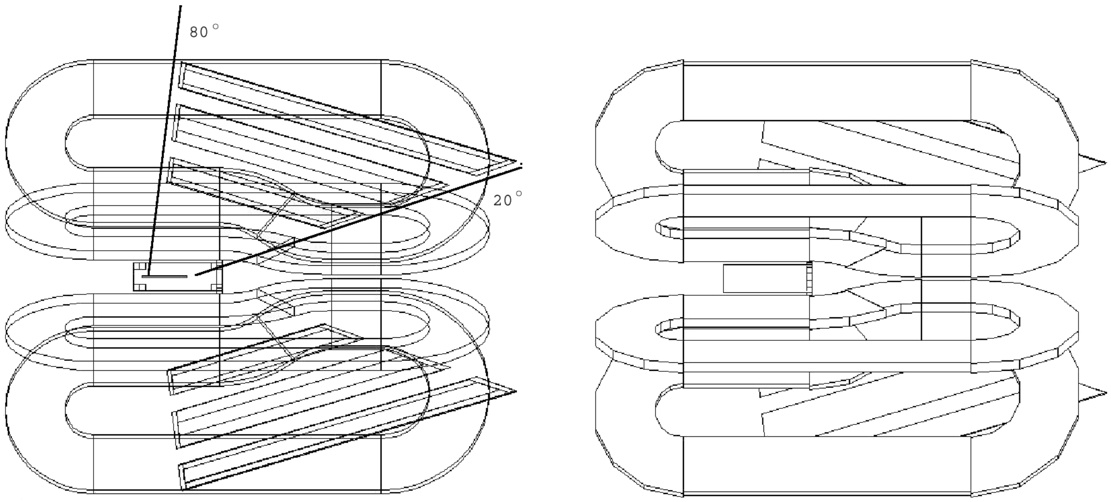

Figure 3-8: Overhead view of the drift chambers in BLAST. The left picture shows the chambers with hidden lines visible. The right picture shows the same setup as it actually is seen.

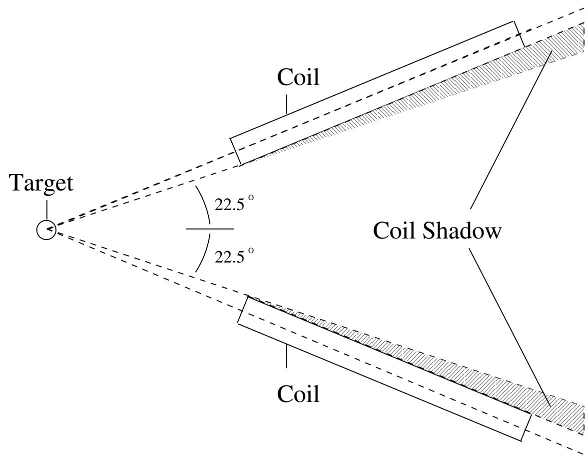

Figure 3-9: View of the coils' shadow regions inside which the drift chambers lie.

The three drift chambers in a sector form a common gas volume. The volume is made gas-tight by placing double layers of 25 μm-thick mylar over the sector's entrance and exit planes. Between the two mylar sheets nitogren gas is flowed to flush away drift chamber gas that escapes. By making a common gas volume out of three drift chambers, energy loss due to the addition of entrance/exit windows is minimized.

The physical design of the drift chambers is largely determined by the geometric restrictions imposed by the magnetic coils. Two opposing sectors are each instrumented with a three-chamber sector as shown in Figs. 3-7 and 3-8. The drift chambers are positioned downstream of the target center and inclined towards the beam line at their downstream side. This is done so that particles coming from the target traverse the chambers at angles of $\sim 90°$. Such positioning requires the chambers to be trapezoidal in all three perpendicular directions.

Due to the 3.5$''$ thickness of the magnetic coils, there exists a "shadow" region behind each coil (Fig. 3-9) into which particles originating from the target cell do not propagate. To achieve the maximum acceptance between the coils, the drift chambers' frames are designed to lie within these shadow regions. The limited size of the shadow region forces the chambers to have relatively thin cross sections as shown in Fig. 3-10.

Each drift chamber sector subtends a polar angular range of $\theta \sim 20°$ - $80°$. At the

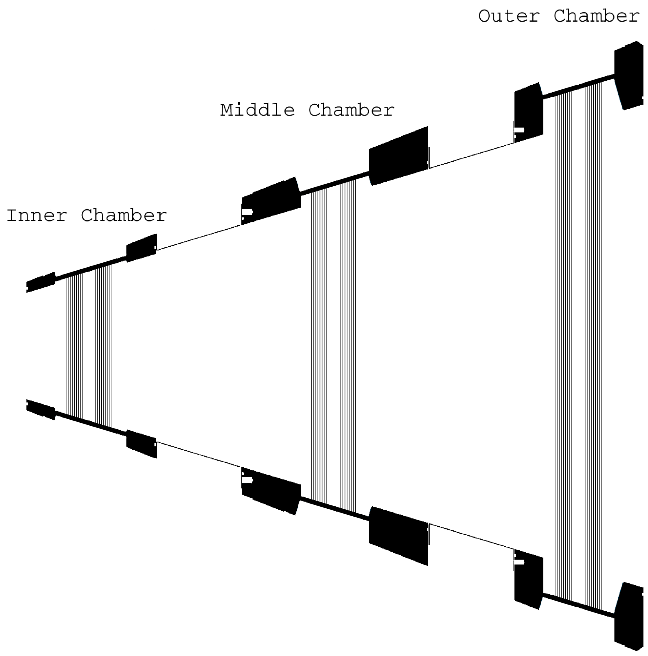

Figure 3-10: Cross section of the drift chambers. Compare with the shadow regions in Fig. 3-9.

downstream side (the $\theta \sim 20°$ side), the sector subtends an azimuthal angular range of $\phi \sim -15°$ - $15°$; at the upstream side (the $\theta \sim 80°$ side), this range increases to $\phi \sim -22°$ - $22°$. The total solid angle subtended by each chamber sector is ~ 0.50 sr.

Each of the three drift chambers in a sector contains multiple drift cells arranged into two parallel rows of "superlayers". In each of the two sectors, there is a total of 159 drift cells distributed as in Tab. 3.1. Each cell consists of 39 wires, three of which are sense wires. In total, there are 9,648 wires in the six BLAST drift chambers; 954

	Superlayer		
	Inner	Outer	Total
Inner Chamber	18	19	37
Middle Chamber	26	27	53
Outer Chamber	34	35	69
Total	78	81	159

Table 3.1: Number of drift cells per superlayer.

of these are sense wires.

The drift chamber gas is Helium:Isobutane(82.3%:17.7%). Within a sector, the drift chamber gas flows into the gas-tight region through multiple holes located on the upstream side of the chambers. Exit holes are located only on the downstream side. The gas entrance and exit holes are arranged to minimize pockets of unrecycled gas. A flow rate of 3 l/min is typical.

3.6 Drift Chamber Construction

The aluminum frames for the drift chambers were built by Allied Mechanical in Ontario, CA, and the disassembled pieces were shipped to the MIT campus where they were later assembled. Dowel pins ensured the alignment of the pieces.

The drift chambers were strung on the MIT campus. Each wire was strung under tension primarily to resist movement in the chambers' electromagnetic field and secondarily to resist gravitational effects. Sense wires were strung at a tension of 50 g while the remaining wires were strung between 50 – 800 g, depending on the length of the wire.

Because of the large number of wires in the chambers, a fully strung chamber is under significant tension ($\sim$ 1 ton). Such large tensions cause deflections of up to a few millimeters in the frame. The chambers were thus pre-stressed by piano wire at tensions simulating the fully-strung chamber. As stringing progressed from one end of the chamber to the other, the piano wires were gradually removed.

The actual stringing of the chambers followed a detailed, systematic method to guarantee uniformity and cleanliness of the chambers. The chambers' frames were cleaned with acetone to remove grease and then with isopropanol to remove any residue. Each hole was also cleaned using clean-room swabs. Temporary 0.25" thick plastic windows were then attached to enclose the chamber. These windows helped keep the chamber interior clean during wiring and protected the wires from accidents.

The wiring took place inside a clean-room (class $\sim$ 1000) at MIT. First, a long, thin needle (up to 1.4 m) was inserted through the proper holes on each side of

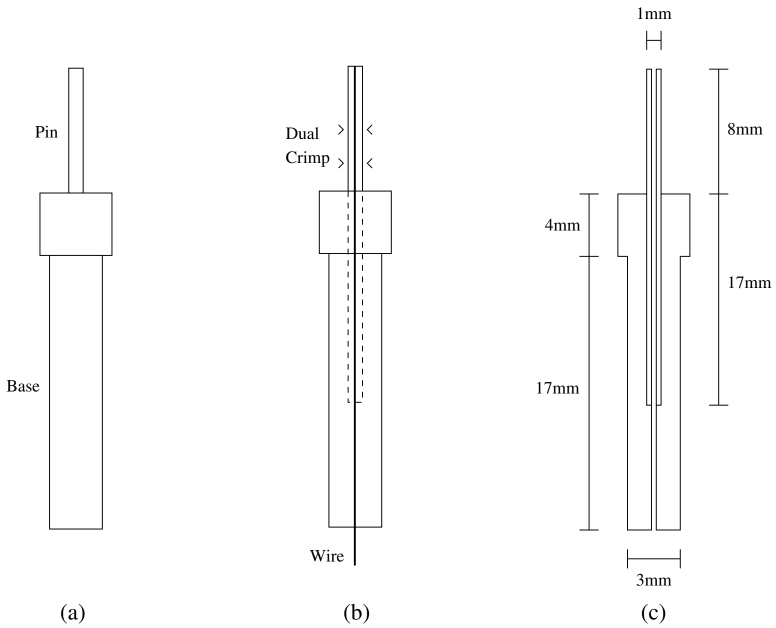

Figure 3-11: A feedthrough used to hold a drift wire. (a) View of the feedthrough (b) A crimped feedthrough holding a wire (c) Dimensions of a feedthrough

the chamber. A feedthrough was then threaded onto the proper wire (tungsten or copper), and the wire was attached to one end of the needle. The needle and wire were then pulled through to the other side of the chamber. The wire was cut from the needle, and a feedthrough was threaded onto it. The feedthrough on the first side was then installed into the hole and crimped. A weight hung over a pulley was then attached to the free end of the wire to tension the wire. The second feedthrough was then installed into the remaining hole and crimped. This process was repeated for all of the wires; the pre-stressing piano wires were gradually removed as the permanent wires were installed.

The schematics of a feedthrough are shown in Fig. 3-11. Each feedthrough consists of a gold-plated copper tube inserted into Delrin [22] insulator. They are designed to stand 1 cm from the chamber frame to avoid sparking between the (grounded) frame and the wires. The feedthroughs are a press-fit in the holes in the chamber. An RTV epoxy resin, Sylgard [21], was applied to the external feedthrough area to make them gas-tight.

To check that the wires were at the desired tensions, the following method was

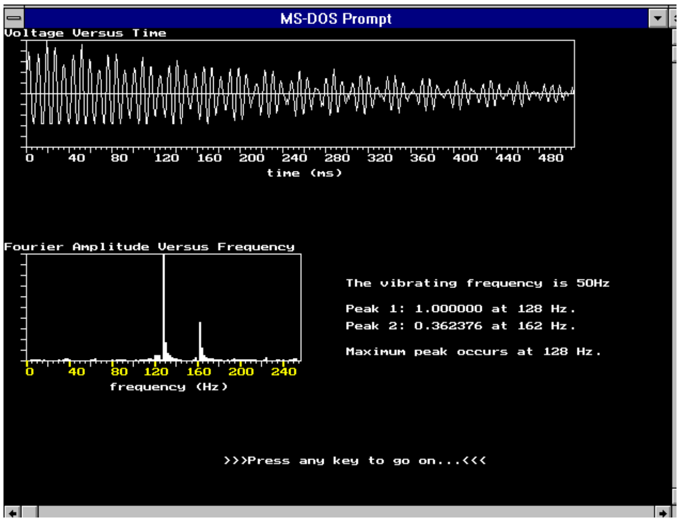

Figure 3-12: Vibration and frequency information for a wire.

employed [39]. One wire was excited by an AC signal superimposed on a high voltage (HV) DC level. The HV induced a charge on neighboring wires which then vibrated in the alternating field. The AC signal was stopped, and the wires quickly (on the order of $\sim$ 100 ms) went to their natural frequency. This frequency was detected as an induced current in the wires. The tension, T, was determined from the natural frequency, f, according to [52]:

$$f = \frac{1}{2L}\sqrt{\frac{T}{\mu}} \tag{3.5}$$

Here, L is the length of the wire and μ is its linear density. A plot of the vibration and frequency output for a typical wire is shown in Fig. 3-12.

3.7 Drift Chamber Electronics

High voltage (HV) must be supplied to the sense, guard, and field wires in each cell in order to produce the desired operating electric field. Additionally, electronics must exist to collect, discriminate, and amplify sense wire signals.

Three positive HV supplies are used to energize the drift cells. One HV supply is used for the sense wires; another is used for the two guard wires located between the sense wires. The third HV supply is used for the remaining field wires; required field wire voltage drops are handled by a chain of resistors connected to ground.

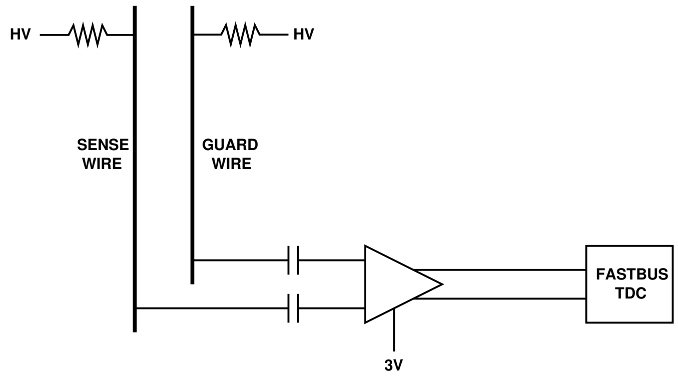

Figure 3-13: Circuit diagram showing drift cell signal readout. A differential amplifier is used to reduce noise.

To reduce noise, the signal readout from each sense wire is connected via a differential amplifier to a neighboring guard wire (see Fig. 3-13). A $3V$ threshold is supplied to the amplifier for further signal discrimination. The resulting ECL signals are then passed to FASTBUS TDC modules [34].

All electronics for the drift cells lie in copper boxes in the recesses between the chambers (see Fig. 3-10). Each box distributes HV and supplies readout electronics for up to five adjacent drift cells in a particular superlayer.

3.8 Drift Chamber Calibration

To reconstruct tracks accurately, the sense wire positions must be known very precisely. Additionally, since the drift chambers are designed to have a resolution of $\sim 120\mu$m, knowledge of the sense wire positions to an accuracy much smaller than this is required. To satisfy these constraints, the drift chambers need to be accurately calibrated.

The time, t_i, at which ionization for a hit on sense wire i in a drift cell reaches the sense wire is related to the in-plane position, x_i, of particle traversal according to the relation:

$$x_i = X_i \pm_i d(T_i - t_i) \quad , \quad i = 0, 1, 2 \tag{3.6}$$

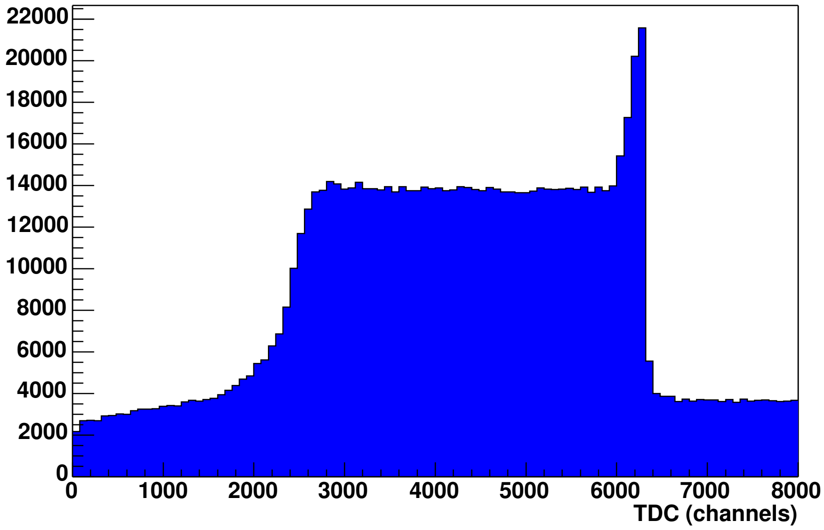

Figure 3-14: Drift chamber TDC spectrum.

Here, X_i and T_i are calibration constants specific to the sense wire, and $d(T_i - t_i)$ is the functional form for the time-to-distance relation for the drift chamber gas in terms of the drift time, $T_i - t_i$. The value of the sign in front of $d(T_i - t_i)$ depends on which side of the sense wire plane the particle traversed; the i subscript is necessary since, in general, the side can change for each wire within a drift cell depending on the particle's trajectory. All of these aspects are described in more detail below.

The calibration constant T_i can be interpreted as the time at which the ionizing charged particle crossed the plane of sense wire i. Drift chamber TDC data in BLAST were taken in common stop mode, the stop being provided by the earliest event in the top/bottom mean-timed photomultiplier signal of the time-of-flight (TOF) scintillators (see Sect. 2.5.2). As a result, $t_i \leq T_i$ for all t_i and the appropriate form of the drift time is $T_i - t_i$.

A typical TDC spectrum for a sense wire is shown in Fig. 3-14. Since data were taken in common stop mode, hits closest to (farthest from) the wire appear at high (low) TDC values. The peak at high TDC values arises from the large variation in isochrones (i.e., lines of constant drift time) in the immediate vicinity of the sense wire which, when coupled with the stochastic nature of ionization, results in an enhancement of drift times slightly away from the wire. Moving away from the

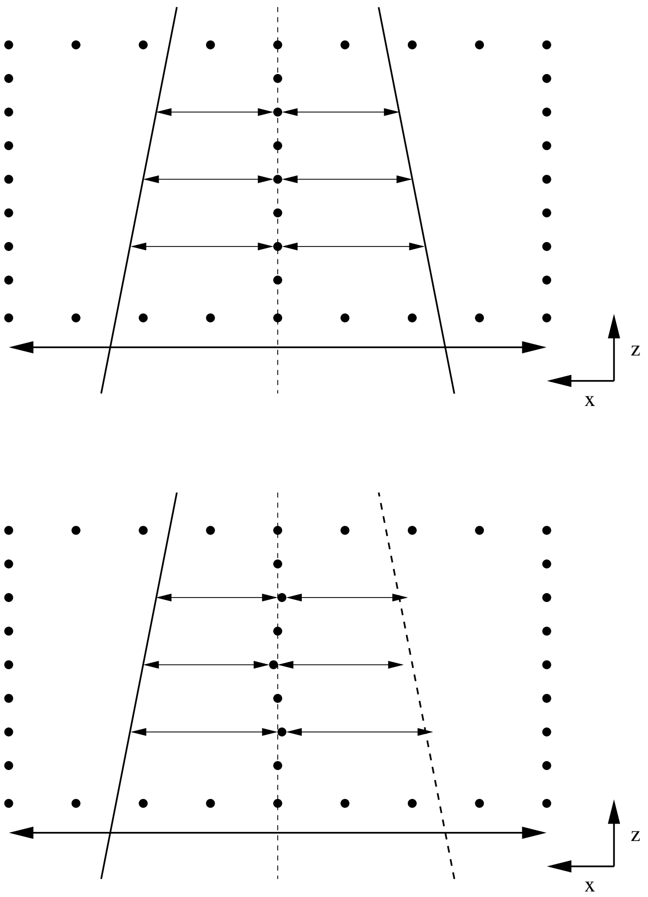

Figure 3-15: Track reconstruction without any sense wire stagger (top) and with 0.5 mm sense wire stagger (bottom). Without stagger, the side of the traversing particle cannot be determined. With stagger, the three hit distances form a straight line only if the correct side is chosen.

sense wires, the TDC values plateau until the edge of the drift cell is reached; the signals then drop back into the noise. The flatness of this plateau is a measure of the efficiency of the gas mixture to allow for ionization propagation all throughout the cell. The entire TDC distribution has a width of ~ 4000 channels. Since one side of a drift cell is 39 mm long and since 1 ns = 2 TDC channels, the average velocity of drifting electrons in the gas is $\sim 20 \mu\text{m/ns}$.

To first order, T_i can be considered constant for all sense wires and equal to the (undelayed) time of the common stop. The relative timing of all of the TOFs has been set up to be the same (within ~ 1 ns) for any relativistic particle coming from the target. However, since a relativistic particle crosses different planes of sense wires at different times, T_i is, in practice, different for each sense wire.

The calibration constant X_i represents the in-plane position of the center of sense wire i. It is made up of two components: a 0.5 mm stagger and deviation about that stagger. The first ($i = 0$) and third ($i = 2$) sense wires in a cell are each staggered 0.5 mm in the $-\hat{x}$ direction while the middle sense wire ($i = 1$) is staggered 0.5 mm in the $+\hat{x}$ direction. In the absence of such a stagger, TDC information would not be sufficient to determine which side of the sense wire plane the particle traversed. However, when a stagger is introduced, the three x_i distances form a straight line only if the correct $\pm_i$ signs have been chosen for all three sense wires. This phenomenon is shown in Fig. 3-15. There are $2^3 - 1 = 7$ sign combinations[1] that need to be tested.

The second contribution to X_i comes from deviations of the wire from its ideal position. Due to machining tolerances during construction, feedthrough holes can lie up to $\sim 20\mu$m away from their ideal positions. Additional deviations can arise from manufacturing errors causing the copper tube in a feedthrough to lie preferentially away from the center of the Delrin insulator as well as from biases due to the actual crimp of the tube. Collectively, these deviations can add up to a total deviation of $\sim 100\mu$m. In order for the drift chambers to have a resolution of $\sim 120\mu$m, these deviations must be accounted for.

The time-to-distance relation, $d(T_i - t_i)$, listed in (3.6) is a very complicated function in principle. In general, it depends on multiple parameters: the sense wire within the cell, the angle that the ionizing particle makes with the $\hat{x}$ axis, the magnetic field along the sense wire, the side from which the ionization came, and the drift time, $T_i - t_i$. For realistic time-to-distance relations, the magnetic field program MAGBOLTZ [8, 13] is used, explicitly taking into account all of these variables. A typical time-to-distance distribution is shown in Fig. 3-16. At small times, the distance is approximated by a cubic polynomial in $T_i - t_i$; at large times, a linear relation is sufficient. Where the two regions meet, continuity is demanded in both

[1] Due to the orientation of the staggers, one of the combinations ($\pm_0 = +$, $\pm_1 = -$, and $\pm_2 = +$) is unphysical and thus is not checked.

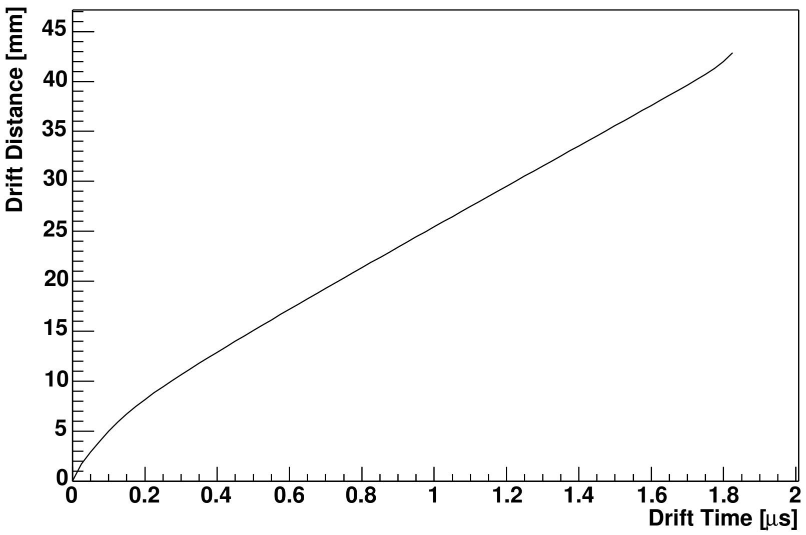

Figure 3-16: Typical plot of drift distance versus drift time. The relation, in general, depends on the sense wire within the cell, the angle that the ionizing particle makes with the $\hat{x}$ axis, the magnetic field along the sense wire, the side from which the ionization came, and the drift time, $T_i - t_i$. A cubic polynomial is fitted to each relation at low drift times; a linear relation is fitted at high drift times.

the approximations as well as in their first derivatives. A higher-order polynomial is needed close to the wire due to the nonlinearities in the magnetic field that appear there.

Approximate values for the X_i and T_i calibration constants are found by using the lowest order approximation for the time-to-distance relation:

$$x_i \approx X_i \pm_i v \cdot (T_i - t_i) \quad , \quad i = 0, 1, 2 \tag{3.7}$$

In this approximation, the velocity, v, of ionized electrons in a cell is assumed to be everywhere constant. More accurate determinations of X_i and T_i utilize iterative techniques involving higher-order polynomial fits.

With appropriately calibrated drift chambers, the intrinsic resolution can be measured. A straight line is fitted to the three sense wire hits within a cell, and the variation in hit position from that line is determined. The process is repeated for numerous events, resulting in a variation distribution. With correctly chosen calibration constants and time-to-distance relations, the distribution is Gaussian and centered at zero. In BLAST, such analysis returns an intrinsic resolution of $\sim 130\mu$m, which is very close to the ideal resolution of 120μm.

3.9 Drift Chamber Reconstruction

Ideally, a charged particle passing through a BLAST drift chamber sector causes hits on eighteen wires[2]: 3 chambers x 2 superlayers per chamber x 3 sense wire hits per superlayer = 18 hits. The information from these hits is collectively used to return an overall momentum and vertex position for the particle causing the hits. The procedure for the drift chamber reconstruction is outlined below:

1. Cell proximity checks are made on hits within a particular superlayer. Groups of hits lying in sufficiently close cells are identified and collectively referred to as a "cluster". Hits not satisfying the proximity checks are discarded.

2. For each of the hits in a cluster, the corresponding distance, (3.6), is determined. Good-fit planes are found; such planes are referred to as "stubs". Within a superlayer, stubs all run parallel to the sense wire planes.

3. Stubs in the two superlayers within each cell are collectively used to determine overall good-fit lines for the chamber referred to as a "segment". In order to extract vertical position information for the particle trajectory, adjacent superlayers lie at a $\pm 5°$ stereo angle with respect to the vertical.

4. A circle is fitted to the three segments in a sector (one for each chamber) to extract an initial approximation to the track of the particle. To the extent that the magnetic field is constant within the particle's trajectory, a circular fit is a reasonable first-order assumption. From this fit, approximate values are determined for the momentum and vertex position of the particle trajectory.

[2]Inefficiency of the wires as well as noise hits can change this number.

	p [%]	θ [deg]	ϕ [deg]	z [cm]
electron	3.2	0.5	0.6	0.9
proton	2.9	0.5	0.6	1.0
design	2.0	0.5	0.5	1.0

Table 3.2: Electron and proton resolutions in BLAST along with design resolutions.

5. Once initial kinematics have been found, an iterative process begins wherein the particle is swum out from the target in small steps to the drift chamber region using the measured magnetic field. The corresponding hit distances are determined and compared with the actual ones. Kinematics are corrected using the Newton-Rhapson method [46], a multi-dimensional version of the more-commonly known one-dimensional Newton's method. The swimming process then starts over again; iteration continues until a sufficiently low χ^2 value is achieved.

High wire efficiency is necessary for reliable, quick reconstruction. While eighteen hits per track is optimal, track reconstruction is possible, with some restrictions, for tracks down to twelve hits. The combinatorics associated with such tracks, though, are large, and these tracks thus have worse resolutions. Each sense wire in BLAST is $\sim 98\%$ efficient. Of the eighteen hits possible in an ideal track, this value implies that $\sim 70\%$ of all tracks have eighteen hits and that $> 99\%$ of all tracks have at least sixteen hits.

Kinematic resolutions in BLAST are determined from elastic electron scattering from the proton. Non-azimuthal momentum kinematics in this reaction (i.e., θ_e, θ_p, p_e, and p_p) are all determined from one variable. As a result, reconstructed values of these variables can be plotted against calculated ones. The widths of the resulting histograms return information directly related to the resolutions of these kinematics. Additionally, resolution information for azimuthal angles (i.e., ϕ_e and ϕ_p) is returned from coplanarity histograms of their sum; vertex resolutions (i.e., z_e and z_p) come from the single vertex position requirement. The resulting kinematic resolutions for the electron and proton are shown in Tab. 3.2 along with design values.

Chapter 4

Data Analysis

4.1 Overview of the Experiment

This work is based on $\sim$ 1100 hours of data taken from the scattering of polarized electron beam off the polarized internal deuterium target in the South Hall Ring. The time-averaged stored current in the ring for the entire experiment was 95 mA. As improvements in the beam and tune were made, the maximum injected beam current per fill increased over the lifetime of the experiment from 100 mA to 140 mA. Beam fills had an average lifetime of $\sim$ 20 min.

The total accumulated charge using the polarized beam and deuterium target was $\sim$ 400 kC. In order to reduce systematics resulting from extended running in the same polarization state, the beam's helicity was flipped with every fill ($\sim$ 20 min), and the target polarization state was switched every 5 min between the vector plus, vector minus, and tensor minus states. At the beginning of a target polarization sequence, the initial target polarization state was randomly chosen, and the remaining two states sequentially followed. Switching the beam and target polarization states in this manner resulted in data being taken in all six beam-target polarization states during every hour of run-time.

4.2 Identification of $^2\vec{\mathrm{H}}(\vec{\mathrm{e}},\mathrm{e}'\mathrm{p})\mathrm{n}$ Events

Data returned from reconstruction were incomplete in discriminating $^2\vec{H}(\vec{e},e'p)n$ events from all of the reaction channels open to the BLAST detector acceptance. Instead, kinematics cuts had to be imposed on the data to separate the desired events. Since the electron and proton are both charged particles, only events with coincident drift chamber tracks in each sector were considered for possible $^2\vec{H}(\vec{e},e'p)n$ events. For these events, the information returned from reconstruction consisted of the following:

- The spherical coordinates for the reconstructed momentum vectors, $\vec{p} \equiv (p,\theta,\phi)$, for both of the left/right sector coincident tracks as well as vertex z positions for each track along the target.
- Drift chamber TDC information as well as the charge of the particle in each of the two coincident tracks in the event.
- TDC and ADC information in each sector for the event for the time-of-flight (TOF) scintillators and Cerenkov counter (CC) detectors.

Due to detector acceptance constraints, the scattered neutron from the reaction was not detected in general when the electron and proton both are. Instead, neutron information was deduced from an event's electron and proton information (see Sec. 4.2.3).

4.2.1 Particle Identification Cuts

The most basic cuts applied to the data were electron-proton ($e-p$) particle identification cuts. Reconstructed $e-p$ events have coincident tracks with respective charges of -1 and $+1$. Additionally, hits were demanded in the time-of-flight (TOF) scintillators in both sectors. To help eliminate unwanted $\pi^- - p$ coincident events, a Cerenkov Counter (CC) detector hit was demanded (refused) in the sectors with negative (positive) charge.

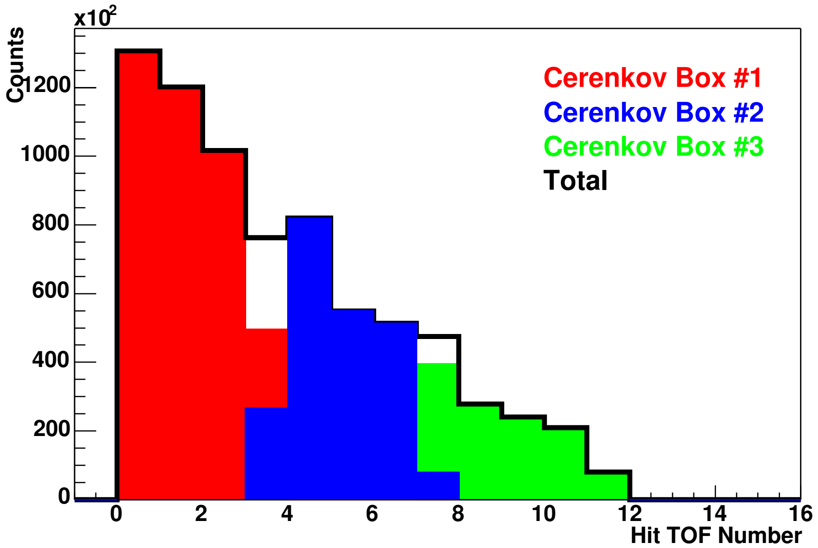

Figure 4-1: TOF scintillator distribution for each of the three downstream Cerenkov counter detectors for electrons originating from the target region. The total distribution for all Cerenkov counter detectors is the sum of the three separate distributions and is shown as the black outline.

4.2.2 Vertex Cuts

Vertex cuts were imposed to ensure that the event originated within the target region as well as to assure that coincident tracks corresponded to the same physical event. Due to the presence of the tungsten collimator upstream of the target region, electron-positron showers originating in the collimator can scatter off hardware surrounding the target region, producing $e-p$ events which scatter into the detector. Such unwanted events were minimized by imposing cuts on the vertex position of each track. The target is 60 cm in length. However, holding field magnets cover only the inner 40 cm. Thus, to ensure reliably polarized deuterons, data were restricted to that 40 cm of target. Additionally, a cut on the relative distance between the vertices in the two coincident tracks was imposed.

To further constrain the region of $e-p$ vertex origination, pairwise cuts were placed on the hit TOF scintillator and CC detector in the electron sector. The CC detectors lie directly in front of and nearly adjacent to the TOF scintillators. Physical restrictions thus exist between which CC-TOF combinations can be hit by a passing electron originating in the target. CC-TOF combinations through which an electron coming from the target region can pass are shown in Fig. 4-1. In general, the acceptance of each CC detector covers that of four consecutive TOF detectors.

4.2.3 Missing Mass Cut

Application of $e-p$ particle identification and vertex origination cuts only ensure that ${}^2\vec{H}(\vec{e},e'p)X$ events remain in the data. Although dominated by $X=n$, the ${}^2\vec{H}(\vec{e},e'p)X$ reaction can also have undetected multiple-particle states (e.g., $X=n\pi^0$ and $p\pi^-$). Additional cuts thus had to be imposed to ensure that $X=n$.

The missing energy, E_M, and missing momentum, $\vec{p}_M$, are defined as the respective total energy and total momentum not accounted for by the detected proton[1]:

$$E_M \equiv \omega + m_d - E_p \tag{4.1}$$

$$\vec{p}_M \equiv \vec{p}_p - \vec{q} \tag{4.2}$$

In terms of these variables, the missing mass, m_M, is defined as:

$$m_M^2 \equiv E_M^2 - p_M^2 \tag{4.3}$$

By demanding that the missing mass be equal to that of the neutron ($m_M = m_n \approx$ 0.940 GeV/c^2), an undetected single neutron final state can be enforced.

Plots of the missing mass are shown in Fig. 4-2 for perpendicular (left-sector electron) and parallel (right-sector electron) kinematics[2]. In both sectors, the peak at $m_M = m_n$ is visible followed by the undetected multiple-particle continuum. Gaussian

[1]The missing momentum vector is sometimes seen in the literature defined to equal the negative of the missing momentum vector as it is defined in (4.2), that is, $\vec{p}^*_M \equiv \vec{q} - \vec{p}_p$. However, in the QE limit, $\vec{p}^*_M \to \vec{p}_n$ whereas $\vec{p}_M \to -\vec{p}_n$. From the results in Section 1.4, the internucleon momentum vector equals the negative of the neutron momentum. Thus, the definition in (4.2) is the consistent one to use. For results expressed with regards to only the magnitude of the missing momentum, both definitions are equivalent: $p^*_M = p_M$.

[2]See Section 1.5.2 for an explanation of the "perpendicular" and "parallel" terminology.

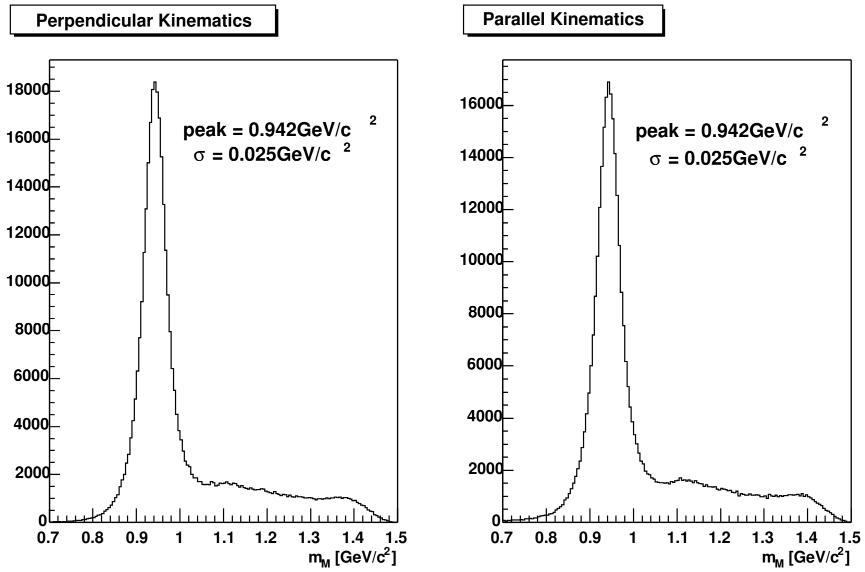

Figure 4-2: Missing mass spectra for perpendicular and parallel kinematics. The peak at $m_M = m_n \approx 0.940$ GeV/c^2 along with the multiple-particle continuum at higher m_M are both visible.

fits to the $m_M = m_n$ peaks in each sector give:

$$(m_M)_{PEAK} = (0.942 \pm 0.025)\,\mathrm{GeV/c^2} \tag{4.4}$$

The uncertainty quoted here (0.025 GeV/c^2) is the σ value resulting from fitting a Gaussian to the peak distribution, not the uncertainty in the determination of the peak.

After the single neutron undetected state, the next lowest-lying undetected missing mass state for $^2\vec{H}(\vec{e}, e'p)X$ is $X = n\pi^0$. It is a multiple-particle state and thus corresponds to a continuum of missing mass values. The lowest missing mass value this state can have is $m_M = m_n + m_{\pi^0} \approx 1.075$ GeV/c^2. Since an undetected neutron corresponds to $m_M = m_n \approx 0.940$ GeV/c^2, pion contamination is minimized by ensuring that the cuts around the $m_M = m_n$ peak are sufficiently below the pion threshold. Since the σ from the Gaussian fit is 0.025 GeV/c$^2 \approx \frac{1}{5}m_\pi$, a full 3-sigma cut was placed around the missing mass peak in the data. For this analysis, the contamination from pion events is thus believed to be small.

4.3 Momentum Corrections

To compensate for reconstruction errors as well as to account for energy loss (which is currently not included in the reconstruction), corrections to the electron and proton momenta were imposed. For a series of bins exhausting the desired Q^2 range, the reconstructed electron and proton momenta were each compared with their respective Monte Carlo momentum plots. In each Q^2 bin, the quasi-elastic electron (proton) momentum peak in the data was multiplied by a correction factor, $f_e(Q^2)$ ($f_p(Q^2)$), causing it to coincide with the Monte Carlo electron (proton) momentum peak:

$$p_e(Q^2)|_{MC\ QE\ peak} = f_e(Q^2) \times p_e(Q^2)|_{Data\ QE\ peak} \tag{4.5}$$

$$p_p(Q^2)|_{MC\ QE\ peak} = f_p(Q^2) \times p_p(Q^2)|_{Data\ QE\ peak} \tag{4.6}$$

For each of the sets of electron and proton momentum correction factors, a polynomial of best-fit was then calculated in terms of the discretized correction factors.

For electrons and protons passing through the left drift chamber sector, the corrections are on the order of 5% and 3%, respectively; electrons and protons passing through the right drift chamber sector have corrections on the order of 2% and 8%, respectively. Since the BLAST detector is a left/right symmetric detector, energy loss in both sectors is expected to be approximately the same for similar particles. The disagreement between the correction factors in either sector for the same particle is thus mostly attributed to left/right disparities in the reconstruction. Plots of the corrected momenta are included in Sec. 4.4.

4.4 Reconstructed Kinematics

Data were analyzed in a momentum transfer range of 0.1 (GeV/c)^2 $< Q^2 <$ 0.5 (GeV/c)^2. Although the BLAST detector is capable of returning information up to $Q^2 \sim 0.8$ (GeV/c)^2, the Cerenkov counter detector cut as well as cross section considerations imposed lower bounds on this upper limit.

A plot comparing the reconstructed Q^2 range versus Monte Carlo calculations is

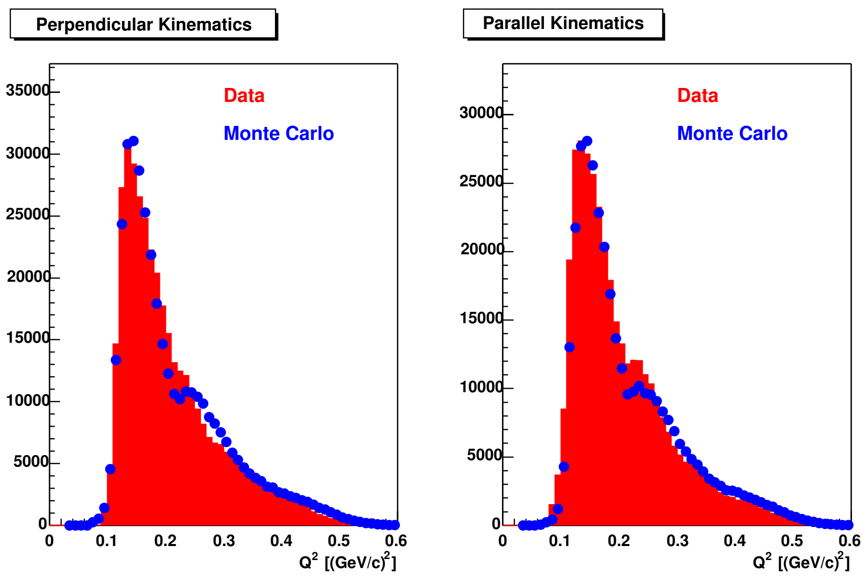

Figure 4-3: Comparison of the reconstructed square of the momentum transfer, Q^2, versus Monte Carlo calculations for perpendicular and parallel kinematics in BLAST. The normalization in the plots is to the maximum peak.

shown in Fig. 4-3. Since detector efficiencies are not measured in BLAST, the normalization of the Monte Carlo to the data is arbitrary; normalization to the maximum peak in each distribution is used for the plots shown here. Overall, good agreement is achieved in both perpendicular and parallel kinematics. The disagreement at intermediate Q^2 values is due to reconstruction inefficiencies in the regions between adjacent CC boxes; attempts to compensate for it are currently being looked into.

Physics results in this analysis are divided into four Q^2 regions:

$$0.1\ (\mathrm{GeV/c})^2 < Q^2 < 0.2\ (\mathrm{GeV/c})^2$$
$$0.2\ (\mathrm{GeV/c})^2 < Q^2 < 0.3\ (\mathrm{GeV/c})^2$$
$$0.3\ (\mathrm{GeV/c})^2 < Q^2 < 0.4\ (\mathrm{GeV/c})^2$$
$$0.4\ (\mathrm{GeV/c})^2 < Q^2 < 0.5\ (\mathrm{GeV/c})^2$$

For each of these Q^2 regions, plots comparing electron and proton kinematics as compared with Monte Carlo calculations are shown in Figs. 4-4 to 4-7. Good agreement between the (corrected) electron and proton momenta is seen for all Q^2 regions. The disagreement in the electron and proton extreme azimuthal angles is attributed to inefficiencies in the reconstruction.

As discussed in Chap. 1, asymmetry results in this work are expressed in terms of p_M, the missing momentum magnitude and in terms of θ_M, the angle between the deuteron polarization vector and the missing momentum vector. Plots of the missing momentum along with its component projections along the "q" coordinate system (see Sec. 1.5.2) are shown in Figs. 4-8 to 4-11. Plots of θ_M are shown in Fig. 4-12.

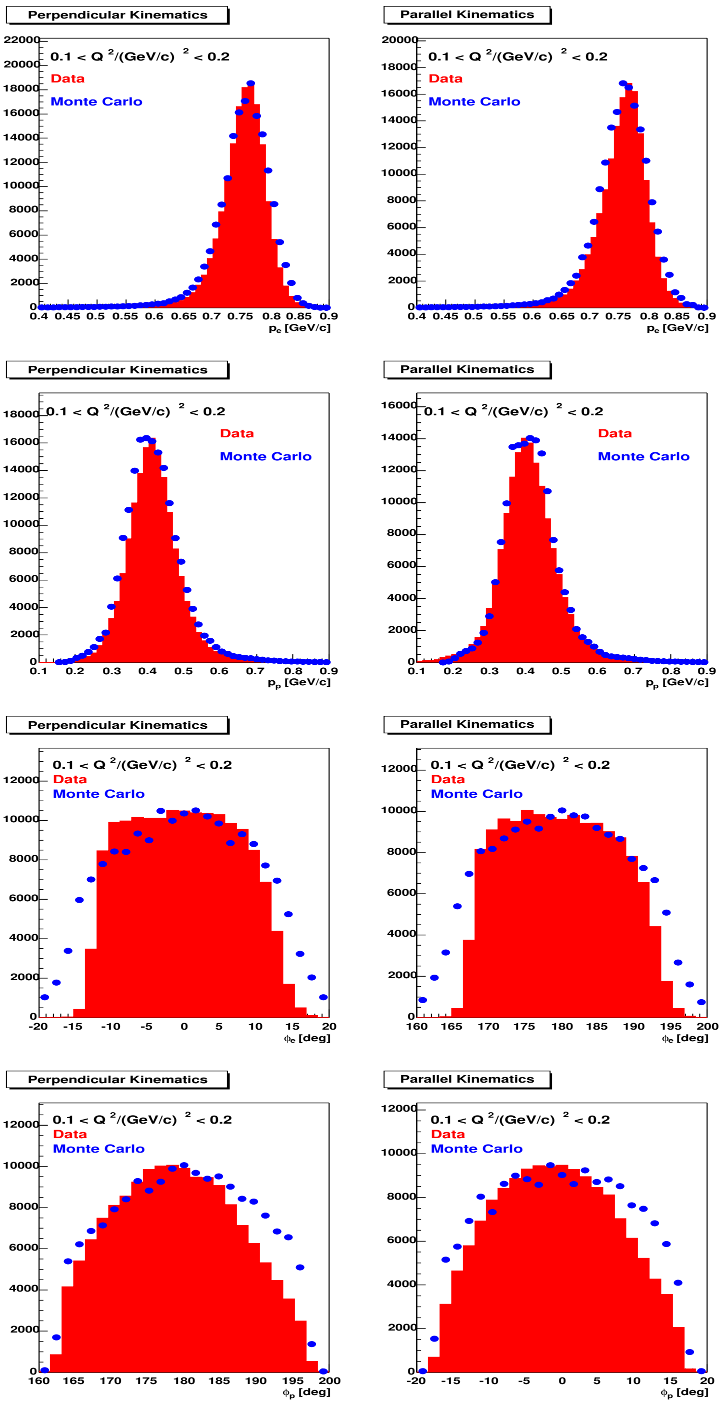

Figure 4-4: Comparison of electron and proton kinematics with Monte Carlo calculations for $0.100\ (\mathrm{GeV/c})^2 < Q^2 < 0.200\ (\mathrm{GeV/c})^2$. From top to bottom, plots are shown of the electron momentum (p_e), the proton momentum (p_p), the electron azimuthal angle (ϕ_e), and the proton azimuthal angle (ϕ_p). The normalization in the plots is to the maximum peak.

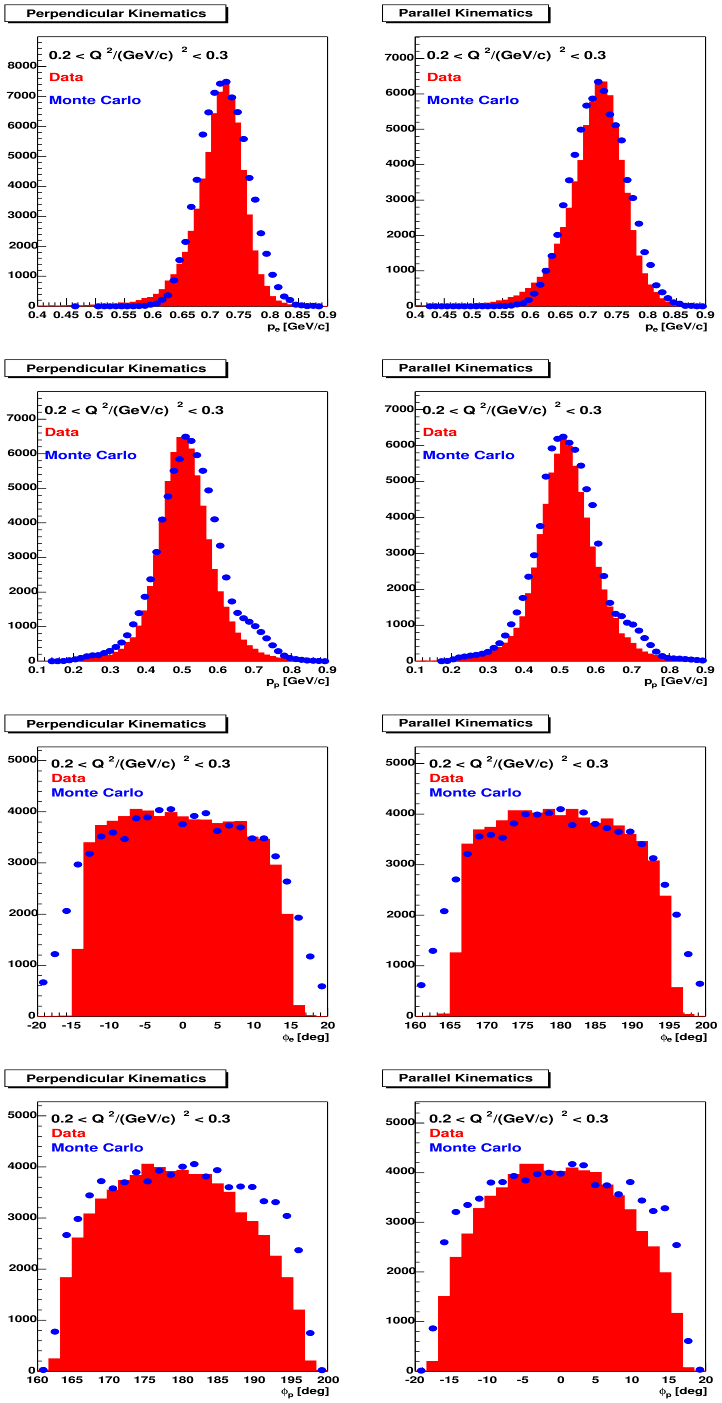

Figure 4-5: Comparison of electron and proton kinematics with Monte Carlo calculations for 0.200 (GeV/c)^2 $< Q^2 <$ 0.300 (GeV/c)^2. From top to bottom, plots are shown of the electron momentum (p_e), the proton momentum (p_p), the electron azimuthal angle (ϕ_e), and the proton azimuthal angle (ϕ_p). The normalization in the plots is to the maximum peak.

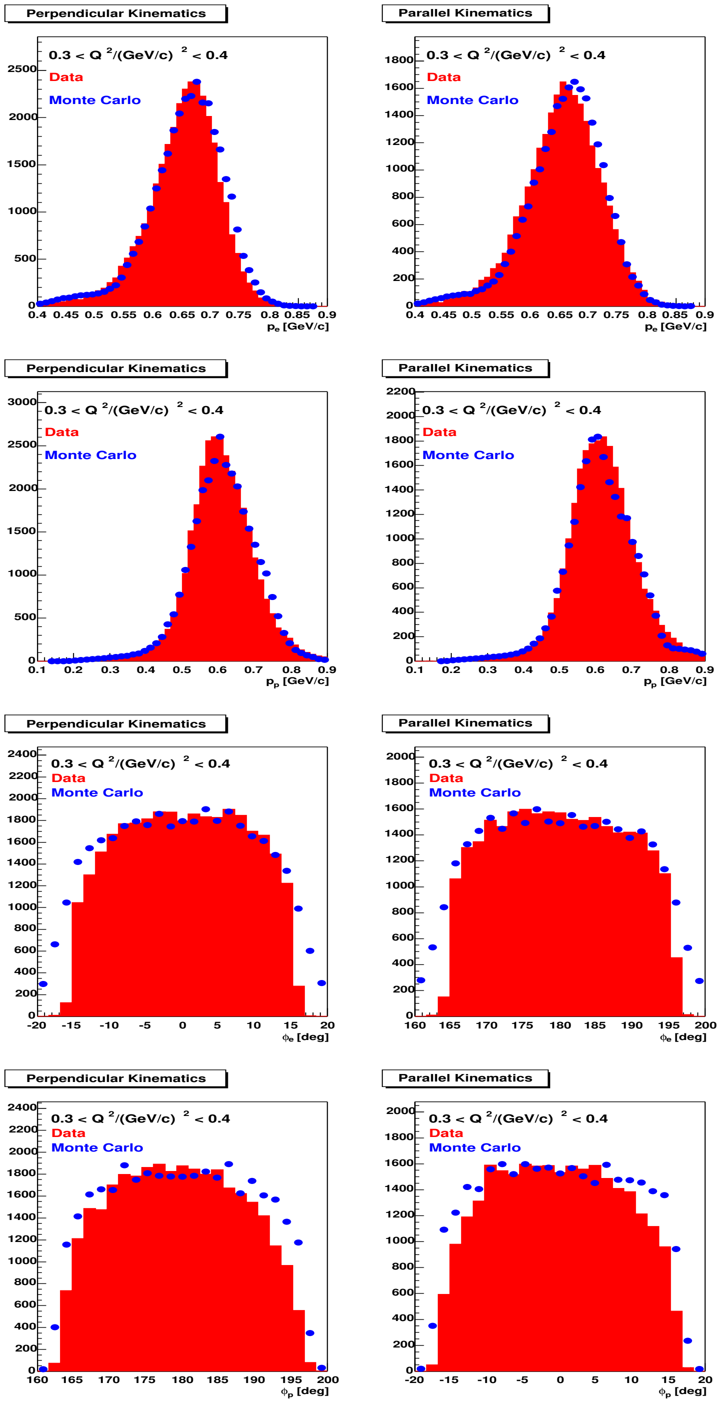

Figure 4-6: Comparison of electron and proton kinematics with Monte Carlo calculations for 0.300 $(\mathrm{GeV/c})^2 < Q^2 <$ 0.400 $(\mathrm{GeV/c})^2$. From top to bottom, plots are shown of the electron momentum (p_e), the proton momentum (p_p), the electron azimuthal angle (ϕ_e), and the proton azimuthal angle (ϕ_p). The normalization in the plots is to the maximum peak.

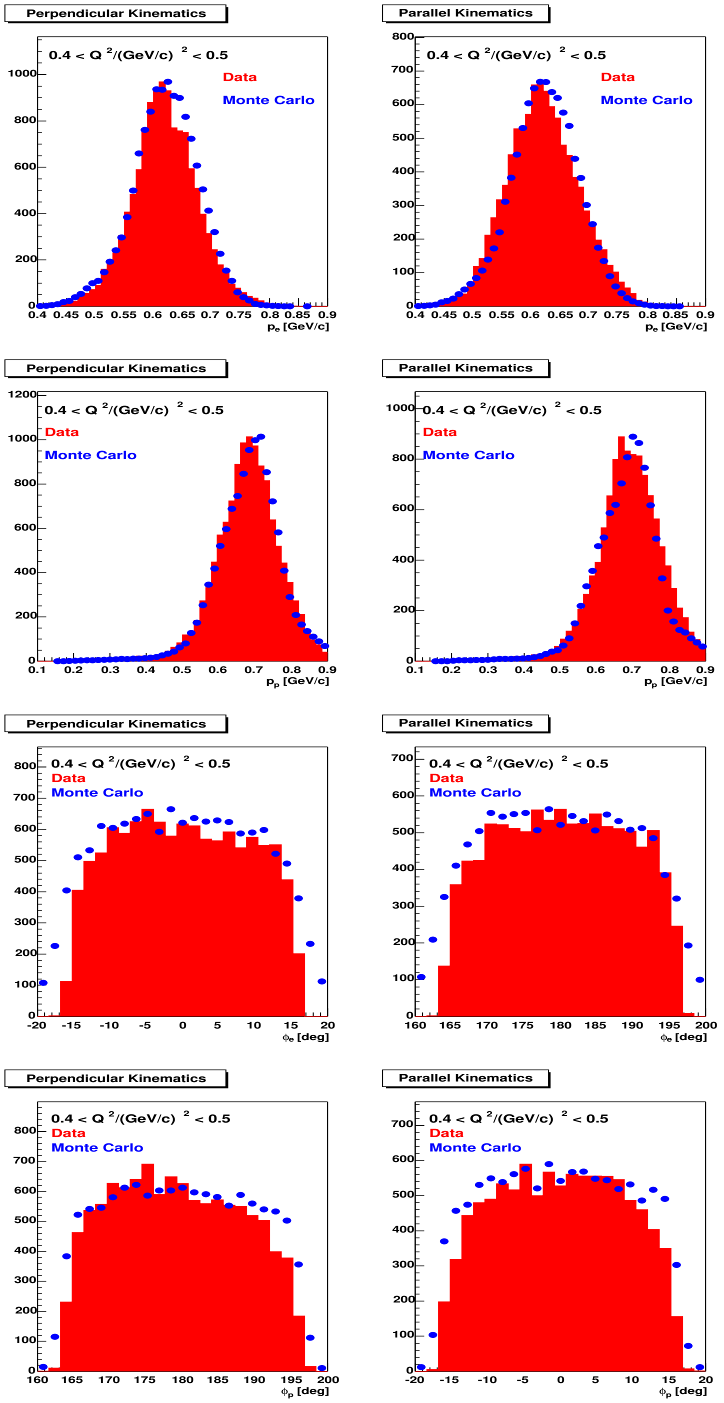

Figure 4-7: Comparison of electron and proton kinematics with Monte Carlo calculations for 0.400 (GeV/c)^2 $< Q^2 <$ 0.500 (GeV/c)^2. From top to bottom, plots are shown of the electron momentum (p_e), the proton momentum (p_p), the electron azimuthal angle (ϕ_e), and the proton azimuthal angle (ϕ_p). The normalization in the plots is to the maximum peak.

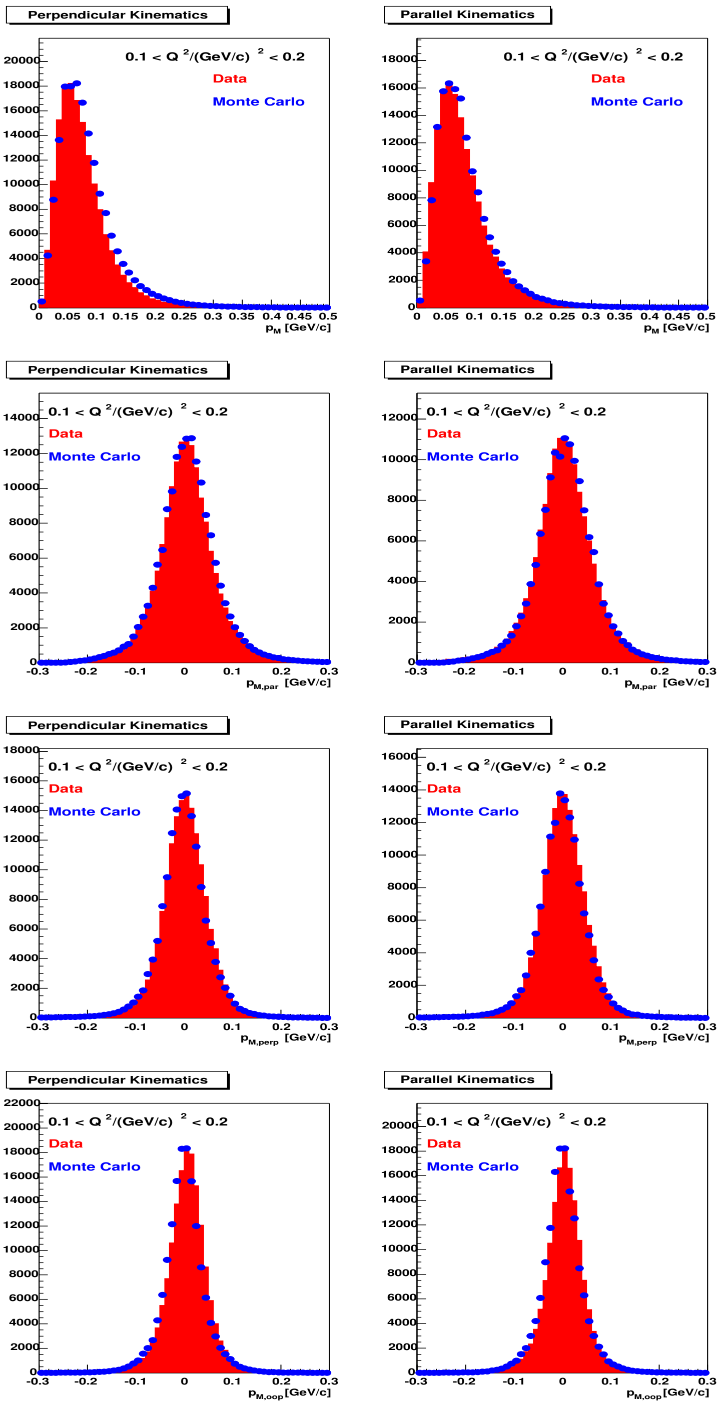

Figure 4-8: Comparison of missing momentum with Monte Carlo calculations for $0.100\ (\mathrm{GeV/c})^2 < Q^2 < 0.200\ (\mathrm{GeV/c})^2$. The top plot is the missing momentum magnitude. The other three, from top to bottom, are plots of the components of the missing momentum vector along the respective $\hat{q}_z$, $\hat{q}_x$, and $\hat{q}_y$ directions. The normalization in the plots is to the maximum peak.

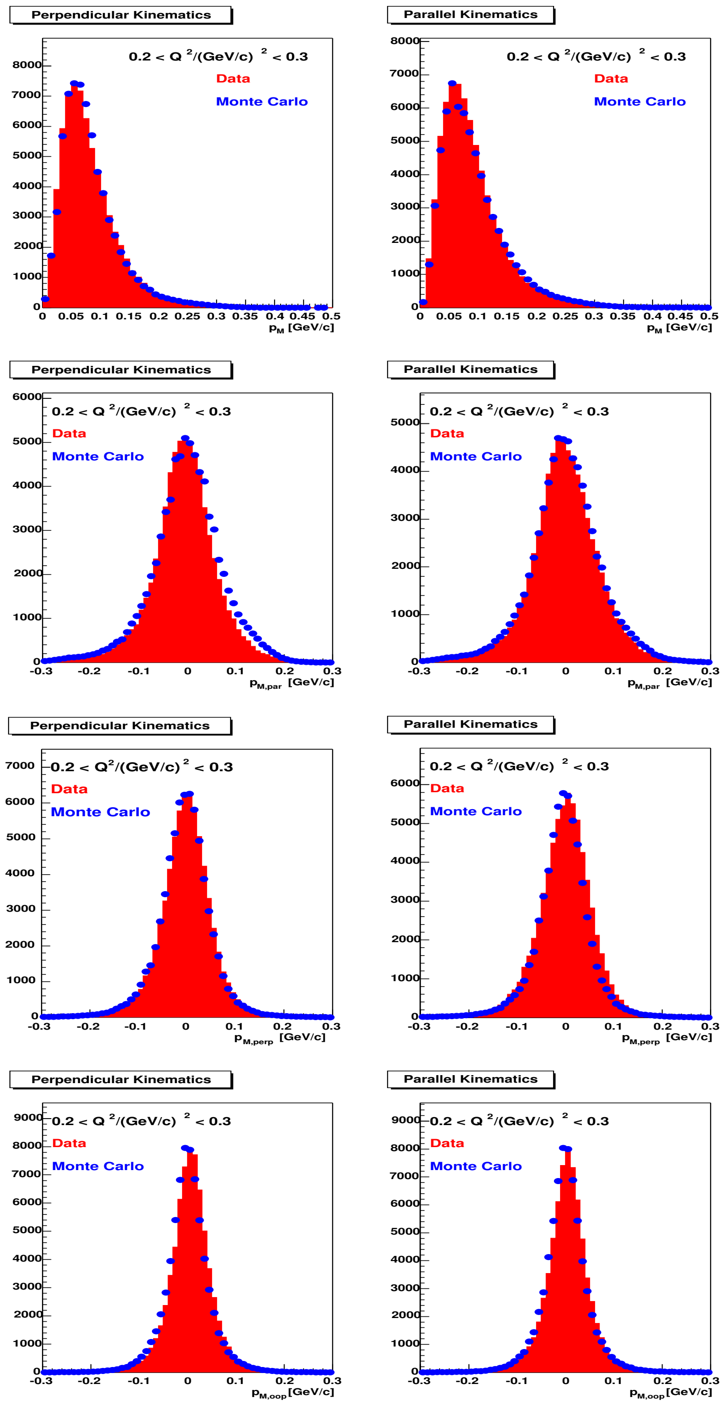

Figure 4-9: Comparison of missing momentum with Monte Carlo calculations for $0.200\ (\mathrm{GeV/c})^2 < Q^2 < 0.300\ (\mathrm{GeV/c})^2$. The top plot is the missing momentum magnitude. The other three, from top to bottom, are plots of the components of the missing momentum vector along the respective $\hat{q}_z$, $\hat{q}_x$, and $\hat{q}_y$ directions. The normalization in the plots is to the maximum peak.

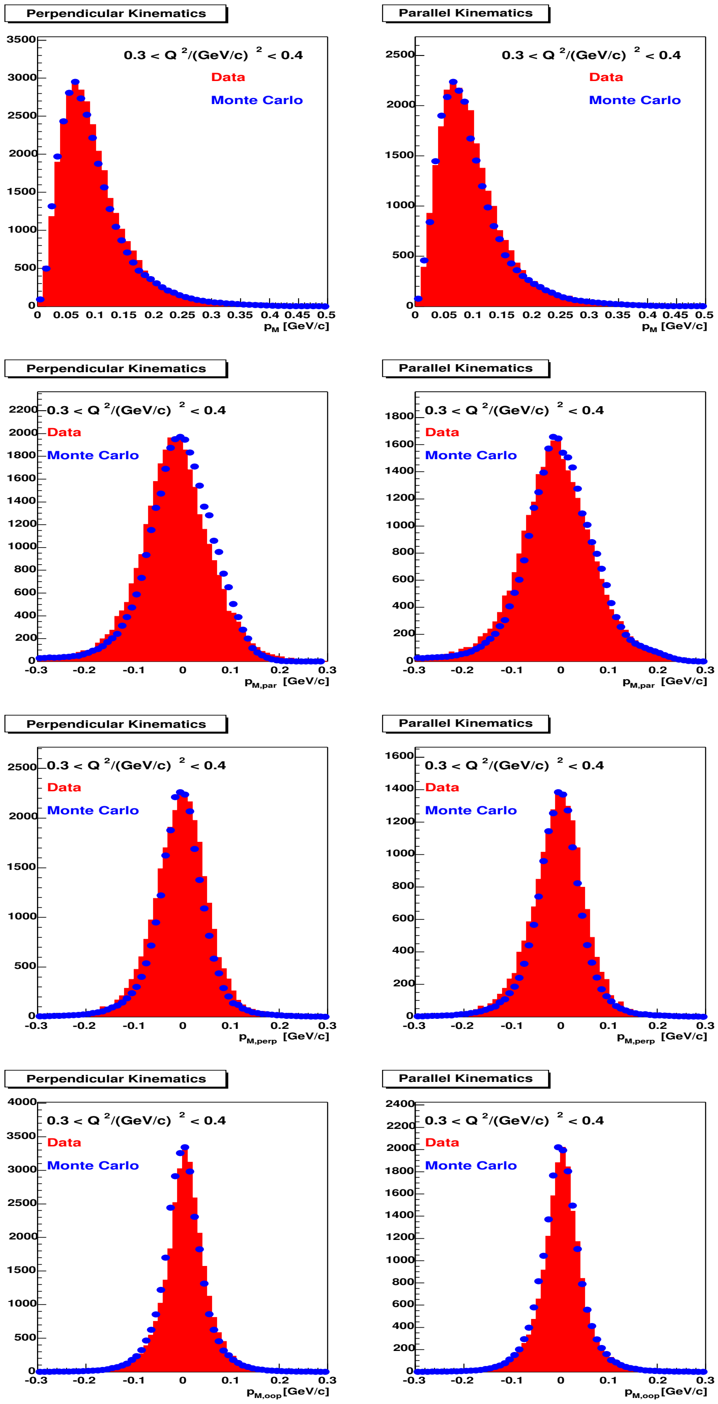

Figure 4-10: Comparison of missing momentum with Monte Carlo calculations for 0.300 (GeV/c)^2 < Q^2 < 0.400 (GeV/c)^2. The top plot is the missing momentum magnitude. The other three, from top to bottom, are plots of the components of the missing momentum vector along the respective $\hat{q}_z$, $\hat{q}_x$, and $\hat{q}_y$ directions. The normalization in the plots is to the maximum peak.

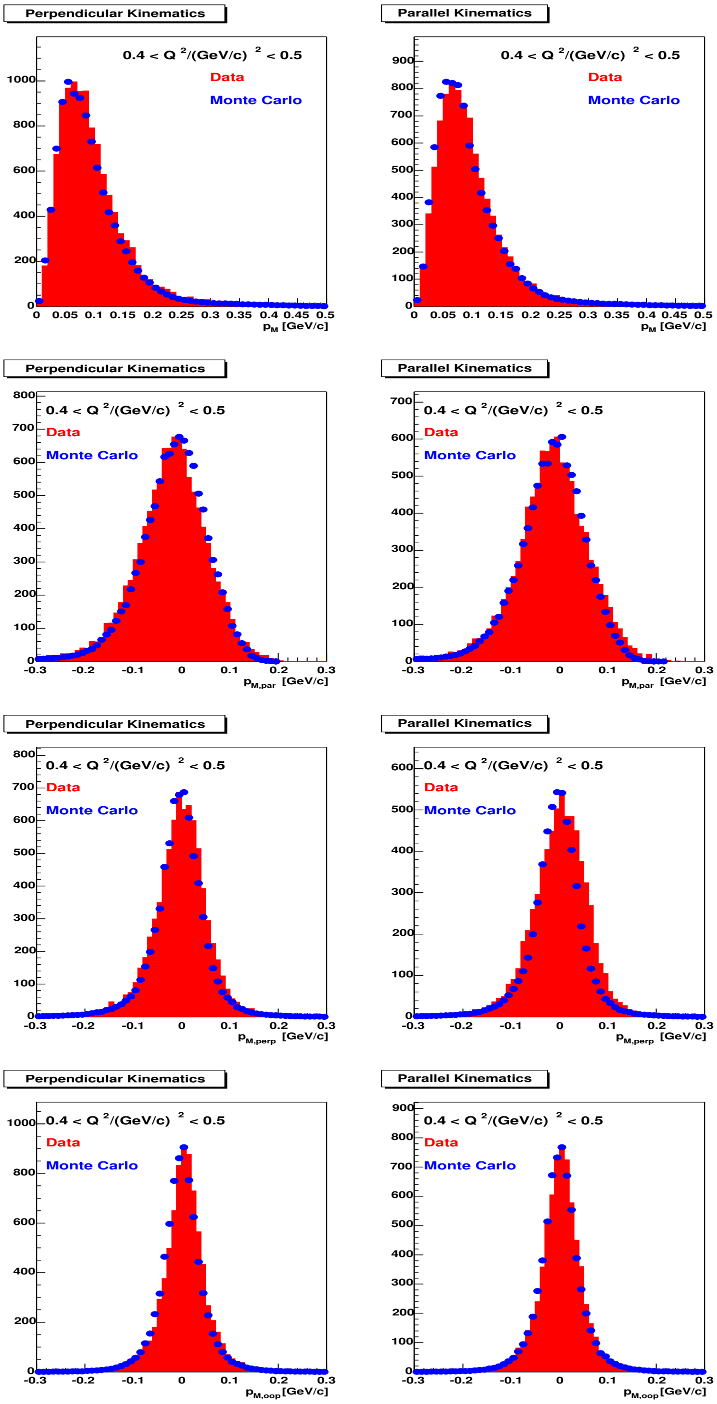

Figure 4-11: Comparison of missing momentum with Monte Carlo calculations for $0.400\ (\mathrm{GeV/c})^2 < Q^2 < 0.500\ (\mathrm{GeV/c})^2$. The top plot is the missing momentum magnitude. The other three, from top to bottom, are plots of the components of the missing momentum vector along the respective $\hat{q}_z$, $\hat{q}_x$, and $\hat{q}_y$ directions. The normalization in the plots is to the maximum peak.

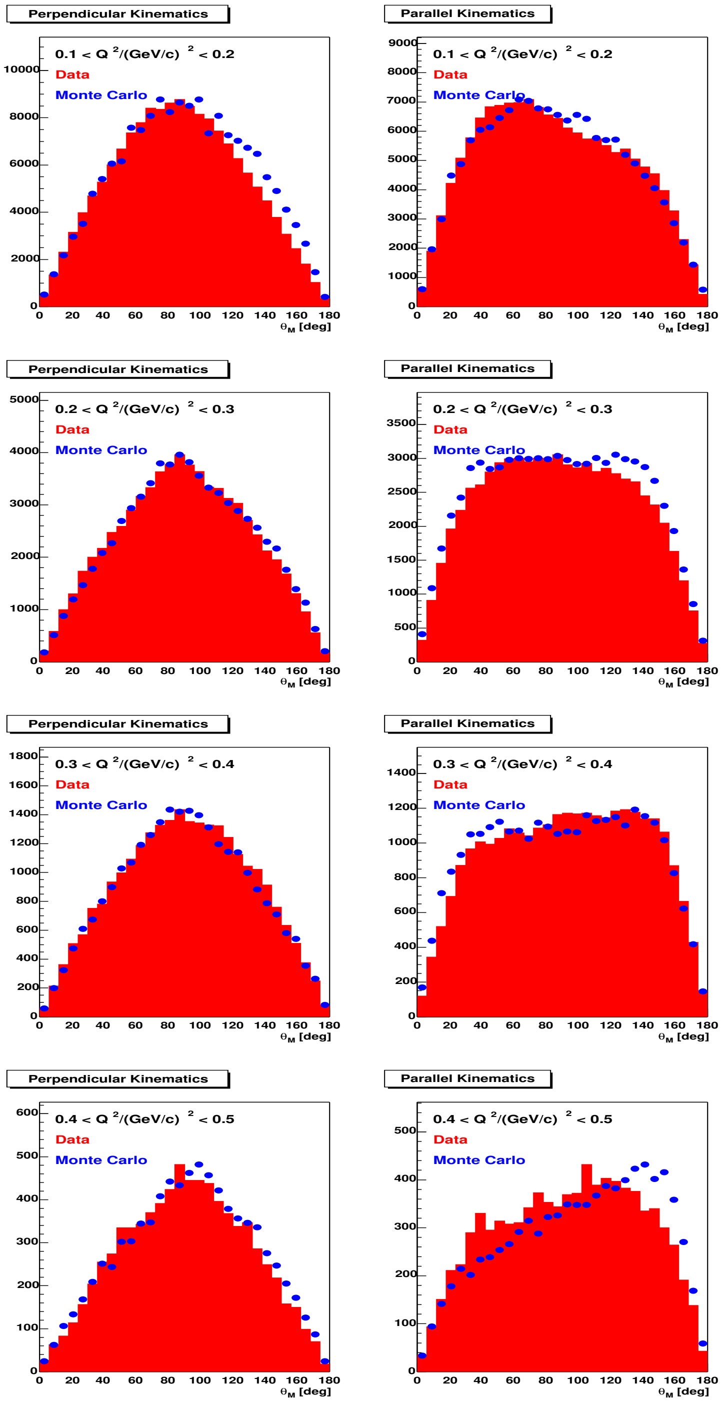

Figure 4-12: Comparison of the angle, θ_M, between the deuteron polarization vector and the missing momentum vector for all four considered Q^2 ranges, in increasing order from top to bottom. The normalization in the plots is to the maximum peak.

4.5 Determination of Asymmetries

Data were recorded in one of six beam-target polarization states. For each of these states, the total accumulated events were divided by the accumulated charge in that state to get a rate (events per unit charge):

$$r\left(h, P_z, P_{zz}\right) = \begin{cases} r(+1,+1,+1) \\ r(-1,+1,+1) \\ r(+1,-1,+1) \\ r(-1,-1,+1) \\ r(+1,\quad 0,-2) \\ r(-1,\quad 0,-2) \end{cases} \tag{4.7}$$

where h, P_z, and P_{zz} are the respective beam helicity and target vector and tensor polarization. The five deuteron electrodisintegration asymmetries, A_d^V, A_d^T, A_e, A_{ed}^V, and A_{ed}^T, can all be expressed as independent linear combinations of these six rates:

$$\begin{pmatrix} 6h\bar{r}A_e \\ \sqrt{\frac{2}{3}}P_z\bar{r}A_d^V \\ \sqrt{\frac{2}{3}}hP_z\bar{r}A_{ed}^V \\ \sqrt{2}P_{zz}\bar{r}A_d^T \\ \sqrt{2}hP_{zz}\bar{r}A_{ed}^T \end{pmatrix} = \begin{pmatrix} +1 & -1 & +1 & -1 & +1 & -1 \\ +1 & +1 & -1 & -1 & 0 & 0 \\ +1 & -1 & -1 & +1 & 0 & 0 \\ +1 & +1 & +1 & +1 & -2 & -2 \\ +1 & -1 & +1 & -1 & -2 & +2 \end{pmatrix} \begin{pmatrix} r(+1,+1,+1) \\ r(-1,+1,+1) \\ r(+1,-1,+1) \\ r(-1,-1,+1) \\ r(+1,\quad 0,-2) \\ r(-1,\quad 0,-2) \end{pmatrix} \tag{4.8}$$

where $\bar{r}$ is the average of the rates in the six polarization states. By expressing results in terms of asymmetries, the luminosity explicitly cancels and is thus not needed.

4.6 Background Asymmetry Corrections

Asymmetries computed from (4.8) are subject to corrections due to background rates. The dominant source of background was quasi-elastic $e - p$ scattering from the aluminum target walls. Since such events originate along the target chamber, the previously-mentioned vertex cuts were not sufficient to exclude them. Instead, these background rates were accounted for by measuring the quasi-elastic $e-p$ rate with an empty target.

Each of the (real) asymmetries in (4.8) can be written in the following form:

$$A^R = \frac{\sum_i g_i r_i^R}{\sum_i r_i^R} \tag{4.9}$$

where the various r_i^R correspond to the six real polarization-state rates listed in (4.7) and where the g_i are scalar constants specific to a particular asymmetry. What is measured, however, is not the real rate but the total rate, r_i^T, equal to the sum of the real rate and the background rate, r_i^B. Since the background rate is the same in each polarization state, the substitution $r_i^R = r_i^T - r_i^B = r_i^T - r^B$ can be made in (4.9) to get the following equation:

$$\begin{aligned} A^R &= \frac{\sum_i g_i \left(r_i^T - r^B\right)}{\sum_i \left(r_i^T - r^B\right)} \\ &= \frac{\sum_i g_i r_i^T - r^B \sum_i g_i}{\sum_i r_i^T - 6r^B} \cdot \frac{\sum_i r_i^T}{\sum_i r_i^T} \\ &= \frac{\sum_i g_i r_i^T}{\sum_i r_i^T} \cdot \frac{\sum_i r_i^T}{\sum_i r_i^T - 6r^B} \\ &= A^T \cdot f^{-1} \end{aligned} \tag{4.10}$$

where A^T is the total (measured) asymmetry and f is the ratio of the real rate to the total rate:

$$f \equiv \frac{\sum_i r_i^T - 6r^B}{\sum_i r_i^T} \tag{4.11}$$

By design, $\sum_i g_i = 0$ for each asymmetry; this fact has been used to reach the above result. Since f has no dependence on the various g_i terms, it follows that this equation is valid for all five of the deuteron electrodisintegration asymmetries.

Plots of f versus p_M and $\cos\theta_M$ are shown in Fig. 4-13. At low p_M, the background rate is very small ($< 1\%$); however, as p_M increases, the background becomes larger until it plateaus around a 5% contribution. The onset of increased background at higher p_M is consistent with the large Fermi momentum in aluminum. The background rate versus $\cos\theta_M$ is roughly constant at $\sim 1\%$. The constancy of this background is due to the fact that all p_M values are averaged over for each $\cos\theta_M$ bin. The low background rate seen in the plots is attributed to good beam tune as well as to good beam halo cleanup from the collimator.

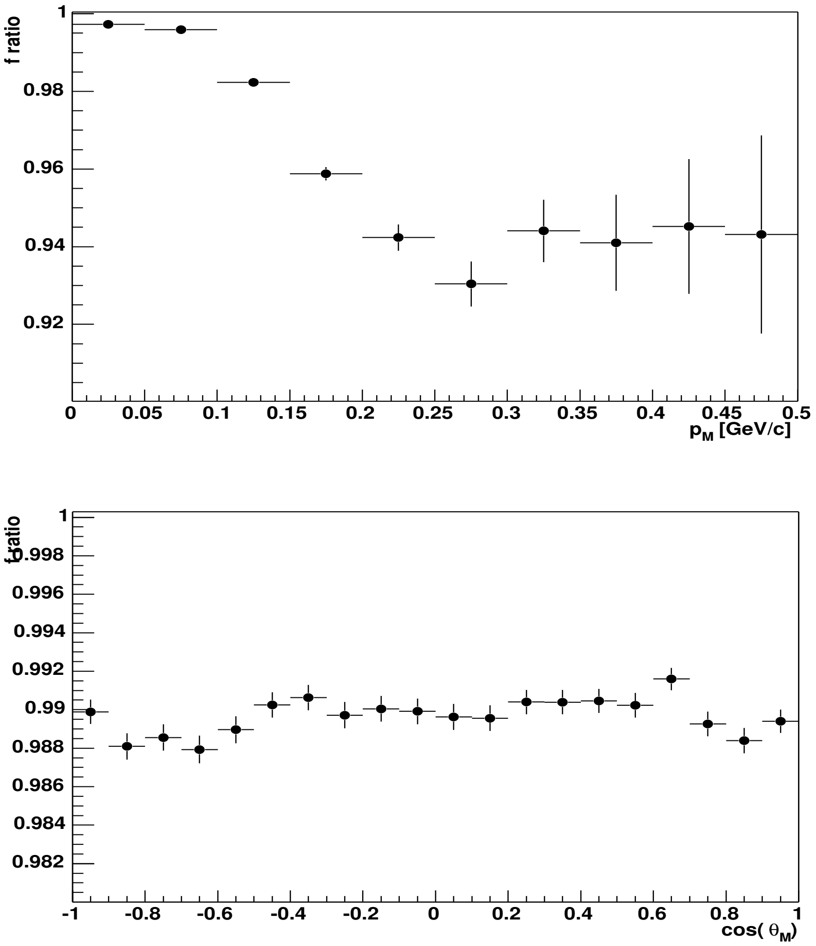

Figure 4-13: Plots of the ratio of the real event rate to the total event rate as a function of p_M, the missing momentum (top plot), and $\cos\theta_M$, the cosine of the angle between the deuteron's polarization vector and the missing momentum vector (bottom plot).

The data in Fig. 4-13 are for ~ 40 kC of empty target data taken at periodic points throughout the run period. In each case, a polynomial of best-fit was computed, and the reconstructed asymmetries were scaled by its inverse, as shown in Fig. 4.10.

4.7 Target Polarization

As seen in (4.8), knowledge of the beam helicity and target vector and tensor polarizations is required in order to extract measurements of the various asymmetries. As discussed in Chap. 2, the beam helicity was determined via a Compton polarimeter. The target vector and tensor polarizations, however, were determined through data analysis.

4.7.1 The Beam-Vector Polarization

The product of the beam helicity and the target vector polarization, hP_z, was extracted from the beam-vector asymmetry, A^V_{ed}, for $^2\vec{H}(\vec{e},e'p)n$ in the quasi-elastic (QE) limit by calculating the ratio of the calculated beam-vector asymmetry, $A^V_{ed,CALC}$, to that of the Monte Carlo one, $A^V_{ed,MC}$:

$$hP_z = \frac{A^V_{ed,CALC}}{A^V_{ed,MC}} \tag{4.12}$$

In this limit, the reaction reduces to elastic $e-p$ scattering with a spectator neutron. Since elastic $e-p$ scattering at low momentum transfers is well understood [10], the theoretical uncertainties due to the choice of internucleon potential and various reaction mechanism contributions are minimized in this limit. Additionally, due to the relatively large cross section of the QE $^2\vec{H}(\vec{e},e'p)n$ reaction as well as the high detector efficiency for electrons and protons, the statistical uncertainties of such events are small. With small theoretical and statistical errors, the value of hP_z can be accurately extracted.

To ensure QE scattering, fits of the data to the Monte Carlo asymmetries were confined to missing momentum values such that $p_M < 0.100$ GeV/c. For each of the four consecutive Q^2 intervals between 0.100 (GeV/c)^2 and 0.500 (GeV/c)^2, a value for hP_z was extracted in both sectors. Missing mass cut dependence was checked by varying the allowed missing mass peak width from $0.5\sigma_{m_M}$ to $3.0\sigma_{m_M}$, where $\sigma_{m_M} = 0.025$ GeV/c^2 as discussed in Sec. 4.2.3. A listing of the extracted hP_z values

hP_z for Perpendicular Kinematics				
Q^2 Range $(\text{GeV/c})^2$	$\lvert m_M - m_n \rvert < F * \sigma_{m_M}$			
	$F = 0.5$	$F = 1.0$	$F = 2.0$	$F = 3.0$
$0.100 < Q^2 < 0.200$	0.573 ± 0.008	0.575 ± 0.006	0.573 ± 0.005	0.572 ± 0.005
$0.200 < Q^2 < 0.300$	0.531 ± 0.009	0.535 ± 0.006	0.527 ± 0.005	0.522 ± 0.005
$0.300 < Q^2 < 0.400$	0.546 ± 0.014	0.533 ± 0.009	0.527 ± 0.007	0.515 ± 0.006
$0.400 < Q^2 < 0.500$	0.535 ± 0.024	0.537 ± 0.014	0.508 ± 0.010	0.500 ± 0.009

hP_z for Parallel Kinematics				
Q^2 Range $(\text{GeV/c})^2$	$\lvert m_M - m_n \rvert < F * \sigma_{m_M}$			
	$F = 0.5$	$F = 1.0$	$F = 2.0$	$F = 3.0$
$0.100 < Q^2 < 0.200$	0.569 ± 0.007	0.566 ± 0.005	0.564 ± 0.004	0.564 ± 0.004
$0.200 < Q^2 < 0.300$	0.553 ± 0.007	0.552 ± 0.005	0.548 ± 0.004	0.540 ± 0.004
$0.300 < Q^2 < 0.400$	0.564 ± 0.013	0.566 ± 0.009	0.545 ± 0.006	0.530 ± 0.006
$0.400 < Q^2 < 0.500$	0.516 ± 0.033	0.551 ± 0.020	0.538 ± 0.013	0.526 ± 0.011

Table 4.1: Extracted hP_z values and statistical errors for perpendicular (top table) and parallel (bottom table) kinematics as a function of Q^2 bin and multiples of the missing mass peak width. As discussed in Sec. 4.2.3, $\sigma_{m_M} = 0.025$ GeV/c^2.

is shown in Tab. 4.1, and a plot of them is shown in Fig. 4-14. For the lowest Q^2 region (0.100 (GeV/c)^2 $< Q^2 <$ 0.200 (GeV/c)^2), the dependence on the missing mass peak width cut is minimal. Additionally, the extracted hP_z values for both perpendicular and parallel kinematics are in statistical agreement. Furthermore, due to the large amount of data at low Q^2, high confidence can be placed in the extraction of the applied kinematic corrections (see Fig. 4.3). For these reasons, the extracted hP_z values for 0.100 (GeV/c)^2 $< Q^2 <$ 0.200 (GeV/c)^2 are believed to be the most reliable. Quoted values for hP_z are thus taken from this Q^2 range alone.

Correcting for the Dipole Approximation

As previously discussed in Chap. 1, the Monte Carlo asymmetries are computed using the formalism of Arenhövel et al. [6, 7]. In this formalism, the proton's electric and magnetic form factors, $G_E(Q^2)$ and $G_M(Q^2)$, are assumed to have a dipole form [5, 31]:

$$G_E(Q^2) = \frac{1}{\mu_p} G_M(Q^2) = G_D(Q^2) \equiv \frac{1}{(1 + Q^2/\Lambda^2)^2} \tag{4.13}$$

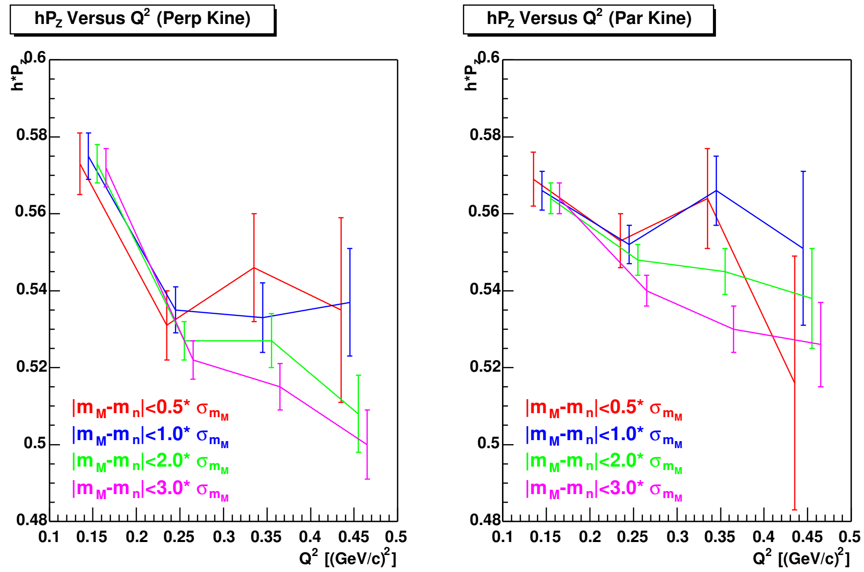

Figure 4-14: Extracted beam-vector polarizations, hP_z, for each of the four consecutive 0.100 (GeV/c)^2 Q^2 regions between 0.100 (GeV/c)^2 and 0.500 (GeV/c)^2. The different colored plots correspond to cuts with increasing multiples of the missing mass width. As discussed in Sec. 4.2.3, $\sigma_{m_M} = 0.025$ GeV/c^2.

where $\mu_p = 2.79$ is the magnetic moment of the proton and $\Lambda^2 = 0.71$ (GeV/c)^2. More recent analysis [17], however, indicates that deviations from the dipole form exist in the Q^2 range of interest here. Empirical fits to all of the available proton form factor data were recently performed by Friedrich and Walcher [27]. Their resulting fits were modeled as a sum of dipoles and exponentials, necessarily deviating from the (single) dipole form approximation.

In order to account for the observed deviation from the dipole form, the hP_z values extracted from the Monte Carlo must be corrected accordingly. In the QE limit, the $^2\vec{H}(\vec{e}, e'p)n$ beam-vector asymmetry reduces to that of the elastic $e - p$ one, which has the following empirical form:

$$A^V_{ed}\Big|_{QE} \rightarrow A^V_{ep} = \frac{\cos\theta^* + \alpha(Q^2)\sin\theta^*\cos\phi^* R(Q^2)}{\beta(Q^2) + \gamma(Q^2)R(Q^2)^2} \tag{4.14}$$

Here, $\alpha(Q^2)$, $\beta(Q^2)$, and $\gamma(Q^2)$ are kinematic functions, and θ^* and ϕ^* are the respective polar and azimuthal angles that the proton polarization vector makes with respect to the three-momentum transfer vector, $\vec{q}$. The remaining term, $R(Q^2)$, in

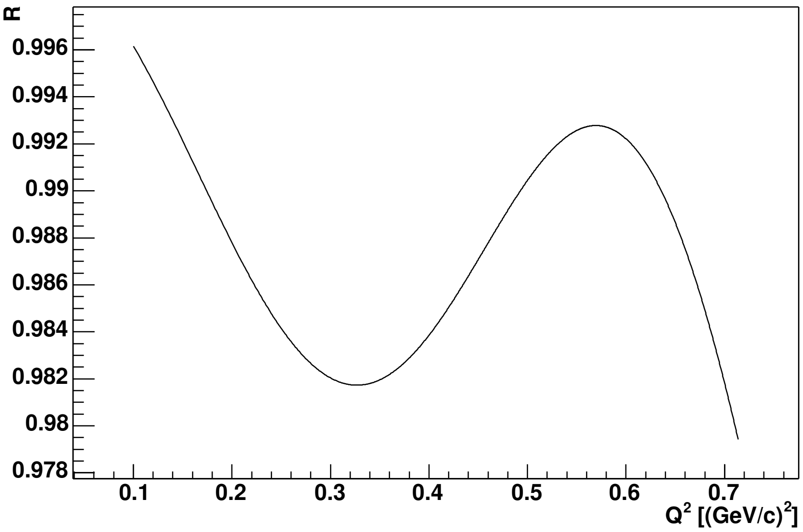

Figure 4-15: Plot of the ratio, R, of the proton's electric and magnetic form factors versus Q^2 using the fit from Friedrich and Walcher [27].

(4.14) is the ratio of the proton's electric and magnetic form factors, scaled by μ_p:

$$R(Q^2) \equiv \frac{\mu_p G_E(Q^2)}{G_M(Q^2)} \tag{4.15}$$

In the dipole approximation, $R(Q^2) \equiv 1$. However, as shown in Fig. 4-15, the fit by Friedrich and Walcher (FW) shows deviations of $R(Q^2)$ from 1 of around 1% in the 0.1 $(\mathrm{GeV/c})^2 < Q^2 < 0.2$ $(\mathrm{GeV/c})^2$ range.

Defining $A^V_{ed,MC,Dipole}$ and $A^V_{ed,MC,FW}$ to be the beam-vector asymmetries determined using the dipole form factors and those from the FW fit, respectively, the extracted hP_z value from the FW fit can be expressed in terms of the dipole hP_z value:

$$\begin{aligned} hP_z|_{FW} &= \frac{A^V_{ed,CALC}}{A^V_{ed,MC,FW}} \\ &= \frac{A^V_{ed,MC,Dipole}}{A^V_{ed,MC,FW}} \cdot \frac{A^V_{ed,CALC}}{A^V_{ed,MC,Dipole}} \\ &= \frac{1}{r}\frac{A^V_{ed,CALC}}{A^V_{ed,MC,Dipole}} \end{aligned}$$

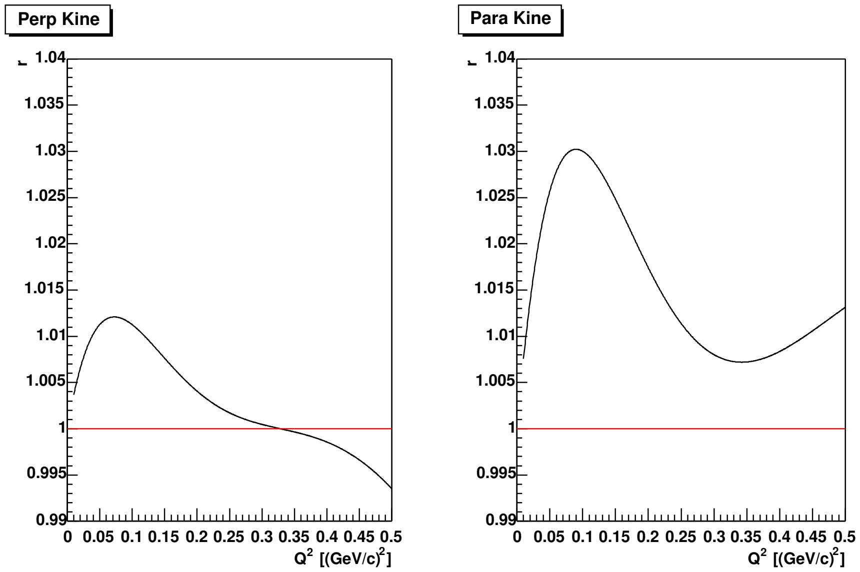

Figure 4-16: Plot of the ratio, r, of the QE beam-vector $\vec{p}(\vec{e}, e'p)$ asymmetry using the FW nucleon form factor fits [27] to that of using the dipole nucleon form factors. The left plot is for perpendicular kinematics while the right is for parallel.

$$= \frac{1}{r}\, hP_z|_{Dipole} \tag{4.16}$$

where $r \equiv A^V_{ed,MC,FW}/A^V_{ed,MC,Dipole}$ is the ratio of the FW beam-vector Monte Carlo asymmetry to that of the dipole one. Plots of r versus Q^2 for perpendicular and parallel kinematics ($\theta^* = \frac{\pi}{2}$ and $\theta^* = 0$, respectively) are shown in Fig. 4-16. In the 0.1 $(\mathrm{GeV/c})^2 < Q^2 < 0.2$ $(\mathrm{GeV/c})^2$ region, $r \approx 1.01$ for perpendicular kinematics while $r \approx 1.02$ for parallel. Adjusting the hP_z values in Tab. 4.1 for 0.1 $(\mathrm{GeV/c})^2 < Q^2 < 0.2$ $(\mathrm{GeV/c})^2$ gives:

$$hP_z|^{\perp}_{FW} = \tfrac{1}{1.01} \cdot 0.572 = 0.567$$
$$hP_z|^{\parallel}_{FW} = \tfrac{1}{1.02} \cdot 0.564 = 0.553$$

A statistically weighted average of these two values gives $hP_z = 0.558 \pm 0.009_{stat}$.

Source	Contribution
Target Polarization Angle	0.004
Dipole Approximation	0.003
NN Potential	0.003
Missing Mass Cut	0.002
TOTAL	0.006

Table 4.2: Systematic error contributions to hP_z. The total systematic error is calculated by adding the separate errors in quadrature.

Systematic Errors of $\mathbf{hP_z}$

A summary of the various sources of systematic error in the determination of hP_z is shown in Tab. 4.2; the separate systematic errors have been added in quadrature to determine the total systematic error.

The largest source of systematic error in hP_z came from the uncertainty in the determination of the target polarization angle, θ_d. As will be discussed in detail in Sec. 4.8.1, the spin angle of the target is known to $\sim 1°$. A measure of the resulting systematic error in hP_z is found by studying how the extracted hP_z value changes with different assumed spin angle values. Fig. 4-17 shows a comparison of the extracted hP_z values for deviations of θ_d of 1° from the nominal value of 32°.

An additional contribution to the systematic error of hP_z came from assuming a single value for the ratio of the FW form factor parameterization to the dipole one over the entire 0.1 (GeV/c)^2 $< Q^2 <$ 0.2 (GeV/c)^2 range where the hP_z extraction is made (see Fig. 4-16). Variations in the NN potential were also considered; a comparison of the beam-vector asymmetries using the Bonn [40, 41], V18 [56], and Paris [32] potentials is shown in Fig. 4-18. The actual extraction of hP_z was done with respect to the Bonn potential. Finally, error due to the missing mass width cut was estimated by examining how the extracted hP_z value changed with differing missing mass width cuts, as shown in Tab. 4.1. Due to the small variation in the 0.1 (GeV/c)^2 $< Q^2 <$ 0.2 (GeV/c)^2 range, a full $3\sigma_{m_M}$ cut was used in the extraction of hP_z. The final extracted value for hP_z with full statistical and systematic errors is:

$$hP_z = 0.558 \pm 0.009_{stat} \pm 0.006_{syst} \tag{4.17}$$

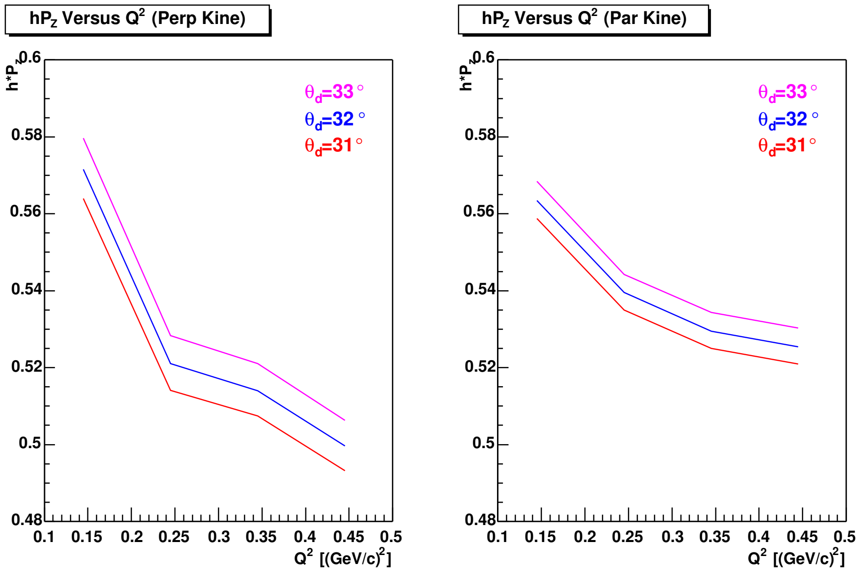

Figure 4-17: Plots of the beam-vector asymmetry, A_{ed}^{V}, as a function of the square of the four-momentum transfer, Q^2, for various deuteron spin angles: $\theta_d = 31°$, $32°$, and $33°$.

where the total systematic error is given by the quadratic sum of the individual systematic errors.

4.7.2 The Tensor Polarization

The tensor polarization, P_{zz}, was extracted from fits of the elastic electron-deuteron T_{20} observable (see Sec. 1.5.1) at low Q^2 [58]. A parameterization of the three deuteron form factors, G_C, G_Q, and G_M, was recently performed [1], using both unpolarized and polarized deuteron cross section data, which modeled the form factors as Fourier transforms of sums of Gaussian charge distributions. The tensor polarization was extracted from normalizing to T_{20} constructed from this parameterization (see (1.31)). Fig. 4-19 shows a plot of the resulting fitted T_{20} observable from elastic $e-d$ data taken simultaneously with the ${}^2\vec{H}(\vec{e}, e'p)n$ data [58]. The resulting tensor polarization value is:

$$P_{zz} = 0.680 \pm 0.016_{stat} \pm 0.060_{syst} \tag{4.18}$$

The dominant source of systematic error in the determination of P_{zz} is due to

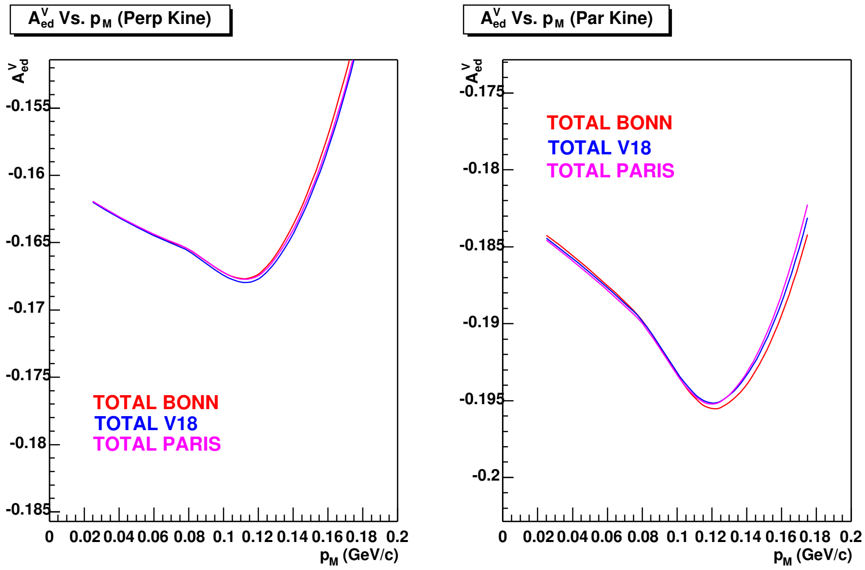

Figure 4-18: Plots of the beam-vector asymmetry, A^V_{ed}, as a function of the missing momentum, p_M, for different internucleon potentials: Bonn [40, 41], V18 [56], and Paris [32]. Each potential includes all reaction mechanism effects (i.e., meson-exchange currents, isobar configurations, final-state interactions, and relativistic corrections).

model uncertainty in the determination of T_{20}. As seen in Fig. 4-19, the spread of the large number of models for T_{20} leads to a large systematic model uncertainty in P_{zz}.

4.8 Asymmetry Systematic Uncertainty

The various asymmetry systematic error contributions are listed in this section. Actual asymmetry results are shown in Chap. 5. There, deuteron electrodisintegration tensor asymmetry data are plotted versus the missing momentum magnitude, p_M, and the cosine of the angle, $\cos\theta_M$, between the missing momentum vector and the deuteron polarization axis. Additionally, deuteron electrodisintegration beam-vector asymmetry data are also plotted versus the missing momentum magnitude.

The dominant sources of systematic error for the tensor asymmetry results plotted versus p_M are the uncertainty due to target spin angle determination (see Sec. 4.8.1) and the uncertainty due to determination of P_{zz} (see Sec. 4.8.2); both contributions

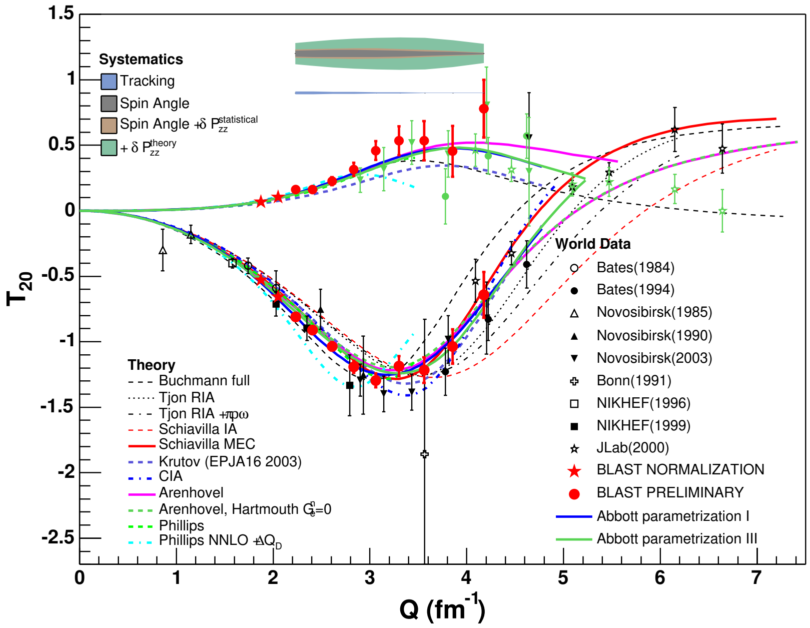

Figure 4-19: Plots of the elastic electron-deuteron T_{20} observable (bottom set of curves) and the T_{21} observable (top set of curves). The BLAST fitted data are in red; the Q bins used to extract the tensor polarization are in red stars. See [58] for a list of references for the various plotted models.

are of comparable magnitude[3]. The dominant source of systematic error for the tensor asymmetry results plotted versus $\cos\theta_M$ is the uncertainty due to the tensor polarization determination (see Sec. 4.8.2). Finally, the dominant source of systematic error for the beam-vector asymmetry results is the uncertainty due to reconstruction (see Sec. 4.8.3).

4.8.1 Spin Angle Uncertainty

Asymmetry results in general depend on the angle, θ_d, of target polarization. Any systematic shift or deviation between the actual target polarization angle and the value used in analysis thus leads to errors.

[3]In general, the amount of systematic error due to various contributions varies on a bin-by-bin basis. For this reason, it is difficult to quote one particular value or percentage effect for a systematic error for all bins. Instead, a complete listing of the numerical values for all of the asymmetries and their respective statistical and systematic error contributions for each plotted bin is shown in the Appendix.

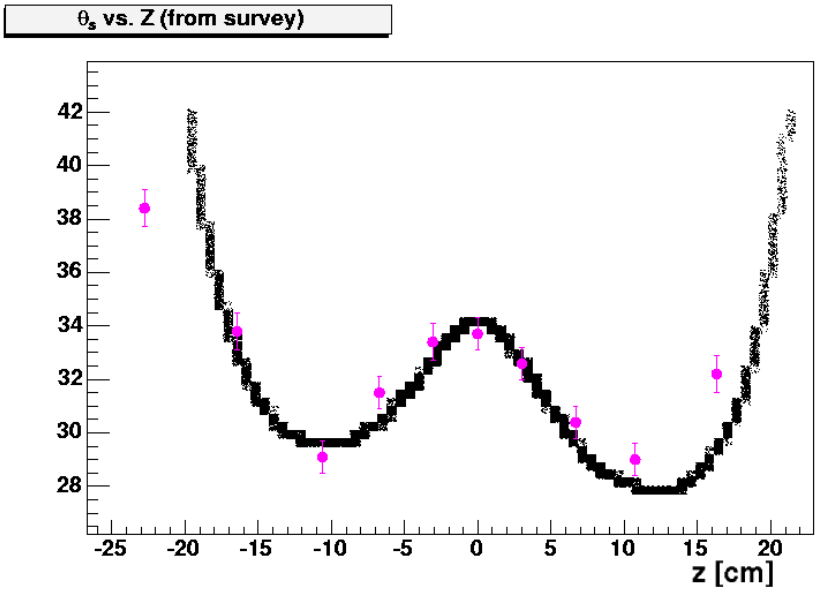

Figure 4-20: Target spin angle distribution versus the vertex position, z. The results of the survey of the holding field are shown in black; the corresponding results from the tensor asymmetry analysis are shown in magenta.

The target polarization angle is fixed by the holding field magnet along the target. Although the polarization angle was nominally set at 32° (relative to the direction of beam flow), variation with vertex position, z, exists on the order of a few degrees. For a more realistic polarization angle distribution, the target holding field was mapped with the BLAST toroid field on. A plot of the resulting polarization angle distribution is shown in Fig. 4-20.

The best analytical measurement of the target polarization angle comes from tensor polarization observables from concurrent elastic electron-deuteron scattering. The corresponding tensor asymmetry has opposite sign for events with electrons scattering into the left and right sectors. In this analysis, the target polarization angle was varied until the extracted tensor polarization, P_{zz}, was equal in both sectors. Using this method, the average deuteron polarization angle was found to be [58] $\theta_d = 31.4° \pm 1.0°$. This value is in good agreement with the average polarization angle value of $\theta_d = 31.32° \pm 0.51°$ extracted from the holding field measurements.

The estimated uncertainty in the target polarization angle is[4] $\sim 1°$. To quantify

[4] To be conservative, the uncertainty of 1° from the T_{20} analysis is assumed here as opposed to the 0.5° from the holding field map.

the systematic error in the various asymmetries as a result of this uncertainty, deviations in the asymmetries were studied by varying the average target polarization angle, as shown in Fig. 4-21. From the plots, the tensor asymmetry versus p_M is the most susceptible to spin angle errors.

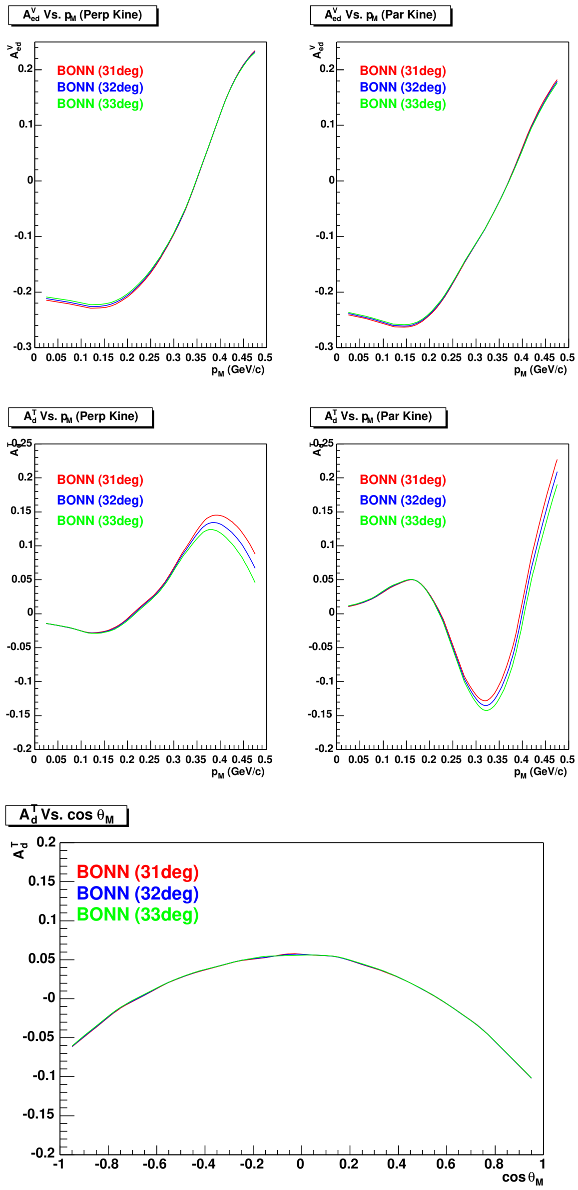

Figure 4-21: Target spin angle variation of the beam-vector asymmetry versus p_M (top), the tensor asymmetry versus p_M (middle), and the tensor asymmetry versus $\cos\theta_M$ (bottom). Average target spin angles of $\theta_D = 31°$, $32°$, and $33°$ are shown.

4.8.2 Target Polarization Uncertainty

Since all of the asymmetries of interest are normalized by either the beam-vector polarization, hP_z, or the tensor polarization, P_{zz}, it follows that any errors in these calculated values lead directly to errors in the calculated asymmetries. In particular, if the actual polarization value, P_A, is different from the calculated one, P_C, then the actual asymmetry, A_A, will differ from the calculated one, A_C, according to:

$$A_A = \frac{P_C}{P_A} A_C \tag{4.19}$$

The corresponding systematic error in the determination of the asymmetry due to the uncertainty in the polarization determination is thus:

$$(\%Err) = 100\% \cdot \frac{A_C - A_A}{A_C} = 100\% \cdot \frac{A_C - \frac{P_C}{P_A} A_C}{A_C} = 100\% \cdot \frac{P_A - P_C}{P_A} \tag{4.20}$$

From Sec. 4.7, the beam-vector polarization is found to be[5] $hP_z = 0.558 \pm 0.009$. Using $P_C = 0.558$ and $P_A = 0.558 + 0.009 = 0.567$, one finds that the systematic error due to uncertainty in hP_z is 1.6%. Similarly, since $P_{zz} = 0.680 \pm 0.062$, the systematic error due to the uncertainty in P_{zz} is 8.4%.

4.8.3 Reconstruction Uncertainty

Kinematic bin drift of data due to misreconstruction errors is a source of systematic error. In particular, kinematic drift in regions where the asymmetry either changes value rapidly or else has a change of sign is notably susceptible to kinematic misreconstruction.

To account for this drift, kinematic correction factors (see Sec. 4.3) were incorporated into the analysis. One noted deficiency, however, of these corrections is that they are derived in the quasi-elastic (QE) kinematic regime. At present, comprehensive kinematic corrections (i.e., QE and non-QE corrections) are not fully implemented

[5] The hP_z statistical and systematic error results from Sec. 4.7 were added in quadrature to obtain this total error.

into analyses. However, to the extent that the data are dominated by QE events, the currently-applied corrections can be expected to be adequate. An estimate of the effect of kinematic drift on the asymmetries is found from considering the change of the asymmetries with different kinematic correction factors in regimes with large asymmetry change and/or zero crossings. A conservative 3% contribution is placed on the systematic error contribution until a more comprehensive set of kinematic corrections can be implemented.

4.8.4 Radiative Correction Uncertainty

Radiative corrections account for corrections to the tree-level deuteron electrodisintegration Feynman diagram assumed in Chap. 1 where the incident or scattered electron radiates a real or virtual photon, thus changing the kinematics of the scattering. The radiated cross section, σ_R, can be expressed in terms of the unradiated one, σ_0, as follows [4]:

$$\sigma_R = (1+\delta)\,\sigma_0 + \sigma_1 \tag{4.21}$$

Here, δ is the factorized correction and σ_1 is the unfactorized bremsstrahlung contribution to the total cross section.

The factorized component, δ, has minimal influence on asymmetries. This can be seen by calculating the explicit form for the difference between radiated and unradiated asymmetries:

$$\begin{aligned}
\Delta A_R &= A_R - A_0 \\
&= \frac{(1+\delta)\,\sigma_0^p + \sigma_1^p}{(1+\delta)\,\sigma_0^u + \sigma_1^u} - \frac{\sigma_0^p}{\sigma_0^u} \\
&= \frac{\sigma_1^p\sigma_0^u - \sigma_0^p\sigma_1^u}{\sigma_0^u\left((1+\delta)\,\sigma_0^u + \sigma_1^u\right)}
\end{aligned} \tag{4.22}$$

where the "u" and "p" superscripts on the cross sections stand for "unpolarized" and "polarized", respectively. If one defines $\delta^{(u/p)} \equiv \sigma_1^{(u/p)}/\sigma_0^{(u/p)}$, then the relative difference between the radiated and unradiated asymmetries takes on the following

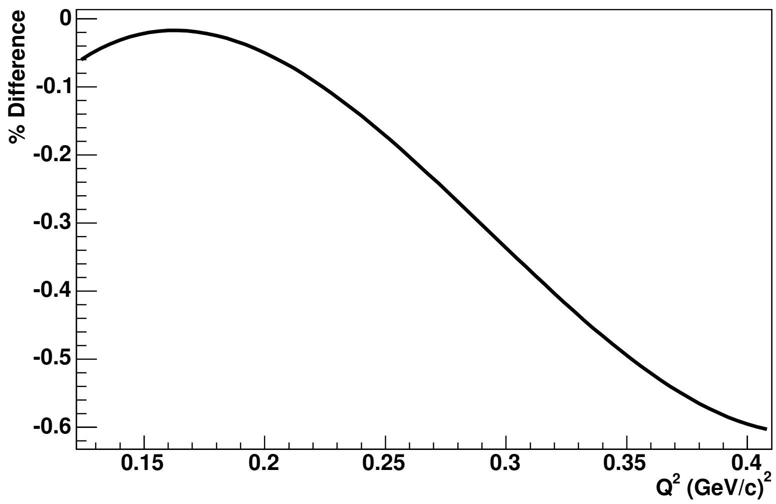

Figure 4-22: Plot of the relative difference between the radiated and unradiated elastic electron-proton asymmetries as a function of Q^2 [42]

simplified form:

$$\Delta_R \equiv \frac{\Delta A_R}{A_0} = \frac{\delta^p - \delta^u}{1 + \delta + \delta^u} \tag{4.23}$$

A plot of Δ_R versus Q^2 is shown in Fig. 4-22. The plot was generated using electron-proton elastic scattering with the MASCARAD code developed by Afanasev et al [3]. The results, however, are still applicable to QE scattering using deuterium. The difference between the radiated and unradiated asymmetries is $< 1\%$ over the entire Q^2 range. Thus, to the extent that QE events dominate the asymmetries, the radiative effects are expected to be negligible. However, until the effects of radiative corrections for both QE and non-QE reactions can be incorporated into the analysis, a conservative 1% contribution is placed on the radiative systematic uncertainty.

4.8.5 Cut Dependence Uncertainty

Cut dependence arises from possible enhancements of certain kinematic regions in which the desired asymmetries differ from the calculated ones. To study such dependence, asymmetries were extracted by imposing various missing mass cuts on the data. As discussed in Sec. 4.2.3, a resolution of $\sigma_{m_M} = 0.025$ GeV/c was found in plots of the missing mass. Comparisons of the various asymmetries of interest with respective cuts of $2\sigma_{m_M}$ and $3\sigma_{m_M}$ are shown in Fig. 4-23. One observes negligible dependence in the beam-vector asymmetry plots and in the tensor plots with respect to $\cos\theta_M$. In the tensor plots with respect to p_M, some variation is seen at high p_M. The variation, though, is smaller than the corresponding decrease in statistical uncertainty achieved in going from a $2\sigma_{m_M}$ to a $3\sigma_{m_M}$ cut.

4.8.6 False Asymmetry Uncertainty

As previously discussed in Chap. 1, the vector, beam, and beam-tensor deuteron electrodisintegration asymmetries (A_d^V, A_e, and A_{ed}^T, respectively) are all expected to be small. One possible reason why these asymmetries would not reconstruct to small values is incorrect assessment of the amount of collected charge in the various polarization states. Another reason is failure of the target deuterons to lie in states with equal vector or tensor polarization magnitudes[6], which is assumed when the target polarization states are rotated during data taking.

Plots of these three asymmetries are shown in Fig. 4-24 for 0.1 (GeV/c)^2 $< Q^2 <$ 0.2 (GeV/c)^2. All false asymmetries are observed to be small and consistent with zero. Similar trends are found in the higher Q^2 range data. The contribution to the uncertainty in the asymmetry determinations due to false asymmetries is thus small and estimated to be less than $\sim 1\%$.

[6]The target produces deuterons polarized in three (vector, tensor) states: $(-P_z, +P_{zz})$, $(+P_z, +P_{zz})$, and $(0, -2P_{zz})$. The magnitude of the vector polarization in the first two states is designed to be the same while the magnitude of the tensor polarzation in the third state is designed to be twice that of the first two.

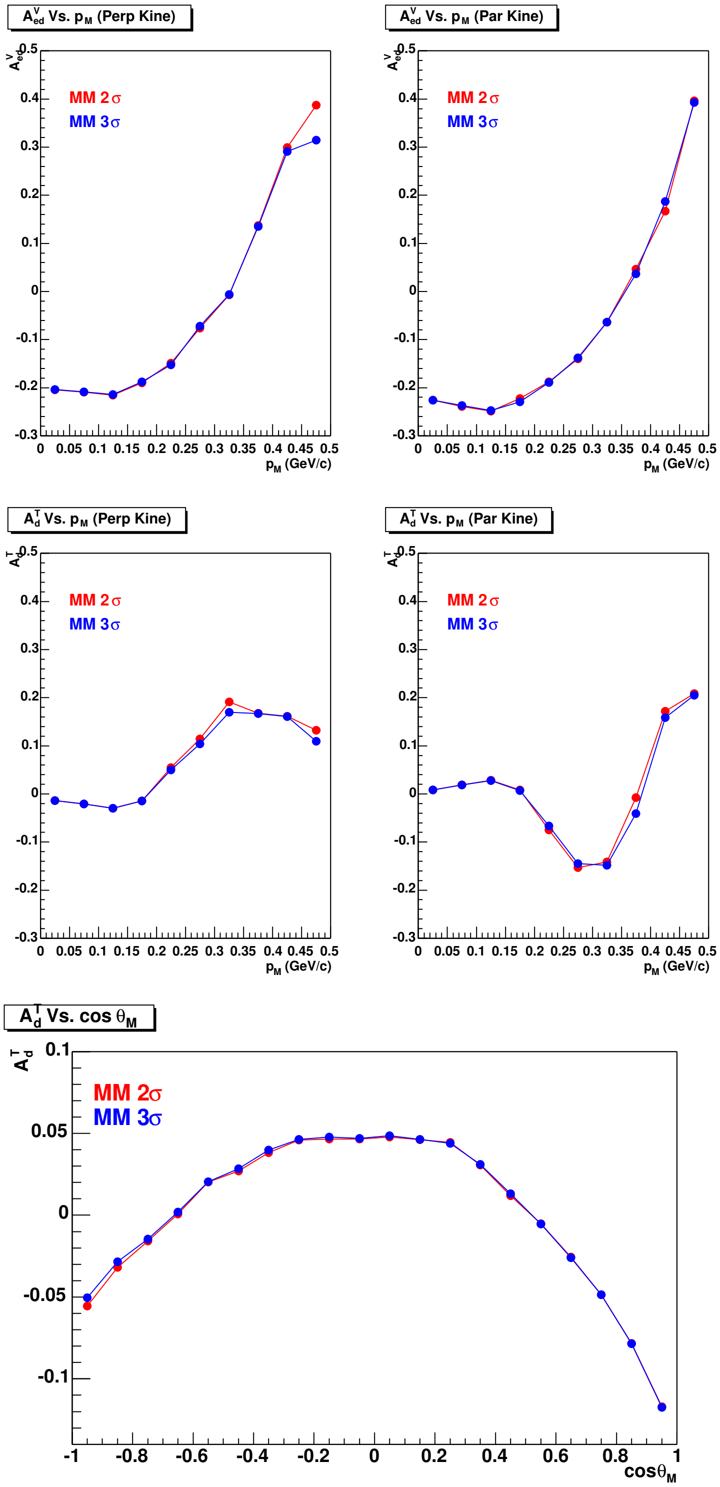

Figure 4-23: Missing mass cut variation of the beam-vector asymmetry versus p_M (top), the tensor asymmetry versus p_M (middle), and the tensor asymmetry versus $\cos\theta_M$ (bottom). As discussed in Sec. 4.2.3, $\sigma = 0.025$ GeV/c^2.

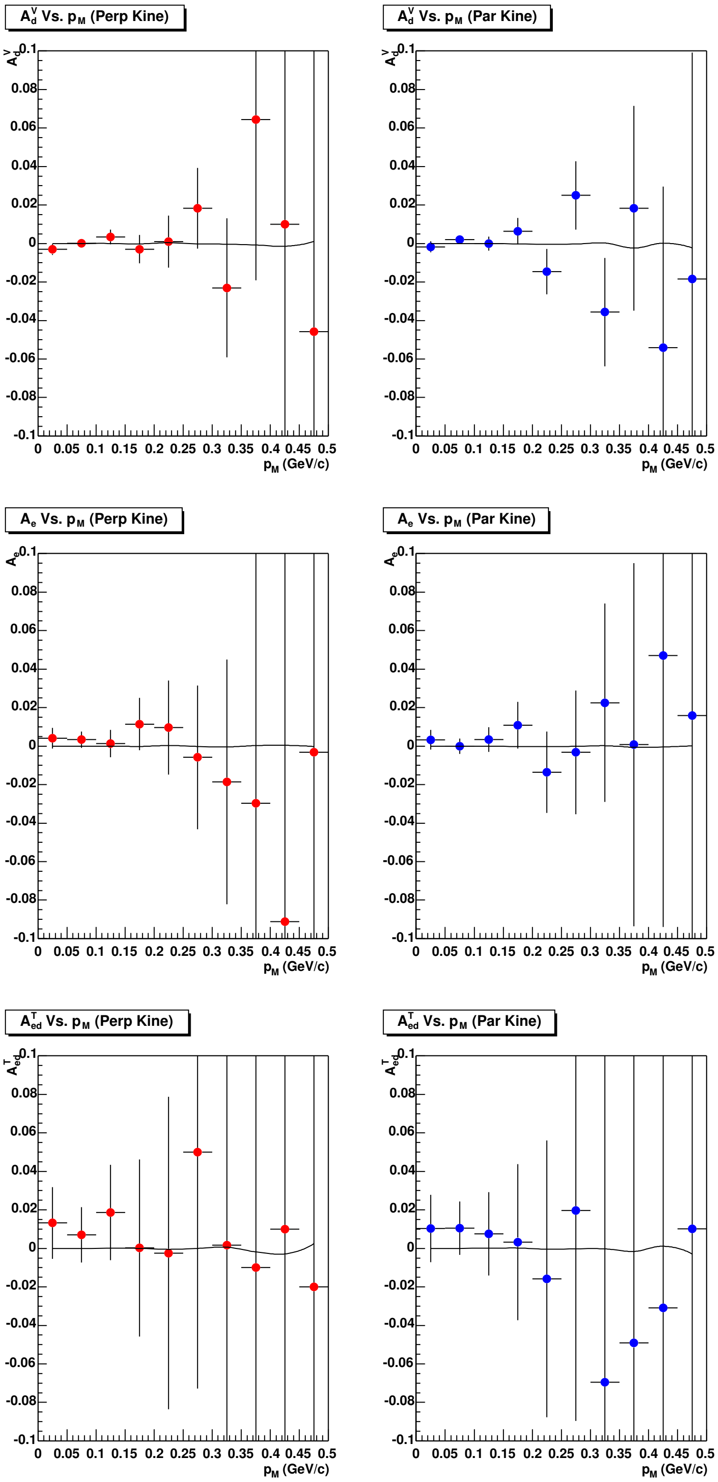

Figure 4-24: Plots of the calculated vector (top), beam (middle), and beam-tensor (bottom) asymmetries versus the missing momentum, p_M, for 0.1 $(\mathrm{GeV/c})^2 < Q^2 <$ 0.2 $(\mathrm{GeV/c})^2$. The solid lines are the corresponding Monte Carlo results.

Chapter 5

Results and Conclusions

5.1 Introduction

Results of measurements of the deuteron electrodisintegration tensor (A_d^T) and beam-vector (A_{ed}^V) asymmetries for a momentum transfer range of 0.1 (GeV/c)$^2 < Q^2 < 0.5$ (GeV/c)^2 are presented here. Tensor asymmetry results are plotted versus the missing momentum magnitude, p_M, and the cosine of the angle, $\cos\theta_M$, between the missing momentum vector and the deuteron polarization axis[1]. The beam-vector asymmetry is plotted versus the missing momentum magnitude, p_M. Numerical values for all of the data shown in this chapter can be found in the Appendix.

5.2 The Tensor Asymmetry, $\mathbf{A_d^T}$, Versus $\mathbf{p_M}$

Figs. 5-1 and 5-2 show tensor asymmetry results for the BLAST data plotted versus p_M for Q^2 ranges between 0.1 (GeV/c)^2 and 0.5 (GeV/c)^2. As discussed in Chap. 1, the perpendicular (parallel) heading in these plots refers to $^2\vec{H}(\vec{e}, e'p)n$ events where the detected electron is in the left (right) sector. Each graph also includes plots of the corresponding theoretical Monte Carlo predictions based on the Bonn potential [40, 41] in the formalism of Arenhövel et al. [6, 7]. The colored curves in these plots

[1] As shown in Chap. 1, it is possible in the PWIA to express the deuteron electrodisintegration tensor asymmetry completely in terms of these two variables.

correspond to successive contributions from various reaction mechanisms to the basic Bonn potential Plane Wave Born Approximation (BONN PWBA) model:

FSI	:	Final State Interactions
MEC	:	Meson Exchange Currents
IC	:	Iosbar Configurations
RC	:	Relativistic Contributions

The total Bonn potential model in these graphs corresponds to the "BONN PWBA + FSI + MEC + IC + RC" plot.

Figs. 5-3 and 5-4 show the tensor asymmetries versus p_M plotted along with various total potential models (i.e., potentials with all reaction mechanisms included). Three total potential models are plotted in these graphs: Bonn [40, 41], V18 [56], and Paris [32].

Finally, Figs. 5-5 and 5-6 show the residuals for each p_M bin of the reconstructed tensor asymmetry as compared with the total Bonn potential model. The residuals in these graphs are defined as the reconstructed asymmetry value minus that of the total Bonn potential model:

$$\Delta A^T_{d,BONN} \equiv A^T_{d,DATA} - A^T_{d,BONN} \tag{5.1}$$

Values of the corresponding residuals resulting from comparison with the total V18 and total Paris models, defined analogously, are listed in the Appendix[2]

[2]The variation between total potential models is not large in general; for conciseness and clarity, only the Bonn residual is shown here. However, numerical values for the residuals from all three models are listed in the Appendix.

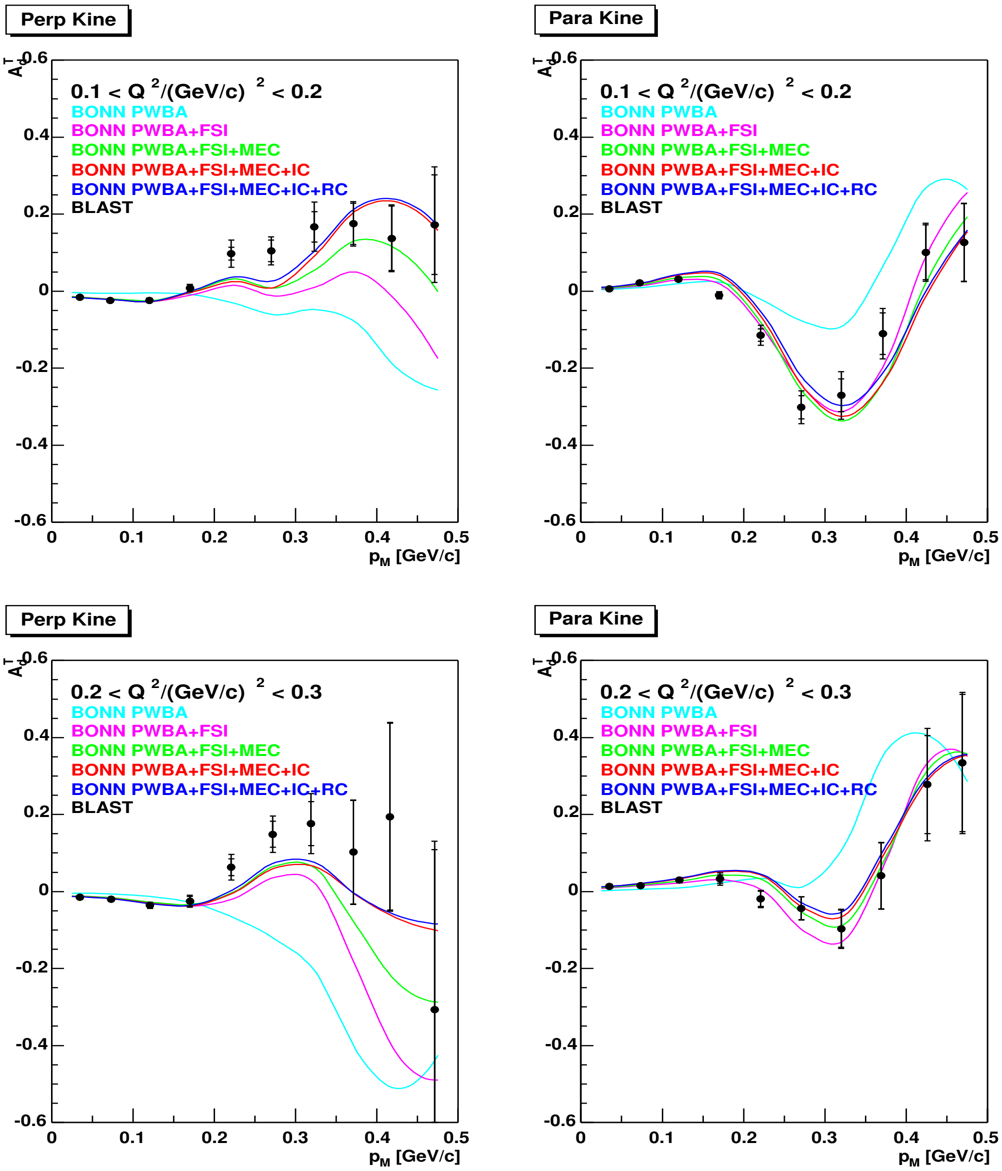

Figure 5-1: Plots of the reconstructed tensor asymmetry, A_d^T, versus the missing momentum, p_M, for perpendicular (left) and parallel (right) kinematics in BLAST. The top set of plots is for momentum transfers of 0.1 (GeV/c)^2 < Q^2 < 0.2 (GeV/c)^2; the bottom set is for 0.2 (GeV/c)^2 < Q^2 < 0.3 (GeV/c)^2. data are shown in black; the inner (outer) error bars on each data point correspond to the statistical (total) error for that point. Numerical values for all of the data shown are listed in the Appendix. The colored lines correspond to Monte Carlo plots of the tensor asymmetry using the Bonn potential with successively added-in contributions from the various reaction mechanisms. BONN PWBA = Bonn potential in the Plane Wave Born Approximation, FSI = Final State Interactions, MEC = Meson Exchange Currents, IC = Isobar Configurations, and RC = Relativistic Contributions. The total Bonn potential model (i.e., BONN PWBA + FSI + MEC + IC + RC) is shown in purple.

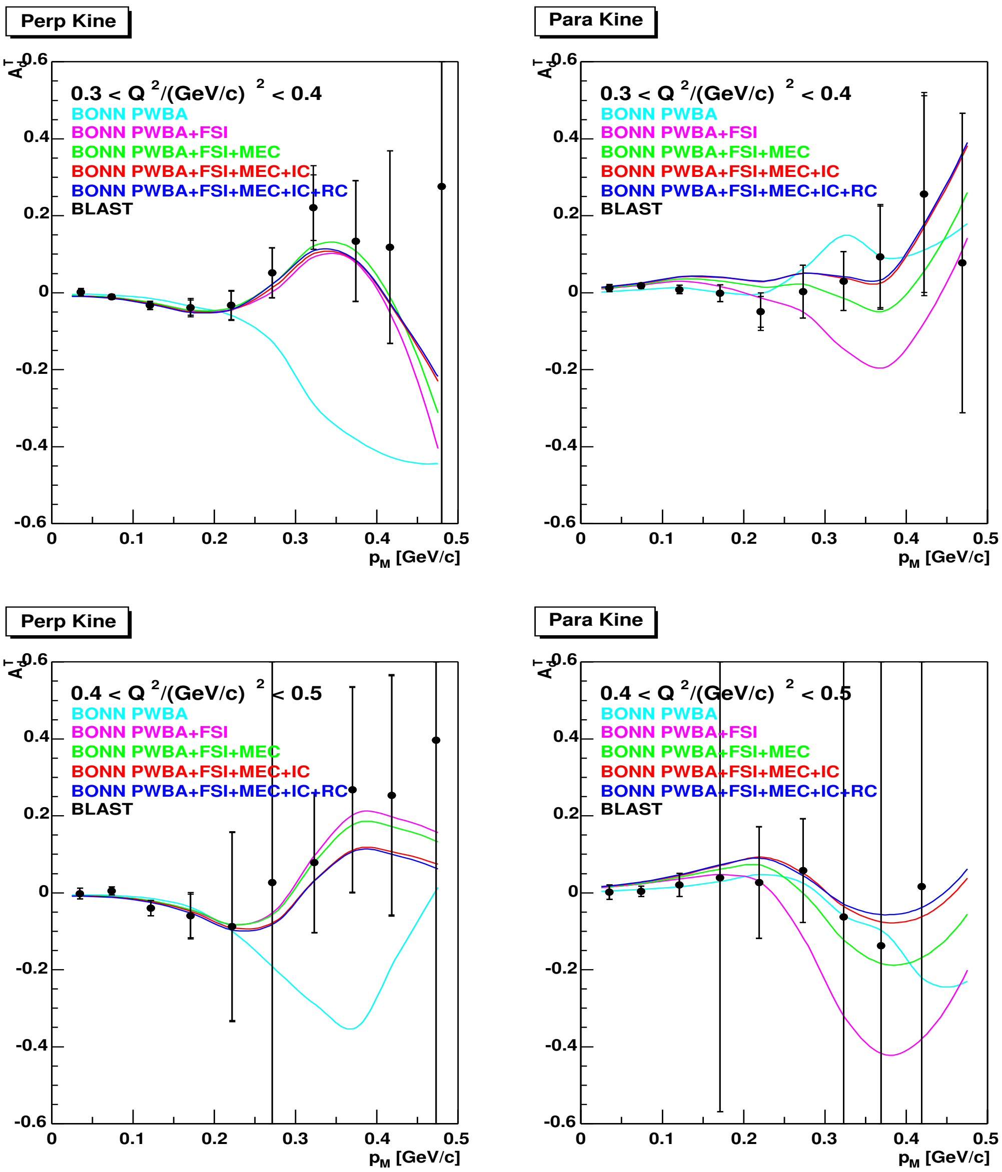

Figure 5-2: Plots of the reconstructed tensor asymmetry, A_d^T, versus the missing momentum, p_M, for perpendicular (left) and parallel (right) kinematics in BLAST. The top set of plots is for momentum transfers of 0.3 $(\mathrm{GeV/c})^2 < Q^2 <$ 0.4 $(\mathrm{GeV/c})^2$; the bottom set is for 0.4 $(\mathrm{GeV/c})^2 < Q^2 <$ 0.5 $(\mathrm{GeV/c})^2$. The setup of these plots is the same as that of Fig. 5-1.

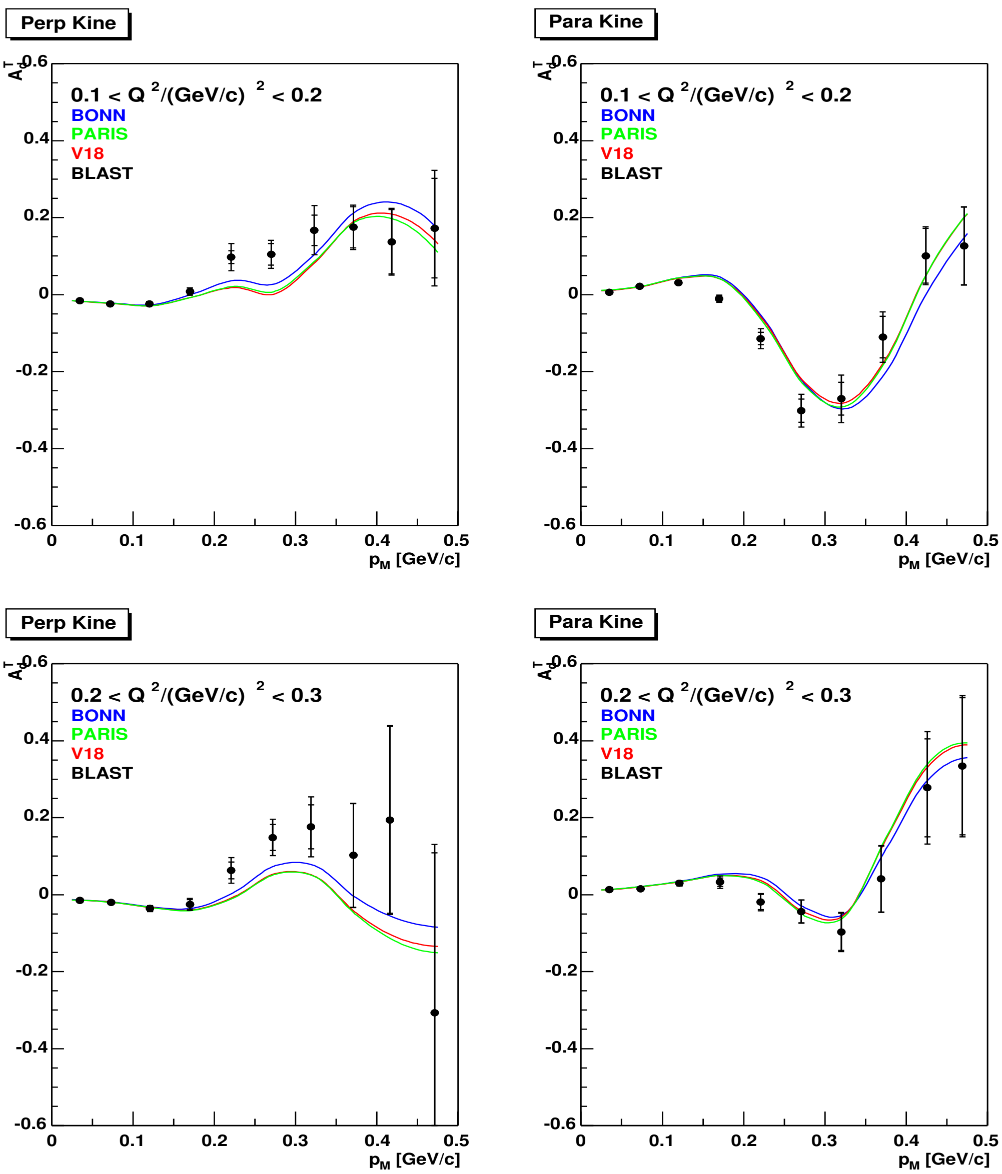

Figure 5-3: Plots of the reconstructed tensor asymmetry, A_d^T, versus the missing momentum, p_M, for perpendicular (left) and parallel (right) kinematics in BLAST. The top set of plots is for momentum transfers of 0.1 $(\mathrm{GeV/c})^2 < Q^2 <$ 0.2 $(\mathrm{GeV/c})^2$; the bottom set is for 0.2 $(\mathrm{GeV/c})^2 < Q^2 <$ 0.3 $(\mathrm{GeV/c})^2$. data are shown in black; the inner (outer) error bars on each data point correspond to the statistical (total) error for that point. Numerical values for all of the data shown are listed in the Appendix. The colored lines correspond to Monte Carlo plots of the tensor asymmetry from different potentials. BONN = Total Bonn potential, V18 = Total V18 potential, and PARIS = Total Paris potential, all including FSI, MEC, IC, and RC effects.

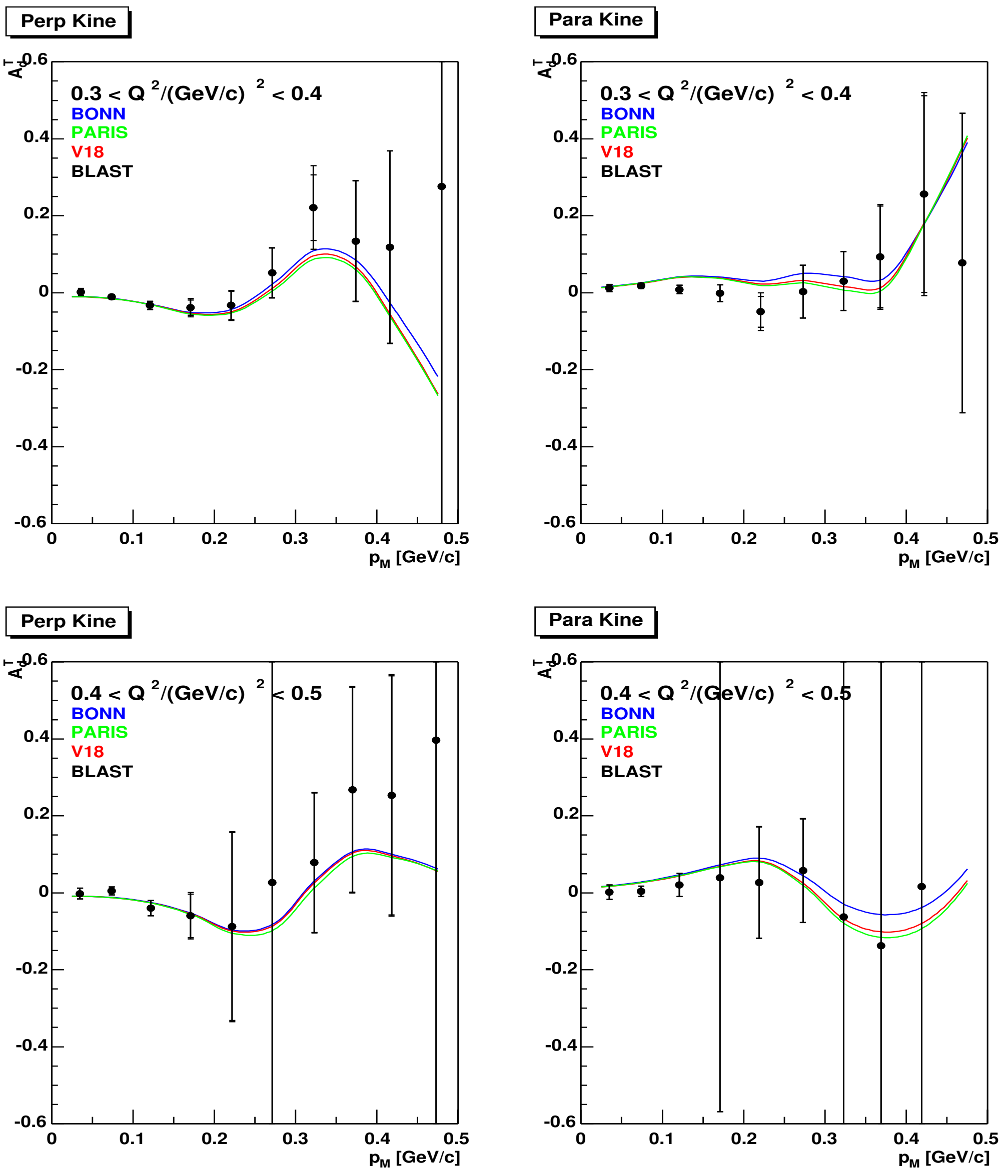

Figure 5-4: Plots of the reconstructed tensor asymmetry, A_d^T, versus the missing momentum, p_M, for perpendicular (left) and parallel (right) kinematics in BLAST. The top set of plots is for momentum transfers of 0.3 (GeV/c)^2 $< Q^2 <$ 0.4 (GeV/c)^2; the bottom set is for 0.4 (GeV/c)^2 $< Q^2 <$ 0.5 (GeV/c)^2. The setup of these plots is the same as that of Fig. 5-3.

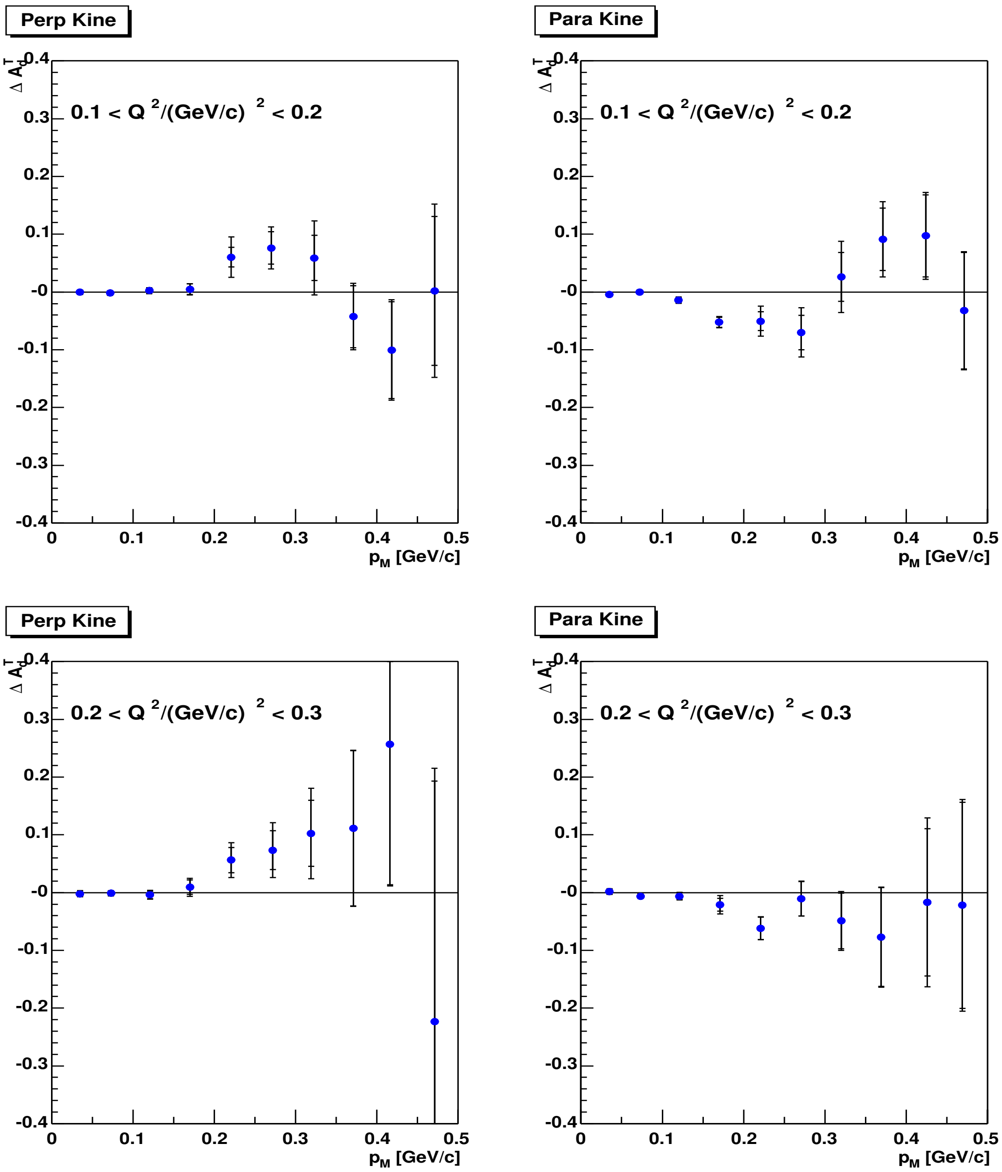

Figure 5-5: Plots of the residuals, ΔA_d^T, of the reconstructed tensor asymmetry, A_d^T, versus the missing momentum, p_M, for perpendicular (left) and parallel (right) kinematics in BLAST as compared with the total Bonn potential model. The top set of plots is for momentum transfers of 0.1 (GeV/c)^2 $< Q^2 <$ 0.2 (GeV/c)^2; the bottom set is for 0.2 (GeV/c)^2 $< Q^2 <$ 0.3 (GeV/c)^2.

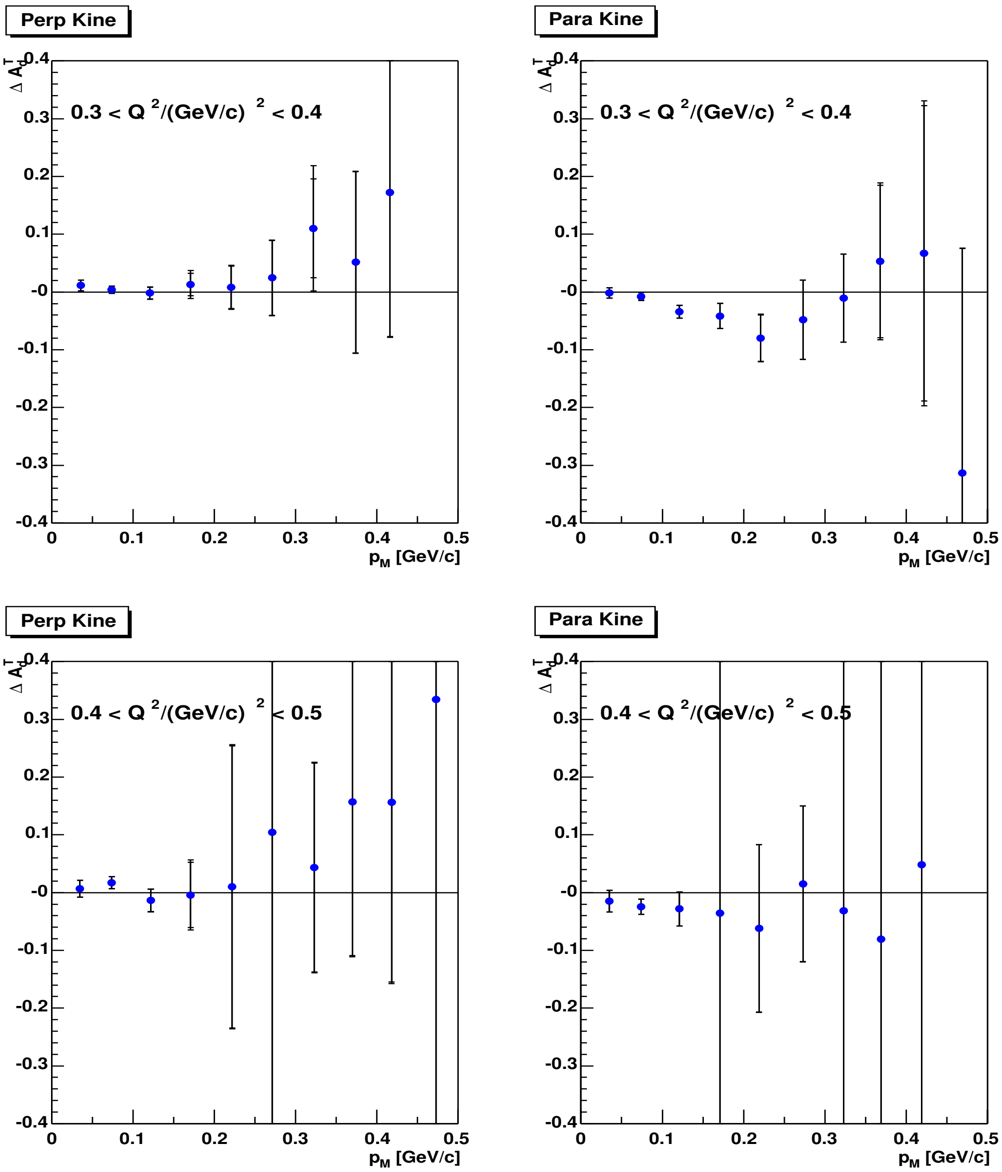

Figure 5-6: Plots of the residuals, ΔA_d^T, of the reconstructed tensor asymmetry, A_d^T, versus the missing momentum, p_M, for perpendicular (left) and parallel (right) kinematics in BLAST as compared with the total Bonn potential model. The top set of plots is for momentum transfers of 0.3 (GeV/c)$^2 < Q^2 <$ 0.4 (GeV/c)^2; the bottom set is for 0.4 (GeV/c)$^2 < Q^2 <$ 0.5 (GeV/c)^2.

5.2.1 Discussion of the Tensor Results Versus $\mathbf{p_M}$

The overall structure predicted by the (total) theoretical models is observed in the reconstructed asymmetries over nearly the entire p_M and Q^2 ranges analyzed. For each Q^2 range, the reconstructed asymmetries have small values at low p_M ($p_M < 0.2$ GeV/c); at larger p_M, the asymmetries' "peaks" and "troughs" (corresponding to perpendicular and parallel kinematics, respectively) are in overall consistent agreement with the theoretical predictions.

Figs. 5-1 and 5-2 support the necessity of including reaction mechanisms in theoretical analyses. The data are overall consistent with the total Bonn potential model results and inconsistent with the Bonn PWBA approximation ones. As seen most noticably in both of the perpendicular kinematics plots in Fig. 5-1, contributions due to FSI, MEC, and IC are significant at low Q^2. For this reason, realistic models of the various reaction mechanisms must be taken into account.

Figs. 5-3 and 5-4, which compare the data results to the three total potential models considered, indicate the onset of D-state structure at lower missing momenta ($\Delta p_M \sim 0.020$ GeV/c) than that predicted by the theories, particularly at low Q^2. All four of the plots in Fig. 5-3 show deviations between the data and theories in the 0.150 GeV/c $< p_M <$ 0.300 GeV/c range. The shift in the onset of D-state structure is supported most strongly by the $p_M = 0.170$ GeV/c reconstructed asymmetry point in the 0.1 (GeV/c)$^2 < Q^2 <$ 0.2 (GeV/c)^2 parallel kinematics plot (i.e., the top right plot in Fig. 5-3). This point lies $\sim 5\sigma$ below the theoretical prediction. As can be inferred from the plot, such a disagreement would be greatly diminished by a theory with D-state effects manifesting themselves at lower p_M. This statement is further supported by the remaining higher p_M data points in this plot which collectively show an overall shift of D-state effects as compared to theory.

χ^2 tests to the three total potential models considered in Figs. 5-3 and 5-4 are shown in Tab. 5.1. The (reduced) χ^2 values are determined according to [12]:

$$\chi^2/\text{d.o.f.} = \frac{\sum_i \frac{\left(A^T_{d,DATA,i} - A^T_{d,THEORY,i}\right)^2}{\sigma^2_{DATA,i}}}{n} \qquad (5.2)$$

Q^2 Range $(\mathrm{GeV/c})^2$	Perp Kine			Par Kine		
	χ^2_{BONN}	χ^2_{V18}	χ^2_{PARIS}	χ^2_{BONN}	χ^2_{V18}	χ^2_{PARIS}
$0.1 < Q^2 < 0.2$	0.981	1.651	1.490	4.565	3.714	3.794
$0.2 < Q^2 < 0.3$	0.981	1.477	1.547	1.465	1.169	1.165
$0.3 < Q^2 < 0.4$	0.394	0.516	0.573	1.869	1.601	1.615
$0.4 < Q^2 < 0.5$	0.404	0.427	0.430	0.512	0.433	0.454

Table 5.1: χ^2 fit values of the reconstructed tensor asymmetries versus p_M. Each χ^2 value was determined by comparing to one of the three total potential models considered: Bonn, V18, and Paris.

where $A^T_{d,DATA,i}$ and $A^T_{d,THEORY,i}$ are the respective reconstructed and theoretical asymmetry values for the ith bin, $\sigma_{DATA,i}$ is the uncertainty in the reconstructed asymmetry value for that bin, and n is the number of bins.

In perpendicular kinematics, reasonable χ^2 values near 1.0 are observed for low Q^2. The difference in χ^2 for the Bonn potential model and the other two models for this Q^2 range is primarily due to the asymmetry points at intermediate p_M (0.200 GeV/c $< p_M <$ 0.350 GeV/c) where the Bonn curve rises higher than the other two and thus produces a better agreement. At higher Q^2 in perpendicular kinematics, the excessively good χ^2 values ($\chi^2 \ll 1.0$) are associated with the large error bars in the data. More data as well as better systematics will help lower the errors and thus increase the predictive power here.

In parallel kinematics, relatively high χ^2 values are seen for the lowest Q^2 range; the other Q^2 ranges, however, produce reasonable χ^2 values overall. For parallel kinematics at the lowest Q^2 range (0.1 $(\mathrm{GeV/c})^2 < Q^2 <$ 0.2 $(\mathrm{GeV/c})^2$), a more thorough analysis shows that the resulting high χ^2 value is largely attributable to the previously-discussed measured asymmetry value at p_M = 0.170 GeV/c. The $\sim 5\sigma$ deviation of the theory from this point biases the χ^2-test for the entire asymmetry.

The residuals plots (Figs. 5-5 and 5-6) show basic agreement with theory at low p_M ($p_M <$ 0.150 GeV/c). At intermediate p_M (0.150 GeV/c$< p_M <$ 0.300 GeV/c), the data show an increase (decrease) in the theoretical predictions for perpendicular (parallel) kinematics, particularly at lower Q^2 (Fig. 5-5). At even higher p_M ($p_M >$ 0.3 GeV/c), this pattern reverses, and the data come into agreement with the theory again at the highest p_M values.

The proposed shift of D-state structure to lower p_M values is most noticeable in the lowest Q^2 parallel and perpendicular plots of the residuals (i.e., the left and right top plots in Fig. 5-5). Here, a clear oscillatory pattern exists in the residuals for $p_M > 0.150$ GeV/c. This oscillatory nature would be greatly diminished by such a shift of structure.

5.3 The Tensor Asymmetry, $\mathbf{A_d^T}$, Versus $\cos\theta_\mathbf{M}$

Figs. 5-7 and 5-8 show tensor asymmetry results for the BLAST data plotted versus $\cos\theta_M$ for Q^2 ranges between 0.1 (GeV/c)^2 and 0.5 (GeV/c)^2. Figs. 5-9 and 5-10 show the tensor asymmetry results along with only the total Bonn potential model[3]. Finally, Figs. 5-11 and 5-12 show the residuals between the reconstructed asymmetries and those predicted by the total Bonn potential model, as defined in (5.2).

[3]There is very little deviation between the three total potential models considered (i.e., Bonn, V18, and Paris) when plotted versus $\cos\theta_M$. For clarity, only the total Bonn potential model asymmetries are shown in these plots.

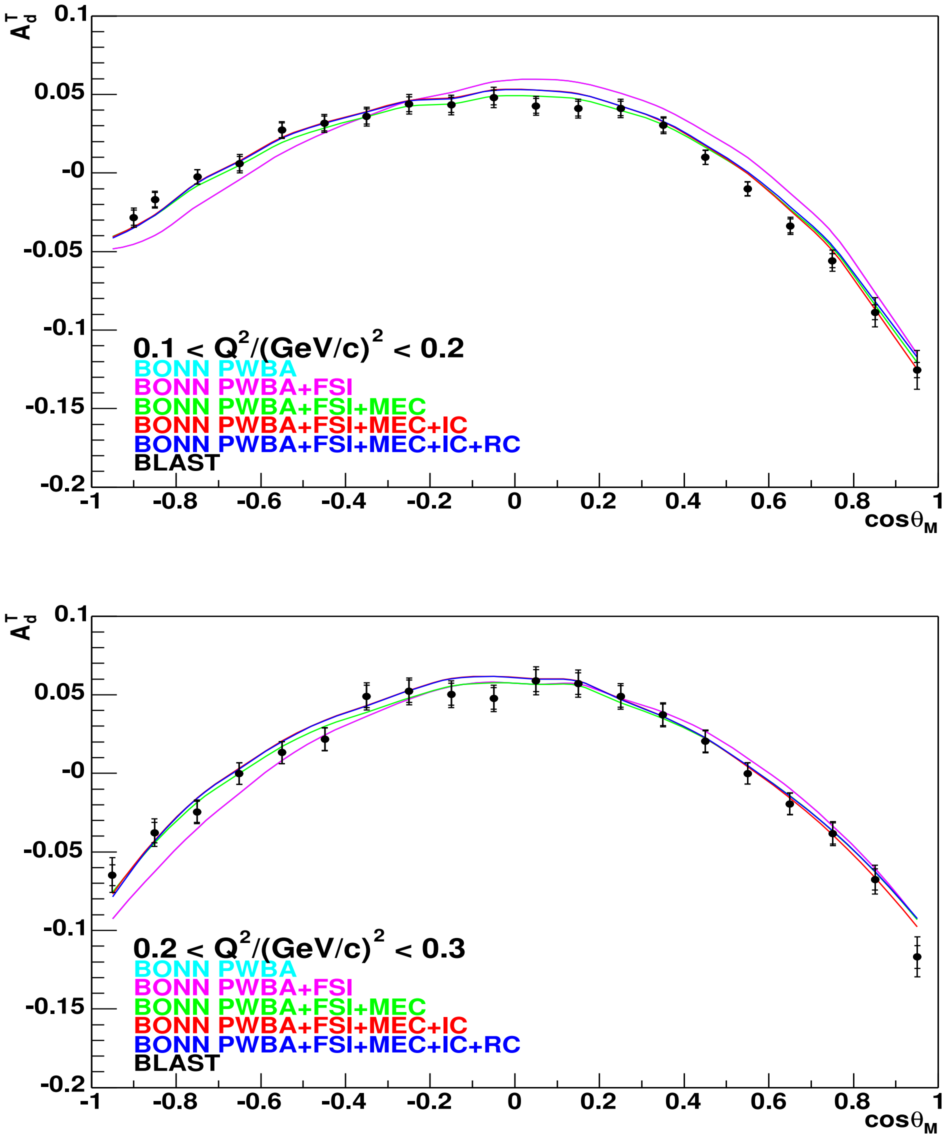

Figure 5-7: Plots of the reconstructed tensor asymmetry, A_d^T, versus $\cos\theta_M$ in BLAST. The top plot is for momentum transfers of 0.1 $(\mathrm{GeV/c})^2 < Q^2 < 0.2$ $(\mathrm{GeV/c})^2$; the bottom one is for 0.2 $(\mathrm{GeV/c})^2 < Q^2 < 0.3$ $(\mathrm{GeV/c})^2$. The setup of these plots is the same as that of Fig. 5-1.

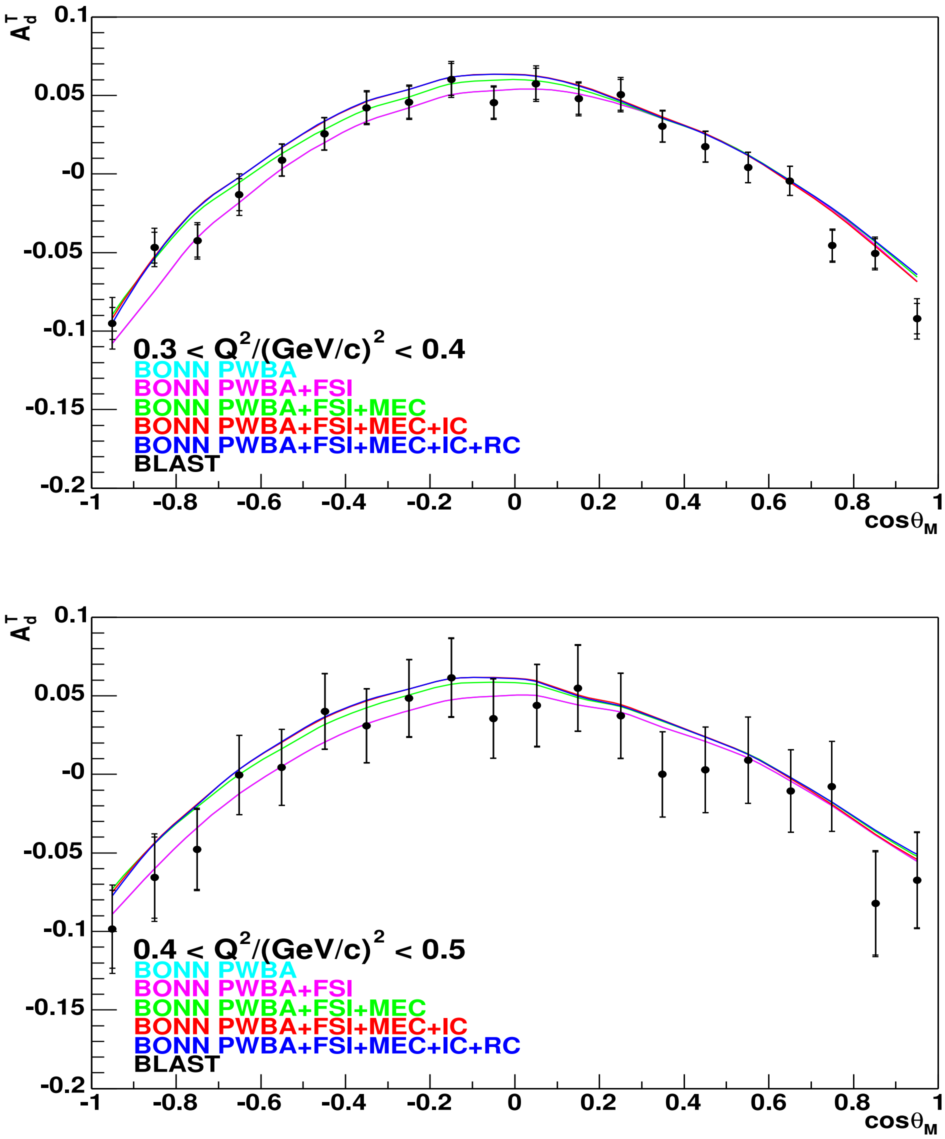

Figure 5-8: Plots of the reconstructed tensor asymmetry, A_d^T, versus $\cos\theta_M$ in BLAST. The top plot is for momentum transfers of 0.3 $(\mathrm{GeV/c})^2 < Q^2 <$ 0.4 $(\mathrm{GeV/c})^2$; the bottom one is for 0.4 $(\mathrm{GeV/c})^2 < Q^2 <$ 0.5 $(\mathrm{GeV/c})^2$. The setup of these plots is the same as that of Fig. 5-1.

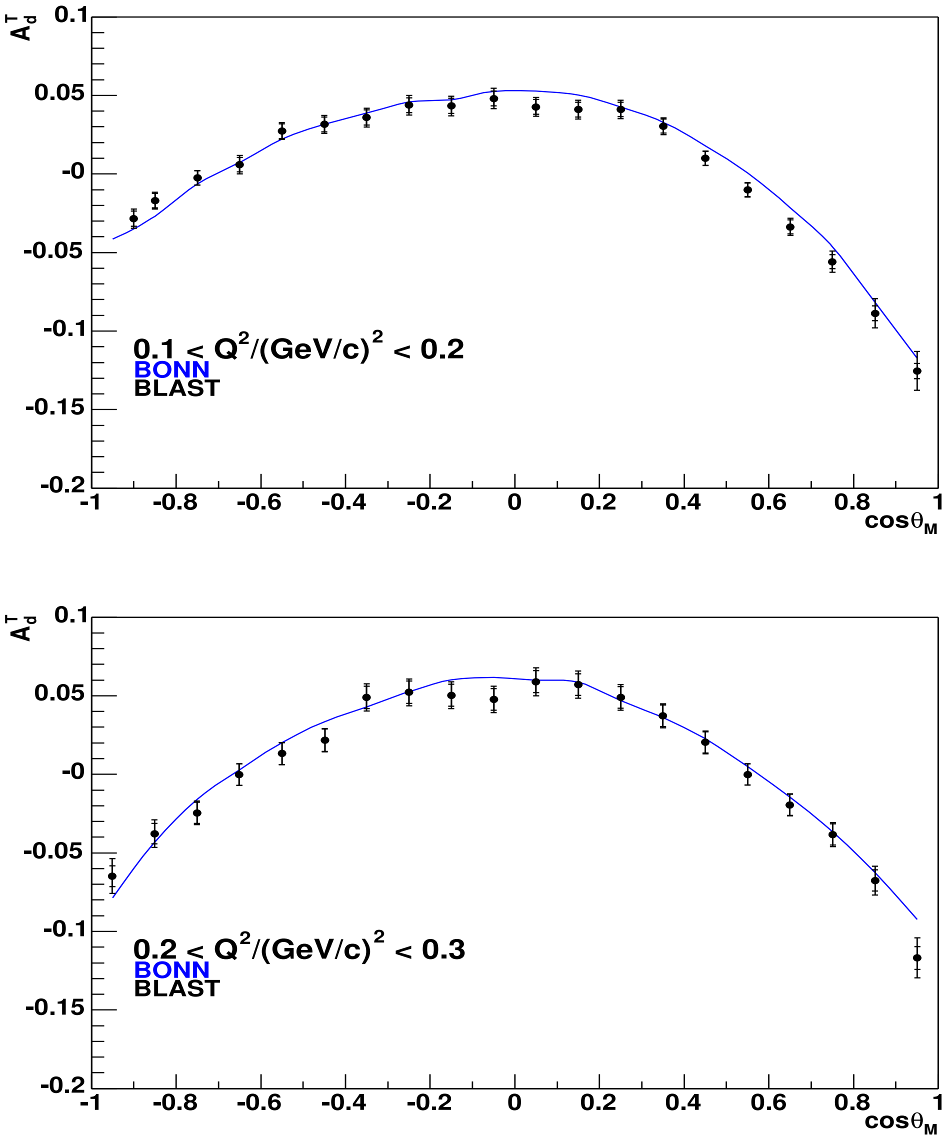

Figure 5-9: Plots of the reconstructed tensor asymmetry, A_d^T, versus $\cos\theta_M$ in BLAST. The top plot is for momentum transfers of 0.1 $(\mathrm{GeV/c})^2 < Q^2 < 0.2$ $(\mathrm{GeV/c})^2$; the bottom one is for 0.2 $(\mathrm{GeV/c})^2 < Q^2 < 0.3$ $(\mathrm{GeV/c})^2$. The setup of these plots is the same as that of Fig. 5-3.

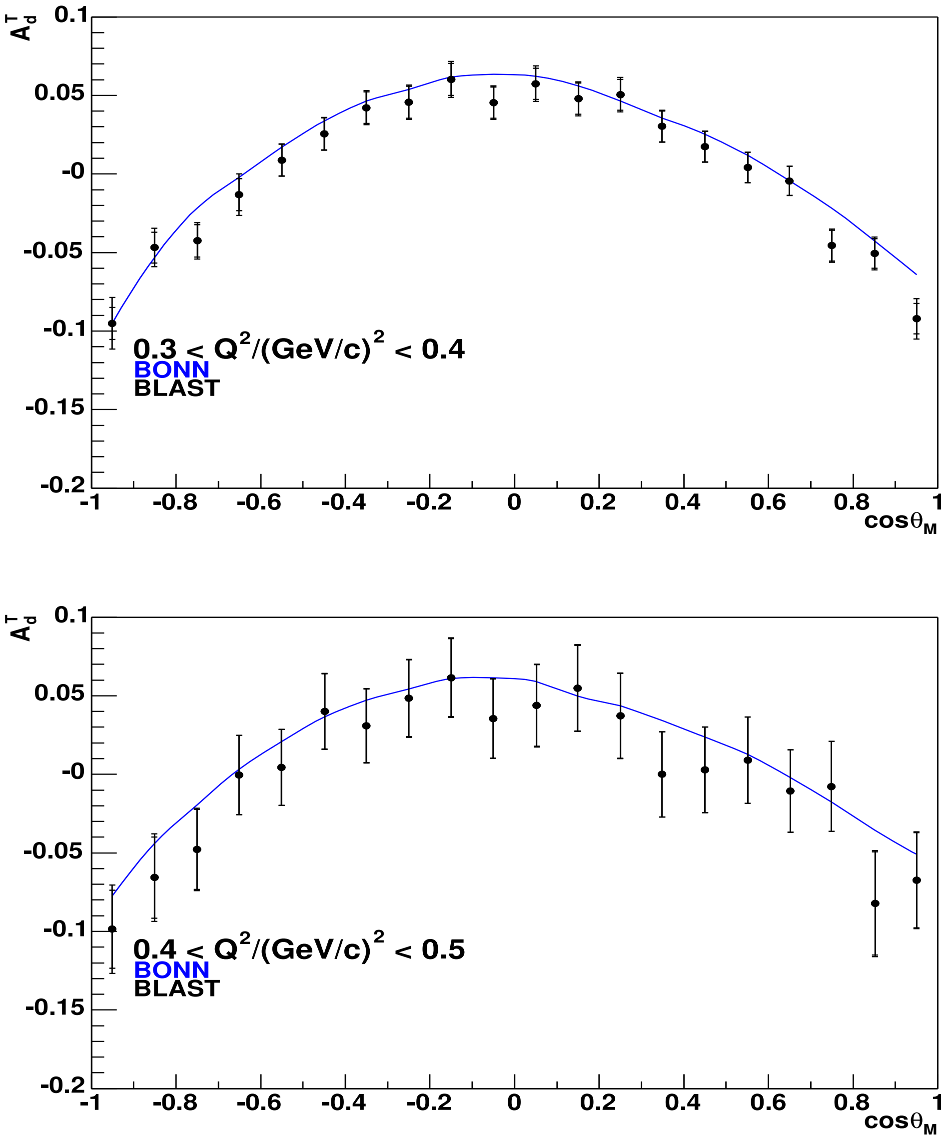

Figure 5-10: Plots of the reconstructed tensor asymmetry, A_d^T, versus $\cos\theta_M$ in BLAST. The top plot is for momentum transfers of 0.3 $(\mathrm{GeV/c})^2 < Q^2 < 0.4$ $(\mathrm{GeV/c})^2$; the bottom one is for 0.4 $(\mathrm{GeV/c})^2 < Q^2 < 0.5$ $(\mathrm{GeV/c})^2$. The setup of these plots is the same as that of Fig. 5-3.

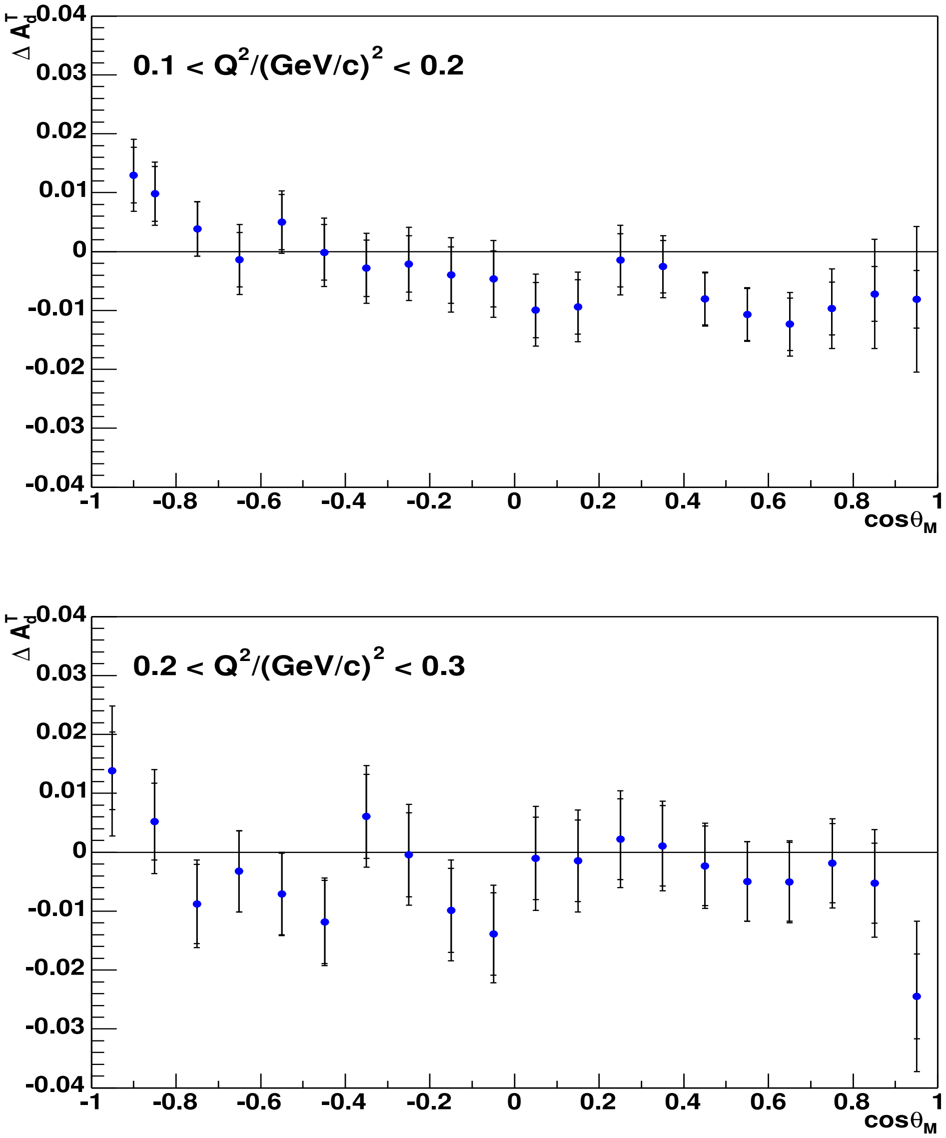

Figure 5-11: Plots of the residuals, ΔA_d^T, of the reconstructed tensor asymmetry, A_d^T, versus $\cos\theta_M$ in BLAST as compared with the total Bonn potential model. The top plot is for momentum transfers of 0.1 $(\mathrm{GeV/c})^2 < Q^2 <$ 0.2 $(\mathrm{GeV/c})^2$; the bottom one is for 0.2 $(\mathrm{GeV/c})^2 < Q^2 <$ 0.3 $(\mathrm{GeV/c})^2$.

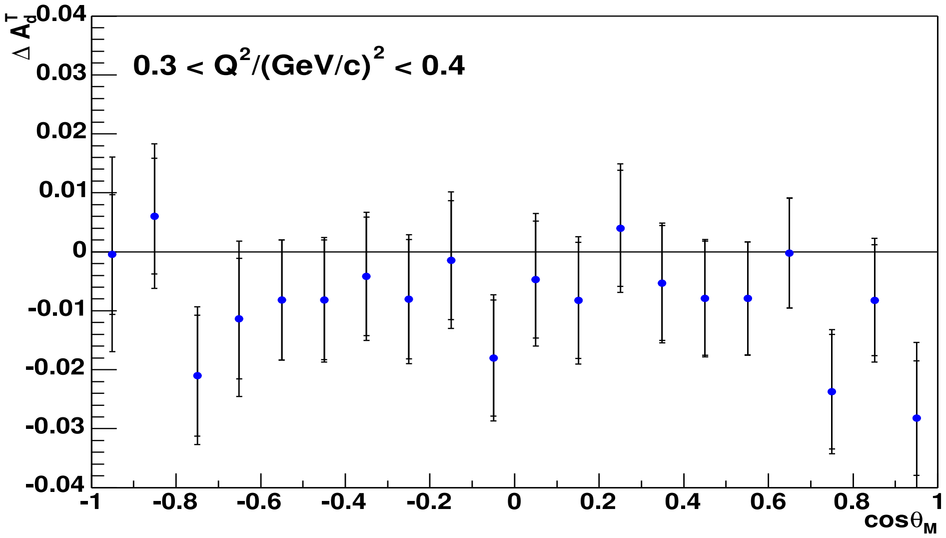

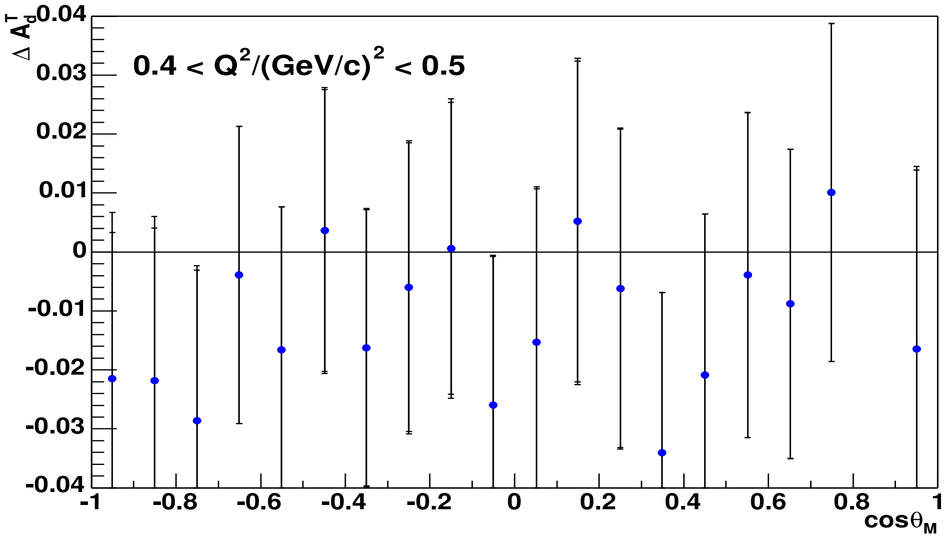

Figure 5-12: Plots of the residuals, ΔA_d^T, of the reconstructed tensor asymmetry, A_d^T, versus $\cos\theta_M$ in BLAST as compared with the total Bonn potential model. The top plot is for momentum transfers of 0.3 (GeV/c)^2 $< Q^2 <$ 0.4 (GeV/c)^2; the bottom one is for 0.4 (GeV/c)^2 $< Q^2 <$ 0.5 (GeV/c)^2.

Q^2 Range $(\mathrm{GeV/c})^2$	χ^2_{BONN}
$0.1 < Q^2 < 0.2$	1.652
$0.2 < Q^2 < 0.3$	0.853
$0.3 < Q^2 < 0.4$	1.100
$0.4 < Q^2 < 0.5$	0.476

Table 5.2: χ^2 fit values of the reconstructed tensor asymmetries versus $\cos\theta_M$. Each χ^2 value was determined by comparing to the total Bonn potential model.

5.3.1 Discussion of the Tensor Results Versus $\cos\theta_\mathbf{M}$

The reconstructed tensor asymmetries versus $\cos\theta_M$ are consistent with the total Bonn potential model over nearly all of the $\cos\theta_M$ and Q^2 ranges analyzed. The only significant disagreement between the data and theory is at $0.0 < \cos\theta_M < 0.6$ for $0.1\ (\mathrm{GeV/c})^2 < Q^2 < 0.2\ (\mathrm{GeV/c})^2$, where the data show slightly smaller asymmetry values in general than what the theory predicts.

These plots once again support the necessity of including reaction mechanism contributions in theoretical analyses. In particular, for the lowest two Q^2 ranges (i.e., the top and bottom plots in Fig. 5-7), the data are seen to be consistent with the total Bonn potential model at $\cos\theta_M < -0.4$. The meson exchange current (MEC) contribution in this region is significant; without including the contribution from this reaction mechanism, the data would be significantly larger than the theoretical prediction.

Reduced χ^2 test values are shown in Tab. 5.2. Reasonable χ^2 values are achieved overall; the relatively large χ^2 value for $0.1\ (\mathrm{GeV/c})^2 < Q^2 < 0.2\ (\mathrm{GeV/c})^2$ is due to the previously-mentioned disagreement between the data and theory for $0.0 < \cos\theta_M < 0.6$. However, in general, the total Bonn potential model appears to be a consistent predictor of the deuteron electrodisintegration tensor asymmetry with respect to $\cos\theta_M$ over the Q^2 ranges considered here.

5.4 The Beam-Vector Asymmetry, $\mathbf{A^V_{ed}}$, Versus $\mathbf{p_M}$

Figs. 5-13 and 5-14 show beam-vector asymmetry results for the BLAST data plotted versus p_M for Q^2 ranges between 0.1 and 0.5 $(\mathrm{GeV/c})^2$. Figs. 5-15 and 5-16 show the beam-vector asymmetry results along with the total Bonn, V18, and Paris models. Finally, Figs. 5-17 and 5-18 show the residuals between the reconstructed asymmetries and those predicted by the total Bonn potential model, as defined in (5.2).

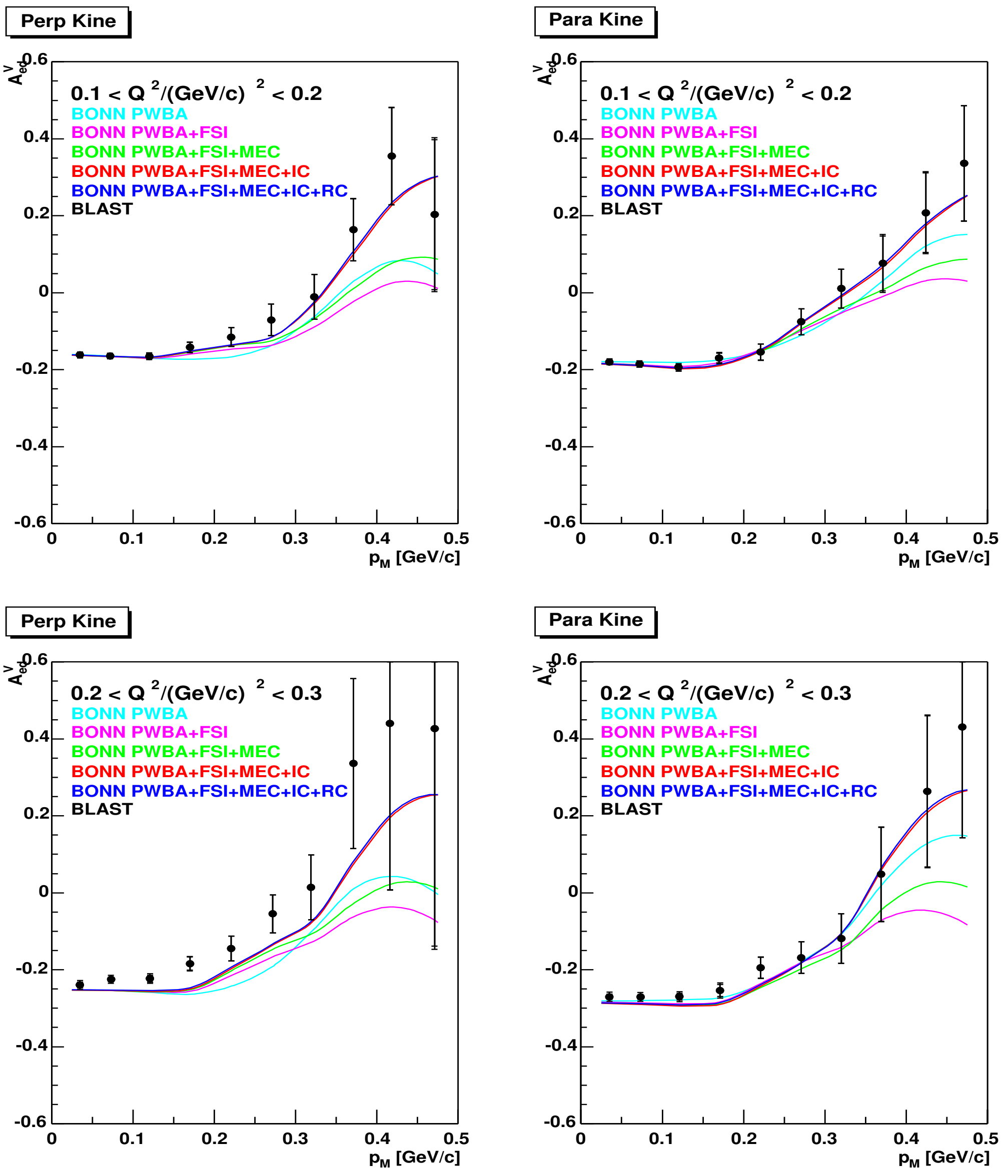

Figure 5-13: Plots of the reconstructed beam-vector asymmetry, A_{ed}^{T}, versus the missing momentum, p_M, for perpendicular (left) and parallel (right) kinematics in BLAST. The top set of plots is for momentum transfers of 0.1 (GeV/c)$^2 < Q^2 <$ 0.2 (GeV/c)^2; the bottom set is for 0.2 (GeV/c)$^2 < Q^2 <$ 0.3 (GeV/c)^2. The setup of these plots is the same as that of Fig. 5-1

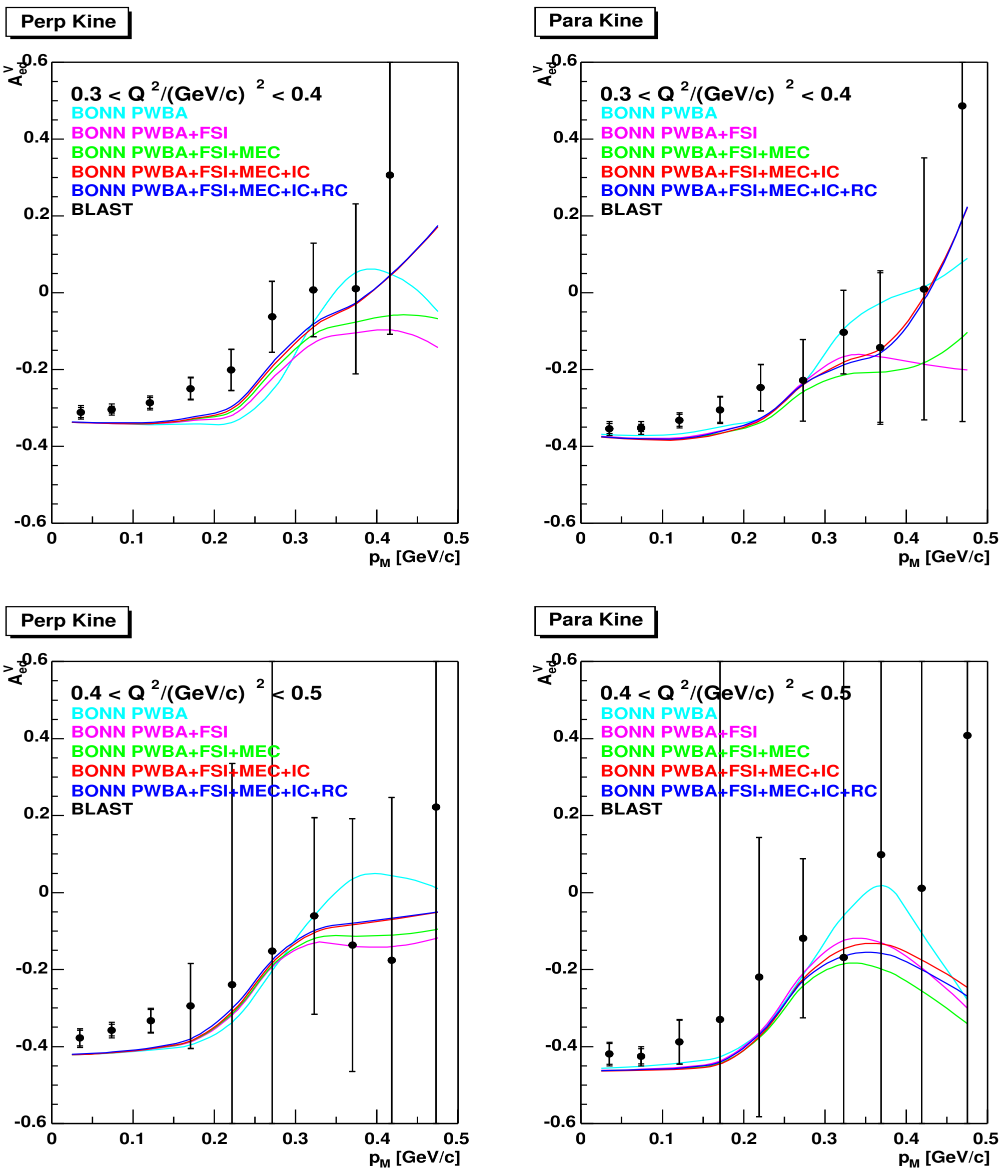

Figure 5-14: Plots of the reconstructed beam-vector asymmetry, A^T_{ed}, versus the missing momentum, p_M, for perpendicular (left) and parallel (right) kinematics in BLAST. The top set of plots is for momentum transfers of 0.3 (GeV/c)^2 < Q^2 < 0.4 (GeV/c)^2; the bottom set is for 0.4 (GeV/c)^2 < Q^2 < 0.5 (GeV/c)^2. The setup of these plots is the same as that of Fig. 5-1.

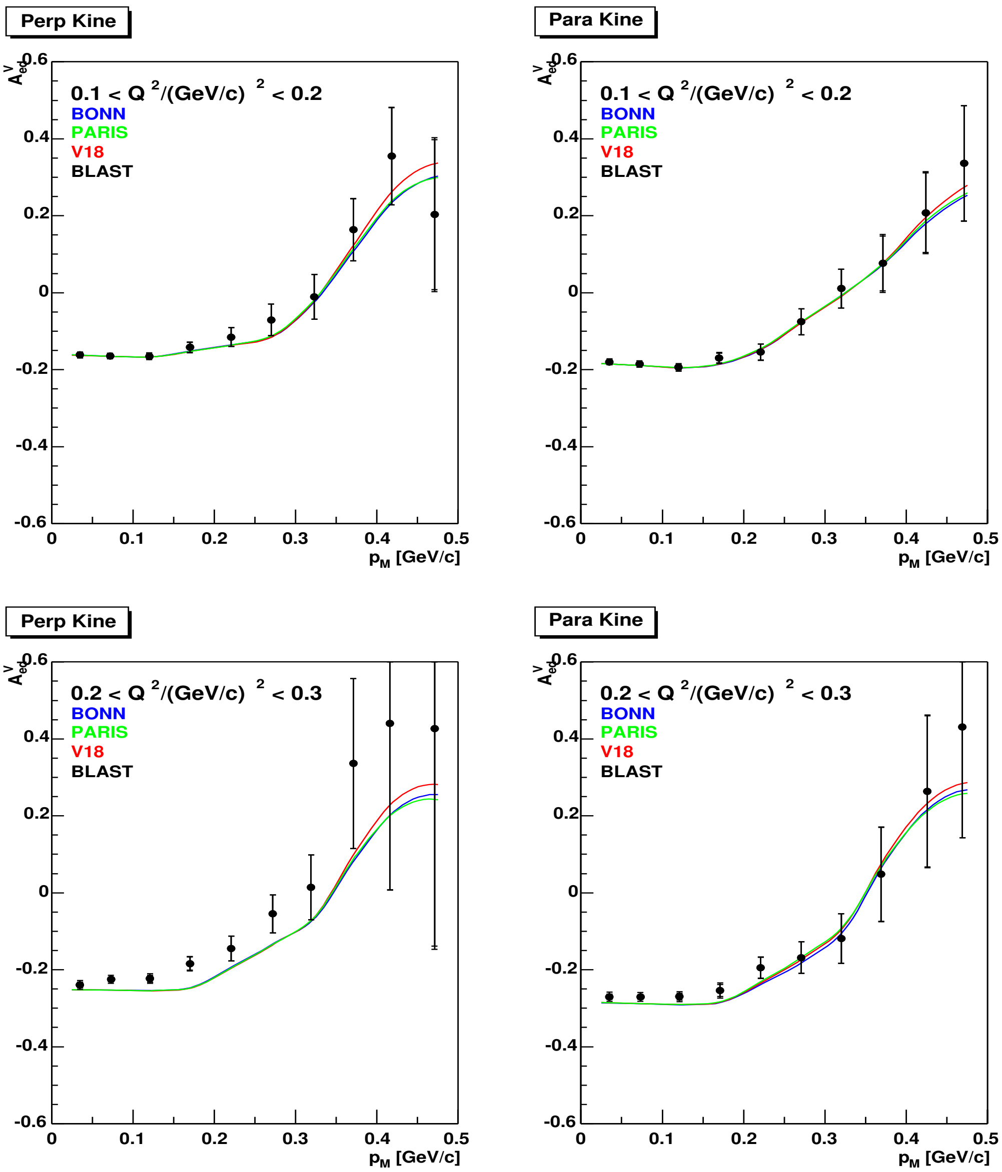

Figure 5-15: Plots of the reconstructed beam-vector asymmetry, A^T_{ed}, versus the missing momentum, p_M, for perpendicular (left) and parallel (right) kinematics in BLAST. The top set of plots is for momentum transfers of 0.1 (GeV/c)^2 < Q^2 < 0.2 (GeV/c)^2; the bottom set is for 0.2 (GeV/c)^2 < Q^2 < 0.3 (GeV/c)^2. The setup of these plots is the same as that of Fig. 5-1.

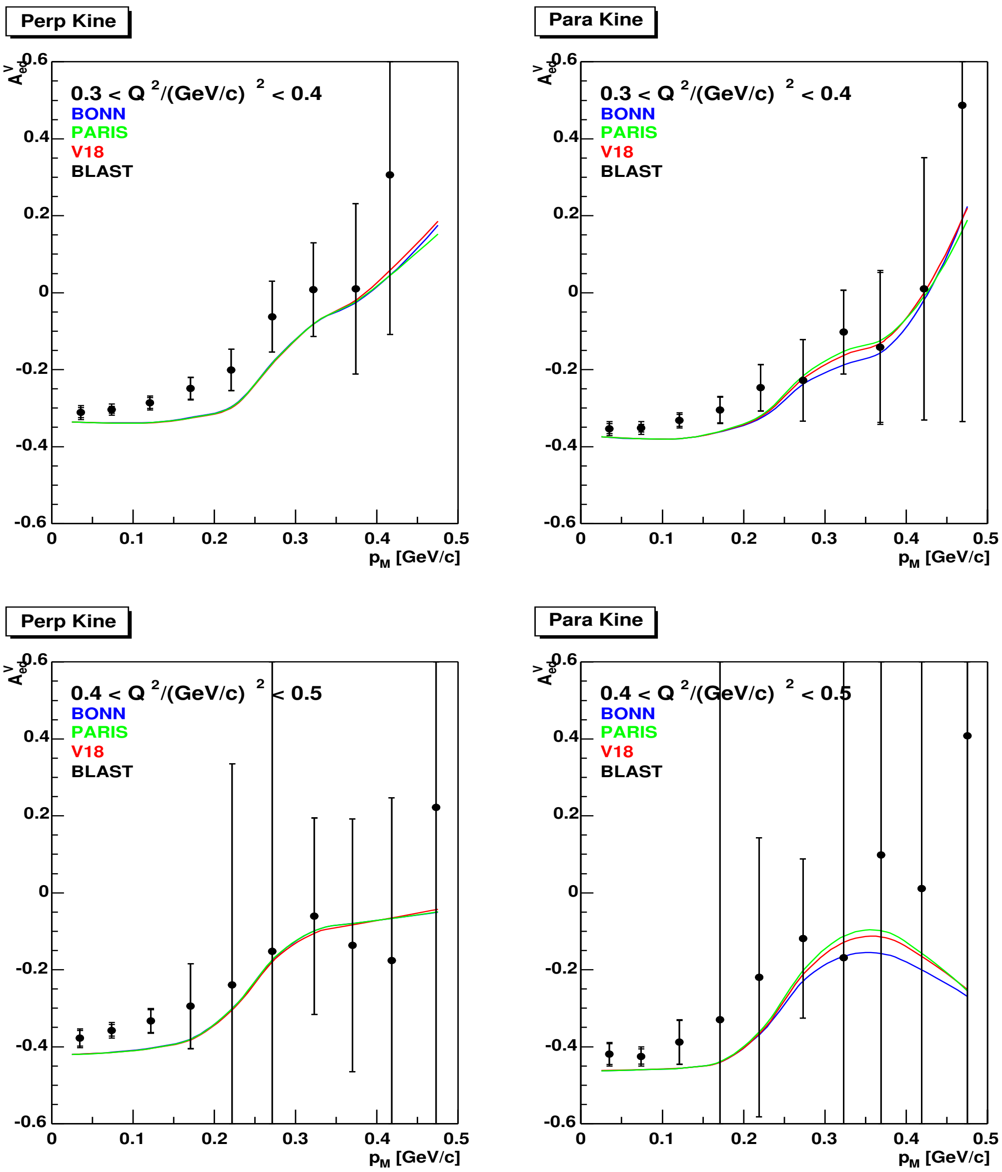

Figure 5-16: Plots of the reconstructed beam-vector asymmetry, A_{ed}^{T}, versus the missing momentum, p_M, for perpendicular (left) and parallel (right) kinematics in BLAST. The top set of plots is for momentum transfers of 0.3 $(\mathrm{GeV/c})^2 < Q^2 < 0.4$ $(\mathrm{GeV/c})^2$; the bottom set is for 0.4 $(\mathrm{GeV/c})^2 < Q^2 < 0.5$ $(\mathrm{GeV/c})^2$. The setup of these plots is the same as that of Fig. 5-3.

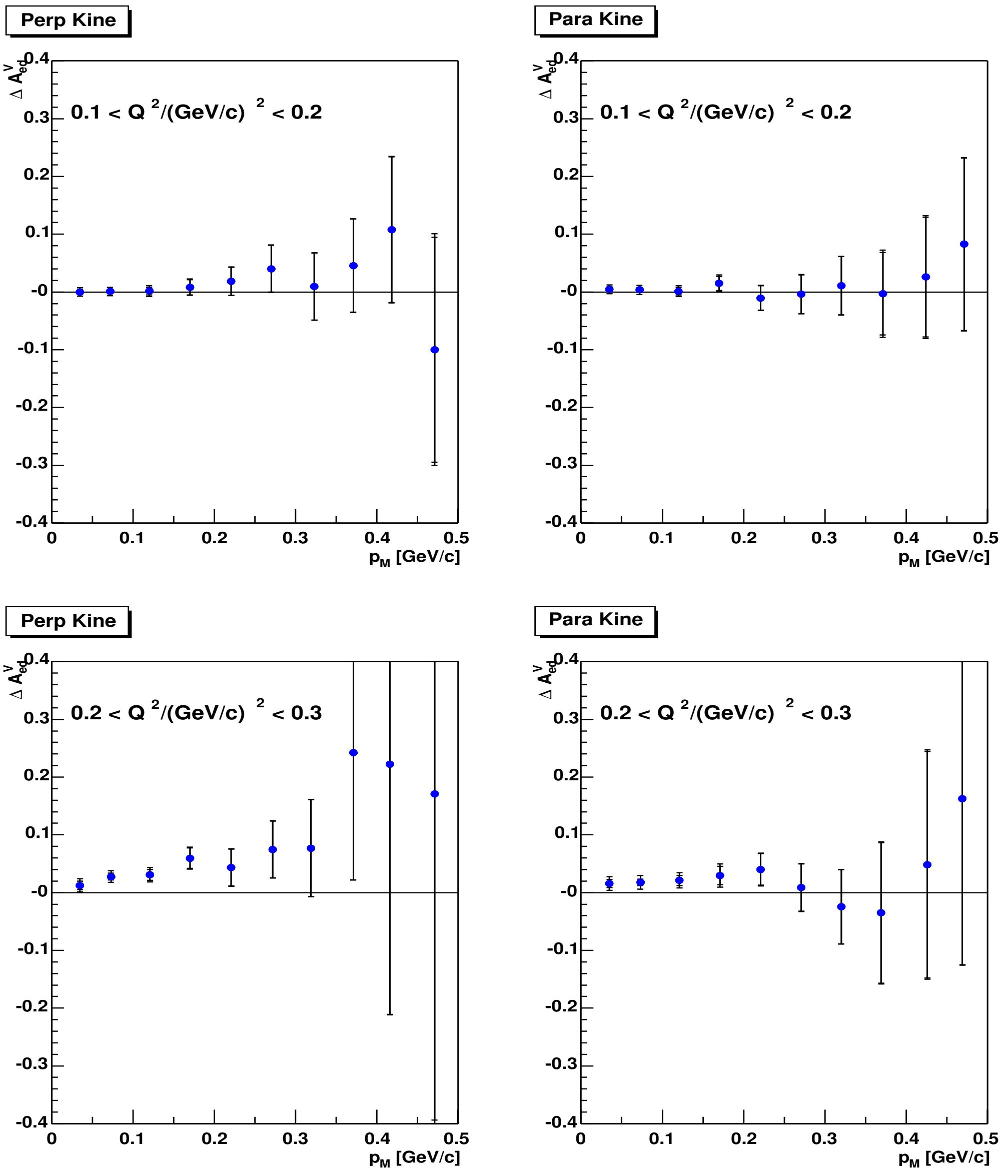

Figure 5-17: Plots of the residuals, ΔA_{ed}^{V}, of the reconstructed beam-vector asymmetry, A_{ed}^{T}, versus the missing momentum, p_M, for perpendicular (left) and parallel (right) kinematics in BLAST as compared with the total Bonn potential model. The top set of plots is for momentum transfers of 0.1 (GeV/c)^2 $< Q^2 <$ 0.2 (GeV/c)^2; the bottom set is for 0.2 (GeV/c)^2 $< Q^2 <$ 0.3 (GeV/c)^2.

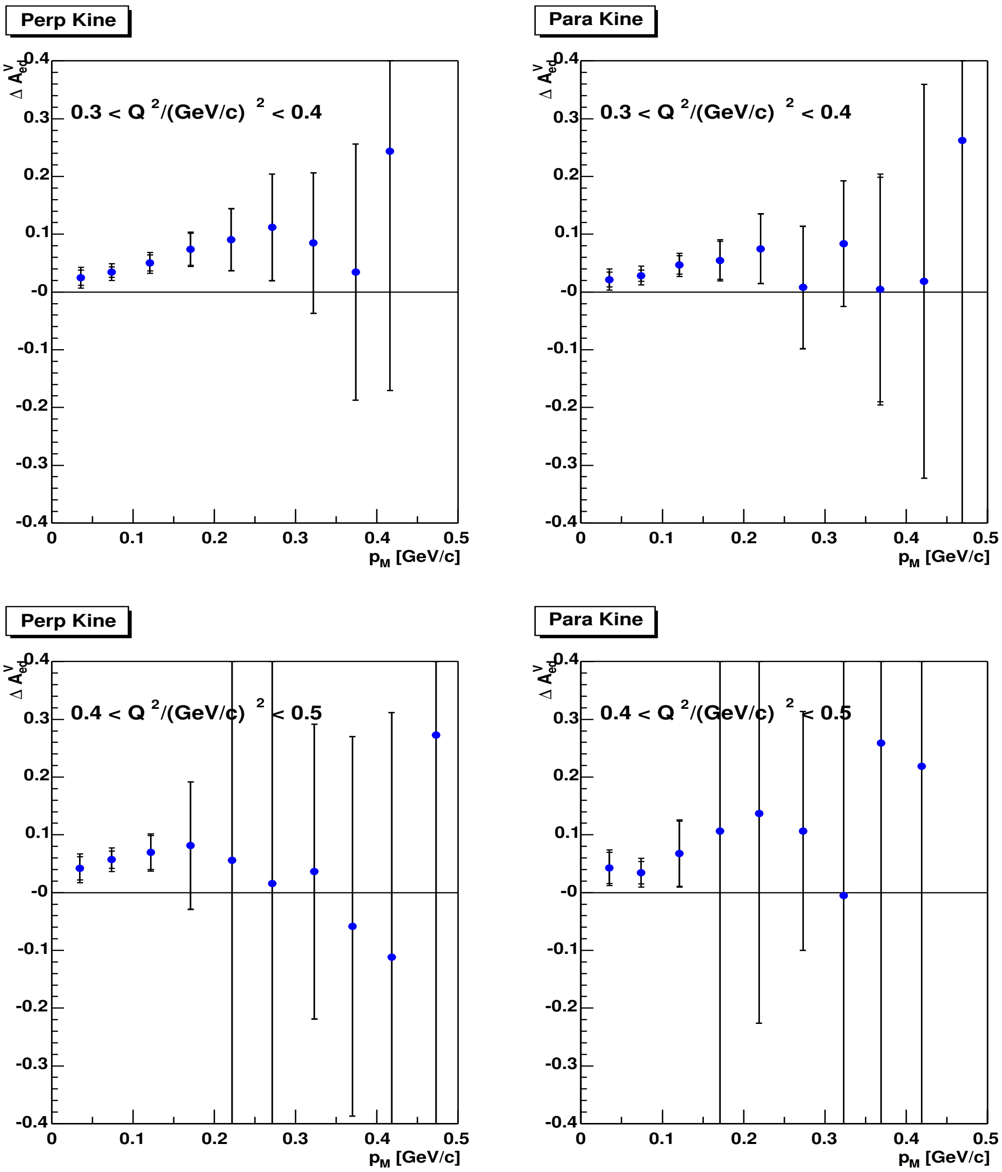

Figure 5-18: Plots of the residuals, ΔA^V_{ed}, of the reconstructed beam-vector asymmetry, A^T_{ed}, versus the missing momentum, p_M, for perpendicular (left) and parallel (right) kinematics in BLAST as compared with the total Bonn potential model. The top set of plots is for momentum transfers of 0.3 (GeV/c)^2 $< Q^2 <$ 0.4 (GeV/c)^2; the bottom set is for 0.4 (GeV/c)^2 $< Q^2 <$ 0.5 (GeV/c)^2.

5.4.1 Discussion of the Beam-Vector Results Versus $\mathbf{p_M}$

The reconstructed beam-vector asymmetries have the general form predicted from theory: a relatively flat plateau at low p_M ($p_M < 0.150$ GeV/c) followed by an upward rise in all kinematics at higher p_M.

Similar to the tensor asymmetry plots, evidence is once again seen in the beam-vector results supporting the necessity of including reaction mechanism effects into theoretical analyses. At high p_M in particular, the low Q^2 plots in perpendicular and parallel kinematics (Fig. 5-13) show consistency with the total Bonn potential model. In the absence of such reaction mechanism contributions, the data would be inconsistent with the theory.

The data at low Q^2 ($0.1\ (\mathrm{GeV/c})^2 < Q^2 < 0.2\ (\mathrm{GeV/c})^2$) agree very well in both perpendicular and parallel kinematics with the theoretical predictions over the entire p_M range analyzed[4]. However, a rise is seen (Figs. 5-15 and 5-16) in the data as compared to the total potential models as Q^2 increases. This rise is most noticeable in perpendicular kinematics and is visible already by the $0.2\ (\mathrm{GeV/c})^2 < Q^2 < 0.3\ (\mathrm{GeV/c})^2$ range. This rise is also clearly seen in the plots of the residuals (Figs. 5-17 and 5-18) which show significant deviations in perpendicular kinematics for the $0.2\ (\mathrm{GeV/c})^2 < Q^2 < 0.3\ (\mathrm{GeV/c})^2$ and $0.3\ (\mathrm{GeV/c})^2 < Q^2 < 0.4\ (\mathrm{GeV/c})^2$ ranges.

One obvious cause for such a rise in the reconstructed asymmetries as compared to the theoretical ones is a Q^2-dependent background incorrectly taken into account. Since the reconstructed asymmetries are modified according to (4.10) in the presence of background rates, it thus follows that background rates depending on Q^2 would modify asymmetries differently; such modifications could then help decrease the observed rise in the reconstructed data. However, Q^2-dependence in the background has been analyzed. In general, the variation in background rates with Q^2 is small ($\sim 1\%$). In order to remove the observed discrepancies between the data and the theory, variations of the order of $\sim 10\%$ are needed. Background variation is thus not believed to be responsible for the observed rise.

[4]Note that the data has been fit to the total model in this Q^2 bin for $p_M < 0.15$ GeV/c in order to determine hP_z for all beam-vector asymmetries.

Another possible reason for such a rise in reconstructed data as compared to theory could be modification of the bound nucleon form factors inside the deuteron from what is assumed in the theory. As previously discussed in Sec. 4.7, the form factors used in the theory for the bound nucleons in the deuteron are the (free) nucleon dipole form factors. The bound nucleon form factors could, in principle, differ from the free dipole ones in two ways: modification due to differences from the dipole approximation and modification due to being bound within the deuteron. Due to complications in the theory, it is not in general straightforward to determine the amount of form factor modification by determining ratios of the reconstructed and theoretical asymmetries. For a more accurate analysis, more realistic nucleon form factor models need to be used in producing theoretical results.

5.5 Conclusion

In this work analysis has been presented on the deuteron electrodisintegration tensor (A_d^T) and beam-vector (A_{ed}^V) asymmetries for Q^2 between 0.1 and 0.5 (GeV/c)^2. Overall, the general form of these asymmetries predicted by theory is consistent with the reconstructed ones. The high-p_M D-state structure predicted by theory is also seen in the data. However, both the reconstructed tensor and beam-vector asymmetry results presented here show evidence of an overall shift of high-p_M structure to slightly lower p_M than that predicted by theory. One possible reason for such a shift could be a modification of the nucleon form factors in the deuteron from the dipole ones assumed in the theory. However, before bound-state nucleon form factor modifications can be discerned, more realistic (free) form factors need to be introduced into the theory.

Chapter 6

Appendix

Numerical values for all of the results shown in Chap. 5 are listed in this appendix.

6.1 Systematic Error Values

The following set of tables gives bin-by-bin numerical values for all of the systematic errors discussed in Sec. 4.8. The headings in each table refer to the following:

Bin	:	bin number
p_M	:	average p_M value for the bin
$\cos\theta_M$	:	average $\cos\theta_M$ value for the bin
σ_{θ_d}	:	error due to determination of the spin angle (see Sec. 4.8.1)
σ_{m_M}	:	error due to missing mass cut (see Sec. 4.8.5)
σ_{hP_z}	:	error due to target polarization (see Sec. 4.8.2)
σ_{Rec}	:	error due to reconstruction (see Sec. 4.8.3)
σ_{Rad}	:	error due to radiative corrections (see Sec. 4.8.4)
σ_{False}	:	error due to false asymmetries (see Sec. 4.8.6)
σ_{Total}^{Syst}	:	total systematic error

Systematic Errors in A_d^T Vs. p_M for Perp Kine, $0.1 < Q^2/(\mathrm{GeV/c})^2 < 0.2$								
Bin	p_M (GeV/c)	σ_{θ_d}	σ_{m_M}	σ_{hP_z}	σ_{Rec}	σ_{Rad}	σ_{False}	σ_{Total}^{Syst}
1	0.035	0.000	0.001	0.001	0.000	0.000	0.000	0.002
2	0.072	0.000	0.001	0.002	0.001	0.000	0.000	0.003
3	0.120	0.000	0.001	0.002	0.001	0.000	0.000	0.003
4	0.170	0.000	0.003	0.001	0.000	0.000	0.000	0.003
5	0.221	0.025	0.028	0.008	0.003	0.001	0.001	0.039
6	0.270	0.005	0.021	0.009	0.003	0.001	0.001	0.023
7	0.323	0.006	0.048	0.014	0.005	0.002	0.002	0.051
8	0.371	0.012	0.006	0.015	0.005	0.002	0.002	0.021
9	0.418	0.019	0.006	0.012	0.004	0.001	0.001	0.023
10	0.471	0.054	0.052	0.015	0.005	0.002	0.002	0.077

Systematic Errors in A_d^T Vs. p_M for Para Kine, $0.1 < Q^2/(\mathrm{GeV/c})^2 < 0.2$								
Bin	p_M (GeV/c)	σ_{θ_d}	σ_{m_M}	σ_{hP_z}	σ_{Rec}	σ_{Rad}	σ_{False}	σ_{Total}^{Syst}
1	0.035	0.000	0.000	0.000	0.000	0.000	0.000	0.001
2	0.072	0.001	0.001	0.002	0.001	0.000	0.000	0.002
3	0.120	0.001	0.002	0.003	0.001	0.000	0.000	0.004
4	0.170	0.000	0.004	0.001	0.000	0.000	0.000	0.004
5	0.221	0.062	0.015	0.010	0.003	0.001	0.001	0.064
6	0.271	0.013	0.003	0.025	0.009	0.003	0.003	0.030
7	0.320	0.015	0.034	0.023	0.008	0.003	0.003	0.045
8	0.371	0.020	0.030	0.009	0.003	0.001	0.001	0.037
9	0.424	0.021	0.012	0.008	0.003	0.001	0.001	0.026
10	0.471	0.011	0.000	0.011	0.004	0.001	0.001	0.016

Systematic Errors in A_d^T Vs. p_M for Perp Kine, $0.2 < Q^2/(\mathrm{GeV/c})^2 < 0.3$								
Bin	p_M (GeV/c)	σ_{θ_d}	σ_{m_M}	σ_{hP_z}	σ_{Rec}	σ_{Rad}	σ_{False}	σ_{Total}^{Syst}
1	0.035	0.000	0.001	0.001	0.000	0.000	0.000	0.002
2	0.073	0.000	0.001	0.002	0.001	0.000	0.000	0.002
3	0.121	0.000	0.002	0.003	0.001	0.000	0.000	0.004
4	0.170	0.002	0.009	0.002	0.001	0.000	0.000	0.009
5	0.221	0.016	0.018	0.005	0.002	0.001	0.001	0.025
6	0.272	0.007	0.029	0.012	0.004	0.001	0.001	0.033
7	0.319	0.007	0.050	0.015	0.005	0.002	0.002	0.053
8	0.371	0.007	0.003	0.009	0.003	0.001	0.001	0.012
9	0.416	0.026	0.008	0.016	0.006	0.002	0.002	0.033
10	0.471	0.096	0.092	0.026	0.009	0.003	0.003	0.136

Systematic Errors in A_d^T Vs. p_M for Para Kine, $0.2 < Q^2/(\mathrm{GeV/c})^2 < 0.3$								
Bin	p_M (GeV/c)	σ_{θ_d}	σ_{m_M}	σ_{hP_z}	σ_{Rec}	σ_{Rad}	σ_{False}	σ_{Total}^{Syst}
1	0.035	0.001	0.000	0.001	0.000	0.000	0.000	0.001
2	0.073	0.001	0.000	0.001	0.000	0.000	0.000	0.002
3	0.121	0.001	0.002	0.002	0.001	0.000	0.000	0.003
4	0.171	0.000	0.011	0.003	0.001	0.000	0.000	0.012
5	0.221	0.010	0.003	0.002	0.001	0.000	0.000	0.011
6	0.271	0.002	0.000	0.004	0.001	0.000	0.000	0.004
7	0.320	0.005	0.012	0.008	0.003	0.001	0.001	0.016
8	0.369	0.007	0.011	0.003	0.001	0.000	0.000	0.014
9	0.426	0.058	0.033	0.023	0.008	0.003	0.003	0.072
10	0.469	0.030	0.000	0.028	0.010	0.003	0.003	0.042

Systematic Errors in A_d^T Vs. p_M for Perp Kine, $0.3 < Q^2/(\mathrm{GeV/c})^2 < 0.4$								
Bin	p_M (GeV/c)	σ_{θ_d}	σ_{m_M}	σ_{hP_z}	σ_{Rec}	σ_{Rad}	σ_{False}	σ_{Total}^{Syst}
1	0.036	0.000	0.000	0.000	0.000	0.000	0.000	0.000
2	0.074	0.000	0.001	0.001	0.000	0.000	0.000	0.001
3	0.121	0.000	0.002	0.003	0.001	0.000	0.000	0.004
4	0.171	0.002	0.014	0.003	0.001	0.000	0.000	0.014
5	0.221	0.009	0.010	0.003	0.001	0.000	0.000	0.013
6	0.271	0.002	0.010	0.004	0.002	0.001	0.001	0.011
7	0.322	0.009	0.063	0.019	0.007	0.002	0.002	0.067
8	0.374	0.009	0.004	0.011	0.004	0.001	0.001	0.016
9	0.416	0.016	0.005	0.010	0.004	0.001	0.001	0.020
10	0.480	0.087	0.083	0.023	0.008	0.003	0.003	0.123

Systematic Errors in A_d^T Vs. p_M for Para Kine, $0.3 < Q^2/(\mathrm{GeV/c})^2 < 0.4$								
Bin	p_M (GeV/c)	σ_{θ_d}	σ_{m_M}	σ_{hP_z}	σ_{Rec}	σ_{Rad}	σ_{False}	σ_{Total}^{Syst}
1	0.035	0.001	0.000	0.001	0.000	0.000	0.000	0.001
2	0.074	0.001	0.000	0.002	0.001	0.000	0.000	0.002
3	0.121	0.000	0.001	0.001	0.000	0.000	0.000	0.001
4	0.171	0.000	0.000	0.000	0.000	0.000	0.000	0.000
5	0.221	0.027	0.007	0.004	0.001	0.000	0.000	0.028
6	0.273	0.000	0.000	0.000	0.000	0.000	0.000	0.000
7	0.323	0.002	0.004	0.003	0.001	0.000	0.000	0.005
8	0.368	0.017	0.025	0.008	0.003	0.001	0.001	0.031
9	0.422	0.054	0.031	0.022	0.008	0.003	0.003	0.066
10	0.469	0.007	0.000	0.006	0.002	0.001	0.001	0.010

Systematic Errors in A_d^T Vs. p_M for Perp Kine, $0.4 < Q^2/(\mathrm{GeV/c})^2 < 0.5$								
Bin	p_M (GeV/c)	σ_{θ_d}	σ_{m_M}	σ_{hP_z}	σ_{Rec}	σ_{Rad}	σ_{False}	σ_{Total}^{Syst}
1	0.035	0.000	0.000	0.000	0.000	0.000	0.000	0.000
2	0.074	0.000	0.000	0.000	0.000	0.000	0.000	0.001
3	0.122	0.000	0.002	0.003	0.001	0.000	0.000	0.004
4	0.171	0.004	0.021	0.005	0.002	0.001	0.001	0.022
5	0.222	0.023	0.026	0.007	0.003	0.001	0.001	0.035
6	0.271	0.001	0.005	0.002	0.001	0.000	0.000	0.006
7	0.323	0.003	0.022	0.007	0.002	0.001	0.001	0.024
8	0.370	0.018	0.009	0.022	0.008	0.003	0.003	0.032
9	0.418	0.034	0.011	0.021	0.008	0.003	0.003	0.043
10	0.473	0.124	0.119	0.033	0.012	0.004	0.004	0.176

Systematic Errors in A_d^T Vs. p_M for Para Kine, $0.4 < Q^2/(\mathrm{GeV/c})^2 < 0.5$								
Bin	p_M (GeV/c)	σ_{θ_d}	σ_{m_M}	σ_{hP_z}	σ_{Rec}	σ_{Rad}	σ_{False}	σ_{Total}^{Syst}
1	0.035	0.000	0.000	0.000	0.000	0.000	0.000	0.000
2	0.074	0.000	0.000	0.000	0.000	0.000	0.000	0.000
3	0.121	0.000	0.001	0.002	0.001	0.000	0.000	0.002
4	0.171	0.000	0.014	0.003	0.001	0.000	0.000	0.014
5	0.219	0.014	0.003	0.002	0.001	0.000	0.000	0.015
6	0.273	0.002	0.001	0.005	0.002	0.001	0.001	0.006
7	0.323	0.004	0.008	0.005	0.002	0.001	0.001	0.010
8	0.369	0.025	0.037	0.012	0.004	0.001	0.001	0.046
9	0.419	0.003	0.002	0.001	0.000	0.000	0.000	0.004
10	0.475	0.063	0.000	0.060	0.021	0.007	0.007	0.090

Systematic Errors in A_{ed}^V Vs. p_M for Perp Kine, $0.1 < Q^2/(\mathrm{GeV/c})^2 < 0.2$								
Bin	p_M (GeV/c)	σ_{θ_d}	σ_{m_M}	σ_{hP_z}	σ_{Rec}	σ_{Rad}	σ_{False}	σ_{Total}^{Syst}
1	0.035	0.002	0.001	0.002	0.005	0.002	0.002	0.006
2	0.072	0.002	0.001	0.002	0.005	0.002	0.002	0.006
3	0.120	0.002	0.001	0.002	0.005	0.002	0.002	0.006
4	0.170	0.002	0.001	0.002	0.004	0.001	0.001	0.006
5	0.221	0.002	0.003	0.001	0.003	0.001	0.001	0.005
6	0.270	0.001	0.004	0.001	0.002	0.001	0.001	0.005
7	0.323	0.000	0.002	0.000	0.000	0.000	0.000	0.002
8	0.371	0.001	0.002	0.002	0.005	0.002	0.002	0.006
9	0.418	0.001	0.010	0.004	0.011	0.004	0.004	0.016
10	0.471	0.001	0.047	0.002	0.006	0.002	0.002	0.047

Systematic Errors in A_{ed}^V Vs. p_M for Para Kine, $0.1 < Q^2/(\mathrm{GeV/c})^2 < 0.2$								
Bin	p_M (GeV/c)	σ_{θ_d}	σ_{m_M}	σ_{hP_z}	σ_{Rec}	σ_{Rad}	σ_{False}	σ_{Total}^{Syst}
1	0.035	0.002	0.000	0.002	0.005	0.002	0.002	0.007
2	0.072	0.002	0.002	0.002	0.006	0.002	0.002	0.007
3	0.120	0.002	0.001	0.002	0.006	0.002	0.002	0.007
4	0.170	0.001	0.005	0.002	0.005	0.002	0.002	0.008
5	0.221	0.001	0.001	0.002	0.005	0.002	0.002	0.006
6	0.271	0.001	0.001	0.001	0.002	0.001	0.001	0.003
7	0.320	0.000	0.000	0.000	0.000	0.000	0.000	0.000
8	0.371	0.014	0.020	0.001	0.002	0.001	0.001	0.025
9	0.424	0.005	0.022	0.002	0.006	0.002	0.002	0.024
10	0.471	0.006	0.003	0.004	0.010	0.003	0.003	0.014

Systematic Errors in A_{ed}^V Vs. p_M for Perp Kine, $0.2 < Q^2/(\text{GeV/c})^2 < 0.3$								
Bin	p_M (GeV/c)	σ_{θ_d}	σ_{m_M}	σ_{hP_z}	σ_{Rec}	σ_{Rad}	σ_{False}	σ_{Total}^{Syst}
1	0.035	0.003	0.001	0.003	0.007	0.002	0.002	0.009
2	0.073	0.003	0.001	0.003	0.007	0.002	0.002	0.009
3	0.121	0.003	0.002	0.003	0.007	0.002	0.002	0.009
4	0.170	0.003	0.002	0.002	0.006	0.002	0.002	0.007
5	0.221	0.002	0.003	0.002	0.004	0.001	0.001	0.006
6	0.272	0.001	0.003	0.001	0.002	0.001	0.001	0.004
7	0.319	0.000	0.002	0.000	0.000	0.000	0.000	0.002
8	0.371	0.002	0.005	0.004	0.010	0.003	0.003	0.013
9	0.416	0.001	0.012	0.005	0.013	0.004	0.004	0.020
10	0.471	0.003	0.099	0.005	0.013	0.004	0.004	0.100

Systematic Errors in A_{ed}^V Vs. p_M for Para Kine, $0.2 < Q^2/(\text{GeV/c})^2 < 0.3$								
Bin	p_M (GeV/c)	σ_{θ_d}	σ_{m_M}	σ_{hP_z}	σ_{Rec}	σ_{Rad}	σ_{False}	σ_{Total}^{Syst}
1	0.035	0.002	0.000	0.003	0.008	0.003	0.003	0.010
2	0.073	0.002	0.002	0.003	0.008	0.003	0.003	0.010
3	0.121	0.002	0.001	0.003	0.008	0.003	0.003	0.010
4	0.171	0.002	0.007	0.003	0.008	0.003	0.003	0.012
5	0.221	0.002	0.002	0.002	0.006	0.002	0.002	0.007
6	0.271	0.001	0.002	0.002	0.005	0.002	0.002	0.006
7	0.320	0.000	0.001	0.001	0.004	0.001	0.001	0.004
8	0.369	0.009	0.013	0.001	0.001	0.000	0.000	0.016
9	0.426	0.006	0.028	0.003	0.008	0.003	0.003	0.030
10	0.469	0.007	0.004	0.005	0.013	0.004	0.004	0.017

Systematic Errors in A_{ed}^{V} Vs. p_M for Perp Kine, $0.3 < Q^2/(\text{GeV/c})^2 < 0.4$								
Bin	p_M (GeV/c)	σ_{θ_d}	σ_{m_M}	σ_{hP_z}	σ_{Rec}	σ_{Rad}	σ_{False}	σ_{Total}^{Syst}
1	0.036	0.004	0.001	0.004	0.009	0.003	0.003	0.012
2	0.074	0.004	0.001	0.004	0.009	0.003	0.003	0.012
3	0.121	0.004	0.002	0.003	0.009	0.003	0.003	0.011
4	0.171	0.004	0.003	0.003	0.007	0.002	0.002	0.010
5	0.221	0.003	0.005	0.002	0.006	0.002	0.002	0.009
6	0.271	0.001	0.004	0.001	0.002	0.001	0.001	0.004
7	0.322	0.000	0.001	0.000	0.000	0.000	0.000	0.001
8	0.374	0.000	0.000	0.000	0.000	0.000	0.000	0.000
9	0.416	0.001	0.009	0.004	0.009	0.003	0.003	0.014
10	0.480	0.005	0.188	0.010	0.024	0.008	0.008	0.190

Systematic Errors in A_{ed}^{V} Vs. p_M for Para Kine, $0.3 < Q^2/(\text{GeV/c})^2 < 0.4$								
Bin	p_M (GeV/c)	σ_{θ_d}	σ_{m_M}	σ_{hP_z}	σ_{Rec}	σ_{Rad}	σ_{False}	σ_{Total}^{Syst}
1	0.035	0.003	0.000	0.004	0.011	0.004	0.004	0.013
2	0.074	0.003	0.003	0.004	0.011	0.004	0.004	0.013
3	0.121	0.003	0.002	0.004	0.010	0.003	0.003	0.012
4	0.171	0.002	0.009	0.004	0.009	0.003	0.003	0.014
5	0.221	0.002	0.002	0.003	0.007	0.002	0.002	0.009
6	0.273	0.002	0.003	0.003	0.007	0.002	0.002	0.009
7	0.323	0.000	0.001	0.001	0.003	0.001	0.001	0.004
8	0.368	0.026	0.038	0.002	0.004	0.001	0.001	0.046
9	0.422	0.000	0.001	0.000	0.000	0.000	0.000	0.001
10	0.469	0.008	0.005	0.006	0.015	0.005	0.005	0.020

Systematic Errors in A_{ed}^V Vs. p_M for Perp Kine, $0.4 < Q^2/(\text{GeV/c})^2 < 0.5$								
Bin	p_M (GeV/c)	σ_{θ_d}	σ_{m_M}	σ_{hP_z}	σ_{Rec}	σ_{Rad}	σ_{False}	σ_{Total}^{Syst}
1	0.035	0.005	0.001	0.005	0.011	0.004	0.004	0.014
2	0.074	0.005	0.002	0.004	0.011	0.004	0.004	0.014
3	0.122	0.005	0.002	0.004	0.010	0.003	0.003	0.013
4	0.171	0.004	0.003	0.004	0.009	0.003	0.003	0.012
5	0.222	0.003	0.005	0.003	0.007	0.002	0.002	0.011
6	0.271	0.002	0.009	0.002	0.005	0.002	0.002	0.010
7	0.323	0.001	0.010	0.001	0.002	0.001	0.001	0.010
8	0.370	0.001	0.002	0.002	0.004	0.001	0.001	0.005
9	0.418	0.001	0.005	0.002	0.005	0.002	0.002	0.008
10	0.473	0.001	0.051	0.003	0.007	0.002	0.002	0.052

Systematic Errors in A_{ed}^V Vs. p_M for Para Kine, $0.4 < Q^2/(\text{GeV/c})^2 < 0.5$								
Bin	p_M (GeV/c)	σ_{θ_d}	σ_{m_M}	σ_{hP_z}	σ_{Rec}	σ_{Rad}	σ_{False}	σ_{Total}^{Syst}
1	0.035	0.004	0.000	0.005	0.013	0.004	0.004	0.015
2	0.074	0.004	0.003	0.005	0.013	0.004	0.004	0.016
3	0.121	0.003	0.002	0.005	0.012	0.004	0.004	0.014
4	0.171	0.003	0.010	0.004	0.010	0.003	0.003	0.015
5	0.219	0.002	0.002	0.003	0.007	0.002	0.002	0.008
6	0.273	0.001	0.002	0.001	0.004	0.001	0.001	0.005
7	0.323	0.001	0.001	0.002	0.005	0.002	0.002	0.006
8	0.369	0.018	0.026	0.001	0.003	0.001	0.001	0.032
9	0.419	0.000	0.001	0.000	0.000	0.000	0.000	0.001
10	0.475	0.007	0.004	0.005	0.012	0.004	0.004	0.016

Systematic Errors in A_d^T Vs. $\cos\theta_M$, $0.1 < Q^2/(\mathrm{GeV/c})^2 < 0.2$								
Bin	$\cos\theta_M$	σ_{θ_d}	σ_{m_M}	σ_{hP_z}	σ_{Rec}	σ_{Rad}	σ_{False}	σ_{Total}^{Syst}
1	-0.900	0.000	0.003	0.002	0.001	0.000	0.000	0.004
2	-0.850	0.000	0.002	0.001	0.001	0.000	0.000	0.003
3	-0.750	0.000	0.000	0.000	0.000	0.000	0.000	0.000
4	-0.650	0.001	0.004	0.000	0.000	0.000	0.000	0.004
5	-0.550	0.000	0.000	0.002	0.001	0.000	0.000	0.003
6	-0.450	0.000	0.002	0.003	0.001	0.000	0.000	0.003
7	-0.350	0.000	0.001	0.003	0.001	0.000	0.000	0.004
8	-0.250	0.000	0.000	0.004	0.001	0.000	0.000	0.004
9	-0.150	0.001	0.001	0.004	0.001	0.000	0.000	0.004
10	-0.050	0.001	0.000	0.004	0.001	0.000	0.000	0.004
11	0.050	0.000	0.001	0.004	0.001	0.000	0.000	0.004
12	0.150	0.000	0.000	0.003	0.001	0.000	0.000	0.004
13	0.250	0.000	0.001	0.003	0.001	0.000	0.000	0.004
14	0.351	0.000	0.000	0.003	0.001	0.000	0.000	0.003
15	0.450	0.000	0.001	0.001	0.000	0.000	0.000	0.001
16	0.550	0.000	0.000	0.001	0.000	0.000	0.000	0.001
17	0.651	0.000	0.001	0.003	0.001	0.000	0.000	0.003
18	0.750	0.000	0.000	0.005	0.002	0.001	0.001	0.005
19	0.851	0.000	0.000	0.007	0.003	0.001	0.001	0.008
20	0.950	0.000	0.000	0.011	0.004	0.001	0.001	0.011

Systematic Errors in A_d^T Vs. $\cos\theta_M$, $0.2 < Q^2/(\mathrm{GeV/c})^2 < 0.3$								
Bin	$\cos\theta_M$	σ_{θ_d}	σ_{m_M}	σ_{hP_z}	σ_{Rec}	σ_{Rad}	σ_{False}	σ_{Total}^{Syst}
1	-0.951	0.001	0.007	0.005	0.002	0.001	0.001	0.009
2	-0.851	0.001	0.005	0.003	0.001	0.000	0.000	0.006
3	-0.751	0.001	0.002	0.002	0.001	0.000	0.000	0.003
4	-0.651	0.000	0.000	0.000	0.000	0.000	0.000	0.000
5	-0.550	0.000	0.000	0.001	0.000	0.000	0.000	0.001
6	-0.449	0.000	0.001	0.002	0.001	0.000	0.000	0.002
7	-0.350	0.000	0.002	0.004	0.001	0.000	0.000	0.005
8	-0.250	0.000	0.000	0.004	0.002	0.001	0.001	0.005
9	-0.150	0.001	0.001	0.004	0.002	0.001	0.001	0.005
10	-0.050	0.001	0.000	0.004	0.001	0.000	0.000	0.004
11	0.050	0.000	0.001	0.005	0.002	0.001	0.001	0.005
12	0.150	0.000	0.000	0.005	0.002	0.001	0.001	0.005
13	0.250	0.001	0.001	0.004	0.001	0.000	0.000	0.005
14	0.350	0.000	0.000	0.003	0.001	0.000	0.000	0.003
15	0.450	0.000	0.002	0.002	0.001	0.000	0.000	0.003
16	0.550	0.000	0.000	0.000	0.000	0.000	0.000	0.000
17	0.650	0.000	0.000	0.002	0.001	0.000	0.000	0.002
18	0.751	0.000	0.000	0.003	0.001	0.000	0.000	0.003
19	0.851	0.000	0.000	0.006	0.002	0.001	0.001	0.006
20	0.951	0.000	0.000	0.010	0.004	0.001	0.001	0.011

Systematic Errors in A_d^T Vs. $\cos\theta_M$, $0.3 < Q^2/(\mathrm{GeV/c})^2 < 0.4$								
Bin	$\cos\theta_M$	σ_{θ_d}	σ_{m_M}	σ_{hP_z}	σ_{Rec}	σ_{Rad}	σ_{False}	σ_{Total}^{Syst}
1	-0.951	0.001	0.010	0.008	0.003	0.001	0.001	0.013
2	-0.851	0.001	0.006	0.004	0.001	0.000	0.000	0.007
3	-0.750	0.002	0.004	0.004	0.001	0.000	0.000	0.006
4	-0.651	0.002	0.008	0.001	0.000	0.000	0.000	0.008
5	-0.550	0.000	0.000	0.001	0.000	0.000	0.000	0.001
6	-0.450	0.000	0.001	0.002	0.001	0.000	0.000	0.003
7	-0.350	0.000	0.002	0.004	0.001	0.000	0.000	0.004
8	-0.250	0.000	0.000	0.004	0.001	0.000	0.000	0.004
9	-0.150	0.001	0.001	0.005	0.002	0.001	0.001	0.006
10	-0.050	0.001	0.000	0.004	0.001	0.000	0.000	0.004
11	0.050	0.000	0.001	0.005	0.002	0.001	0.001	0.005
12	0.151	0.000	0.000	0.004	0.001	0.000	0.000	0.004
13	0.250	0.001	0.001	0.004	0.002	0.001	0.001	0.005
14	0.349	0.000	0.000	0.003	0.001	0.000	0.000	0.003
15	0.450	0.000	0.002	0.001	0.001	0.000	0.000	0.002
16	0.551	0.000	0.000	0.000	0.000	0.000	0.000	0.000
17	0.650	0.000	0.000	0.000	0.000	0.000	0.000	0.000
18	0.750	0.000	0.000	0.004	0.001	0.000	0.000	0.004
19	0.851	0.000	0.000	0.004	0.002	0.001	0.001	0.005
20	0.950	0.000	0.000	0.008	0.003	0.001	0.001	0.008

Systematic Errors in A_d^T Vs. $\cos\theta_M$, $0.4 < Q^2/(\mathrm{GeV/c})^2 < 0.5$								
Bin	$\cos\theta_M$	σ_{θ_d}	σ_{m_M}	σ_{hP_z}	σ_{Rec}	σ_{Rad}	σ_{False}	σ_{Total}^{Syst}
1	-0.951	0.001	0.010	0.008	0.003	0.001	0.001	0.013
2	-0.851	0.001	0.008	0.006	0.002	0.001	0.001	0.010
3	-0.751	0.002	0.004	0.004	0.001	0.000	0.000	0.006
4	-0.651	0.000	0.000	0.000	0.000	0.000	0.000	0.000
5	-0.551	0.000	0.000	0.000	0.000	0.000	0.000	0.000
6	-0.449	0.000	0.002	0.003	0.001	0.000	0.000	0.004
7	-0.350	0.000	0.001	0.003	0.001	0.000	0.000	0.003
8	-0.250	0.000	0.000	0.004	0.001	0.000	0.000	0.004
9	-0.150	0.001	0.001	0.005	0.002	0.001	0.001	0.006
10	-0.051	0.001	0.000	0.003	0.001	0.000	0.000	0.003
11	0.052	0.000	0.001	0.004	0.001	0.000	0.000	0.004
12	0.149	0.000	0.000	0.005	0.002	0.001	0.001	0.005
13	0.250	0.000	0.001	0.003	0.001	0.000	0.000	0.003
14	0.349	0.000	0.000	0.000	0.000	0.000	0.000	0.000
15	0.450	0.000	0.000	0.000	0.000	0.000	0.000	0.000
16	0.551	0.000	0.000	0.001	0.000	0.000	0.000	0.001
17	0.652	0.000	0.000	0.001	0.000	0.000	0.000	0.001
18	0.749	0.000	0.000	0.001	0.000	0.000	0.000	0.001
19	0.852	0.000	0.000	0.007	0.002	0.001	0.001	0.007
20	0.950	0.000	0.000	0.006	0.002	0.001	0.001	0.006

6.2 Asymmetry Values and Total Errors

The following set of tables gives bin-by-bin numerical values for all of the asymmetry values as well as their corresponding statistical, total systematic, and total overall errors. The headings in each table refer to the following:

Bin	:	bin number
p_M	:	average p_M value for the bin
$\cos\theta_M$	:	average $\cos\theta_M$ value for the bin
A_d^T	:	tensor asymmetry value
A_{ed}^V	:	beam-vector asymmetry value
σ_{Stat}	:	total statistical error
σ_{Syst}	:	total systematic error
σ_{Tot}	:	overall total error

A_d^T Values Vs. p_M for Perp Kine, $0.1 < Q^2/(\mathrm{GeV/c})^2 < 0.2$					
Bin	p_M (GeV/c)	A_d^T	σ_{Stat}	σ_{Syst}	σ_{Tot}
1	0.035	-0.016	0.003	0.002	0.004
2	0.072	-0.024	0.003	0.003	0.004
3	0.120	-0.024	0.005	0.003	0.005
4	0.170	0.008	0.009	0.003	0.010
5	0.221	0.097	0.017	0.039	0.043
6	0.270	0.104	0.028	0.023	0.036
7	0.323	0.167	0.039	0.051	0.064
8	0.371	0.175	0.054	0.021	0.058
9	0.418	0.137	0.084	0.023	0.087
10	0.471	0.173	0.129	0.077	0.150

A_d^T Values Vs. p_M for Para Kine, $0.1 < Q^2/(\mathrm{GeV/c})^2 < 0.2$					
Bin	p_M (GeV/c)	A_d^T	σ_{Stat}	σ_{Syst}	σ_{Tot}
1	0.035	0.006	0.003	0.001	0.003
2	0.072	0.021	0.003	0.002	0.003
3	0.120	0.031	0.005	0.004	0.006
4	0.170	-0.011	0.009	0.004	0.010
5	0.221	-0.114	0.016	0.064	0.066
6	0.271	-0.302	0.030	0.030	0.043
7	0.320	-0.271	0.043	0.045	0.062
8	0.371	-0.110	0.054	0.037	0.065
9	0.424	0.101	0.071	0.026	0.075
10	0.471	0.127	0.101	0.016	0.102

A_d^T Values Vs. p_M for Perp Kine, $0.2 < Q^2/(\mathrm{GeV/c})^2 < 0.3$					
Bin	p_M (GeV/c)	A_d^T	σ_{Stat}	σ_{Syst}	σ_{Tot}
1	0.035	-0.015	0.005	0.002	0.005
2	0.073	-0.020	0.004	0.002	0.004
3	0.121	-0.036	0.007	0.004	0.008
4	0.170	-0.025	0.013	0.009	0.016
5	0.221	0.063	0.022	0.025	0.034
6	0.272	0.149	0.034	0.033	0.047
7	0.319	0.176	0.057	0.053	0.078
8	0.371	0.102	0.135	0.012	0.135
9	0.416	0.194	0.243	0.033	0.245
10	0.471	-0.307	0.417	0.136	0.438

A_d^T Values Vs. p_M for Para Kine, $0.2 < Q^2/(\mathrm{GeV/c})^2 < 0.3$					
Bin	p_M (GeV/c)	A_d^T	σ_{Stat}	σ_{Syst}	σ_{Tot}
1	0.035	0.014	0.005	0.001	0.005
2	0.073	0.015	0.004	0.002	0.004
3	0.121	0.029	0.006	0.003	0.007
4	0.171	0.032	0.011	0.012	0.016
5	0.221	-0.019	0.019	0.011	0.022
6	0.271	-0.044	0.030	0.004	0.030
7	0.320	-0.097	0.048	0.016	0.051
8	0.369	0.041	0.086	0.014	0.087
9	0.426	0.278	0.127	0.072	0.146
10	0.469	0.334	0.178	0.042	0.183

A_d^T Values Vs. p_M for Perp Kine, $0.3 < Q^2/(\mathrm{GeV/c})^2 < 0.4$					
Bin	p_M (GeV/c)	A_d^T	σ_{Stat}	σ_{Syst}	σ_{Tot}
1	0.036	0.002	0.009	0.000	0.009
2	0.074	-0.011	0.006	0.001	0.006
3	0.121	-0.033	0.010	0.004	0.011
4	0.171	-0.039	0.020	0.014	0.024
5	0.221	-0.033	0.037	0.013	0.039
6	0.271	0.052	0.065	0.011	0.066
7	0.322	0.221	0.085	0.067	0.109
8	0.374	0.134	0.157	0.016	0.157
9	0.416	0.119	0.250	0.020	0.250
10	0.480	0.276	95.819	0.123	95.819

A_d^T Values Vs. p_M for Para Kine, $0.3 < Q^2/(\mathrm{GeV/c})^2 < 0.4$					
Bin	p_M (GeV/c)	A_d^T	σ_{Stat}	σ_{Syst}	σ_{Tot}
1	0.035	0.012	0.009	0.001	0.009
2	0.074	0.018	0.007	0.002	0.007
3	0.121	0.008	0.011	0.001	0.011
4	0.171	-0.001	0.022	0.000	0.022
5	0.221	-0.050	0.040	0.028	0.049
6	0.273	0.003	0.069	0.000	0.069
7	0.323	0.030	0.076	0.005	0.076
8	0.368	0.093	0.132	0.031	0.136
9	0.422	0.257	0.256	0.066	0.264
10	0.469	0.077	0.389	0.010	0.389

A_d^T Values Vs. p_M for Perp Kine, $0.4 < Q^2/(\text{GeV/c})^2 < 0.5$					
Bin	p_M (GeV/c)	A_d^T	σ_{Stat}	σ_{Syst}	σ_{Tot}
1	0.035	-0.002	0.014	0.000	0.014
2	0.074	0.005	0.010	0.001	0.010
3	0.122	-0.040	0.019	0.004	0.020
4	0.171	-0.060	0.057	0.022	0.061
5	0.222	-0.088	0.244	0.035	0.247
6	0.271	0.026	2.091	0.006	2.091
7	0.323	0.078	0.181	0.024	0.183
8	0.370	0.268	0.266	0.032	0.268
9	0.418	0.253	0.311	0.043	0.314
10	0.473	0.397	2.380	0.176	2.387

A_d^T Values Vs. p_M for Para Kine, $0.4 < Q^2/(\text{GeV/c})^2 < 0.5$					
Bin	p_M (GeV/c)	A_d^T	σ_{Stat}	σ_{Syst}	σ_{Tot}
1	0.035	0.001	0.019	0.000	0.019
2	0.074	0.004	0.013	0.000	0.013
3	0.121	0.020	0.030	0.002	0.030
4	0.171	0.039	0.608	0.014	0.608
5	0.219	0.027	0.145	0.015	0.146
6	0.273	0.057	0.135	0.006	0.135
7	0.323	-0.063	11.938	0.010	11.938
8	0.369	-0.138	2.904	0.046	2.904
9	0.419	0.016	1.063	0.004	1.063
10	0.475	0.712	178.654	0.090	178.654

A_{ed}^V Values Vs. p_M for Perp Kine, $0.1 < Q^2/(\text{GeV/c})^2 < 0.2$					
Bin	p_M (GeV/c)	A_{ed}^V	σ_{Stat}	σ_{Syst}	σ_{Tot}
1	0.035	-0.162	0.004	0.006	0.008
2	0.072	-0.164	0.004	0.006	0.007
3	0.120	-0.165	0.006	0.006	0.009
4	0.170	-0.142	0.013	0.006	0.014
5	0.221	-0.115	0.024	0.005	0.025
6	0.270	-0.071	0.041	0.005	0.041
7	0.323	-0.011	0.058	0.002	0.058
8	0.371	0.164	0.081	0.006	0.081
9	0.418	0.355	0.126	0.016	0.127
10	0.471	0.203	0.195	0.047	0.200

A_{ed}^V Values Vs. p_M for Para Kine, $0.1 < Q^2/(\text{GeV/c})^2 < 0.2$					
Bin	p_M (GeV/c)	A_{ed}^V	σ_{Stat}	σ_{Syst}	σ_{Tot}
1	0.035	-0.180	0.004	0.007	0.008
2	0.072	-0.185	0.004	0.007	0.008
3	0.120	-0.194	0.006	0.007	0.010
4	0.170	-0.169	0.012	0.008	0.015
5	0.221	-0.155	0.021	0.006	0.022
6	0.271	-0.076	0.034	0.003	0.034
7	0.320	0.011	0.051	0.000	0.051
8	0.371	0.076	0.071	0.025	0.076
9	0.424	0.208	0.104	0.024	0.106
10	0.471	0.336	0.149	0.014	0.150

A_{ed}^V Values Vs. p_M for Perp Kine, $0.2 < Q^2/(\mathrm{GeV/c})^2 < 0.3$					
Bin	p_M (GeV/c)	A_{ed}^V	σ_{Stat}	σ_{Syst}	σ_{Tot}
1	0.035	-0.240	0.007	0.009	0.012
2	0.073	-0.225	0.006	0.009	0.010
3	0.121	-0.223	0.009	0.009	0.013
4	0.170	-0.184	0.017	0.007	0.019
5	0.221	-0.145	0.032	0.006	0.033
6	0.272	-0.055	0.049	0.004	0.049
7	0.319	0.014	0.084	0.002	0.084
8	0.371	0.336	0.221	0.013	0.221
9	0.416	0.441	0.433	0.020	0.434
10	0.471	0.427	0.565	0.100	0.574

A_{ed}^V Values Vs. p_M for Para Kine, $0.2 < Q^2/(\mathrm{GeV/c})^2 < 0.3$					
Bin	p_M (GeV/c)	A_{ed}^V	σ_{Stat}	σ_{Syst}	σ_{Tot}
1	0.035	-0.270	0.007	0.010	0.012
2	0.073	-0.271	0.006	0.010	0.012
3	0.121	-0.270	0.009	0.010	0.013
4	0.171	-0.254	0.016	0.012	0.020
5	0.221	-0.195	0.027	0.007	0.028
6	0.271	-0.168	0.041	0.006	0.041
7	0.320	-0.119	0.065	0.004	0.065
8	0.369	0.048	0.122	0.016	0.123
9	0.426	0.263	0.196	0.030	0.198
10	0.469	0.431	0.288	0.017	0.288

A_{ed}^V Values Vs. p_M for Perp Kine, $0.3 < Q^2/(\mathrm{GeV/c})^2 < 0.4$					
Bin	p_M (GeV/c)	A_{ed}^V	σ_{Stat}	σ_{Syst}	σ_{Tot}
1	0.036	-0.312	0.013	0.012	0.018
2	0.074	-0.304	0.009	0.012	0.015
3	0.121	-0.287	0.014	0.011	0.018
4	0.171	-0.249	0.028	0.010	0.030
5	0.221	-0.201	0.053	0.009	0.054
6	0.271	-0.062	0.092	0.004	0.092
7	0.322	0.008	0.122	0.001	0.122
8	0.374	0.010	0.222	0.000	0.222
9	0.416	0.306	0.415	0.014	0.415
10	0.480	0.814	333.056	0.190	333.056

A_{ed}^V Values Vs. p_M for Para Kine, $0.3 < Q^2/(\mathrm{GeV/c})^2 < 0.4$					
Bin	p_M (GeV/c)	A_{ed}^V	σ_{Stat}	σ_{Syst}	σ_{Tot}
1	0.035	-0.353	0.013	0.013	0.018
2	0.074	-0.352	0.010	0.013	0.016
3	0.121	-0.332	0.016	0.012	0.020
4	0.171	-0.305	0.033	0.014	0.036
5	0.221	-0.247	0.060	0.009	0.061
6	0.273	-0.228	0.106	0.009	0.106
7	0.323	-0.102	0.109	0.004	0.109
8	0.368	-0.142	0.195	0.046	0.200
9	0.422	0.010	0.341	0.001	0.341
10	0.469	0.487	0.822	0.020	0.822

A_{ed}^V Values Vs. p_M for Perp Kine, $0.4 < Q^2/(\mathrm{GeV/c})^2 < 0.5$					
Bin	p_M (GeV/c)	A_{ed}^V	σ_{Stat}	σ_{Syst}	σ_{Tot}
1	0.035	-0.378	0.020	0.014	0.025
2	0.074	-0.357	0.015	0.014	0.020
3	0.122	-0.333	0.030	0.013	0.032
4	0.171	-0.295	0.110	0.012	0.111
5	0.222	-0.239	0.574	0.011	0.574
6	0.271	-0.152	11.362	0.010	11.362
7	0.323	-0.061	0.255	0.010	0.255
8	0.370	-0.136	0.328	0.005	0.328
9	0.418	-0.176	0.423	0.008	0.423
10	0.473	0.222	1.997	0.052	1.998

A_{ed}^V Values Vs. p_M for Para Kine, $0.4 < Q^2/(\mathrm{GeV/c})^2 < 0.5$					
Bin	p_M (GeV/c)	A_{ed}^V	σ_{Stat}	σ_{Syst}	σ_{Tot}
1	0.035	-0.420	0.027	0.015	0.031
2	0.074	-0.425	0.020	0.016	0.025
3	0.121	-0.388	0.056	0.014	0.058
4	0.171	-0.330	4.774	0.015	4.774
5	0.219	-0.220	0.363	0.008	0.363
6	0.273	-0.119	0.207	0.005	0.207
7	0.323	-0.169	37.199	0.006	37.199
8	0.369	0.099	2.706	0.032	2.706
9	0.419	0.011	1.481	0.001	1.481
10	0.475	0.408	121.324	0.016	121.324

A_d^T Values Vs. $\cos\theta_M$, $0.1 < Q^2/(\mathrm{GeV/c})^2 < 0.2$					
Bin	$\cos\theta_M$	A_d^T	σ_{Stat}	σ_{Syst}	σ_{Tot}
1	-0.900	-0.028	0.005	0.004	0.006
2	-0.850	-0.017	0.005	0.003	0.005
3	-0.750	-0.002	0.005	0.000	0.005
4	-0.650	0.006	0.005	0.004	0.006
5	-0.550	0.027	0.005	0.003	0.005
6	-0.450	0.032	0.005	0.003	0.006
7	-0.350	0.036	0.005	0.004	0.006
8	-0.250	0.044	0.005	0.004	0.006
9	-0.150	0.043	0.005	0.004	0.006
10	-0.050	0.048	0.005	0.004	0.007
11	0.050	0.043	0.005	0.004	0.006
12	0.150	0.041	0.005	0.004	0.006
13	0.250	0.041	0.005	0.004	0.006
14	0.351	0.030	0.004	0.003	0.005
15	0.450	0.010	0.004	0.001	0.005
16	0.550	-0.010	0.004	0.001	0.005
17	0.651	-0.034	0.004	0.003	0.005
18	0.750	-0.056	0.004	0.005	0.007
19	0.851	-0.089	0.005	0.008	0.009
20	0.950	-0.125	0.005	0.011	0.012

A_d^T Values Vs. $\cos\theta_M$, $0.2 < Q^2/(\mathrm{GeV/c})^2 < 0.3$					
Bin	$\cos\theta_M$	A_d^T	σ_{Stat}	σ_{Syst}	σ_{Tot}
1	-0.951	-0.065	0.007	0.009	0.011
2	-0.851	-0.038	0.007	0.006	0.009
3	-0.751	-0.025	0.007	0.003	0.007
4	-0.651	-0.000	0.007	0.000	0.007
5	-0.550	0.013	0.007	0.001	0.007
6	-0.449	0.022	0.007	0.002	0.007
7	-0.350	0.049	0.007	0.005	0.009
8	-0.250	0.052	0.007	0.005	0.009
9	-0.150	0.050	0.007	0.005	0.009
10	-0.050	0.048	0.007	0.004	0.008
11	0.050	0.059	0.007	0.005	0.009
12	0.150	0.057	0.007	0.005	0.009
13	0.250	0.049	0.007	0.005	0.008
14	0.350	0.037	0.007	0.003	0.008
15	0.450	0.020	0.007	0.003	0.007
16	0.550	-0.000	0.007	0.000	0.007
17	0.650	-0.019	0.007	0.002	0.007
18	0.751	-0.038	0.007	0.003	0.008
19	0.851	-0.068	0.007	0.006	0.009
20	0.951	-0.117	0.007	0.011	0.013

A_d^T Values Vs. $\cos\theta_M$, $0.3 < Q^2/(\mathrm{GeV/c})^2 < 0.4$					
Bin	$\cos\theta_M$	A_d^T	σ_{Stat}	σ_{Syst}	σ_{Tot}
1	-0.951	-0.095	0.010	0.013	0.016
2	-0.851	-0.047	0.010	0.007	0.012
3	-0.750	-0.043	0.010	0.006	0.012
4	-0.651	-0.013	0.010	0.008	0.013
5	-0.550	0.009	0.010	0.001	0.010
6	-0.450	0.026	0.010	0.003	0.011
7	-0.350	0.042	0.010	0.004	0.011
8	-0.250	0.046	0.010	0.004	0.011
9	-0.150	0.060	0.010	0.006	0.012
10	-0.050	0.045	0.010	0.004	0.011
11	0.050	0.057	0.010	0.005	0.011
12	0.151	0.048	0.010	0.004	0.011
13	0.250	0.050	0.010	0.005	0.011
14	0.349	0.030	0.010	0.003	0.010
15	0.450	0.017	0.010	0.002	0.010
16	0.551	0.004	0.010	0.000	0.010
17	0.650	-0.004	0.009	0.000	0.009
18	0.750	-0.046	0.010	0.004	0.011
19	0.851	-0.051	0.009	0.005	0.010
20	0.950	-0.092	0.010	0.008	0.013

A_d^T Values Vs. $\cos\theta_M$, $0.4 < Q^2/(\mathrm{GeV/c})^2 < 0.5$					
Bin	$\cos\theta_M$	A_d^T	σ_{Stat}	σ_{Syst}	σ_{Tot}
1	-0.951	-0.099	0.025	0.013	0.028
2	-0.851	-0.066	0.026	0.010	0.028
3	-0.751	-0.048	0.025	0.006	0.026
4	-0.651	-0.000	0.025	0.000	0.025
5	-0.551	0.004	0.024	0.000	0.024
6	-0.449	0.040	0.024	0.004	0.024
7	-0.350	0.031	0.023	0.003	0.024
8	-0.250	0.048	0.024	0.004	0.025
9	-0.150	0.062	0.025	0.006	0.025
10	-0.051	0.036	0.025	0.003	0.025
11	0.052	0.044	0.026	0.004	0.026
12	0.149	0.055	0.027	0.005	0.028
13	0.250	0.037	0.027	0.003	0.027
14	0.349	0.000	0.027	0.000	0.027
15	0.450	0.003	0.027	0.000	0.027
16	0.551	0.009	0.028	0.001	0.028
17	0.652	-0.011	0.026	0.001	0.026
18	0.749	-0.008	0.029	0.001	0.029
19	0.852	-0.082	0.033	0.007	0.034
20	0.950	-0.067	0.030	0.006	0.031

6.3 Residual Values

The following set of tables gives bin-by-bin residual values for all of the asymmetry values as well as their corresponding total overall errors. The headings in each table refer to the following:

Bin	:	bin number
p_M	:	average p_M value for the bin
$\cos\theta_M$	:	average $\cos\theta_M$ value for the bin
ΔA_{BONN}	:	residual as compared to the total Bonn model
$\sigma_{\Delta A_{BONN}}$	:	total error for the Bonn model residual
ΔA_{V18}	:	residual as compared to the total V18 model
$\sigma_{\Delta A_{V18}}$	:	total error for the V18 model residual
ΔA_{PARIS}	:	residual as compared to the total Paris model
$\sigma_{\Delta A_{PARIS}}$	:	total error for the Paris model residual

A_d^T Residuals Vs. p_M for Perp Kine, $0.1 < Q^2/(\mathrm{GeV/c})^2 < 0.2$							
Bin	p_M (GeV/c)	ΔA_{BONN}	$\sigma_{\Delta A_{BONN}}$	ΔA_{V18}	$\sigma_{\Delta A_{V18}}$	ΔA_{PARIS}	$\sigma_{\Delta A_{PARIS}}$
1	0.035	-0.000	0.004	-0.000	0.004	-0.000	0.004
2	0.072	-0.002	0.004	-0.001	0.004	-0.001	0.004
3	0.120	0.002	0.005	0.005	0.005	0.005	0.005
4	0.170	0.005	0.010	0.013	0.010	0.013	0.010
5	0.221	0.060	0.043	0.079	0.043	0.076	0.043
6	0.270	0.076	0.036	0.102	0.036	0.096	0.036
7	0.323	0.059	0.064	0.081	0.064	0.077	0.064
8	0.371	-0.043	0.058	-0.020	0.058	-0.016	0.058
9	0.418	-0.101	0.087	-0.068	0.087	-0.055	0.087
10	0.471	0.002	0.150	0.041	0.150	0.063	0.150

A_d^T Residuals Vs. p_M for Para Kine, $0.1 < Q^2/(\mathrm{GeV/c})^2 < 0.2$							
Bin	p_M (GeV/c)	ΔA_{BONN}	$\sigma_{\Delta A_{BONN}}$	ΔA_{V18}	$\sigma_{\Delta A_{V18}}$	ΔA_{PARIS}	$\sigma_{\Delta A_{PARIS}}$
1	0.035	-0.005	0.003	-0.005	0.003	-0.005	0.003
2	0.072	0.000	0.003	0.000	0.003	-0.000	0.003
3	0.120	-0.014	0.006	-0.012	0.006	-0.014	0.006
4	0.170	-0.052	0.010	-0.048	0.010	-0.047	0.010
5	0.221	-0.051	0.066	-0.046	0.066	-0.040	0.066
6	0.271	-0.070	0.043	-0.073	0.043	-0.065	0.043
7	0.320	0.026	0.062	0.010	0.062	0.019	0.062
8	0.371	0.091	0.065	0.057	0.065	0.062	0.065
9	0.424	0.097	0.075	0.048	0.075	0.047	0.075
10	0.471	-0.032	0.102	-0.083	0.102	-0.084	0.102

A_d^T Residuals Vs. p_M for Perp Kine, $0.2 < Q^2/(\mathrm{GeV/c})^2 < 0.3$							
Bin	p_M (GeV/c)	ΔA_{BONN}	$\sigma_{\Delta A_{BONN}}$	ΔA_{V18}	$\sigma_{\Delta A_{V18}}$	ΔA_{PARIS}	$\sigma_{\Delta A_{PARIS}}$
1	0.035	-0.002	0.005	-0.002	0.005	-0.002	0.005
2	0.073	-0.001	0.004	-0.001	0.004	-0.000	0.004
3	0.121	-0.004	0.008	-0.002	0.008	-0.002	0.008
4	0.170	0.009	0.016	0.014	0.016	0.015	0.016
5	0.221	0.056	0.034	0.068	0.034	0.070	0.034
6	0.272	0.073	0.047	0.094	0.047	0.096	0.047
7	0.319	0.102	0.078	0.130	0.078	0.131	0.078
8	0.371	0.111	0.135	0.151	0.135	0.155	0.135
9	0.416	0.257	0.245	0.306	0.245	0.317	0.245
10	0.471	-0.223	0.438	-0.173	0.438	-0.156	0.438

A_d^T Residuals Vs. p_M for Para Kine, $0.2 < Q^2/(\mathrm{GeV/c})^2 < 0.3$							
Bin	p_M (GeV/c)	ΔA_{BONN}	$\sigma_{\Delta A_{BONN}}$	ΔA_{V18}	$\sigma_{\Delta A_{V18}}$	ΔA_{PARIS}	$\sigma_{\Delta A_{PARIS}}$
1	0.035	0.002	0.005	0.002	0.005	0.001	0.005
2	0.073	-0.006	0.004	-0.006	0.004	-0.006	0.004
3	0.121	-0.006	0.007	-0.005	0.007	-0.006	0.007
4	0.171	-0.021	0.016	-0.018	0.016	-0.017	0.016
5	0.221	-0.062	0.022	-0.052	0.022	-0.048	0.022
6	0.271	-0.010	0.030	0.002	0.030	0.011	0.030
7	0.320	-0.049	0.051	-0.047	0.051	-0.042	0.051
8	0.369	-0.077	0.087	-0.102	0.087	-0.106	0.087
9	0.426	-0.017	0.146	-0.051	0.146	-0.059	0.146
10	0.469	-0.022	0.183	-0.056	0.183	-0.061	0.183

A_d^T Residuals Vs. p_M for Perp Kine, $0.3 < Q^2/(\text{GeV/c})^2 < 0.4$							
Bin	p_M (GeV/c)	ΔA_{BONN}	$\sigma_{\Delta A_{BONN}}$	ΔA_{V18}	$\sigma_{\Delta A_{V18}}$	ΔA_{PARIS}	$\sigma_{\Delta A_{PARIS}}$
1	0.036	0.011	0.009	0.012	0.009	0.012	0.009
2	0.074	0.004	0.006	0.005	0.006	0.005	0.006
3	0.121	-0.002	0.011	-0.001	0.011	-0.000	0.011
4	0.171	0.013	0.024	0.016	0.024	0.017	0.024
5	0.221	0.008	0.039	0.014	0.039	0.018	0.039
6	0.271	0.024	0.066	0.035	0.066	0.043	0.066
7	0.322	0.110	0.109	0.123	0.109	0.132	0.109
8	0.374	0.051	0.157	0.069	0.157	0.077	0.157
9	0.416	0.172	0.250	0.205	0.250	0.210	0.250
10	0.480	0.494	95.819	0.539	95.819	0.544	95.819

A_d^T Residuals Vs. p_M for Para Kine, $0.3 < Q^2/(\text{GeV/c})^2 < 0.4$							
Bin	p_M (GeV/c)	ΔA_{BONN}	$\sigma_{\Delta A_{BONN}}$	ΔA_{V18}	$\sigma_{\Delta A_{V18}}$	ΔA_{PARIS}	$\sigma_{\Delta A_{PARIS}}$
1	0.035	-0.002	0.009	-0.001	0.009	-0.001	0.009
2	0.074	-0.008	0.007	-0.006	0.007	-0.007	0.007
3	0.121	-0.034	0.011	-0.032	0.011	-0.033	0.011
4	0.171	-0.041	0.022	-0.038	0.022	-0.037	0.022
5	0.221	-0.080	0.049	-0.072	0.049	-0.068	0.049
6	0.273	-0.048	0.069	-0.029	0.069	-0.023	0.069
7	0.323	-0.011	0.076	0.015	0.076	0.024	0.076
8	0.368	0.053	0.136	0.071	0.136	0.079	0.136
9	0.422	0.067	0.264	0.065	0.264	0.066	0.264
10	0.469	-0.313	0.389	-0.325	0.389	-0.330	0.389

A_d^T Residuals Vs. p_M for Perp Kine, $0.4 < Q^2/(\mathrm{GeV/c})^2 < 0.5$							
Bin	p_M (GeV/c)	ΔA_{BONN}	$\sigma_{\Delta A_{BONN}}$	ΔA_{V18}	$\sigma_{\Delta A_{V18}}$	ΔA_{PARIS}	$\sigma_{\Delta A_{PARIS}}$
1	0.035	0.007	0.014	0.007	0.014	0.007	0.014
2	0.074	0.017	0.010	0.018	0.010	0.018	0.010
3	0.122	-0.014	0.020	-0.013	0.020	-0.012	0.020
4	0.171	-0.004	0.061	-0.003	0.061	-0.001	0.061
5	0.222	0.010	0.247	0.013	0.247	0.019	0.247
6	0.271	0.104	2.091	0.109	2.091	0.121	2.091
7	0.323	0.043	0.183	0.048	0.183	0.062	0.183
8	0.370	0.157	0.268	0.161	0.268	0.169	0.268
9	0.418	0.156	0.314	0.161	0.314	0.164	0.314
10	0.473	0.334	2.387	0.342	2.387	0.340	2.387

A_d^T Residuals Vs. p_M for Para Kine, $0.4 < Q^2/(\mathrm{GeV/c})^2 < 0.5$							
Bin	p_M (GeV/c)	ΔA_{BONN}	$\sigma_{\Delta A_{BONN}}$	ΔA_{V18}	$\sigma_{\Delta A_{V18}}$	ΔA_{PARIS}	$\sigma_{\Delta A_{PARIS}}$
1	0.035	-0.015	0.019	-0.013	0.019	-0.014	0.019
2	0.074	-0.024	0.013	-0.023	0.013	-0.023	0.013
3	0.121	-0.028	0.030	-0.025	0.030	-0.026	0.030
4	0.171	-0.036	0.608	-0.031	0.608	-0.031	0.608
5	0.219	-0.062	0.146	-0.054	0.146	-0.052	0.146
6	0.273	0.015	0.135	0.035	0.135	0.041	0.135
7	0.323	-0.032	11.938	0.008	11.938	0.019	11.938
8	0.369	-0.081	2.904	-0.036	2.904	-0.021	2.904
9	0.419	0.048	1.063	0.089	1.063	0.102	1.063
10	0.475	0.651	178.654	0.680	178.654	0.688	178.654

A_{ed}^{V} Residuals Vs. p_M for Perp Kine, $0.1 < Q^2/(\mathrm{GeV/c})^2 < 0.2$							
Bin	p_M (GeV/c)	ΔA_{BONN}	$\sigma_{\Delta A_{BONN}}$	ΔA_{V18}	$\sigma_{\Delta A_{V18}}$	ΔA_{PARIS}	$\sigma_{\Delta A_{PARIS}}$
1	0.035	0.000	0.008	0.000	0.008	0.000	0.008
2	0.072	0.001	0.007	0.001	0.007	0.001	0.007
3	0.120	0.002	0.009	0.002	0.009	0.002	0.009
4	0.170	0.008	0.014	0.010	0.014	0.009	0.014
5	0.221	0.019	0.025	0.020	0.025	0.019	0.025
6	0.270	0.040	0.041	0.040	0.041	0.037	0.041
7	0.323	0.009	0.058	0.004	0.058	0.004	0.058
8	0.371	0.046	0.081	0.029	0.081	0.039	0.081
9	0.418	0.108	0.127	0.078	0.127	0.104	0.127
10	0.471	-0.100	0.200	-0.134	0.200	-0.096	0.200

A_{ed}^{V} Residuals Vs. p_M for Para Kine, $0.1 < Q^2/(\mathrm{GeV/c})^2 < 0.2$							
Bin	p_M (GeV/c)	ΔA_{BONN}	$\sigma_{\Delta A_{BONN}}$	ΔA_{V18}	$\sigma_{\Delta A_{V18}}$	ΔA_{PARIS}	$\sigma_{\Delta A_{PARIS}}$
1	0.035	0.005	0.008	0.005	0.008	0.005	0.008
2	0.072	0.004	0.008	0.004	0.008	0.004	0.008
3	0.120	0.001	0.010	0.001	0.010	0.001	0.010
4	0.170	0.015	0.015	0.014	0.015	0.013	0.015
5	0.221	-0.010	0.022	-0.012	0.022	-0.014	0.022
6	0.271	-0.004	0.034	-0.003	0.034	-0.006	0.034
7	0.320	0.011	0.051	0.013	0.051	0.011	0.051
8	0.371	-0.003	0.076	-0.007	0.076	-0.006	0.076
9	0.424	0.026	0.106	0.009	0.106	0.019	0.106
10	0.471	0.083	0.150	0.057	0.150	0.077	0.150

A_{ed}^{V} Residuals Vs. p_M for Perp Kine, $0.2 < Q^2/(\mathrm{GeV/c})^2 < 0.3$							
Bin	p_M (GeV/c)	ΔA_{BONN}	$\sigma_{\Delta A_{BONN}}$	ΔA_{V18}	$\sigma_{\Delta A_{V18}}$	ΔA_{PARIS}	$\sigma_{\Delta A_{PARIS}}$
1	0.035	0.012	0.012	0.012	0.012	0.012	0.012
2	0.073	0.028	0.010	0.028	0.010	0.028	0.010
3	0.121	0.031	0.013	0.032	0.013	0.031	0.013
4	0.170	0.060	0.019	0.061	0.019	0.061	0.019
5	0.221	0.044	0.033	0.047	0.033	0.046	0.033
6	0.272	0.075	0.049	0.077	0.049	0.076	0.049
7	0.319	0.077	0.084	0.072	0.084	0.073	0.084
8	0.371	0.243	0.221	0.224	0.221	0.237	0.221
9	0.416	0.222	0.434	0.196	0.434	0.226	0.434
10	0.471	0.171	0.574	0.145	0.574	0.185	0.574

A_{ed}^{V} Residuals Vs. p_M for Para Kine, $0.2 < Q^2/(\mathrm{GeV/c})^2 < 0.3$							
Bin	p_M (GeV/c)	ΔA_{BONN}	$\sigma_{\Delta A_{BONN}}$	ΔA_{V18}	$\sigma_{\Delta A_{V18}}$	ΔA_{PARIS}	$\sigma_{\Delta A_{PARIS}}$
1	0.035	0.016	0.012	0.015	0.012	0.015	0.012
2	0.073	0.018	0.012	0.017	0.012	0.017	0.012
3	0.121	0.021	0.013	0.020	0.013	0.020	0.013
4	0.171	0.029	0.020	0.028	0.020	0.027	0.020
5	0.221	0.040	0.028	0.035	0.028	0.032	0.028
6	0.271	0.009	0.041	-0.001	0.041	-0.006	0.041
7	0.320	-0.025	0.065	-0.035	0.065	-0.038	0.065
8	0.369	-0.035	0.123	-0.047	0.123	-0.040	0.123
9	0.426	0.049	0.198	0.032	0.198	0.052	0.198
10	0.469	0.163	0.288	0.144	0.288	0.172	0.288

A_{ed}^{V} Residuals Vs. p_M for Perp Kine, $0.3 < Q^2/(\mathrm{GeV/c})^2 < 0.4$							
Bin	p_M (GeV/c)	ΔA_{BONN}	$\sigma_{\Delta A_{BONN}}$	ΔA_{V18}	$\sigma_{\Delta A_{V18}}$	ΔA_{PARIS}	$\sigma_{\Delta A_{PARIS}}$
1	0.036	0.025	0.018	0.025	0.018	0.025	0.018
2	0.074	0.035	0.015	0.035	0.015	0.035	0.015
3	0.121	0.050	0.018	0.051	0.018	0.051	0.018
4	0.171	0.074	0.030	0.076	0.030	0.075	0.030
5	0.221	0.091	0.054	0.094	0.054	0.092	0.054
6	0.271	0.112	0.092	0.115	0.092	0.113	0.092
7	0.322	0.085	0.122	0.085	0.122	0.084	0.122
8	0.374	0.034	0.222	0.028	0.222	0.032	0.222
9	0.416	0.244	0.415	0.230	0.415	0.246	0.415
10	0.480	0.638	333.056	0.629	333.056	0.661	333.056

A_{ed}^{V} Residuals Vs. p_M for Para Kine, $0.3 < Q^2/(\mathrm{GeV/c})^2 < 0.4$							
Bin	p_M (GeV/c)	ΔA_{BONN}	$\sigma_{\Delta A_{BONN}}$	ΔA_{V18}	$\sigma_{\Delta A_{V18}}$	ΔA_{PARIS}	$\sigma_{\Delta A_{PARIS}}$
1	0.035	0.022	0.018	0.021	0.018	0.021	0.018
2	0.074	0.028	0.016	0.028	0.016	0.028	0.016
3	0.121	0.047	0.020	0.047	0.020	0.047	0.020
4	0.171	0.055	0.036	0.054	0.036	0.053	0.036
5	0.221	0.075	0.061	0.071	0.061	0.067	0.061
6	0.273	0.008	0.106	-0.007	0.106	-0.015	0.106
7	0.323	0.084	0.109	0.059	0.109	0.048	0.109
8	0.368	0.004	0.200	-0.021	0.200	-0.026	0.200
9	0.422	0.018	0.341	-0.001	0.341	0.011	0.341
10	0.469	0.262	0.822	0.266	0.822	0.298	0.822

A_{ed}^{V} Residuals Vs. p_M for Perp Kine, $0.4 < Q^2/(\text{GeV/c})^2 < 0.5$							
Bin	p_M (GeV/c)	ΔA_{BONN}	$\sigma_{\Delta A_{BONN}}$	ΔA_{V18}	$\sigma_{\Delta A_{V18}}$	ΔA_{PARIS}	$\sigma_{\Delta A_{PARIS}}$
1	0.035	0.042	0.025	0.042	0.025	0.042	0.025
2	0.074	0.057	0.020	0.057	0.020	0.058	0.020
3	0.122	0.070	0.032	0.071	0.032	0.070	0.032
4	0.171	0.081	0.111	0.083	0.111	0.082	0.111
5	0.222	0.056	0.574	0.059	0.574	0.056	0.574
6	0.271	0.016	11.362	0.020	11.362	0.014	11.362
7	0.323	0.036	0.255	0.043	0.255	0.036	0.255
8	0.370	-0.059	0.328	-0.055	0.328	-0.058	0.328
9	0.418	-0.112	0.423	-0.113	0.423	-0.112	0.423
10	0.473	0.273	1.998	0.265	1.998	0.272	1.998

A_{ed}^{V} Residuals Vs. p_M for Para Kine, $0.4 < Q^2/(\text{GeV/c})^2 < 0.5$							
Bin	p_M (GeV/c)	ΔA_{BONN}	$\sigma_{\Delta A_{BONN}}$	ΔA_{V18}	$\sigma_{\Delta A_{V18}}$	ΔA_{PARIS}	$\sigma_{\Delta A_{PARIS}}$
1	0.035	0.043	0.031	0.043	0.031	0.043	0.031
2	0.074	0.034	0.025	0.034	0.025	0.035	0.025
3	0.121	0.067	0.058	0.067	0.058	0.067	0.058
4	0.171	0.107	4.774	0.107	4.774	0.105	4.774
5	0.219	0.137	0.363	0.134	0.363	0.128	0.363
6	0.273	0.107	0.207	0.089	0.207	0.079	0.207
7	0.323	-0.005	37.199	-0.042	37.199	-0.058	37.199
8	0.369	0.259	2.706	0.215	2.706	0.200	2.706
9	0.419	0.219	1.481	0.185	1.481	0.178	1.481
10	0.475	0.677	121.324	0.660	121.324	0.662	121.324

A_d^T Residuals Vs. $\cos\theta_M$, $0.1 < Q^2/(\mathrm{GeV/c})^2 < 0.2$			
Bin	$\cos\theta_M$	ΔA_{BONN}	$\sigma_{\Delta A_{BONN}}$
1	-0.900	0.013	0.006
2	-0.850	0.010	0.005
3	-0.750	0.004	0.005
4	-0.650	-0.001	0.006
5	-0.550	0.005	0.005
6	-0.450	-0.000	0.006
7	-0.350	-0.003	0.006
8	-0.250	-0.002	0.006
9	-0.150	-0.004	0.006
10	-0.050	-0.005	0.007
11	0.050	-0.010	0.006
12	0.150	-0.009	0.006
13	0.250	-0.001	0.006
14	0.351	-0.003	0.005
15	0.450	-0.008	0.005
16	0.550	-0.011	0.005
17	0.651	-0.012	0.005
18	0.750	-0.010	0.007
19	0.851	-0.007	0.009
20	0.950	-0.008	0.012

A_d^T Residuals Vs. $\cos\theta_M$, $0.2 < Q^2/(\mathrm{GeV/c})^2 < 0.3$			
Bin	$\cos\theta_M$	ΔA_{BONN}	$\sigma_{\Delta A_{BONN}}$
1	-0.951	0.014	0.011
2	-0.851	0.005	0.009
3	-0.751	-0.009	0.007
4	-0.651	-0.003	0.007
5	-0.550	-0.007	0.007
6	-0.449	-0.012	0.007
7	-0.350	0.006	0.009
8	-0.250	-0.000	0.009
9	-0.150	-0.010	0.009
10	-0.050	-0.014	0.008
11	0.050	-0.001	0.009
12	0.150	-0.001	0.009
13	0.250	0.002	0.008
14	0.350	0.001	0.008
15	0.450	-0.002	0.007
16	0.550	-0.005	0.007
17	0.650	-0.005	0.007
18	0.751	-0.002	0.008
19	0.851	-0.005	0.009
20	0.951	-0.024	0.013

A_d^T Residuals Vs. $\cos\theta_M$, $0.3 < Q^2/(\mathrm{GeV/c})^2 < 0.4$			
Bin	$\cos\theta_M$	ΔA_{BONN}	$\sigma_{\Delta A_{BONN}}$
1	-0.951	-0.000	0.016
2	-0.851	0.006	0.012
3	-0.750	-0.021	0.012
4	-0.651	-0.011	0.013
5	-0.550	-0.008	0.010
6	-0.450	-0.008	0.011
7	-0.350	-0.004	0.011
8	-0.250	-0.008	0.011
9	-0.150	-0.001	0.012
10	-0.050	-0.018	0.011
11	0.050	-0.005	0.011
12	0.151	-0.008	0.011
13	0.250	0.004	0.011
14	0.349	-0.005	0.010
15	0.450	-0.008	0.010
16	0.551	-0.008	0.010
17	0.650	-0.000	0.009
18	0.750	-0.024	0.011
19	0.851	-0.008	0.010
20	0.950	-0.028	0.013

A_d^T Residuals Vs. $\cos\theta_M$, $0.4 < Q^2/(\mathrm{GeV/c})^2 < 0.5$			
Bin	$\cos\theta_M$	ΔA_{BONN}	$\sigma_{\Delta A_{BONN}}$
1	-0.951	-0.021	0.028
2	-0.851	-0.022	0.028
3	-0.751	-0.029	0.026
4	-0.651	-0.004	0.025
5	-0.551	-0.017	0.024
6	-0.449	0.004	0.024
7	-0.350	-0.016	0.024
8	-0.250	-0.006	0.025
9	-0.150	0.001	0.025
10	-0.051	-0.026	0.025
11	0.052	-0.015	0.026
12	0.149	0.005	0.028
13	0.250	-0.006	0.027
14	0.349	-0.034	0.027
15	0.450	-0.021	0.027
16	0.551	-0.004	0.028
17	0.652	-0.009	0.026
18	0.749	0.010	0.029
19	0.852	-0.047	0.034
20	0.950	-0.016	0.031

Bibliography

[1] D. Abbott et al. Phenomenology of the deuteron electromagnetic form factors. *Eur. Phys. J.*, A7:421–427, 2000.

[2] W. E. Adams. *Pockels cells: Theory, test procedures, characteristics*, 1968. UCRL-50463.

[3] A. Afanasev, I. Akushevich, and N. Merenkov. Model independent radiative corrections in processes of polarized electron-nucleon elastic scattering. *Phys. Rev.*, D64:113009, 2001.

[4] I. Akushevich, A. Ilyichev, and N. Shumeiko. Radiative effects in scattering of polarized leptons by polarized nucleons and light nuclei. hep-ph/0106180, 2001.

[5] W. Albrecht et al. Elastic electron-proton scattering at momentum transfers up to 245 fm^{-2}. *Phys. Rev. Lett.*, 18:1014, 1967.

[6] H. Arenhovel, W. Leidemann, and E. L. Tomusiak. The role of the neutron electric form-factor in d(e,e'N)N including polarization observables. *Z. Phys.*, A331:123–138, 1988.

[7] H. Arenhovel, W. Leidemann, and E. L. Tomusiak. Exclusive deuteron electrodisintegration with polarized electrons and a polarized target. *Phys. Rev.*, C46:455–470, 1992.

[8] A. G. A. M. Armstrong, C. P. Riley, and J. Simkin. *TOSCA User Guide: Three-Dimensional Static Electromagnetic / Electrostatic Analysis Package: Version 3.1 May 1982.* RL-81-070.

[9] R. Arnold, C. Carlson, and F. Gross. Polarization transfer in elastic scattering from nucleons and deuterons. *Phys. Rev.*, C23:363–374, 1981.

[10] J. Arrington. How well do we know the electromagnetic form factors of the proton? *Phys. Rev.*, C68:034325, 2003.

[11] A. Beiser. *Concepts of Modern Physic.* McGraw-Hill, 1995.

[12] P. Bevington and D. Robinson. *Data Reduction and Error Analysis for the Physical Sciences.* McGraw-Hill Science, 2002.

[13] S. Biagi. Monte carlo simulation of electron drift and diffusion in counting gases under the influence of electric and magnetic fields. *Nucl. Instr. and Meth.*, A42:234–240, 1999.

[14] The BLAST Collaboration. *MIT-Bates South Hall Ring Technical Design Report*, 1994. Internal report.

[15] W. Blum and L. Rolandi. *Particle Detection with Drift Chambers.* Springer-Verlag, 1993.

[16] CERN Application Software Group. *GEANT: Detector Description and Simulation Tool*, 1994.

[17] C. Crawford. *Precision Measurement of the Proton Electric to Magentic Form Factor Ratio with BLAST.* PhD thesis, Massachusetts Institute of Technology, 2005.

[18] L. Dalesio et al. The Experimental Physics and Industrial Control System architecture: Past, present, and future. Technical report, Los Alamos National Laboratory, 2005.

[19] T. W. Donnelly and A. S. Raskin. Considerations of polarization in inclusive electron scattering from nuclei. *Ann. of Phys.*, 169:247–351, 1986.

[20] K. Dow. Personal correspondence.

[21] Dow Corning. *Sylgard High Voltage Insulator Coating*, 2003. Product Information Sheet.

[22] DuPont, Inc. *Delrin Acetal Resin*, 1956. Product Information Sheet.

[23] M. Farkhondeh et al. Operation of the MIT-Bates polarized source for a high average current storage ring. In *Proceedings for the SPIN 2004 Conference, Trieste, Italy*, 2005.

[24] M. Ferro-Luzzi et al. Measurement of tensor analyzing powers for elastic electron scattering from a polarized h-2 target internal to a storage ring. *Phys. Rev. Lett.*, 77:2630–2633, 1996.

[25] J. L. Forest et al. Femtometer toroidal structures in nuclei. *Phys. Rev.*, C54:646–667, 1996.

[26] W. Franklin et al. The MIT-Bates South Hall Ring: A unique instrument for studying polarization. In *Proceedings for the SPIN 2004 Conference, Trieste, Italy*, 2005.

[27] J. Friedrich and T. Walcher. A coherent interpretation of the form factors of the nucleon in terms of a pion cloud and constituent quarks. *Eur. Phys. J.*, A17:607–623, 2003.

[28] M. Garcon and J. W. Van Orden. The deuteron: Structure and form factors. *Adv. Nucl. Phys.*, 26:293, 2001.

[29] E. Ihloff et al. Hydrogen/deuterium polarized target at MIT-Bates. In *Proceedings for the SPIN 2004 Conference, Trieste, Italy*, 2005.

[30] J. D. Jackson. *Classical Electrodynamics*. John Wiley and Sons, New York, 1998.

[31] P. Kirk et al. Elastic electron-proton scattering at large four momentum transfer. *Phys. Rev.*, D8:63–91, 1973.

[32] M. Lacombe et al. Parametrization of the paris NN potential. *Phys. Rev.*, C21:861–873, 1980.

[33] LeCroy Research Systems. *2373 16 x 16 Memory Lookup Unit*, 1995. Product Data Sheet, www.lecroy.com.

[34] LeCroy Research Systems. *1875A 15-Bit High Resolution Time-To-Digital Converter*, 1996. Product Data Sheet, www.lecroy.com.

[35] LeCroy Research Systems. *1881M Fast Converting, 13-Bit Charge Analog-to-Digital Converter*, 1996. Product Data Sheet, www.lecroy.com.

[36] LeCroy Research Systems. *3420 Constant Fraction Discriminator*, 1996. Product Data Sheet, www.lecroy.com.

[37] LeCroy Research Systems. *1458HP High Density HV Crate*, 1997. Operator's manual.

[38] LeCroy Research Systems. *3412/3412E 16-Channel, 200 MHz Discriminators*, 1997. Product Data Sheet, www.lecroy.com.

[39] T. Lee. Tension measuring device for blast wire chambers. BLAST Internal report, 2005.

[40] R. Machleidt. The high-precision, charge-dependent bonn nucleon-nucleon potential (cd-bonn). *Phys. Rev.*, C63:024001, 2001.

[41] R. Machleidt, K. Holinde, and C. Elster. The bonn meson exchange model for the nucleon nucleon interaction. *Phys. Rept.*, 149:1–89, 1987.

[42] N. Meitanis. Personal correspondence.

[43] D. Nikolenk et al. Measurement of the tensor analyzing powers t20 and t21 in elastic electron-deuteron scattering. *Phys. Rev. Lett.*, 70:072501, 2003.

[44] I. Passchier et al. Spin-momentum correlations in quasielastic electron scattering from deuterium. *Phys. Rev. Lett.*, 88:102302, 2002.

[45] G. Poulis. *Aspects of Polarization In Quasi-Free Electron Scattering*. PhD thesis, Massachusetts Institute of Technology, 1992.

[46] W. Press et al. *Numerical Recipes in C.* Cambridge University Press, 1998.

[47] A. S. Raskin and T. W. Donnelly. Polarization in coincidence electron scattering from nuclei. *Ann. of Phys.*, 191:78–142, 1989.

[48] A. Roth. *Vacuum Technology.* North-Holland, Amsterdam, 1982.

[49] Saint-Gobain Ceramics and Plastics. *BC-400, BC-404, BC-408, BC-412, BC-416 Premium Plastic Scintillators*, 2002. Product Data Sheet.

[50] J. J. Sakurai. *Modern Quantum Mechanics.* Addison-Wesley, 1994.

[51] F. Sauli. *Principles of Operation of Multiwire Proportional and Drift Chambers.* Lectures given in the Academic Programme of CERN 1975-1976, 1977.

[52] R. Serway. *Physics for Scientists and Engineers With Modern Physics.* Holt Rinehart and Winston, 1996.

[53] E. Tsentalovich. Personal correspondence.

[54] K. Unser. The parametric current transformer: A beam current monitor deleveoped for LEP. *AIP Conf. Proc.*, 252:266–275, 1991.

[55] F. Werner and H. Arenhovel. Electrodisintegration of deuterium including nucleon detection in coincidence. *Nucl. Phys.*, A314:253–286, 1979.

[56] R. B. Wiringa, V. G. J. Stoks, and R. Schiavilla. An accurate nucleon-nucleon potential with charge independence breaking. *Phys. Rev.*, C51:38–51, 1995.

[57] S. Wong. *Introductory Nuclear Physics.* John Wiley and Sons, Inc., 1998.

[58] C. Zhang. Personal correspondence.

[59] Z. Zhou. *A Study of the Spin Dependence of Electron Scattering from a Tensor Polarized Deuterium Internal Target.* PhD thesis, University of Wisconsin - Madison, 1992.

[60] Z. L. Zhou et al. Performance of a polarized deuterium internal target in a medium-energy electron storage ring. *Nucl. Instrum. Meth.*, A378:40–56, 1996.

[61] V. Ziskin. *Measurement of the Electric Form Factor of the Neutron at Low Q^2 from a Vector Polarized Deuterium Target at BLAST*. PhD thesis, Massachusetts Institute of Technology, 2005.

[62] T. Zwart. *Polarized Electrons at the Bates Accelerator Center South Hall Ring: Extracted Beams and Internal Targets*. PhD thesis, Boston University, 1986.